



HAL
open science

Influence of the Pressure on the Multiferroicity of RMn₂O₅

Wei Peng

► **To cite this version:**

Wei Peng. Influence of the Pressure on the Multiferroicity of RMn₂O₅. Strongly Correlated Electrons [cond-mat.str-el]. Université Paris Saclay (COMUE), 2018. English. NNT: 2018SACLS296 . tel-01897078v2

HAL Id: tel-01897078

<https://theses.hal.science/tel-01897078v2>

Submitted on 2 Nov 2018

HAL is a multi-disciplinary open access archive for the deposit and dissemination of scientific research documents, whether they are published or not. The documents may come from teaching and research institutions in France or abroad, or from public or private research centers.

L'archive ouverte pluridisciplinaire **HAL**, est destinée au dépôt et à la diffusion de documents scientifiques de niveau recherche, publiés ou non, émanant des établissements d'enseignement et de recherche français ou étrangers, des laboratoires publics ou privés.

Influence of the Pressure on the Multiferroicity of RMn_2O_5

Thèse de doctorat de l'Université Paris-Saclay
préparée à Université Paris-Sud

École doctorale n° 564: Physique en Île de France
Spécialité de doctorat: Physique

Thèse présentée et soutenue à Orsay, le 18 Septembre 2018, par

M. Wei PENG

Composition du jury:

M. Fabrice Bert	Professeur	Président
Université Paris-Sud, Laboratoire de Physique des Solides		
Mme Gwenaëlle Rousse	Maître de Conférences	Rapporteur
Sorbonne Université / Collège de France, Chimie du solide et énergie		
M. Pierre Bordet	Directeur de recherche	Rapporteur
CNRS, Institut Néel		
Mme Virginie Simonet	Directrice de recherche	Examinatrice
CNRS, Institut Néel		
Mme Pascale Foury-Leylekian	Professeur	Directrice
Université Paris-Sud, Laboratoire de Physique des Solides		
M. Victor Balédent	Maître de Conférences	Co-Directeur
Université Paris-Sud, Laboratoire de Physique des Solides		

Résumé en français

Introduction

On entend par multiferroïques des matériaux qui présentent simultanément plus d'un ordre ferroïque primaire en une seule phase, qui sont habituellement couplés les uns aux autres. Un grand nombre de matériaux multiferroïques avec diverses structures et compositions ont été récemment découverts. Ils présentent de nouveaux phénomènes physiques, dont certains ne peuvent être expliqués par les mécanismes existants. Parmi ces multiferroïques, les multiferroïques magnétoélectriques attirent énormément l'attention, en raison de leur physique fascinante, des mécanismes intéressants et de leurs applications industrielles potentielles.

Selon la thermodynamique, l'effet magnétoélectrique peut être compris dans le cadre théorique de Landau. L'effet ME est obtenu à partir de l'expansion de l'énergie libre, c'est-à-dire:

$$F(\mathbf{E}, \mathbf{H}) = F_0 - \mathbf{P}_i^S \mathbf{E}_i - \mathbf{M}_i^S \mathbf{H}_i - \frac{1}{2} \varepsilon_0 \varepsilon_{ij} \mathbf{E}_i \mathbf{E}_j - \frac{1}{2} \mu_0 \mu_{ij} \mathbf{H}_i \mathbf{H}_j - \alpha_{ij} \mathbf{E}_i \mathbf{H}_j - \frac{1}{2} \beta_{ijk} \mathbf{E}_i \mathbf{H}_j \mathbf{H}_k - \frac{1}{2} \gamma_{ijk} \mathbf{H}_i \mathbf{E}_j \mathbf{E}_k - \dots \quad (1)$$

Alors la polarisation est:

$$\mathbf{P}_i(\mathbf{E}, \mathbf{H}) = -\frac{\partial F}{\partial \mathbf{E}_i} = \mathbf{P}_i^S + \varepsilon_0 \varepsilon_{ij} \mathbf{E}_j + \alpha_{ij} \mathbf{H}_j + \frac{1}{2} \beta_{ijk} \mathbf{H}_j \mathbf{H}_k + \gamma_{ijk} \mathbf{H}_i \mathbf{E}_j + \dots \quad (2)$$

et l'aimantation est:

$$\mathbf{M}_i(\mathbf{E}, \mathbf{H}) = -\frac{\partial F}{\partial \mathbf{H}_i} = \mathbf{M}_i^S + \mu_0 \mu_{ij} \mathbf{H}_j + \alpha_{ij} \mathbf{E}_i + \beta_{ijk} \mathbf{E}_i \mathbf{H}_j + \frac{1}{2} \gamma_{ijk} \mathbf{E}_j \mathbf{E}_k + \dots \quad (3)$$

- F_0 est l'énergie libre de l'état fondamental, \mathbf{E} and \mathbf{H} représentent respectivement le champ électrique et le champ magnétique, \mathbf{P}^S and \mathbf{M}^S dénote la polarisation spontanée et l'aimantation, les indices (i, j, k) sont les trois composantes d'une variable en coordonnées spatiales, ε_0 et μ_0 se réfèrent à la perméabilité et à la susceptibilité magnétique du vide.
- ε_{ij} et μ_{ij} représentent les tenseurs de susceptibilité diélectrique et magnétique du second ordre.
- α_{ij} sont les composantes du tenseur α qui dénote l'effet magnétoélectrique linéaire.
- β_{ijk} et γ_{ijk} désignent les coefficients du tenseur du troisième ordre.

α_{ij} sont les composantes du tenseur α faisant référence à l'effet magnétoélectrique linéaire. Ils correspondent à la polarisation électrique induite (aimantation) en appliquant un champ magnétique (électrique). Le reste des termes correspond aux effets magnétoélectriques de haut ordre caractérisés par les tenseurs β et γ . L'effet le plus intéressant est la présence de α_{ij} . Il est appelé l'effet ME linéaire, ou simplement l'effet ME. Cette convention sera utilisée dans la thèse. Bien qu'il y ait de nombreux aspects intéressants dans les matériaux magnétoélectriques, dans la thèse, nous nous concentrerons spécifiquement sur les composés multiferroïques monophasiques présentant (anti) ferromagnétisme et (anti) ferroélectricité simultanément.

Selon les différents mécanismes microscopiques de la ferroélectricité, il existe deux groupes de multiferroïques, que nous appelons multiferroïques de type I et de type II. Pour les composés

multiferroïques de type I, la ferroélectricité et le magnétisme ont des sources différentes et sont présents indépendamment, ils sont donc faiblement couplés. Pour les multiferroïques de type II, la ferroélectricité est générée par des états magnétiquement ordonnés, impliquant un fort couplage entre les deux ordres ferroïques. Ces matériaux attirent énormément l'attention en raison des questions fondamentales qui y sont liées. Pour plus de détails voir le chapitre 2.

Nous nous concentrons sur le système multiferroïque de type II RMn_2O_5 . La structure est représentée dans la Figure F.1. Il est composé de chaînes d'octaèdres Mn^{4+}O_6 qui courent le long de l'axe c , séparées par des couches d'ions R^{3+} ou de bipyramides Mn^{3+}O_5 . Dans le plan (a, b) , deux chaînes en zig-zag d'octaèdres Mn^{4+}O_6 et de pyramides Mn^{3+}O_5 par maille s'étendent le long de l'axe a et sont empilées suivant la direction b . Dans ce plan, il existe trois interactions de superéchange magnétiques inéquivalentes entre les ions Mn: J_3 et J_4 pour les couples $\text{Mn}^{3+} - \text{Mn}^{4+}$, et J_5 entre deux spins Mn^{3+} . Au sein des chaînes, les interactions J_4 et J_5 induisent un caractère antiferromagnétique (AFM) alors que les couplages J_3 entre les chaînes sont magnétiquement frustrés. Le long de l'axe c , il existe deux interactions d'échange AFM $\text{Mn}^{4+} - \text{Mn}^{4+}$, selon qu'il se trouve un plan de pyramides Mn^{3+} ou de terre rare R^{3+} entre deux octaèdres Mn^{4+} successifs. Dans le premier cas, une forte frustration magnétique apparaît car il y a deux interactions J_4 et deux interactions J_3 $\text{Mn}^{4+} - \text{Mn}^{3+}$ en compétition avec J_2 . Il en résulte un ordre entre les deux ions Mn^{4+} qui est toujours FM. Pour J_1 , il est plus complexe et fortement dépendant de la terre rare (son magnétisme et le nombre de ses électrons $4f$) et des paramètres structuraux fins. En particulier, J_1 est fortement affecté par la distance et l'angle entre les cations et les oxygènes impliqués dans les couplages de super-échange. Dans certains membres de la série, il existe une interaction supplémentaire $\text{Mn}^{3+} - \text{R}^{3+}$, notée J_6 .

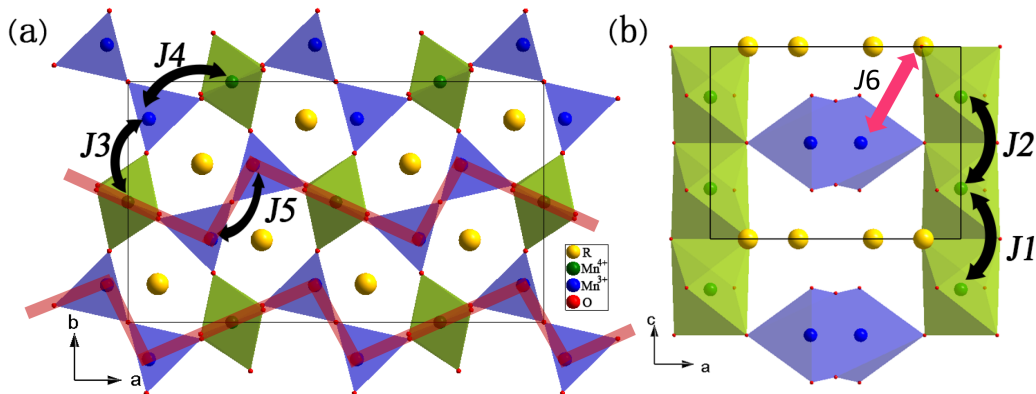


Figure F.1 – Projections de la structure cristalline de RMn_2O_5 le long de (a) c et (b) b . Les différentes interactions d'échange J_i sont indiquées.

Dans les composés RMn_2O_5 , les spins des ions Mn sont quasi-colinéaires indépendamment de la nature de R^{3+} et se situent généralement dans le plan (a, b) . Cependant, l'orientation de la structure magnétique et la ferroélectricité dépendent fortement de la nature de R^{3+} .

La taille de R^{3+} affecte également la séquence des ordres magnétiques. Tous les membres ayant de faibles rayons ioniques des terres rares ($Z > 62$ (Sm)), qui sont ferroélectriques, subissent presque la même série de transitions. Au-dessous d'environ 40 K, une transition magnétique paramagnétique (PM) incommensurable (HT-ICM) est observée à T_N , correspondant à un vecteur de propagation ICM $\mathbf{q} = (\frac{1}{2} - \delta_x, 0, \frac{1}{4} + \delta_z)$, qui varie selon la température et la nature de R^{3+} . En refroidissant, les valeurs de δ_x et δ_z s'approchent progressivement de zéro, et la structure magnétique se bloque dans une phase magnétique commensurable (CM) à $T_1 \sim 35$ K. Ceci est généralement associé à la transition ferroélectrique. La polarisation électrique augmente lorsque la température diminue. La température de Curie (T_C) varie également selon la nature de R^{3+} . Au-dessous de $T_2 \sim 25$ K, il y a une transition abrupte vers une structure magnétique incommensurable à basse température (LT-ICM). En entrant dans LT-ICM, la valeur de la polarisation électrique chute à une valeur beaucoup plus petite. À basse température ($T_R \sim 8$ K), une transition magnétique supplémentaire se stabilise pour certains membres de la série et est généralement attribuée à l'ordre des moments R^{3+} . Elle se produit soit avec le même

vecteur de propagation que l'ordre des Mn soit avec un vecteur de propagation différent. $\mathbf{q} = (\frac{1}{2}, 0, 0)$ pour Gd, Dy et Sm ou $\mathbf{q} = (0, 0, \frac{1}{2})$ pour Pr.

Mécanisme microscopique de la ferroélectricité

Il y a principalement deux mécanismes microscopiques de ferroélectricité induite par le magnétisme, l'interaction inverse Dzyaloshinskii-Moriya et le mécanisme de striction d'échange. L'observation de tous les spins le long de l'axe c dans le SmMn_2O_5 exclut totalement le mécanisme d'interaction Dzyaloshinskii-Moriya pour les composés RMn_2O_5 .

Comme indiqué sur la Figure F.2, en raison de la présence de deux chaînes zig-zag AFM par unité de cellule, deux des quatre termes J_3 sont frustrés. Dans la symétrie du groupe $Pbam$, les quatre termes J_3 s'annulent par symétrie. Cependant, dans le vrai groupe d'espace Pm , ce n'est pas le cas. Le modèle de striction d'échange est basé sur l'abaissement de l'énergie magnétique en levant l'égalité des quatre termes d'échange magnétique impliquant J_3 . Afin de réduire la frustration, les ions O ou Mn peuvent se déplacer pour augmenter les termes J_3 des paires bleues, qui présentent un ordre AFM et ne sont pas frustrés et diminuer les termes J_3 pour les paires rouges. En effet ces paires rouges magnétiquement frustrées présentent un ordre FM qui coûte en énergie d'Heisenberg. Tous les ions Mn^{3+} et O^{2+} se déplacent dans la même direction, conduisant à une polarisation électrique globale le long de l'axe b .

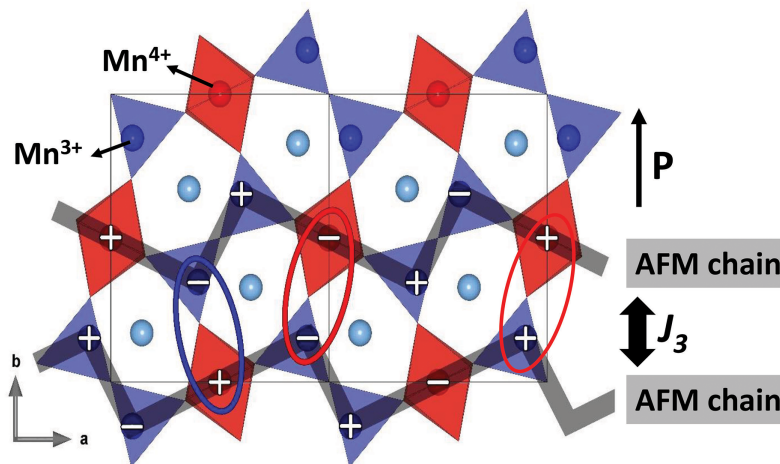


Figure F.2 – Projection dans le plan (a, b) des moments magnétiques le long de c représentés par les symboles $+$ et $-$. Les lignes grises représentent les chaînes AFM couplées par les interactions d'échange J_3 (représentées par des ellipses rouges et bleues: rouge pour l'ordre FM, bleu pour l'ordre AFM).

La différence de propriétés multiferroïques en fonction des rayons du R^{3+} peut être attribuée à l'effet de pression chimique provoqué par la taille de R^{3+} . La pression externe peut avoir un effet similaire car les positions atomiques sont fortement influencées par la pression externe. Cela est mis en évidence par le fait que sous pression, la ferroélectricité de RMn_2O_5 est fortement renforcée. Ceci a été attribué à l'apparition d'une phase magnétique commensurable PCM induite par la pression. Nos objectifs sont de déterminer la structure magnétique exacte de la phase PCM et de comprendre son mécanisme de stabilisation.

Étude principale

Nous avons réalisé des expériences de diffraction des neutrons sur poudre de RMn_2O_5 ($\text{R} = \text{Pr, Dy, Gd}$ et Sm) ainsi que des expériences de diffraction des rayons X sur poudre de RMn_2O_5 ($\text{R} = \text{Pr, Nd, Sm, Gd, Tb}$ et Dy) sous pression. Les détails expérimentaux sont présentés au chapitre 3.

La phase PCM des composés RMn_2O_5 ($\text{R} = \text{Pr}, \text{Dy}, \text{Gd}$ et Sm) étudiés dans cette thèse présente toujours le même vecteur de propagation proportionnel $\mathbf{q}_{\text{PCM}} = (\frac{1}{2}, 0, \frac{1}{2})$, déjà observé précédemment pour $\text{Y}\text{Mn}_2\text{O}_5$ et $\text{Tb}\text{Mn}_2\text{O}_5$. Cela montre le caractère universel de cette phase. Ce vecteur de propagation correspond au point D de la zone de Brillouin. Il y a deux représentations irréductibles de Pm au point $(\frac{1}{2}, 0, \frac{1}{2})$, D_1 et D_2 :

- D_1 : les moments magnétiques de Mn^{3+} sont obligés d'être le long de l'axe c , alors que les moments magnétiques de R^{3+} sont dans le plan (a, b) . Pas de contraintes sur les orientations de Mn^{4+} moments.
- D_2 : les directions des moments sont contraires à la représentation D_1 .

Nous considérons également un troisième modèle de symétrie plus basse: $P1$. Cette considération débloque la contrainte sur les spins de R^{3+} et Mn^{3+} pour être perpendiculaire, appelée *planaire*.

- *planaire*: les moments magnétiques de Mn^{3+} , Mn^{4+} et R^{3+} dans le plan (a, b) .

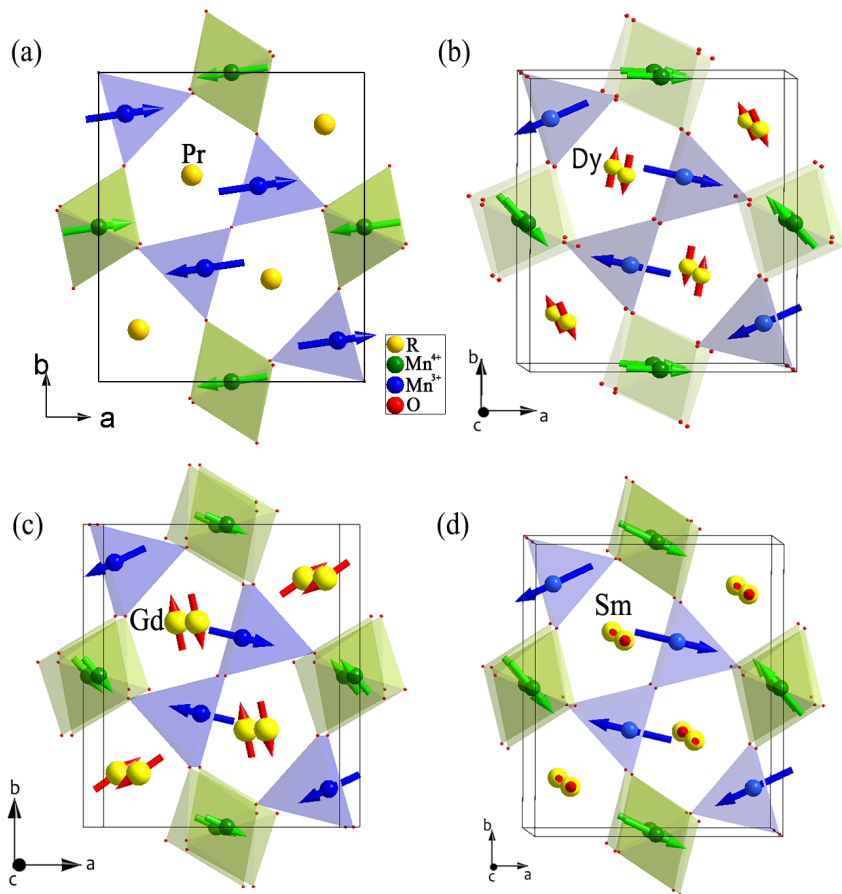


Figure F.3 – Structure magnétique de la phase PCM de (a) PrMn_2O_5 à 8 GPa, 6K. (b) DyMn_2O_5 à 6.6 GPa, 18 K. L'amplitude des moments de Dy^{3+} a été multipliée par un facteur 3. (c) GdMn_2O_5 à 8.4 GPa, 32 K. L'amplitude des moments de Gd^{3+} a été multipliée par un facteur 8. (d) SmMn_2O_5 à 10.3 GPa, 32 K. Les moments de Sm^{3+} sont situés le long de l'axe c . L'amplitude des moments de Sm^{3+} a été multipliée par un facteur 2.

Pour DyMn_2O_5 et GdMn_2O_5 , le modèle planaire correspond bien à la phase PCM et est plus physiquement acceptable que les autres (anisotropie des ions R^{3+} et Mn respectée). Pour SmMn_2O_5 , comme l'anisotropie de Sm^{3+} est le long de l'axe c , le modèle D_2 vérifie l'anisotropie de tous les spins. Pour PrMn_2O_5 , les modèles *planaire* et D_2 sont identiques, le moment de Pr^{3+} étant presque

nul. La structure magnétique correspondante de la phase PCM pour les différents composés étudiés est représentée sur la Figure F.3.

Pour les composés RMn_2O_5 ($R = \text{Dy}, \text{Gd}$ et Sm) étudiés, cette phase PCM remplace la phase ICM sous pression. Avec l'augmentation de la pression, la phase PCM se développe au détriment de la phase CM et la température critique de cette phase PCM augmente avec la pression. Cependant, pour l'état fondamental à basse température, la phase CM est toujours dominante même à haute pression. La phase PCM ne peut exister qu'en tant que phase unique à haute température. Le diagramme de phase pour l'ensemble des composés étudiés est illustré sur la Figure F.4

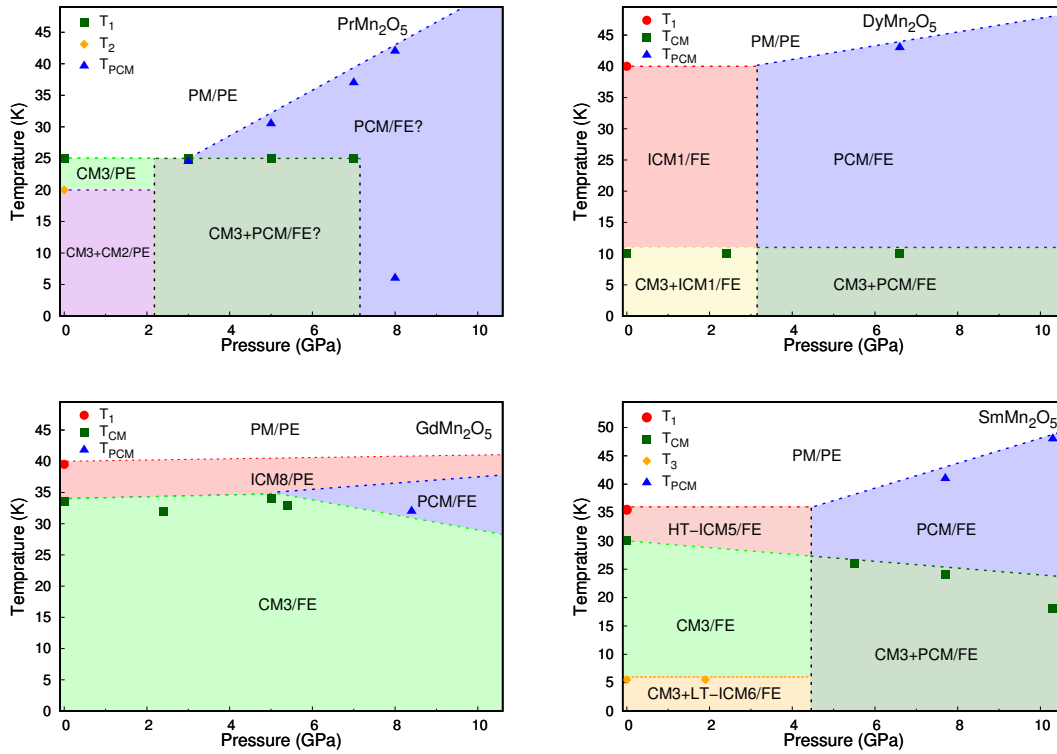


Figure F.4 – Diagramme de phases (p,T) des RMn_2O_5 ($R = \text{Pr}, \text{Dy}, \text{Gd}$ and Sm).

A pression ambiante, la phase CM, associée à $\mathbf{k}_z = 0$, est observée pour les composés RMn_2O_5 avec un spin R^{3+} élevé tel que $R = \text{Dy}, \text{Gd}$ et Sm . Cette phase ($\mathbf{k}_z = 0$) est dominante à basse température jusqu'à une certaine pression. Quant à la phase PCM ($\mathbf{k}_z = \frac{1}{2}$), elle est favorisée par un fort terme d'échange J_1 dans l'hamiltonien. Une pression externe semble augmenter ce terme d'échange J_1 . Ceci est mis en évidence par des mesures de rayons X sur poudre à température ambiante. Ces mesures sont également corroborées par des calculs DFT en bon accord avec les expériences. Grâce aux calculs de DFT, nous avons pu obtenir les positions des atomes d'oxygène difficiles à extraire de la mesure des rayons X. A travers la position atomique des ions O et Mn, nous avons extrait les informations concernant l'évolution des interactions d'échange J_i en fonction de la pression. Nous mettons ainsi en évidence que J_1 augmente sous pression, ce qui confirme encore le mécanisme présenté ci-dessus. D'autre part, le terme J_6 dans l'Hamiltonian, au-dessus d'une certaine température peut être très faible, même pour des composés avec un fort spin R^{3+} . En effet, les valeurs des moments des spins des R^{3+} extraits de nos raffinements magnétiques à haute pression et à température intermédiaire sont inférieures à $1 \mu\text{B}$.

La concurrence entre les termes J_1 et J_6 peut être exprimée par la figure présentée dans la Figure F.5. Cette figure montre les régions du diagramme de phases (p, T) pour lesquelles le terme $J_i \mathbf{S}_j \cdot \mathbf{S}_k$ dans le hamiltonien (nommé \mathcal{H}_i) est dominant.

Le cas de PrMn_2O_5 est particulier car il présente deux phases CM à pression ambiante et le système est non ferroélectrique. Ces deux phases CM correspondent à la mise en ordre indépendante des deux sous-réseaux de Mn. Ces deux sous réseaux sont alors orthogonaux entre eux. Notez également que le

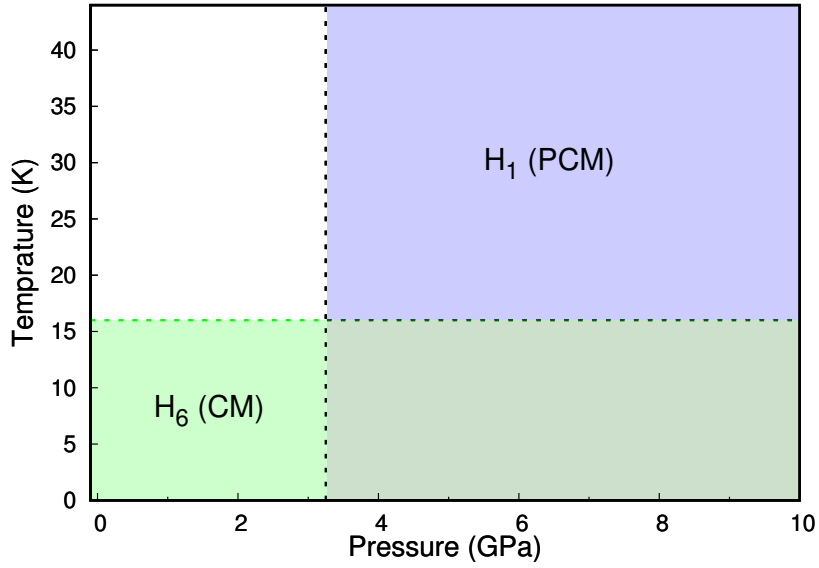


Figure F.5 – Diagramme de phases température - pression concernant le Hamiltonien $\mathcal{H}_i = -J_i \mathbf{S}_j \cdot \mathbf{S}_k$ ($i = 1$ et 6), \mathbf{S}_j et \mathbf{S}_k font référence au spin correspondant de Mn^{3+} , Mn^{4+} ou R^{3+} associé au J_i .

terme J_6 dans le hamiltonien est négligeable car le spin de Pr^{3+} est presque nul. Pour PrMn_2O_5 , les modèles D_2 et *planaires* sont identiques car les spins sur Pr^{3+} sont nuls. Enfin, le composé présente sous pression un comportement de type ferroélectrique. Ceci est dû au fait que sous pression, les deux sous-réseaux de Mn s'ordonnent en une phase unique présentant de plus des spins quasi-colinéaires.

Titre : Influence de la pression sur la multiferroïcité de RMn_2O_5

Mots clés : multiferroïque, pression, RMn_2O_5 , magnéto-électrique couplage

Résumé : La série de RMn_2O_5 multiferroïques a été largement étudiée en raison de son fort couplage magnéto-électrique. L'origine de la ferroélectricité a été clarifiée en tant que mécanisme de striction d'échange. Comme les variations des distances interatomiques modifiées par la pression externe peuvent grandement affecter les propriétés multiferroïques, il est essentiel de comprendre l'origine microscopique de cet effet.

Nous avons déterminé la structure magnétique de la phase magnétique commensurable induite par la pression (PCM) et dessiné le diagramme de phase $p - T$. Sur la base d'un équilibre énergétique subtil entre l'interaction d'échange J_1 , l'interaction d'échange R-Mn J_6 et l'anisotropie de la terre rare, nous avons proposé un mécanisme de stabilisation des différentes phases magnétiques en fonction de la pression pour les différents composés avec R=Dy, Gd et Sm. L'augmentation de J_1 sous pression à température ambiante obtenue grâce à l'étude par diffraction X confirme ce mécanisme. Une explication supplémentaire a été proposée pour le cas particulier de PrMn_2O_5 . Ces résultats ouvrent certainement la voie à une compréhension complète de l'origine de l'influence de la pression dans la famille RMn_2O_5 .

Title: Influence of the pressure on the multiferroicity of RMn_2O_5

Keywords: multiferroic, pressure, RMn_2O_5 , magneto-electric coupling

Abstract: The series of multiferroic RMn_2O_5 has been extensively studied due to its strong magneto-electric coupling. The ferroelectricity origin has been clarified as the exchange striction mechanism. As the variations of the interatomic distances modified by the external pressure can greatly affect the multiferroic properties, it is essential to understand the microscopic origin of this effect.

In this thesis, we have systematically studied the multiferroic properties of the RMn_2O_5 compounds by using powder X-rays diffraction and powder neutron diffraction (PND) under pressure. We have determined the magnetic structure of the pressure induced commensurate magnetic (PCM) phase and drawn the $p - T$ phase diagram. Based on a subtle energy balance among the exchange interaction J_1 , the R-Mn exchange interaction J_6 and the anisotropy of the rare earth, we have proposed a mechanism for stabilizing the different magnetic phases as a function of the pressure for the different compounds with R = Dy, Gd and Sm. The enhanced J_1 under pressure at room temperature from the X-ray diffraction study further confirms this mechanism. An additional explanation has been proposed for the special case of the PrMn_2O_5 . These results certainly pave the way to fully understand the origin of the pressure influence in the RMn_2O_5 family.

Acknowledgment

My thanks go first to Pascale Foury-Leylekian, dear thesis director and Victor Balédent, dear thesis co-director. I thank them for having entrusted me with the responsibilities of my scientific productions. I thank all the members of my thesis committee for their insightful remarks and encouragement. I would like to thank the two reporters: Rousse Gwenaelle from Sorbonne Université / Collège de France and Pierre Bordet from CNRS, Institut Néel. I thank them for having formulated the appropriate scientific remarks. I also thank the two examiners Virginie Simonet from CNRS, Institut Néel / Université Grenoble Alpes and Fabrice Bert from Université Paris-Sud / Université Paris-Saclay, who have agreed to consider this thesis.

I would like to thank the China Scholarship Council (CSC) for their funding support of my PhD study. I also thank the education office, embassy of the People's Republic of China in the French Republic for helping me live a better life in France.

A very special gratitude goes out to my supervisor Pascale Foury-Leylekian and co-supervisor Victor Balédent, who provide me the opportunity and welcome me to join the MATRIX group and lead me to the laboratory and research facilities. Both of them give me a lot of support in work and in life. Without their precious help, it would not be possible for me to have such meaningful and joyful Ph.D. life in France.

I thank Denis Petermann, Stéphan Rouziere and Philippe Duret for helping me deal with the setup problems during the X-rays diffraction experiments in LPS. I also thank Pierre-Antoine Albouy for resolving my problems in work and in life and for the nicely talking in Chinese, English and French.

My sincere thanks also go to Claude Pasquier for his guidance of my doctoral school process as a EDPIF deputy director of the university of Paris-Saclay and a ED deputy director of Physique en Ile de France of the university of Paris-Saclay. I would like to thank David Le Bolloc'h, my parrain, and Edwin Kermarrec, my tutor, for their concerns and encouragement.

I would like to thank Véronique Thieulart for the help of the administration of the lab, thank Marie-France Mariotto and Sabine Hoarau for the help of train tickets' reservation for scientific experiments, summer/winter school and conference, thank Ciham Zaaboul-Aliane for helping me reimburse the fees of my trips for scientific proposes.

Furthermore, I want to thank other members of the MATRIX group in LPS: Geoffrey Monet, Danilo Rosa Nunes, Xiang Shi, Rajesh Bhandary, Pascale Launois, Erwan-Nicolas Paineau, Stéphane Cabaret and Gilles Guillier. I appreciate the nice and friendly atmosphere with your accompany.

I would like to express my sincere gratitude to our collaborators. I am very impressive by their hard work and always benefit from our collaborations. I thank Martha Greenblatt for synthesizing sample for us. The good quality of the samples makes our experiments performed well. I thank Marie-Bernadette Lepetit, Elisa Rebolini and Antoine Vaunat for the calculation work of my thesis. Special thank also goes out to Marie-Bernadette Lepetit for the discussion and guidance of the theory knowledge, which gives me invaluable benefits. I thank Claude Pasquier, Pascale Auban-Senzier and Melissa Gooch for the ferroelectric properties measurements, which makes our results more convincible. I thank Ghassen Yahia, Sumanta Chattopadhyay, Isabelle Mirebeau, Maxime Deutsch, sylvain Petit, Françoise Damay for the very helpful discussions and the appropriate scientific remarks for our work.

I would like to thank the ILL facilities for providing the neutron resource for our experiments. With

a special mention to Thomas Hansen in D20 and Claire Colin in D1B, both of them give us a lot of support during the powder neutron diffraction under pressure experiments.

感谢支持鼓励我的家庭，尤其是我的父亲、母亲、哥哥、嫂子，以及我的女朋友希希。你们永远是最珍贵的宝藏。

I want to express my sincere gratitude to my mother, my father, my brother, my sister-in-law and my girlfriend CC. You are and always will be my most valuable treasures.

And finally, last but by no means least, many thanks to all those I have met and whom I have not had a chance to say thank you.

Contents

Résumé en français	iii
Abstract	ix
Acknowledgment	xi
List of Abbreviations	xvii
Introduction	xix
1 Multiferroic Materials	1
1.1 Why Multiferroics?	1
1.2 Magnetoelectric Effect	2
1.3 ME Multiferroics	4
1.3.1 Symmetry Considerations	4
1.3.2 Classifying Multiferroics	4
1.4 Type I Magnetoelectric Multiferroics	5
1.4.1 Perovskite Multiferroics	5
1.4.2 Ferroelectricity due to Lone Pair Electrons	7
1.4.3 Ferroelectricity due to Charge Ordering	7
1.4.4 "Geometric" Ferroelectricity	8
1.5 Type II Magnetoelectric Multiferroics	9
1.5.1 Multiferroics in Spiral Magnetic Structures	9
1.5.2 Multiferroics in Collinear Magnetic Structures	12
1.5.3 Other Mechanism (Spin-Dependent Hybridization)	14
2 RMn₂O₅ Multiferroics	17
2.1 Why RMn ₂ O ₅ ?	18
2.2 Common Features	18
2.2.1 General Structure	18
2.2.2 General parameters and Chemical Pressure Effect	21
2.2.3 Sequence of Magnetic Ordering	22
2.2.4 Ferroelectric Properties of the RMn ₂ O ₅ Compounds	22
2.3 Microscopic Mechanism of Ferroelectricity	24
2.4 Specificities Upon the Nature of R ³⁺	25
2.4.1 Propagation Wave Vector	26
2.4.2 Spiral Structure in DyMn ₂ O ₅	26
2.4.3 Spin Ordering along the <i>c</i> Axis of the RMn ₂ O ₅ with R = Sm, La and Er	26
2.4.4 an Abnormally High Electric Polarization in GdMn ₂ O ₅	26
2.5 Multiferroic Properties Affected by External Parameters	27
2.5.1 Multiferroic Behavior under Magnetic Field	27
2.5.2 Multiferroic Behavior under an External Pressure	31
2.6 Electromagnons in RMn ₂ O ₅	33
2.7 The Aims of Our Work	34

3	Experimental Techniques	37
3.1	X-ray Scattering	38
3.1.1	Fundamental Properties	38
3.1.2	Scattering Theory	39
3.1.3	X-ray Diffractometer	42
3.1.4	Powder X-ray Diffraction Intensity	42
3.1.5	Powder X-ray Diffraction Instruments	46
3.2	Neutron Scattering and Diffraction	49
3.2.1	Basic Principles	50
3.2.2	Elastic Neutron Scattering	53
3.2.3	Intensity Corrections	55
3.2.4	Neutron Scattering Instruments	55
3.2.5	Pressure Cell	57
3.3	Powder Diffraction Refinements	58
3.3.1	Rietveld Analysis	58
3.3.2	FullProf Suite	61
3.4	Ferroelectric Properties Measurement	62
3.5	Sample Synthesis Process and Characterization	62
4	Pressure-dependent x-ray diffraction of multiferroic RMn_2O_5	65
4.1	Basics of Density Functional Theory (DFT)	65
4.2	Experimental Details	66
4.3	Ab Initio Calculations	69
4.4	Results	69
4.5	Analysis and Discussion	75
5	Powder Neutron Diffraction of RMn_2O_5 under Pressure	81
5.1	Introduction	82
5.2	Information Concerning the Magnetic Structures Determined in This Chapter:	83
5.3	Study of PrMn_2O_5 under Pressure	85
5.3.1	Introduction: Magnetic Structure at Ambient Pressure	85
5.3.2	Dielectric Properties under Pressure	86
5.3.3	Powder Neutron Diffraction (PND) Experiment under Pressure	86
5.3.4	Analysis of the PND under Pressure	87
5.3.5	Discussion	90
5.4	Study of DyMn_2O_5 under Pressure	92
5.4.1	Introduction: Magnetic Structure at Ambient Pressure	92
5.4.2	PND Experiment under Pressure	93
5.4.3	Analysis of the PND under Pressure	93
5.4.4	Discussion	97
5.5	Study of GdMn_2O_5 under Pressure	99
5.5.1	Introduction	99
5.5.2	PND Experiment under Pressure	100
5.5.3	Analysis of the PND under Pressure	100
5.5.4	Discussion	104
5.6	Study of SmMn_2O_5 under Pressure	105
5.6.1	Introduction: Magnetic Structure at Ambient Pressure	105
5.6.2	PND Experiment under Pressure	105
5.6.3	Analysis of the PND under Pressure	105
5.6.4	Discussion	109

6 Conclusion and Perspectives	113
6.1 Conclusion	113
6.2 Perspectives	115
List of Figures	117
List of Tables	123
Bibliography	125
Résumé	135

List of Abbreviations

ME:	magnetoelectric
MRAM:	magnetoresistive random access memory
SDW:	spin density wave
DM:	Dzyaloshinskii–Moriya
ES:	exchange striction
KNB:	spin current model
PM:	paramagnetic
FM:	ferromagnetic
AFM:	antiferromagnetic
PE:	paraelctric
FE:	ferroelctric
ICM:	incommensurate magnetic
HT-ICM:	high-temperature incommensurate magnetic
LT-ICM:	low-temperature incommensurate magnetic
CM:	commensurate magnetic
PCM:	pressure induced commensurate magnetic
T_C :	Curie temperature
T_N :	Néel temperature
T_R :	phase transition temperature attributed to the R^{3+} moments
RXMS:	resonant X-ray magnetic scattering
CMD:	colossal magnetodielectric
DFT:	density functional theory
ILL:	Institute Laue Langevin
PND:	powder neutron diffraction

Introduction

The intrinsic coupling of electricity and magnetism is one of the cornerstones of modern physics, the first reference goes back to the paper of Curie [1] in 1894. However, the actual research started with the theoretical physical work of Landau and Lifshitz [2] in 1960. Then, Dzyaloshinskii [3] predicted that antiferromagnet Cr_2O_3 should exhibit a linear magnetoelectric effect, which was indeed experimentally confirmed by Astrov [4] the following year. Since then, a rapid development not only concerning the magnetoelectric effect, but also on other type of ferroic couplings followed. In 1997, Schmid [5] first put forward the term of multiferroic to describe all these materials. These multiferroics were studied in the 1960s and 1970s but were then neglected mainly due to the fact that single-phase materials with both properties could not be produced.

In the very beginning of the 21st century, because of the interesting and challenging issues concerning magnetics and ferroelectrics in perovskite materials, the scientific community started to intensively investigate the fundamental theoretical origin of magnetic ferroelectrics [6]. The problem is that the transition metal d electrons, which are essential for magnetism, reduce the tendency for an off-center ferroelectric distortion. It seems that magnetism and ferroelectricity are mutually exclusive. On one side, experimental breakthroughs appeared in 2003, with the fabrication of films of the most popular multiferroic material, BiFeO_3 [7]. BiFeO_3 belonging to type-I multiferroics, the coupling of electricity and magnetism in bulk BiFeO_3 is quite weak. But the multiferroic properties of BiFeO_3 thin films have been greatly enhanced. On the otherside, a novel class of multiferroics was discovered: TbMnO_3 [8] and TbMn_2O_5 [9]. They are type-II multiferroics, in which ferroelectricity is induced by the magnetically ordered phases. The magnetoelectric coupling thus is strong by nature. The details of these two types of multiferroics will be discussed in Chapter 1. Since then, the research of multiferroic materials developed rapidly, both from a theoretical point of view and for practical applications. It led to an enormous increase of activity in this field [10–12]. As we can see from the Figure 1, the number of publications increased exponentially since the beginning of the 21st century.

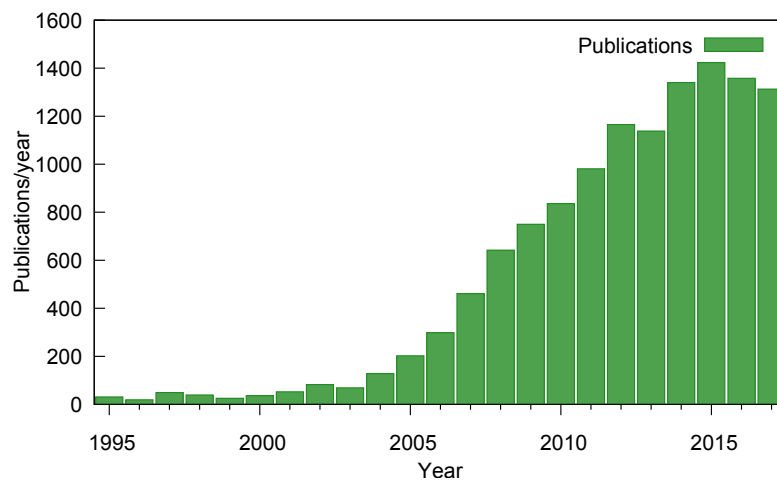


Figure 1 – Number of publications per year on multiferroics from year 1995 to 2017. Data from the [web of science](#) (key word:multiferroic OR magnetoelectric)

In this work, we will focus on the type-II multiferroics RMn_2O_5 (R=rare earth, Bi or Y) family. The properties of the RMn_2O_5 compounds are very sensitive to the ionic radii of R^{3+} [13] which

corresponds to a chemical pressure. In addition, the ferroelectric properties of the RMn_2O_5 are strongly pressure dependent [14]. However, until now, nearly no accurate study of the magnetic and crystallographic structures under pressure have been performed. It comes from the experimental difficulty of such experiments. It is however very interesting and necessary to study the structural and magnetic properties under pressure in order to understand the mechanism of the multiferroicity in the RMn_2O_5 series.

Chapter 1 will present the basic concepts and the different multiferroic materials. Chapter 2 presents the RMn_2O_5 family. Chapter 3 describes the experimental techniques and methods used in this thesis, mainly powder X-ray diffraction and powder neutron diffraction scattering under pressure with the description of the experimental setups. Chapter 4 is devoted to experimental results obtained by powder X-ray diffraction under pressure at room temperature. In Chapter 5, we present the powder neutron diffraction results under pressure, including the determination of the magnetic structure, and of the ferroelectric properties. We then discuss the microscopic mechanism stabilizing the magnetic phase under pressure. Finally, Chapter 6 summarizes the main results of this thesis and provides some perspectives for further studies.

1

Multiferroic Materials

Contents

1.1 Why Multiferroics?	1
1.2 Magnetoelectric Effect	2
1.3 ME Multiferroics	4
1.3.1 Symmetry Considerations	4
1.3.2 Classifying Multiferroics	4
1.4 Type I Magnetoelectric Multiferroics	5
1.4.1 Perovskite Multiferroics	5
1.4.2 Ferroelectricity due to Lone Pair Electrons	7
1.4.3 Ferroelectricity due to Charge Ordering	7
1.4.4 "Geometric" Ferroelectricity	8
1.5 Type II Magnetoelectric Multiferroics	9
1.5.1 Multiferroics in Spiral Magnetic Structures	9
1.5.2 Multiferroics in Collinear Magnetic Structures	12
1.5.3 Other Mechanism (Spin-Dependent Hybridization)	14

This chapter exposes the general concepts and the motivations for the present work. The fundamental background of multiferroics is first recalled in Section 1.1. The motivations for this exceptional materials are also given. The incompatibility between ferroelectricity and magnetism due to the " d^0 " vs " d^n " problem is discussed in Section 1.3. The Section 1.3 has also addressed approaches of multiferroics using symmetry considerations. In Section 1.4 and Section 1.5, the two types of multiferroics are presented.

1.1 Why Multiferroics?

The term "multiferroics" was coined by Schmid in 1994. Multiferroics refer to materials which exhibit simultaneously more than one primary ferroic order in a single phase [5]. For a long time, one believed that there are only three forms of ferroic order: ferroelectricity (polarization), ferroelasticity (strain) or ferromagnetism (magnetization).

The coupling of these orders in multiferroics is presented in Figure 1.1. The observation of ferrotoroidic domains leads to a fourth ferroic order for ordered arrangement of magnetic vortices [15]. The effect of parity operations of space and time for the four primary ferroic orders can be seen in

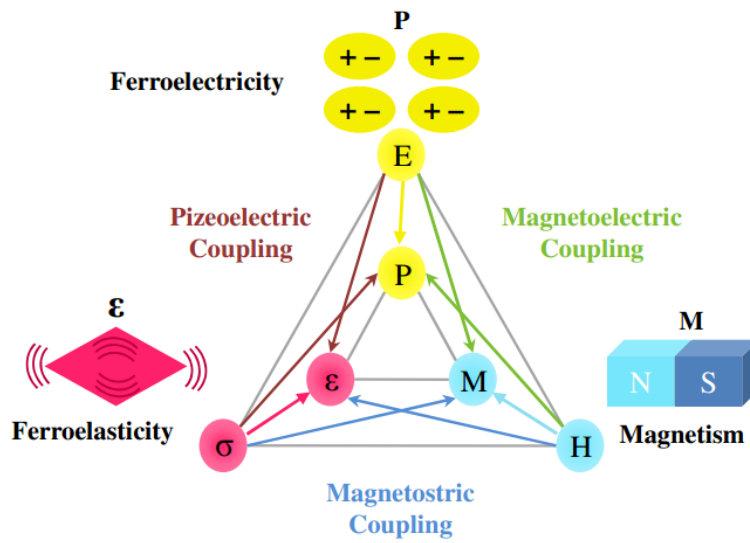


Figure 1.1 – The electric field \mathbf{E} , magnetic field \mathbf{H} , and stress control of the electric polarization \mathbf{P} , magnetization \mathbf{M} , and strain σ , respectively. In a ferroic material, \mathbf{P} , \mathbf{M} , or ϵ are spontaneously formed to produce ferromagnetism, ferroelectricity, or ferroelasticity, respectively [11].

Figure 1.2. So far most well-studied multiferroic materials belong to the transition metal compounds, in particular, the $3d$ transition metals with perovskite or layered perovskite structures. A great number of new materials with various structures and compositions were recently discovered. They exhibit novel physical phenomena, certain of which cannot be explained by the existent mechanisms. The multiferroics attract enormous attention, due to their fascinating physics, the interesting mechanisms, particularly for magnetoelectric multiferroics, and their potential industrial applications .

	Space	Invariant	Change
Time		Invariant	Change
Invariant		Ferroelastic 	Ferroelectric
Change		Ferromagnetic 	Ferrotoroidic

Figure 1.2 – Four primary forms of ferroic order under the parity operations of space and time [15].

1.2 Magnetolectric Effect

The magnetoelectric (ME) coupling can induce a proportional electric polarization (magnetization) by applying an external magnetic (electric) field, as shown in Figure 1.3. This cross-correlation between the magnetic and electric properties is very interesting for potential industrial applications.

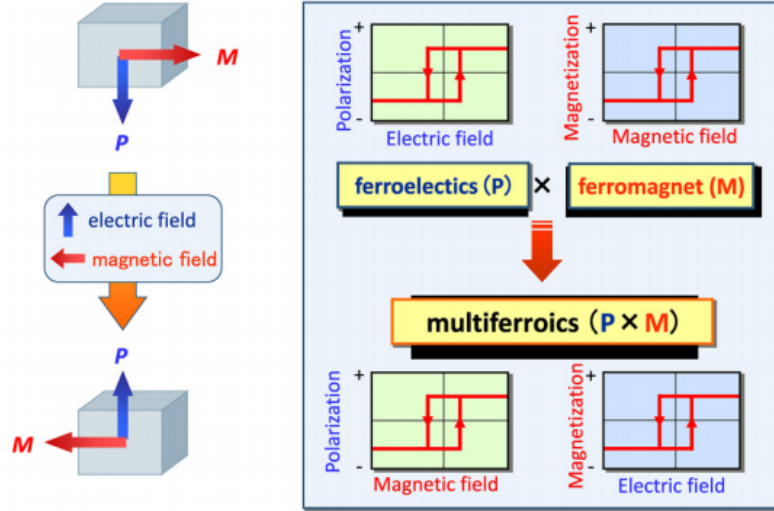


Figure 1.3 – Sketches of ferroelectricity and ferromagnetism as well as the mutual control between them in magnetoelectric coupling [16].

According to the thermodynamic, the magnetoelectric effect can be understood within the Landau theory framework. The ME effect is obtained from the expansion of the free energy [10], i.e.

$$F(\mathbf{E}, \mathbf{H}) = F_0 - \mathbf{P}_i^S \mathbf{E}_i - \mathbf{M}_i^S \mathbf{H}_i - \frac{1}{2} \varepsilon_0 \varepsilon_{ij} \mathbf{E}_i \mathbf{E}_j - \frac{1}{2} \mu_0 \mu_{ij} \mathbf{H}_i \mathbf{H}_j - \alpha_{ij} \mathbf{E}_i \mathbf{H}_j - \frac{1}{2} \beta_{ijk} \mathbf{E}_i \mathbf{H}_j \mathbf{H}_k - \frac{1}{2} \gamma_{ijk} \mathbf{H}_i \mathbf{E}_j \mathbf{E}_k - \dots \quad (1.1)$$

Then the polarization is:

$$\mathbf{P}_i(\mathbf{E}, \mathbf{H}) = -\frac{\partial F}{\partial \mathbf{E}_i} = \mathbf{P}_i^S + \varepsilon_0 \varepsilon_{ij} \mathbf{E}_j + \alpha_{ij} \mathbf{H}_j + \frac{1}{2} \beta_{ijk} \mathbf{H}_j \mathbf{H}_k + \gamma_{ijk} \mathbf{H}_i \mathbf{E}_j + \dots \quad (1.2)$$

and the magnetization is:

$$\mathbf{M}_i(\mathbf{E}, \mathbf{H}) = -\frac{\partial F}{\partial \mathbf{H}_i} = \mathbf{M}_i^S + \mu_0 \mu_{ij} \mathbf{H}_j + \alpha_{ij} \mathbf{E}_i + \beta_{ijk} \mathbf{E}_i \mathbf{H}_j + \frac{1}{2} \gamma_{ijk} \mathbf{E}_j \mathbf{E}_k + \dots \quad (1.3)$$

- F_0 : the ground state free energy, \mathbf{E} and \mathbf{H} represent the electric field and magnetic field, respectively, \mathbf{P}^S and \mathbf{M}^S denote the spontaneous polarization and magnetization, subscripts (i, j, k) are the three components of a variable in spatial coordinates, ε_0 and μ_0 refer to the dielectric and magnetic susceptibilities of vacuum.
- ε_{ij} and μ_{ij} : the second-order tensors of dielectric and magnetic susceptibilities.
- α_{ij} : the components of the tensor α which denotes the linear magnetoelectric effect.
- β_{ijk} and γ_{ijk} : the third-order tensor coefficients.

α_{ij} are the components of tensor α referring to the linear magnetoelectric effect. They correspond to the induced electric polarization (magnetization) by applying a magnetic (electric) field. The rest of the terms corresponds to the high-order magnetoelectric effects characterized by tensors β and γ . The most interesting effect is the presence of α_{ij} . It is referred as the linear ME effect, or simply the ME effect. This convention will be used in the thesis. Although there are many interesting aspects in magnetoelectric materials [17], in the thesis, we will focus specifically on the single-phase multiferroic compounds exhibiting (anti)ferromagnetism and (anti)ferroelectricity simultaneously.

1.3 ME Multiferroics

1.3.1 Symmetry Considerations

From the symmetry point of view, the electric (charge) dipole \mathbf{P} breaks the space-inversion symmetry while is invariant by the time reversal symmetry. A spontaneous polarization comes from a structural distortion of the high-symmetry paraelectric (PE) phase breaking the spacial inversion symmetry. In contrast, the magnetic moment \mathbf{M} breaks the time-reversal symmetry but keeps the space-inversion symmetry. Among all the 233 Shubnikov magnetic point groups, only 13 point groups, i.e. 1, 2, 2', m , m' , 3, 3 m' , 4, 4 $m'm'$, $m'm2'$, $m'm'2'$, 6 and 6 $m'm'$, allow the simultaneous existence of spontaneous electric polarization and magnetization. This limitation in the crystallographic symmetry explains why multiferroics are rare. Even so, some compounds in these 13 point groups above, actually do not show any multiferroicity [10]. To discover new multiferroics, approaches besides simple symmetry considerations are needed.

Most traditional ferroelectrics are transition metal oxides with perovskite structure (ABO_3), such as BaTiO_3 and $(\text{Pb}, \text{Zr})\text{TiO}_3$. So the first attempts to find out or synthesize multiferroics have mostly concentrated on this class of compounds. However, all conventional ferroelectric perovskite oxides with transition metal ions have empty d shells. Magnetism, on the contrary, requires transition-metal or rare-earth ions with partially filled d or f shell. The difference of filling of the d shells at the B-site required for ferroelectricity and magnetism makes these two ordered states mutually exclusive (details in Section 1.4.1). Still, some compounds with ABO_3 perovskite structure, such as BiMnO_3 or BiFeO_3 , are multiferroics, which will be addressed in details in Section 1.4.2.

The Landau theory is a concise way to formulate a general expression of phase transitions. The free energy near the phase transition can be developed as a series expression of the order parameters. For a ferromagnetic/ferroelectric without external magnetic/electric fields, this formulation can be written as:

$$\begin{aligned} F_m &= F_{m0} + \alpha_m \mathbf{M}^2 + \beta_m \mathbf{M}^4 + \dots, \\ F_p &= F_{p0} + \alpha_p \mathbf{P}^2 + \beta_p \mathbf{P}^4 + \dots, \end{aligned} \quad (1.4)$$

- F_{m0} (F_{p0}): the original free energy without magnetism (electric polarization)
- α_m , α_p , β_m and β_p : the Landau coefficients.

The odd power orders of \mathbf{M} and \mathbf{P} are absent because of the invariance of the energy is a scalar quantity under both time-reversal and space-inversion operations. A term like \mathbf{M}^3 will break the time reversal symmetry, thus F_m will change when the time sequence is reversed, which is physically impossible. The symmetry restriction makes the "lowest" power order for simple magnetoelectric coupling terms at zero field being $\mathbf{P}^2\mathbf{M}^2$. Such a coupling term is of fourth order, which is much weaker compared to the primary ferroic order terms \mathbf{P}^2 or \mathbf{M}^2 . This means the magnetoelectric coupling is very weak.

Thanks to recent theoretical works, other terms beyond this conventional magnetoelectric coupling have been introduced. For example, when a single magnetic moment only breaks the time-reversal symmetry, the space-inversion symmetry can be broken by a spatial collection of magnetic moments, thus couple with ferroelectric order at first order. This part will be addressed in details in Section 1.5.

1.3.2 Classifying Multiferroics

When considering the microscopic conditions for the coexistence of magnetism and ferroelectricity, it should be noted that, while the microscopic nature of the magnetic order is, the same for all ferromagnetic materials (an exchange interaction of localized magnetic moments), this is not the case for ferroelectricity. There are many different mechanisms leading to ferroelectricity and different types of ferroelectrics. Therefore, to design or understand multiferroic systems, the main challenge is to figure out the origin of the ferroelectricity.

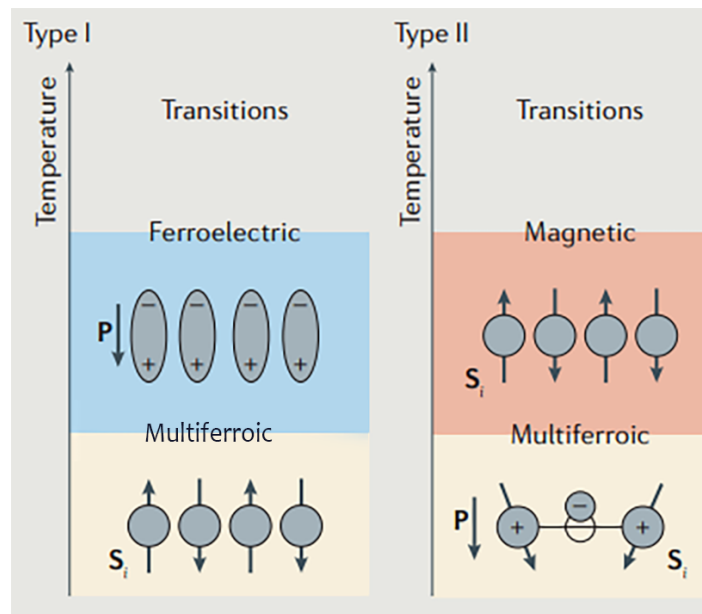


Figure 1.4 – Types of multiferroicity [18].

According to the different microscopic mechanisms of ferroelectricity, there are two groups of multiferroics, which we call type-I and type-II multiferroics [19]. As shown in Figure 1.4, for the compounds in type-I multiferroics, ferroelectricity and magnetism have different sources and they are stabilized independently. The ferroelectricity often occurs at higher temperature than that of the magnetism, and exhibits quite large spontaneous electric polarization ($10 - 100 \mu\text{C} \cdot \text{cm}^{-2}$). Such as, BiFeO_3 ($T_C \sim 1100 \text{ K}$, $T_N = 643 \text{ K}$, $\mathbf{P} \sim 90 \mu\text{C} \cdot \text{cm}^{-2}$) [20] and hexagonal YMnO_3 ($T_C \sim 914 \text{ K}$, $T_N = 80 \text{ K}$, $\mathbf{P} \sim 6 \mu\text{C} \cdot \text{cm}^{-2}$) [21, 22]. Although, there also exists a certain coupling between ferroelectricity and magnetism in these type-I materials, it is usually very weak. At the beginning of this century, a novel class of multiferroics was discovered [8, 9], which is called type-II multiferroics. These are systems in which ferroelectricity is generated by magnetically ordered states, implying a strong coupling between the two ferroic orders. These materials attract enormous attention due to the interesting fundamental issues.

1.4 Type I Magnetolectric Multiferroics

Most Type-I multiferroics are usually good ferroelectrics with critical temperatures of magnetic and ferroelectric transitions far above room temperature. Although the coupling between the magnetism and the ferroelectricity is rather weak, these materials can be used as four-states memories for magnetoresistive random access memories (MRAM), because in such case it is important to have independent polarization and magnetic orders. For other applications, the challenge for this group is to keep a large spontaneous polarization, but also enhance the ME coupling. Depending on the mechanism of the ferroelectricity, we can single out some of the major subgroups of the type-I multiferroic, but there are certainly others.

1.4.1 Perovskite Multiferroics

Most of the classical ferroelectrics belong to the perovskite family in which the ferroelectricity is due to the "ferroelectric-active" transition metal ions, such as BaTiO_3 or $(\text{Pb}, \text{Zr})\text{TiO}_3$ (PZT). However, after inspection of these hundreds of magnetic perovskites [23] and hundreds of ferroelectric perovskites [24], one can conclude that there seems to exist a mutual exclusion between the magnetism and the ferroelectricity because there is practically no overlap between these two groups of properties.

The perovskite materials usually present cubic structure at high temperature with a small B-site

cation at the center of an octahedron of oxygen ions and a large A-site cation at the unit cell corners. In particular, they undergo a phase transition from a high-temperature, high-symmetry paraelectric phase, to a low-symmetry polarized phase at low temperature accompanied by an off-center shift of the B-site transition metal ions, as shown in Figure 1.5(a). The B-site ions shift from the center of O_6 octahedron to the direction of one oxygen, generating a net polarization and thus the ferroelectricity. Ferroelectrics have spontaneous polarization that can be switched by an electric field. In parallel, there are a large number of magnetic oxides in perovskite or perovskite-like structures. As we mentioned above in Section 1.3.1, the different requirements for the filling of the transition metal ion d shells (at the B-site) makes the magnetic and ferroelectric ordered states mutually exclusive.

More specifically, in perovskite systems, the off-center shifts of transition metal ions form strong covalent bonds with surrounding oxygens using the empty d states. However, the presence of odd d electrons in d^n configurations prevents this in magnetic perovskites [6]. This mechanism can be described as a second-order Jahn–Teller effect. In $BaTiO_3$, the empty d states of the transition metal ions Ti^{4+} may be used to form strong covalency with the surrounding oxygen anions. The shift of the transition metal ion from the centrosymmetric positions to one (or more) oxygen(s), in order to establish a strong covalent bond with the oxygen(s), weakens the bonds with other oxygens. The hybridization matrix element t_{pd} , defined as the overlap between the wave functions of electrons in Ti and O, turns to $t_{pd}(1 \pm gu)$. In the linear approximation, the energy can be expressed as terms of the type $\sim (-t_{pd}^2/\Delta)$, where Δ is the charge transfer gap (see Figure 1.5(b)), which cancel each other. But the 2nd-order approximation produces an additional energy difference:

$$\delta E = -(t_{pd}(1 + gu))^2/\Delta - (t_{pd}(1 - gu))^2/\Delta + 2t_{pd}^2/\Delta = -2t_{pd}^2(gu)^2/\Delta \quad (1.5)$$

- u : the distortion.
- g : the coupling constant.

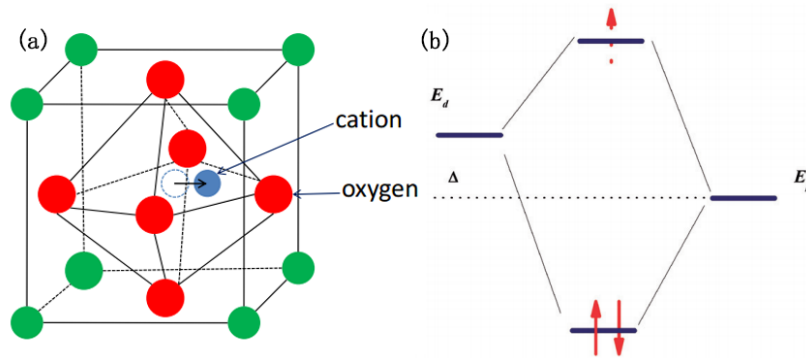


Figure 1.5 – (a) Shift of transition metal ion towards one of the oxygens, and (b) schematic energy levels with empty d levels (solid arrows) and with partially filled d levels (dashed arrow) [12].

If the total energy gain $\sim u^2$ is larger than the energy loss due to the ordinary elastic energy $\sim Bu^2/2$ of the lattice distortion, a distortion would be energetically favorable, leading to ferroelectricity. In Figure 1.5(b), if the transition metal ion has an empty d shell, only the bonding bands would be occupied (solid arrows), thus this process leads to an energy gain. However, if there is an additional d electron on the corresponding d orbital (dashed arrow in Figure 1.5(b)), this electron will occupy an antibonding hybridized state, thus the electronic gain of energy will be smaller than the elastic cost of energy $Bu^2/2$. This explains the absence of ferroelectricity for ions with a partially filled d shell [12, 25]. Magnetism and "classical" ferroelectricity therefore appear to be mutually exclusive, what is called " d^0 " vs " d^n " problem. But this mutual exclusion is not a "theorem". In most cases a magnetic d^n ion is stable in the center of its O_6 octahedron, but there may be the cases where it is not. In the same way, the presence of a d^0 cation does not guarantee the ferroelectricity (for example in $CaMnO_3$).

1.4.2 Ferroelectricity due to Lone Pair Electrons

There are some exceptions to the "exclusion rule" in perovskite family mentioned above: BiFeO_3 , BiMnO_3 and PbVO_3 . All these materials contain only magnetic transition metal ions Fe^{3+} (d^5), Mn^{3+} (d^4) and V^{2+} (d^5), all are ferroelectric and simultaneously magnetic. In these systems, the main instability leading to ferroelectricity is largely driven by the A-ions. These A-ions, such as Bi^{3+} and Pb^{2+} , are known to have the so-called lone pairs—two valence electrons ($6s^2$), which are not hybridized and do not participate in chemical bonds. This gives high polarizability of the corresponding ions, which is believed to induce strong ferroelectricity. From a microscopic point of view, it can be explained that the particular orientation of these lone pairs may create local dipoles, which finally can lead to a ferroelectric or anti-ferroelectric order (see Figure 1.6). This mechanism is a 2nd order Jahn-Teller effect, just like the case of the ferroelectricity " d^0 ". Thus the ferroelectricity due to lone pairs is also called "proper" (the ferroelectricity mainly comes from the structural instability toward the polar state) [26].

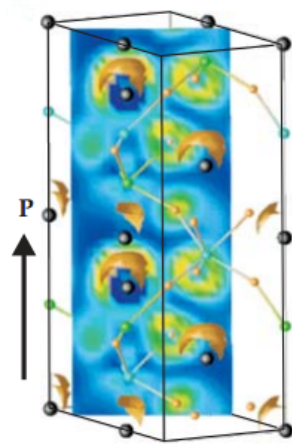


Figure 1.6 – A calculation of the charge density in multiferroic BiFeO_3 . The gold blobs are the Bi^{3+} ions' (black) lone-pair electrons; their alignment results in a ferroelectric polarization (\mathbf{P}) [27].

1.4.3 Ferroelectricity due to Charge Ordering

Another mechanism that can lead to ferroelectricity is the charge ordering, originating from the electronic correlations rather than a relative displacement between anions and cations associated with the 2nd order Jahn–Teller effect mentioned above. It is often observed in transition metal compounds with different valences.

If there is a structure consisting of dimers with equivalent sites, as in Figure 1.7(a). Obviously, its structure is centrosymmetric and non-ferroelectric. However, if there is an extra charge ordering, as in Figure 1.7(b), it makes the dimer sites inequivalent, producing a dipole (double arrows in Figure 1.7(b)). This will form a net electric polarization, leading the entire system to be ferroelectric. If some of the ions are magnetic, then the systems can become multiferroics.

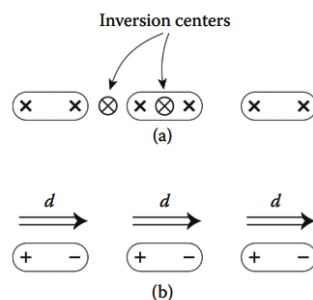


Figure 1.7 – Illustration of how charge ordering can lead to ferroelectricity (the inversion centers are marked by \otimes) [28].

In the system of $\text{Pr}_{1/2}\text{Ca}_{1/2}\text{MnO}_3$ [29] or nickelates YNiO_3 [26], both sites and bonds could turn out to be non-centrosymmetric after charge ordering. This leads to ferroelectricity (see Figure 1.8). Figure 1.8(a) is the charge-ordering with a simple checkerboard pattern characterized by the alternation of Mn^{3+} and Mn^{4+} sites. Figure 1.8(b) corresponds to charges localized not on the sites but on the bonds. In these two simple cases, the structure can remain centrosymmetric and non-ferroelectric. Besides these two pure states, the intermediate pattern is shown in Figure 1.8(c). It is clear that the system is ferroelectric because the charge-ordering does not present an inversion symmetry. Another possible mechanism is when the bonds are inequivalent due to the structure, the site-centered charge order appears on top of that, which can also lead to ferroelectricity. This is the case in the quasi-1D organic ferroelectric $(\text{TMTTF})_2\text{X}$ [30].

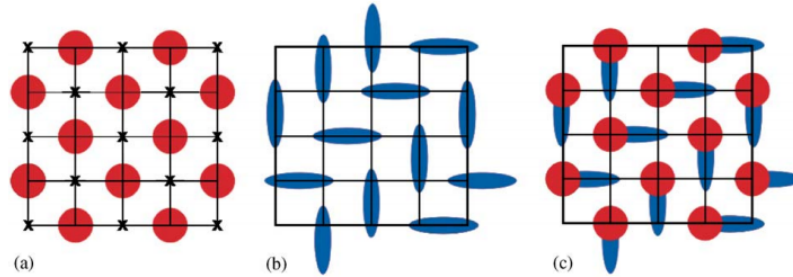


Figure 1.8 – (a) Site-centered charge ordering in half-doped manganites like $\text{Pr}_{1/2}\text{Ca}_{1/2}\text{MnO}_3$, (b) bond-centred ordering, and (c) combined ordering, giving ferroelectricity [29].

1.4.4 "Geometric" Ferroelectricity

The ferroelectrics addressed above are the "proper" ferroelectric. However, there are many multiferroics with "improper" ferroelectricity. Their ferroelectricity is a secondary effect of a primary ordering. The best known systems in this subgroup are the hexagonal RMnO_3 ($\text{R} = \text{Y}$ or small rare earths). Despite the similar formula ABO_3 , they have quite different crystal and electronic structures compared to the perovskites materials mentioned above.

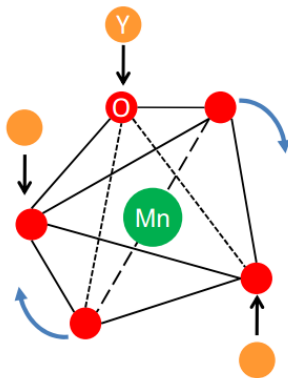


Figure 1.9 – The geometric mechanism responsible for the ferroelectricity in the YMnO_3 at low temperature [22].

In the system of hexagonal YMnO_3 , the Mn^{3+} ions are not located in the O_6 octahedron (as for conventional perovskites), but in the center of a O_5 trigonal bipyramid. In addition, Y ions, are not in a 12-fold, but in a 7-fold coordination. The origin of the ferroelectricity in hexagonal manganites has been a subject of debate because these manganites do not possess either " d^0 " or "isolated pair electrons ($6s^2$)". The structural study has shown that the ferroelectricity in hexagonal YMnO_3 has nothing to do with the magnetic Mn^{3+} , but is caused by a preliminary structural transition associated with the tilting of the practically rigid MnO_5 blocks. This tilting provides the tendency to a close packing with the oxygen ions moving closer to the small Y ions. This leads to a loss of the inversion symmetry. The electric dipoles are mainly formed rather by Y–O pairs than by Mn–O pairs [22] (see Figure 1.9).

1.5 Type II Magnetoelectric Multiferroics

The type II multiferroics are a novel class of multiferroics, in which the ferroelectricity exists only in a magnetically ordered state. The multiferroicity is driven by a particular type of magnetic ordering [8, 9]. The crystal structure of this kind of multiferroic is centrosymmetric and thus considered to be non-ferroelectric. However, due to a particular type of magnetic order, as well as the magnetic frustration, atomic displacements releasing the magnetic frustration cause inversion symmetry breaking. The ferroelectricity is thus "improper".

One can divide type-II multiferroics into two groups: those in which the ferroelectricity is caused by non-collinear magnetic structures (Section 1.5.1) and those in which the ferroelectricity appears from collinear up-up-down-down($\uparrow\uparrow\downarrow\downarrow$) magnetic structures (Section 1.5.2).

1.5.1 Multiferroics in Spiral Magnetic Structures

Most of the type-II multiferroics known until now belong to this subgroup. Ferroelectricity appears associated with spiral magnetic structures. The structures of these systems are often incommensurate compared to the underlying crystal lattice. In a crystal, the general Heisenberg Hamiltonian for all the (i, j) pairs of atoms of the many electrons system can be expressed:

$$\mathcal{H} = \sum_n J_{ij} \mathbf{S}_i \cdot \mathbf{S}_j \quad (1.6)$$

- J_{ij} : the exchange interaction of atom i and j .
- \mathbf{S}_i and \mathbf{S}_j : the Heisenberg spin moment at site i and site j .

There are different types of spin structures relevant to this subgroup, see Figure 1.10. Figure 1.10(a) is the proper screw type, with spins rotating in the plane perpendicular to the propagation wave vector. Figure 1.10(b) is the cycloidal type, with the spin rotating in the plane which contains the propagation wave vector. Figure 1.10(c) is the longitudinal-conical type, with the propagation wave vector perpendicular to the spiral plane. And Figure 1.10(d) is the transverse-conical type, with the propagation wave vector parallel to the spiral plane. In most cases, ferroelectricity is produced by the cycloidal magnetic structures of Figure 1.10(b).

The nonlinear coupling between static \mathbf{P} and \mathbf{M} comes from the interplay of charge, spin, orbital and lattice degrees of freedom. Whether the coupling can induce polarization in a magnetically ordered state largely depends on the form of the magnetic structure. If the magnetic structure is constituted of spatially inhomogeneous spins (\mathbf{M} varies over the crystal), a third-order term of the form $\mathbf{P}\mathbf{M}\partial\mathbf{M}$ (flexomagnetoelectric term in [31]) is possible. That is to say, the coupling between a homogeneous electric polarization and a magnetization can be linear in \mathbf{P} and contains one gradient of \mathbf{M} . In the simplest case of cubic symmetry crystals, the coupling term inducing electric polarization is [32]:

$$\mathbf{P} \propto [(\mathbf{M} \cdot \nabla)\mathbf{M} - \mathbf{M}(\nabla \cdot \mathbf{M})] \quad (1.7)$$

According to this equation, if all the magnetic moments are uniformly aligned, for example, in the case of an ideal ferromagnetic order, the gradient of \mathbf{M} is zero, and so is the polarization. That's why the multiferroicity is usually associated with complex magnetic orders as observed in frustrated systems. Indeed, frustration plays a major role to have spatial variations of magnetization. The propagation wave vector in frustrated systems depends on the competing exchange interactions J and usually is incommensurate.

For instance, a one-dimensional spin chain with a ferromagnetic interaction $J < 0$ between neighboring spins has a uniform ground state with parallel spins. If there is an additional antiferromagnetic next-nearest-neighbor interaction $J' > 0$, The Heisenberg model becomes $\mathcal{H} = \sum_n [J\mathbf{S}_n \cdot \mathbf{S}_{n+1} + J'\mathbf{S}_n \cdot \mathbf{S}_{n+2}]$. If $J' / |J| > 1/4$, it will frustrate this simple ordering (see Figure 1.11(b)). The frustrated ground state

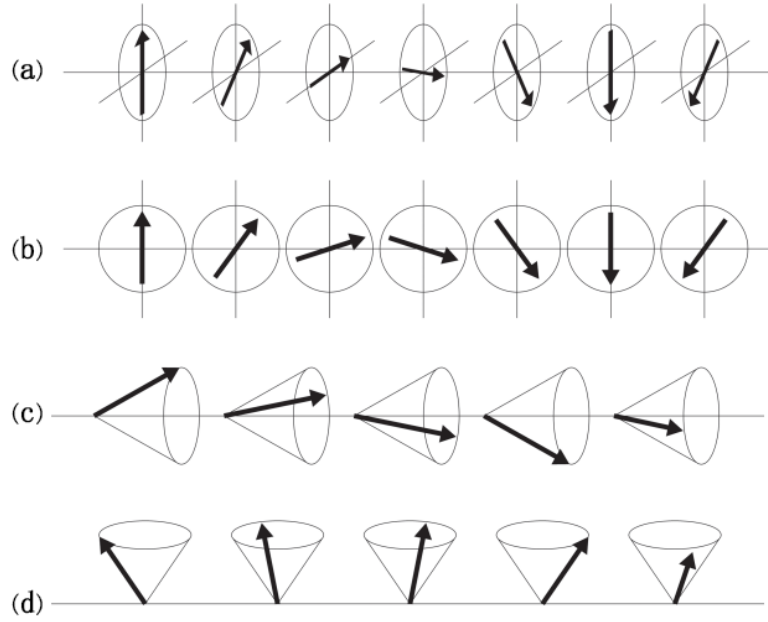


Figure 1.10 – Schematic illustrations of types of spiral magnetic structure that may give rise to multiferroicity [28].

is characterized by a magnetic spiral order called spiral spin density wave (SDW). It can be expressed as [33]:

$$\mathbf{S}_n = S_1 \mathbf{e}_1 \cos \mathbf{Q} \cdot \mathbf{x}_n + S_2 \mathbf{e}_2 \sin \mathbf{Q} \cdot \mathbf{x}_n \quad (1.8)$$

- \mathbf{Q} : the propagation vector in the reciprocal space
- \mathbf{x}_n : the position vector in the direct space
- S_1, S_2 : the components of the magnetic moments along the orthogonal unit vectors $\mathbf{e}_1, \mathbf{e}_2$
- the value of the wave vector \mathbf{Q} is given by $\cos(Q/2) = J'/4J$

When S_1 , or S_2 , is zero, Equation (1.8) becomes of the type $\mathbf{S}_n = \mathbf{S} \cos \mathbf{Q} \cdot \mathbf{x}_n$, it is the case of sinusoidal spin density wave (SDW). It cannot induce ferroelectricity due to cosine term which is not invariant by spatial inversion as shown in Figure 1.11(a). When S_1 and S_2 are both non-zero, Equation (1.8) describes a spiral spin order. The spiral spin order spontaneously breaks time-reversal symmetry (like any other magnetic ordering), and the spatial inversion is also broken because it would change the direction of rotation of the spins in the spiral. Thus, the symmetry of the spiral state allows for a simultaneous presence of ferroelectricity and ferromagnetism and can lead to multiferroicity.

Combining Equation (1.7) and Equation (1.8), we can obtain :

$$\mathbf{M} = M_1 \mathbf{e}_1 \cos \mathbf{Q} \cdot \mathbf{x}_n + M_2 \mathbf{e}_2 \sin \mathbf{Q} \cdot \mathbf{x}_n \quad (1.9)$$

$$\begin{aligned} \mathbf{P} &\propto [(\mathbf{M} \cdot \nabla) \mathbf{M} - \mathbf{M}(\nabla \cdot \mathbf{M})] \\ &= \left(\mathbf{M}_x \frac{\partial}{\partial x} + \mathbf{M}_y \frac{\partial}{\partial y} \right) \mathbf{M} - \mathbf{M} \left(\frac{\partial \mathbf{M}_x}{\partial x} + \frac{\partial \mathbf{M}_y}{\partial y} \right) \\ &= \left(\mathbf{M}_x \frac{\partial \mathbf{M}_x}{\partial x} + \mathbf{M}_y \frac{\partial \mathbf{M}_x}{\partial y} \quad \mathbf{M}_x \frac{\partial \mathbf{M}_y}{\partial x} + \mathbf{M}_y \frac{\partial \mathbf{M}_y}{\partial y} \right) - \left(\mathbf{M}_x \left(\frac{\partial \mathbf{M}_x}{\partial x} + \frac{\partial \mathbf{M}_y}{\partial y} \right) \quad \mathbf{M}_y \left(\frac{\partial \mathbf{M}_x}{\partial x} + \frac{\partial \mathbf{M}_y}{\partial y} \right) \right) \\ &= \left(\mathbf{M}_y \frac{\partial \mathbf{M}_x}{\partial y} - \mathbf{M}_x \frac{\partial \mathbf{M}_y}{\partial y} \quad \mathbf{M}_x \frac{\partial \mathbf{M}_y}{\partial x} - \mathbf{M}_y \frac{\partial \mathbf{M}_x}{\partial x} \right) \end{aligned} \quad (1.10)$$

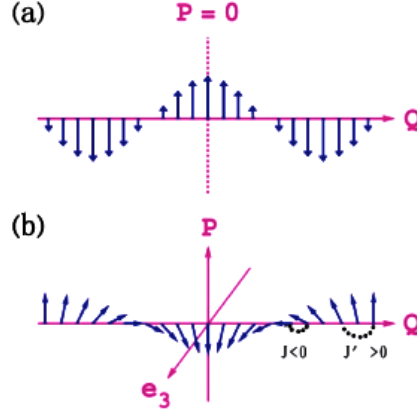


Figure 1.11 – Spin order for a one-dimensional spin chain with competing exchange interactions (a) sinusoidal. (b) spiral ground state [33].

If we consider \mathbf{e}_1 and \mathbf{e}_2 as in the Figure 1.12(a), then

$$\begin{aligned}\frac{\partial \mathbf{M}_x}{\partial x} &= Q M_1 \sin \mathbf{Q} \cdot \mathbf{x}_n = -\frac{\partial \mathbf{M}_x}{\partial y} \\ \frac{\partial \mathbf{M}_y}{\partial y} &= Q M_2 \cos \mathbf{Q} \cdot \mathbf{x}_n = -\frac{\partial \mathbf{M}_y}{\partial x}\end{aligned}$$

$$\Rightarrow \mathbf{P} \propto [(\mathbf{M} \cdot \nabla) \mathbf{M} - \mathbf{M}(\nabla \cdot \mathbf{M})] = Q M_1 M_2 (\mathbf{e}_1 + \mathbf{e}_2) \quad (1.11)$$

it means that the induced electric dipole is orthogonal both to \mathbf{Q} and \mathbf{e}_3 (\mathbf{e}_3 is the spin-rotation axis $\mathbf{e}_3 = \mathbf{e}_1 \times \mathbf{e}_2$), as shown in Figure 1.11(b). The induced electric dipole moment \mathbf{P} can be expressed:

$$\mathbf{P} \parallel \mathbf{e}_3 \times \mathbf{Q} \quad (1.12)$$

In the most common case of cycloidal structures, the ferroelectricity can be explained by the inverse Dzyaloshinskii–Moriya (DM) model. The antisymmetric DM interaction can be expressed as:

$$\mathcal{H}_{DM} = \mathbf{D}_{12} \cdot (\mathbf{S}_1 \times \mathbf{S}_2) \quad (1.13)$$

- \mathbf{D}_{12} : the Dzyaloshinskii vector [34, 35].

This interaction \mathcal{H}_{DM} is proportional to the spin–orbit coupling constant. It is a relativistic correction to the usual superexchange. It is presented in Figure 1.12(a). \mathbf{D}_{12} is proportional to the spin-orbit coupling constant λ and the displacement of the oxygen ion from the center of the metal ions bond (full red circles), $\mathbf{D}_{12} \propto \lambda \mathbf{x} \times \mathbf{r}_{12}$. This interaction results in the canting of collinear spins \mathbf{S}_1 and \mathbf{S}_2 . In the spiral magnetic ordering systems, it is the inverse effect. The spiral magnetic structure has canted neighboring spins. In addition, the vector product $\mathbf{S}_1 \times \mathbf{S}_2$ has the same sign for all pairs of neighboring spins. The DM interaction favors the shift of the oxygen ions from the axis between ions supporting spins to gain in DM energy. This induces an electric polarization perpendicular to the vector product between spins [36]. The DM interaction favors non-collinear spin ordering. For example, in the antiferromagnetic LaCu_2O_4 system, weak ferromagnetism can be induced by the DM interaction (see Figure 1.12(b)).

The spin–orbit coupling (not necessarily the DM interaction) distorts the electronic cloud surrounding the ions. This may lead to a pure electronic charge dipole. The spin current (KNB) theory [37] was proposed to explain this issue by using the quantum perturbation theory to the Hubbard model with spin–orbit coupling. The induced charge dipole is thus proportional to r_{ij} and the vector product of spins \mathbf{S}_i and \mathbf{S}_j ,

$$\mathbf{P} \sim \mathbf{r}_{ij} \times (\mathbf{S}_i \times \mathbf{S}_j) \quad (1.14)$$

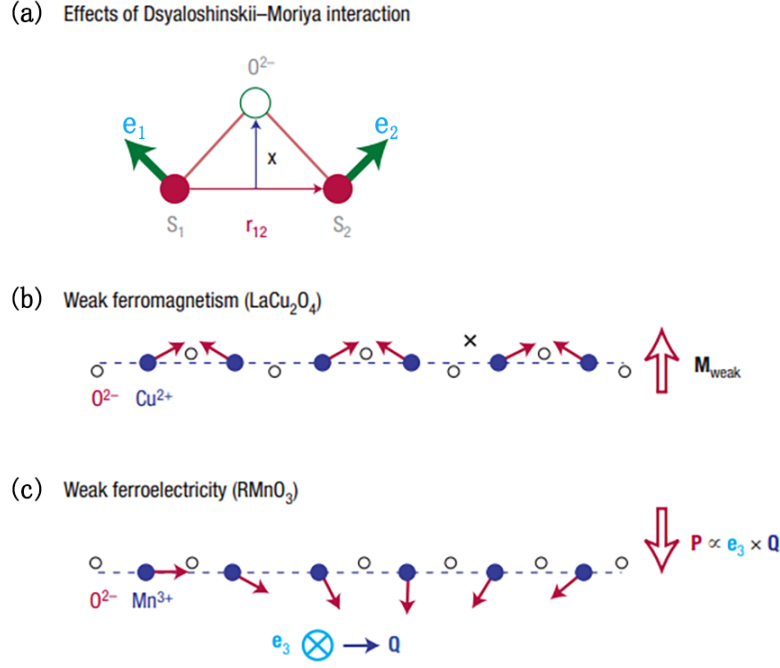


Figure 1.12 – (a) Effects of the antisymmetric Dzyaloshinskii–Moriya interaction. (b) antiferromagnets LaCu_2O_4 layers system. (c) cycloidal magnetic structure of RMnO_3 system [26].

- \mathbf{r}_{ij} : the vector from site i to site j .

For the cycloidal magnetic structures, the electric polarization is:

$$\mathbf{P} \sim \mathbf{Q} \times (\mathbf{S}_i \times \mathbf{S}_j) \sim \mathbf{Q} \times \mathbf{e} \quad (1.15)$$

- \mathbf{Q} : the wave vector of the cycloid
- \mathbf{e} : the axis of rotation of the spins in the cycloid.

The KNB theory considers no ionic displacement contribution. It is based on a spin current. The KNB theory can be viewed as the counterpart of the DM interaction.

1.5.2 Multiferroics in Collinear Magnetic Structures

Another type of magnetically driven ferroelectrics concerns materials in which ferroelectricity appears in collinear magnetic structures. Let us consider the one-dimensional Ising spin chain $\sigma = \pm 1$ (see Figure 1.13), with $\mathcal{H} = \sum_n [J\sigma_n\sigma_{n+1} + J'\sigma_n\sigma_{n+2}]$. The nearest-neighbor ferromagnetic interaction (J) and next-nearest-neighbor antiferromagnetic interaction (J') has the ground state up–up–down–down ($\uparrow\uparrow\downarrow\downarrow$) if $J' / |J| > 1/2$ [38].

In this case, a ferroelectricity can be induced by the magnetism through an exchange striction (ES) mechanism (also called magnetostriction). The simplest example is shown in Figure 1.14. With a lattice chain made of ions with different charges, which is centrosymmetric (as in Figure 1.14 (a)). Due to the present of $J' > |J|/2$, the magnetic structure has the up–up–down–down ($\uparrow\uparrow\downarrow\downarrow$) configuration (Figure 1.14 (b)). In order to favor the ferromagnetic (FM) exchange between neighboring spins, atomic displacements can occur and lead to inequivalent bounds. The FM bonds shorten, while the AFM bonds stretch, thus the inversion symmetry would be broken and an electronic polarization yields along the spin chain, as shown in Figure 1.14 (c).

Experimentally, there are many multiferroic systems presenting this mechanism of ferroelectricity: $\text{Ca}_3\text{CoMnO}_6$ [39] (one-dimensional Ising spin chain), the orthorhombic HoMnO_3 [40] (two-dimensional E-type antiferromagnets), CdV_2O_4 [41], TbMn_2O_5 [42] and others.

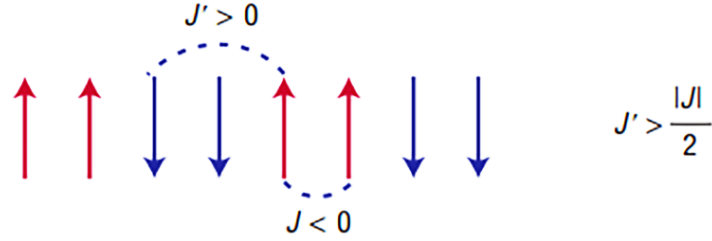


Figure 1.13 – Chain of Ising spins $\sigma_n = \pm 1$ with up–up–down–down ($\uparrow\uparrow\downarrow\downarrow$) ground state [26].

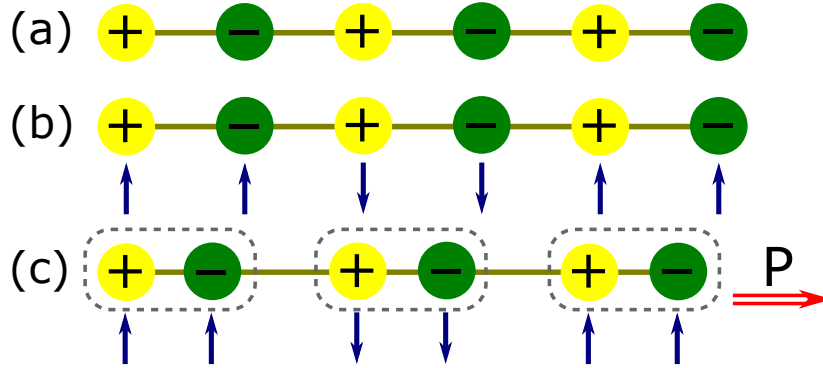


Figure 1.14 – (a) One-dimensional chain with alternating charges. (b) one-dimensional chain with alternating spins and up–up–down–down ($\uparrow\uparrow\downarrow\downarrow$) spins. (c) exchange striction (ES) mechanism (magnetostriction), which shortens the ferromagnetic bonds, thus generates a ferroelectric polarization along the chain.

The orthorhombic HoMnO_3 is a good example to explain how the ES mechanism leads to a polarization. HoMnO_3 prefers the hexagonal structure (type-I multiferroics) by nature, but by proper synthesis method, meta-stable orthorhombic structure can be obtained (type-II multiferroics). Below 42 K, the Mn spins of the system become ordered from a paramagnetic state to a sinusoidal AFM state. Upon cooling, the Mn spins become an E-type AFM state at 26 K [40]. This E-type AFM is characterized by the FM collinear zig-zag chains in the (a, c) plane, coupled AFM as shown in Figure 1.15. Along the pseudo-cubic directions (the diagonal direction of the (a, c) plane), the E-type AFM orders are up–up–down–down ($\uparrow\uparrow\downarrow\downarrow$). Since there are only Mn^{3+} and Mn^{4+} in this system, the ES mechanism is more complex than the simplest mechanism mentioned above. In this case, the Mn ionic displacements do not directly lead to a polarization. But the exchange interactions J_{ij} depend not only on the bond length but also the bond angle through oxygen (super exchange), the ES mechanism can modulate the Mn – O – Mn angles in coherence with the up–up–down–down ($\uparrow\uparrow\downarrow\downarrow$) magnetic order. The octahedral rotation associated with the uniform displacement results in a net polarization along the a -axis [36].

The ES mechanism based on the spin–lattice coupling, i.e. a symmetric exchange between two neighboring spins, can induce a global striction along a specific crystallographic direction Π_{ij} . The electronic polarization is expected to be proportional to the scalar product of \mathbf{S}_i and \mathbf{S}_j :

$$\mathbf{P}_{ij} \propto \Pi_{ij}(\mathbf{S}_i \cdot \mathbf{S}_j). \quad (1.16)$$

Note that this mechanism does not require any spin–orbit interaction, thus the induced electric polarization is generally stronger than that of magnetic spiral structures. However, the direction of the electric polarization has no relationship with the direction of the spins but is determined by the symmetry of the crystal. Its direction is difficult to modify by a magnetic field. This will be addressed in Chapter 2.

In the past decade, the orthorhombic RMnO_3 family and $\text{Ca}_3\text{CoMnO}_6$ have been adopted as the model to explain the discovery of new type-II multiferroics. The manganites RMn_2O_5 (R = rare earth,

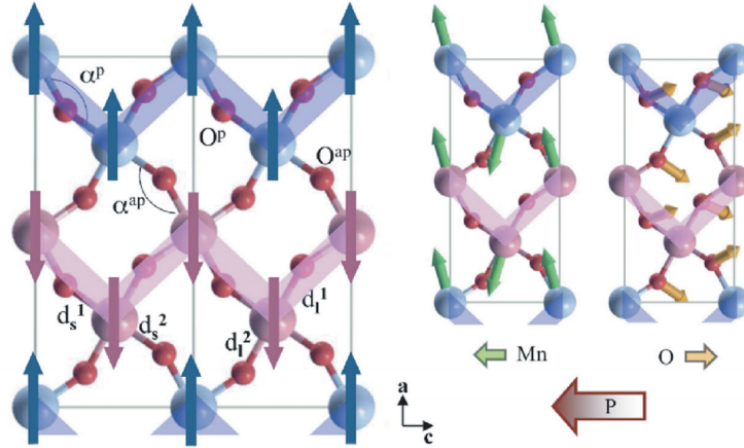


Figure 1.15 – The (a, c) plane structure (in the $Pbnm$ notation) and magnetic (E-type antiferromagnetic) structure of orthorhombic RMnO_3 . The spins are denoted by arrows. The particular zigzag spin chains are highlighted by shaded areas. α^P and α^{AP} denote the Mn – O – Mn bond angles between the parallel and antiparallel spin pairs, respectively, noting that they are different due to the ES mechanism. [43]

Y, and Bi) were supposed to follow a similar mechanism. However, due to their more complex crystal structures and complicated magnetic and ferroelectric phase transitions, the microscopic mechanism of their multiferroicity was not definitively established until recently [44]. This part will be detailed in Chapter 2.

1.5.3 Other Mechanism (Spin-Dependent Hybridization)

In the case of a helical magnetic structure, for which the rotation plane of the spins is perpendicular to the propagation vector, $\mathbf{D}_{12} = 0$ as \mathbf{r}_{12} is parallel to $\mathbf{S}_1 \times \mathbf{S}_2$, thus another microscopic mechanism has been proposed by Arima based on the spin-orbit coupling [45] (called metal-ligand hybridization). It involves the variation due to the spin-orbit coupling of the hybridization between the d orbitals of the magnetic ion and the p orbitals of oxygen. The local polarization is expressed for each metal cation as:

$$\mathbf{P} = \sum_i (\mathbf{e}_i \cdot \mathbf{S}_i)^2 \mathbf{e}_i \quad (1.17)$$

where the summation is over all the bonds and \mathbf{e}_i denotes the bond direction, as shown in Figure 1.16. A distinct difference here is that only a single magnetic site is considered for a local electric dipole, while the DM interaction involves two magnetic sites.

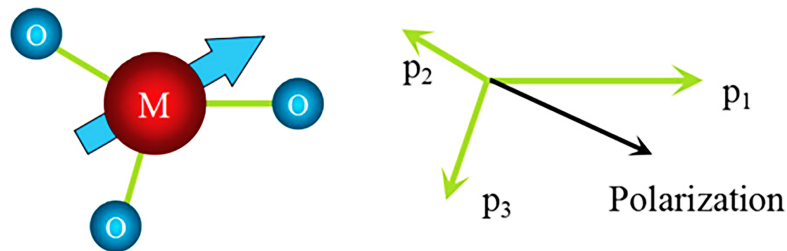


Figure 1.16 – A metal ion in an anion cage can break the inversion symmetry (left), in case of a metal-ligand hybridization because it gives rise to spin-dependent dipoles for the three different bonds allowing a net electric polarization (right). [46].

Summary of this Chapter

In this chapter we have shown the fascinating physical phenomena of multiferroic materials and their promising potential applications in Section 1.1. We have focused on the most studied ME multiferroics (Section 1.2). General considerations to combine ferroelectricity and magnetism have been presented in Section 1.3.1. We have shown that the induced ferroelectricity due to magnetic orders (Section 1.3.1) is the basic mechanism for type II multiferroics. Finally we have listed several representative mechanisms for both type I and type II multiferroics in Section 1.4 and Section 1.5. It is summarized in Table 1.1.

Table 1.1 – Classification of multiferroics due to different microscopic mechanism of ferroelectricity [19].

Classification	Mechanisms	Representatives	ME coupling
Type-I	Perovskites	BaTiO ₃	Weak
	Lone pairs (6s ²)	BiFeO ₃ , PbVO ₃	
	Charge ordering	Pr _{1/2} Ca _{1/2} MnO ₃ , RNiO ₃	
	Geometric	YMnO ₃	
Type-II	Spiral magnetic	TbMnO ₃	Strong
	Collinear magnetic	HoMnO ₃ , TbMn ₂ O ₅	

2

RMn₂O₅ Multiferroics

Contents

2.1	Why RMn₂O₅?	18
2.2	Common Features	18
2.2.1	General Structure	18
2.2.2	General parameters and Chemical Pressure Effect	21
2.2.3	Sequence of Magnetic Ordering	22
2.2.4	Ferroelectric Properties of the RMn ₂ O ₅ Compounds	22
2.3	Microscopic Mechanism of Ferroelectricity	24
2.4	Specificities Upon the Nature of R³⁺	25
2.4.1	Propagation Wave Vector	26
2.4.2	Spiral Structure in DyMn ₂ O ₅	26
2.4.3	Spin Ordering along the <i>c</i> Axis of the RMn ₂ O ₅ with R = Sm, La and Er	26
2.4.4	an Abnormally High Electric Polarization in GdMn ₂ O ₅	26
2.5	Multiferroic Properties Affected by External Parameters	27
2.5.1	Multiferroic Behavior under Magnetic Field	27
2.5.1.1	Magnetic Field H Parallel to the <i>a</i> Axis	28
2.5.1.2	Magnetic Fields H Parallel to the <i>b</i> Axis	30
2.5.1.3	Magnetic Fields H Parallel to the <i>c</i> Axis	30
2.5.2	Multiferroic Behavior under an External Pressure	31
2.6	Electromagnons in RMn₂O₅	33
2.7	The Aims of Our Work	34

This chapter presents the structure and properties of the RMn₂O₅ family of multiferroics. The motivation for these particular compounds is first shown in Section 2.1. Their common electric and magnetic features are given in Section 2.2. In Section 2.3, we address the ES mechanism for this family, which differs from the one in Chapter 1 Section 1.5.2. The selected specialties due to the R³⁺ are presented in Section 2.4. We also discuss the external factors, which influence their multiferroic properties, in Section 2.5. In the end, we show the aims of this thesis in Section 2.7.

2.1 Why RMn_2O_5 ?

The family RMn_2O_5 ($R = \text{rare earth, Y or Bi}$) was first described in 1964 [47], but its multiferroic properties were discovered only recently. The experimental discovery of remarkable magnetoelectric coupling in TbMn_2O_5 [9] is one of the reasons that makes the RMn_2O_5 family exceptional and interesting to study.

In this family, TbMn_2O_5 first drew attention because it allows to strikingly reverse the electric polarization by applying a magnetic field [9] (see Figure 2.13(a)). Shortly, DyMn_2O_5 was found to present a colossal magnetodielectric effect [48] (see Figure 2.15). Another surprising feature has been observed in TmMn_2O_5 : below 5 K, by applying a magnetic field of approximately 0.5 T along the c axis, it exhibits a reversible electric polarization flop from the a axis (\mathbf{P}_a) to the b axis (\mathbf{P}_b). It corresponds to a magnetic phase transition from incommensurate magnetic (ICM) \mathbf{P}_a phase to another ICM \mathbf{P}_b phase [49] (see Figure 2.17). Later, a giant tunability of the ferroelectric polarization ($\Delta\mathbf{P} = 5000 \mu\text{C} \cdot \text{m}^{-2}$) has been discovered in GdMn_2O_5 by applying a magnetic field [50]. In addition, the electromagnon is reported to be the origin of the colossal magneto-dielectric effect in YMn_2O_5 and TbMn_2O_5 [51] (see Figure 2.23). Therefore, these new physical phenomena and fascinating multiferroic properties emerging in the RMn_2O_5 compounds need to be understood.

2.2 Common Features

2.2.1 General Structure

As claimed in a recent work [52], the RMn_2O_5 compounds crystallize in the ferroelectric Pm space group at room temperature. It differs from the average $Pbam$ orthorhombic space group, generally considered, by weak deformations related mainly to the oxygen positions and in a less extend to the Mn positions. The real space group Pm is only possible to experimentally detect with single crystal due to the weak intensity of the absent Bragg reflections of $Pbam$ space group. In addition, the monoclinic angles of the Pm space are very close to 90° ($90.01(1)^\circ$) [52], which can not be distinguished even by powder diffraction. The tables of the structure of DyMn_2O_5 described within the two space groups are given in Table 2.1 and Table 2.2. In the following we will mainly use the description of the structure in the $Pbam$ space group.

Table 2.1 – Atomic positions of DyMn_2O_5 at 298 K in the $Pbam$ space group. The lattice parameters are $a = 7.2940 \text{ \AA}$, $b = 8.5510 \text{ \AA}$, $c = 5.6875 \text{ \AA}$. [53]

Atom	Wyckoff positions	x	y	z
Dy	$4g(x, y, 0)$	0.1387	0.1716	0
Mn1	$4f(0, 1/2, z)$	0	0.5	0.2548
Mn2	$4h(x, y, 1/2)$	0.4119	0.3500	0.5
O1	$4e(0, 0, z)$	0	0	0.2741
O2	$4g(x, y, 0)$	0.1647	0.4452	0
O3	$4h(x, y, 1/2)$	0.1537	0.4354	0.5
O4	$8i(x, y, z)$	0.3951	0.2082	0.2414

The structure is composed of chains of Mn^{4+}O_6 octahedra running along the c axis, separated by layers of R^{3+} ions or Mn^{3+}O_5 bipyramids (represented in Figure 2.1). Within the (a, b) plane, two zig-zag chains of Mn^{4+}O_6 octahedra and Mn^{3+}O_5 pyramids in the unit cell run along the a axis and are stacked along the b direction.

Table 2.2 – Atomic positions of DyMn₂O₅ at 300 K in the *Pm* space group. The lattice parameters are $a = 7.2931 \text{ \AA}$, $b = 8.5025 \text{ \AA}$, $c = 5.6743 \text{ \AA}$. $\gamma = 90^\circ$. [52]

Atom	Wyckoff positions	x	y	z
Dy1 ₁	1 <i>a</i>	0.138964	0.171696	1
Dy1 ₂	1 <i>a</i>	-0.138953	-0.171402	-1
Dy1 ₃	1 <i>a</i>	0.638745	0.328455	-1
Dy1 ₄	1 <i>a</i>	-0.638650	-0.328396	1
Mn1 ₁	2 <i>c</i>	0.00027	0.49993	1.25550
Mn1 ₂	2 <i>c</i>	0.50034	0.00017	-1.25549
Mn2 ₁	1 <i>b</i>	0.41162	0.35041	0.5
Mn2 ₂	1 <i>b</i>	-0.41197	-0.35002	-0.5
Mn2 ₃	1 <i>b</i>	0.91181	0.14942	-0.5
Mn2 ₄	1 <i>b</i>	-0.91191	-0.15032	0.5
O1 ₁	2 <i>c</i>	0.0003	-0.00065	0.27409
O1 ₂	2 <i>c</i>	0.5002	0.50265	-0.27048
O2 ₁	1 <i>a</i>	0.16290	0.44480	0
O2 ₂	1 <i>a</i>	-0.1674	-0.44552	0
O2 ₃	1 <i>a</i>	0.66178	0.05594	0
O2 ₄	1 <i>a</i>	-0.6592	-0.05567	0
O3 ₁	1 <i>b</i>	0.14701	0.41971	0.5
O3 ₂	1 <i>b</i>	-0.1514	-0.43336	-0.5
O3 ₃	1 <i>b</i>	0.65281	0.06249	-0.5
O3 ₄	1 <i>b</i>	-0.6548	-0.0612	0.5
O4 ₁	2 <i>c</i>	0.39543	0.20296	0.25333
O4 ₂	2 <i>c</i>	-0.40123	-0.20960	-0.23719
O4 ₃	2 <i>c</i>	0.89595	0.29307	-0.2425
O4 ₄	2 <i>c</i>	-0.89174	-0.29566	0.24629

In this plane, there are three inequivalent magnetic super-exchange interactions between Mn ions: J_3 and J_4 for the Mn^{3+} - Mn^{4+} couples, and J_5 between two Mn^{3+} spins. Within the chains, the J_4 and J_5 interactions induce an antiferromagnetic (AFM) character while the J_3 couplings between the chains are magnetically frustrated. Along the c axis, there are two different Mn^{4+} - Mn^{4+} super-exchange interactions, depending on whether it is the Mn^{3+} (J_2) or R^{3+} (J_1) ions in between the Mn^{4+} layers. In the first case, a strong magnetic frustration appears since there are two J_4 and two J_3 Mn^{4+} - Mn^{3+} interactions competing with J_2 . It results in an effective order between the two Mn^{4+} ions that is always FM [54, 55]. For J_1 , it is more complex and strongly dependent on the rare earth (its magnetism and number of $4f$ electrons) and on the detailed structural parameters. In particular, it is greatly affected by the distances and angles between cations and oxygens involved in the super-exchange couplings. For certain members of the series, there is an additional Mn^{3+} - R^{3+} interaction, denoted as J_6 [56, 57], shown as a pink arrow in Figure 2.1(b). All the super-exchange interactions J_i ($i = 1, 2, 3, 4, 5$) can be expected to be antiferromagnetic (AFM). However, in these structures the Mn^{4+} through J_2 are always FM ordered. Their values have been determined for TbMn_2O_5 compound (with J_3 set to zero. $J_1 = J_2 = 0.4$ meV, $J_4 = 2.9$ meV and $J_5 = 3.5$ meV) [54].

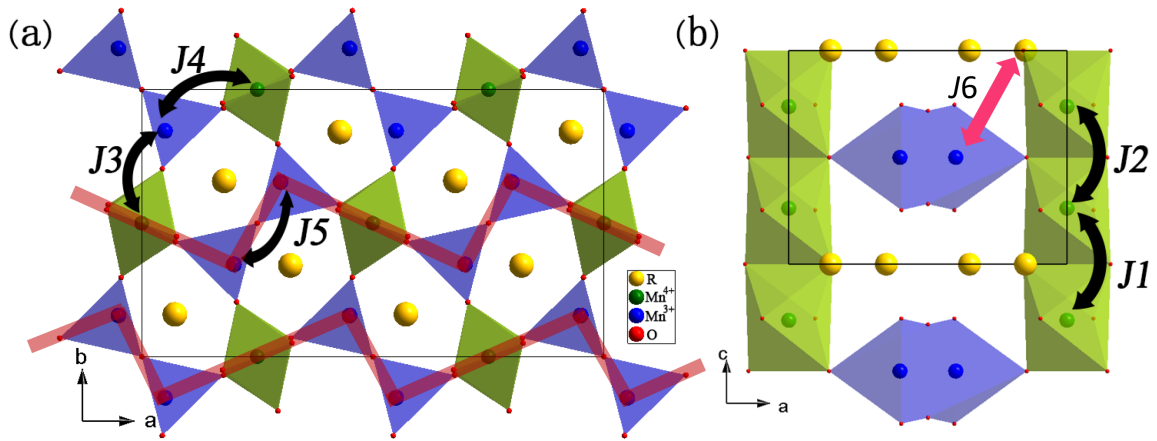


Figure 2.1 – Projections of the crystal structure of RMn_2O_5 along (a) c and (b) b axis. The different J_i exchange interactions are indicated.

In the RMn_2O_5 compounds, the spins of the Mn ions are quasi-collinear regardless of the nature of R^{3+} and generally lie in the (a, b) plane. As shown in the Figure 2.2, the orders of the Mn spins for TbMn_2O_5 , HoMn_2O_5 and DyMn_2O_5 have the same configuration within the (a, b) plane. And the amplitude of the magnetic moments of Mn^{3+} and Mn^{4+} (usually moment of Mn^{3+} is around $3 \mu\text{B}$ and moment of Mn^{4+} is around $2 \mu\text{B}$) are much less than expected (paramagnetic value of Mn^{3+} is $4.9 \mu\text{B}$ and of Mn^{4+} is $3.9 \mu\text{B}$). But the direction of the spins strongly depends on the nature of the R^{3+} . As presented in Figure 2.2, for Tb^{3+} and Ho^{3+} , the spins are roughly along the a axis, while for Dy^{3+} , they are along the b axis. It makes it more essential to elucidate the microscopic mechanism responsible for their multiferroicity.

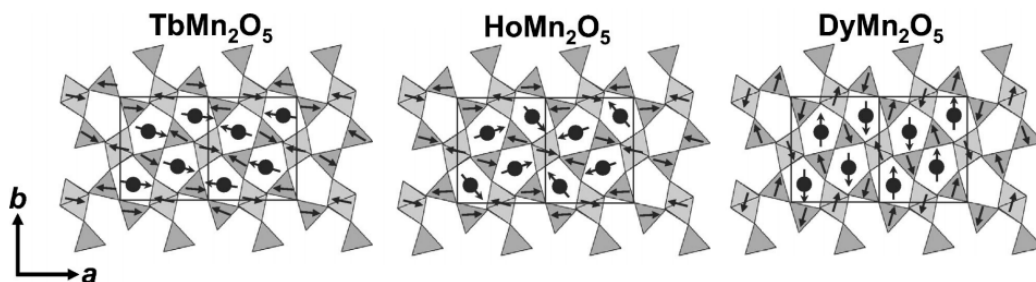


Figure 2.2 – The CM structures of TbMn_2O_5 (27 K), HoMn_2O_5 (26 K) and DyMn_2O_5 (2 K) in the (a, b) plane. The unit cells are doubled along the a axis. [58]

2.2.2 General parameters and Chemical Pressure Effect

The rare earth elements with weights and electrons distribution are shown in Figure 2.3. With increasing the size of the ionic radii of the R^{3+} (from the right to the left in Figure 2.3), the lattice parameters of RMn_2O_5 increase nearly linear, as illustrated in Figure 2.4.

57	58	59	60	61	62	63	64	65	66	67	68	69	70	71
La	Ce	Pr	Nd	Pm	Sm	Eu	Gd	Tb	Dy	Ho	Er	Tm	Yb	Lu
Lanthanum	Cerium	Praseodymium	Neodymium	Promethium (145)	Samarium	Europium	Gadolinium	Terbium	Dysprosium	Holmium	Erbium	Thulium	Ytterbium	Lutetium
138.91	140.12	140.91	144.24	(145)	150.36	151.96	157.25	158.93	162.50	164.93	167.26	168.93	173.05	174.97

Figure 2.3 – The rare earth elements with weights and electrons distribution. From Wikipedia.

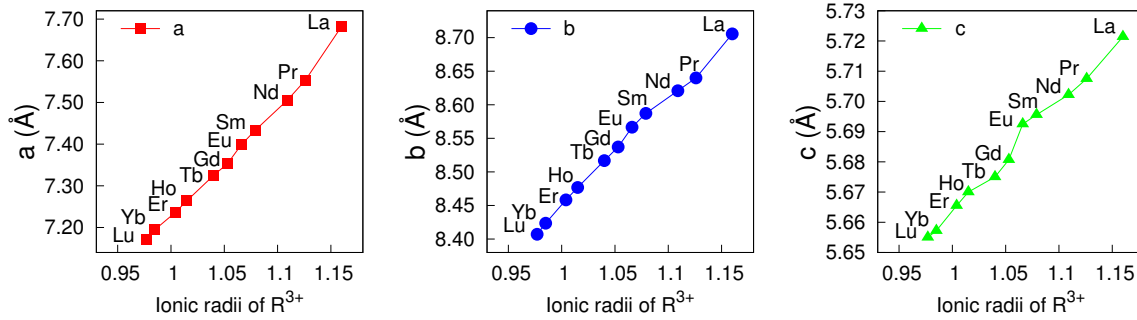


Figure 2.4 – Dependence of the lattice parameters of the RMn_2O_5 compounds at room temperature and ambient pressure as a function of the ionic radii of R^{3+} . [13]

The multiferroic behaviors observed for the various compounds of the RMn_2O_5 series are different, but with similar magnetic orders. The RMn_2O_5 compounds with large ionic radii R^{3+} , as La and Pr do not present a detectable electric polarization and can be considered as paraelectric [55, 59, 60]. While the compounds with smaller rare earths ($Z > 62$ (Sm)) present a finite polarization along the b crystallographic axis. The intermediate size member $NdMn_2O_5$ exhibits only a minute polarization, two orders of magnitude weaker than that of the other members [60]. Unlike the nearly linear evolution of the unit cell parameter as a function of the rare earth size, the electric polarization seems does not evolve linearly with the ionic radii of R^{3+} , as presented in Figure 2.5(a).

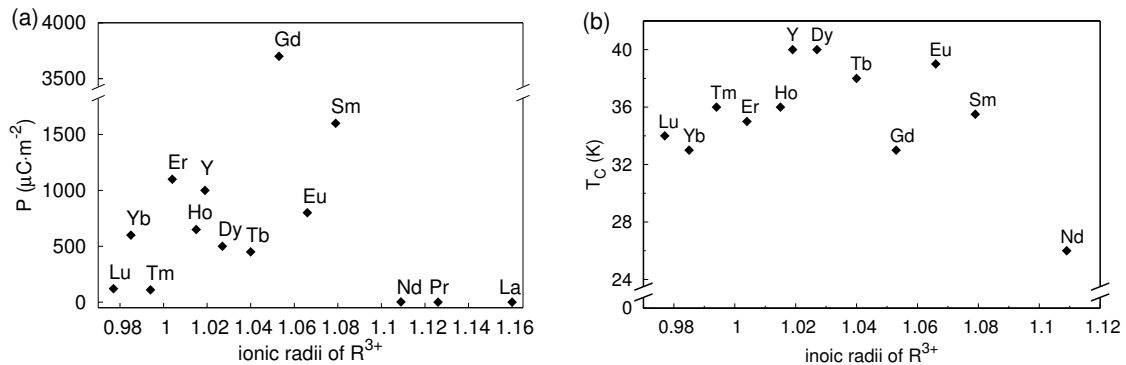


Figure 2.5 – (a) Dependence of the electric polarization of the RMn_2O_5 compounds at ambient pressure as a function of the ionic radii of R^{3+} . Data from Ref. [48, 50, 60–68]. (b) Relation between the T_C of RMn_2O_5 and the ionic radii of R^{3+} . Data from Ref. [42, 50, 60, 62–66, 69, 70].

Note that the electric polarization of the $GdMn_2O_5$ compound is much larger than that of the others. One of the reasons for these differences of multiferroic properties can be attributed to the chemical pressure effect caused by the size of R^{3+} , as the radius of R^{3+} decreases from La to Lu with

the increase of the number of $4f$ electrons. The crystallographic structure undergoes a pressure-like effect called "chemical pressure". This effect strongly affects the multiferroic properties. However, although the ionic radius is almost linear in the "chemical pressure" effect, the multiferroic properties turned to show a threshold. The number of $4f$ electrons is also of particular importance. Indeed, it is involved in the J_6 interaction. In addition, according to the parity of the $4f$ electrons of R^{3+} , the R^{3+} can be non-Kramers (even number) and Kramers (odd number). For Kramer ions, following the Kramers theorem, the electric state is degenerated by time-reversal symmetry. But under a weak local magnetic field, the energy state and the minimum of energy depend on the direction of the magnetic field. The R^{3+} moment is thus strongly anisotropic and never nil. As for the non-Kramers ions R^{3+} , the doublet is composed of equiprobable spin configurations of opposite spins. The magnetic moments thus shrinks and is close to nil. There are of course other important factors needed to take into account to understand the influence of the nature of R^{3+} on the multiferroic properties of the RMn_2O_5 series.

2.2.3 Sequence of Magnetic Ordering

The size of R^{3+} also affects the sequence of magnetic orderings. All members with small ionic radius of the rare earths ($Z > 64$ (Gd)), which are ferroelectric, undergo nearly the same series of transitions (see Figure 2.6). Below ~ 40 K, a paramagnetic (PM) to a high-temperature incommensurate magnetic (HT-ICM) transition is observed at T_N , corresponding to an ICM propagation vector $\mathbf{q} = (\frac{1}{2}-\delta_x, 0, \frac{1}{4}+\delta_z)$, which varies upon the temperature and the nature of R^{3+} [14, 55, 58, 71–73] and it could be paraelectric (PE) or ferroelectric (FE) depending on the R^{3+} . On further cooling, the values of δ_x and δ_z smoothly approach zero, and the magnetic structure locks into a commensurate magnetic (CM) phase at $T_1 \sim 35$ K. This is usually associated with the ferroelectric transition. The electric polarization increases upon decreasing temperature. The Curie temperature (T_C) also varies upon the nature of R^{3+} , as illustrated in Figure 2.5(b). Below $T_2 \sim 25$ K, there is an abrupt transition to a low-temperature incommensurate magnetic (LT-ICM) structure. Upon entering the LT-ICM, the value of the electrical polarization drops to a much smaller value. At low temperature ($T_R \sim 8$ K) an additional magnetic transition stabilizes in certain members of the series, and is usually attributed to the R^{3+} moments ordering. It can occur with the same propagation wave vector as the Mn ordering or with a different propagation wave vector. In this last case, the ordering is generally commensurate with a propagation wave vector $\mathbf{q} = (\frac{1}{2}, 0, 0)$ (for Gd, Dy and Sm) or $\mathbf{q} = (0, 0, \frac{1}{2})$ (for Pr)

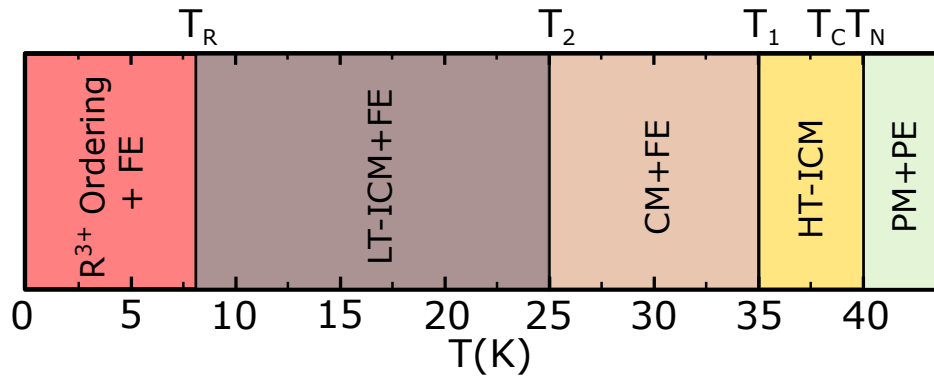


Figure 2.6 – Magnetic and electric phase diagram of the RMn_2O_5 compounds. Here, PM, ICM, CM, PE, and FE are abbreviated forms used to denote paramagnetic, incommensurate magnetic, commensurate magnetic, paraelectric, and ferroelectric states, respectively.

2.2.4 Ferroelectric Properties of the RMn_2O_5 Compounds

The various phase transitions of the RMn_2O_5 compounds are characterized by λ -like anomalies in the temperature evolution of the specific heat C_p / T . The dielectric constant ϵ and the specific heat C_p as a function of temperature of TbMn_2O_5 and DyMn_2O_5 are presented in Figure 2.7.

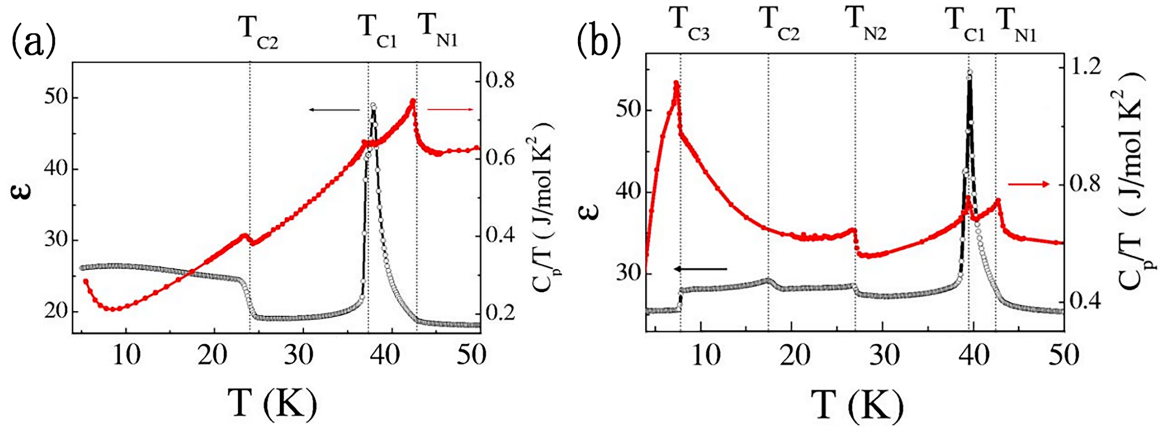


Figure 2.7 – Dielectric constant ϵ along b open circles, left scale and specific heat C_p/T closed circles, right scale of (a) TbMn_2O_5 and (b) DyMn_2O_5 [14]

Generally, below the Néel temperature (T_{N1}), the ICM phase appears with $\mathbf{q} = (\frac{1}{2}-\delta_x, 0, \frac{1}{4}+\delta_z)$. It is well shown in the curve of the specific heat C_p/T , but not obvious through the curve of dielectric constant ϵ . Then the Curie temperature (T_{C1}) emerges at a temperature slightly below T_{N1} , which usually coincides with the lock-in of the magnetic phase into the CM phase. Decreasing temperature to T_{C2} , the CM phase unlocks to the LT-ICM phase, which can easily be observed in the dielectric constant ϵ curve.

Furthermore, below T_{C3} , some compounds can exhibit another phase transition due to the R^{3+} moments ordering. For DyMn_2O_5 , this transition corresponding to a spin reorientation [70] and is characterized by a clear change for both the dielectric constant ϵ and the specific heat C_p/T . In addition, there is another spin reorientation transition at T_{N2} observed for DyMn_2O_5 but not for TbMn_2O_5 , as shown in Figure 2.7.

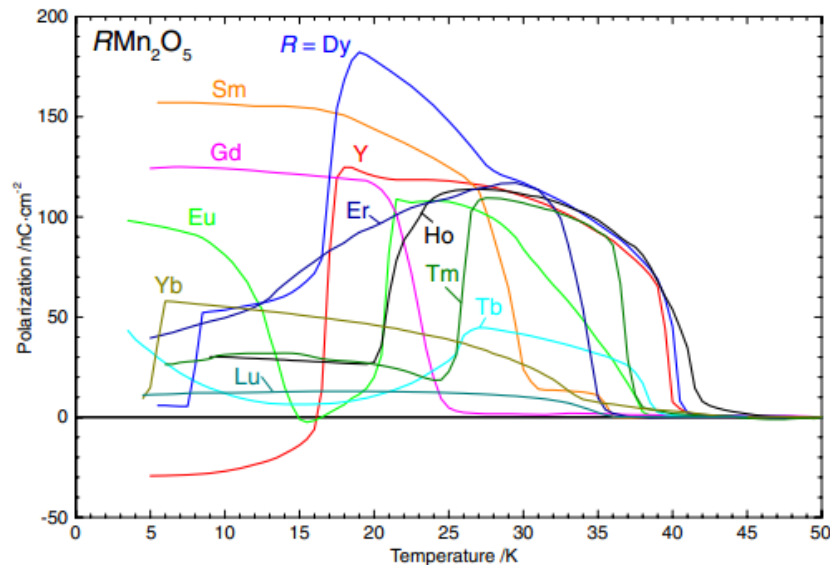


Figure 2.8 – Temperature dependence of the electric polarization for RMn_2O_5 (R = Y, Sm, Eu, Gd, Tb, Dy, Ho, Er, Tm, Yb and Lu) by heating. [74]

These transitions can also be seen in the temperature evolution of the electric polarization. Generally, for all the RMn_2O_5 compounds, the electric polarization in the CM phase is observed along the b axis. The temperature dependence of the polarization for RMn_2O_5 (R = Y, Sm, Eu, Gd, Tb, Dy, Ho, Er, Tm, Yb and Lu) is illustrated in Figure 2.8. The prototype of the RMn_2O_5 compounds is TbMn_2O_5 . Below

the Curie temperature (T_{C1}), the electric polarization starts to increase, associated with a CM phase. Upon cooling to T_{C2} , the CM phase transforms to the LT-ICM phase with significant decrease of the electric polarization.

Above ~ 30 K, the $\mathbf{P}(T)$ of RMn_2O_5 ($R = \text{Y, Dy, Ho, Er, and Tm}$) nearly coincides but with different Curie temperature. These results suggest that the polarization of RMn_2O_5 ($R = \text{Y, Dy, Ho, Er, and Tm}$) may have a common origin due to the Mn ions regardless of R . NdMn_2O_5 only forms a weak CM phase below 5 K and presents a tiny polarization [60]. YbMn_2O_5 does not have the CM phase [67] and exhibits a small polarization. Note that for TmMn_2O_5 and YbMn_2O_5 [49, 67], the electric polarization flops at ~ 5.5 K, which is not showed in the figure. LuMn_2O_5 shows a similar polarization behavior than that of YbMn_2O_5 and NdMn_2O_5 , which suggests that the LuMn_2O_5 probably does not have a CM phase (or a weak one), however its magnetic structure has never been investigated. Finally, there is no common feature concerning $\mathbf{P}(T)$ in the LT-ICM phase.

2.3 Microscopic Mechanism of Ferroelectricity

As mentioned in Chapter 1 Figure 1.12, the antisymmetric Dzyaloshinskii–Moriya interaction favours non-collinear spin ordering, through a vector field of the type $\mathbf{S}_n \times \mathbf{S}_{n+1}$. However, for the RMn_2O_5 family, the spins order quasi-collinearly. To explain the ME mechanism of this particular series, Chapon *et al.* proposed the adjusted ES mechanism for TbMn_2O_5 [42] and YMn_2O_5 [75]. The magnetic structure of the ICM phase of YMn_2O_5 is illustrated in Figure 2.9(a).

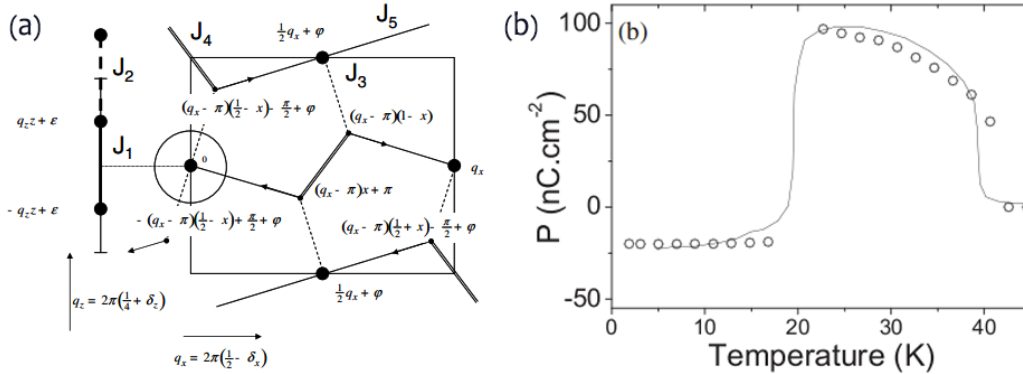


Figure 2.9 – (a) A schematic representation of the magnetic structure of the ICM phase of YMn_2O_5 . Magnetic exchange pathways are also indicated. (b) Symbols: electrical polarization of YMn_2O_5 , as calculated from Equation (2.1). Solid line: experimental values of the electrical polarization, extracted from [76]. [75]

The electrical polarization is proportional to a simple scalar field of $\mathbf{S}_n \cdot \mathbf{S}_{n+1}$. Based on the contribution of the symmetric interchain exchange interaction to the magnetoelastic coupling [42] and the phase factors, the *net* electric polarization can be obtained by multiplying the magnetic terms by the b axis component of the underlying polar field, shown with arrows in Figure 2.9(a), it can be expressed as:

$$\begin{aligned} \mathbf{P}^{ICM} &= 4CS_3 \cdot \mathbf{S}_4 \cos(q_z) z' \cos((q_x - \pi)(\frac{1}{2} - x) - \frac{\pi}{2} + \varphi) \times \cos(\varepsilon) \sin(\varphi) \\ &= 4CS_3 \cdot \mathbf{S}_4 \cos(2\pi(\frac{1}{4} + \delta_z) z') \cos(2\pi\delta_x(\frac{1}{2} - x)) \times \cos(\varepsilon) \sin(\varphi) \end{aligned} \quad (2.1)$$

- C : the magnetoelastic coupling constant.
- S_3 and S_4 : the magnetic moments on the Mn^{3+} and Mn^{4+} , respectively.
- δ_x and δ_z : the incommensurability parameters.

- Along the c axis, the moments follow a sinusoidal modulation, their amplitudes relate to the fractional coordinate z' , $z' = z - \frac{1}{2}$, with a phase shift ε with respect to the origin.
- φ : the global phase shift between the adjacent chains.

The temperature dependence of the spontaneous polarization has been calculated through Equation (2.1), which turned out to be in good agreement with the experimental curve of YMn_2O_5 from the Ref. [76], as shown in Figure 2.9(b).

This model involving an ES scenario, in which a structural relaxation induced by the relaxation of competing Heisenberg terms creates polar atomic displacements, have never been totally proven until recently [44]. In the $SmMn_2O_5$ compound [44], the magnetic moments are perfectly aligned (see Figure 2.10) along the c axis. This rules out the scenario of the antisymmetric Dzyaloshinskii–Moriya interaction definitely. For the $SmMn_2O_5$ compound, the propagation wave vector is $\mathbf{q} = (\frac{1}{2}, 0, 0)$ and the spins are along the c axis. So the electric polarization induced by ES can be expressed as a scalar product between neighboring spins:

$$\mathbf{P} \propto \mathbf{S}_i \cdot \mathbf{S}_j \quad (2.2)$$

- \mathbf{S}_i and \mathbf{S}_j : the spins involved in the exchange between Mn^{3+} and Mn^{4+} through the frustrated exchange term J_3 .

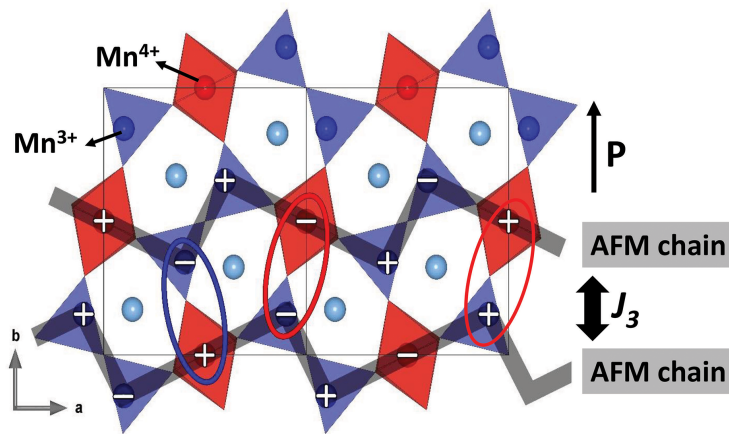


Figure 2.10 – Projection in the (a, b) plane of the magnetic moments along c represented by + and – symbols. The gray lines represent the AFM chains coupled through the J_3 exchange interactions (represented as red and blue ellipses: red for FM order; blue for AFM order).

Due to the presence of two AFM zig-zag chains per unit cell, two of the four J_3 terms are frustrated (indicated by red ellipses). In the $Pbam$ group symmetry, the four J_3 terms cancel by symmetry. However, in the real Pm space group [52], it is not the case. The ES model is based on the lowering of the magnetic energy by lifting the equality of the four magnetic exchange terms involving J_3 . To release the frustration, O or Mn ions can move to increase the J_3 terms for blue pairs, which present an AFM order and are not frustrated. The ions can also move to decrease the J_3 terms for red pairs related by a FM order, energetically unfavorable. All the Mn^{3+} and O^{2+} ions shift to the same direction (as shown by red arrows in Figure 2.10), leading to a global electric polarization along the b axis.

2.4 Specificities Upon the Nature of R^{3+}

Although the RMn_2O_5 compounds have some common features, some properties can be quite different depending on R^{3+} . As mentioned above, the electric polarization (Figure 2.5(a)) and T_C (Figure 2.5(b)) do not evolve linearly and even monotonously with the R^{3+} ionic radius. In addition, $PrMn_2O_5$ and $LaMn_2O_5$ are non-ferroelectric. And there are also other particularities in this series. The phase transition of the RMn_2O_5 compounds are briefly summarized in Figure 2.11.

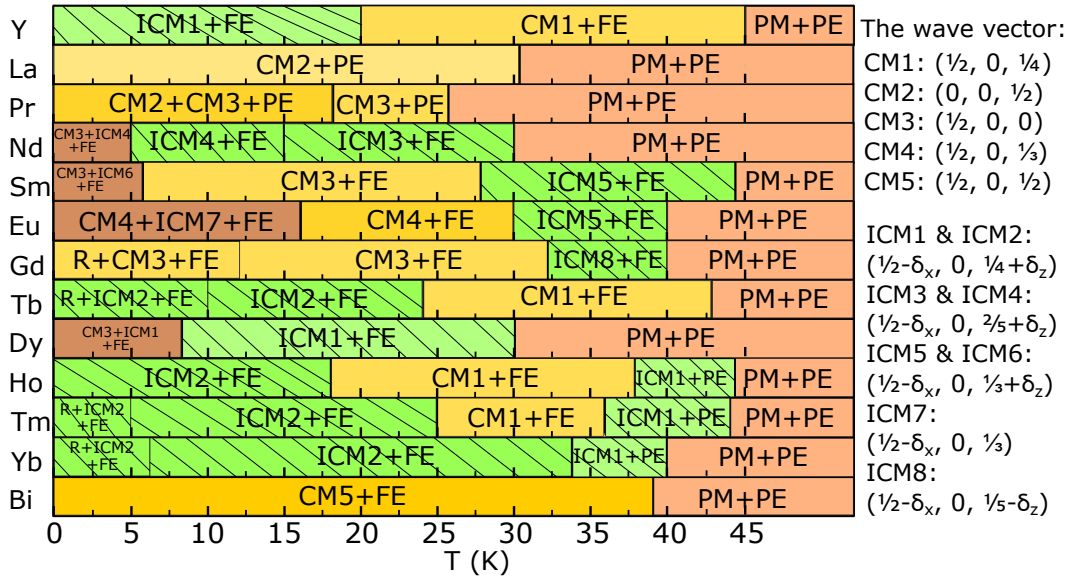


Figure 2.11 – The phase transitions of the RMn_2O_5 compounds and the corresponding magnetic propagation wave vectors presented on the right side. R means the low temperature R^{3+} ordering, which is stabilized at the same propagation wave vector as the Mn ordering. The values of δ_x (δ_z) range between 0.012 ~ 0.028 (-0.013 ~ 0.027). [42, 44, 56–60, 65, 67, 77–81]

2.4.1 Propagation Wave Vector

Upon cooling, most of the compounds undergo a ICM-CM phase transition, concomitantly associated with the ferroelectricity, the polarization being the largest in the CM phase. However, some compounds have no ICM phase. It is the case for La ($\mathbf{q}_M = (0, 0, \frac{1}{2})$) [78], Bi ($\mathbf{q}_M = (\frac{1}{2}, 0, \frac{1}{2})$) [81], and Pr ($\mathbf{q}_{M1} = (\frac{1}{2}, 0, 0)$ and $\mathbf{q}_{M2} = (0, 0, \frac{1}{2})$) [78]. On the other hand, the ICM phase appears in the entire temperature range of YbMn_2O_5 [67] and NdMn_2O_5 [60].

2.4.2 Spiral Structure in DyMn_2O_5

As we mentioned above, the phase transitions of the RMn_2O_5 compounds are similar. Below ~25 K, there is an abrupt transition to a low-temperature incommensurate phase. This magnetic phase is generally quasi-collinear [75]. In the case of DyMn_2O_5 , Ratcliff *et al.* [70] reported that the Mn^{4+} spins show a spiral arrangement around 22 K. Recently, we found that both Mn^{3+} and Mn^{4+} spins present an incommensurate structure with a spiral arrangement along the c axis. In addition, at low temperature, ~8 K, an additional magnetic transition is stabilized due to the ordering of Dy^{3+} [68]. In addition, another superexchange interaction is identified in various experiments. It corresponds to a J_6 exchange interaction between $\text{Dy}^{3+} - \text{Mn}^{3+}$ spins at low temperature [56], implying a $3d - 4f$ coupling.

2.4.3 Spin Ordering along the c Axis of the RMn_2O_5 with $\text{R} = \text{Sm}, \text{La}$ and Er

Generally, the magnetic moments lie in the (a, b) plane for the RMn_2O_5 compounds. But this is not the case for the SmMn_2O_5 compound. As proposed after the resonant X-ray magnetic scattering (RXMS) experiments by Y. Ishii *et al.* [79]. They found that all the magnetic moments have a dominant c axis component.

In the case of ErMn_2O_5 , only the spins of Mn^{3+} are along the c axis at ~4 K [71]. As for LaMn_2O_5 , only the spins of Mn^{4+} lie along the c axis [78].

2.4.4 an Abnormally High Electric Polarization in GdMn_2O_5

As we mentioned above, the GdMn_2O_5 compound exhibits the largest electric polarization ($\mathbf{P} = 3600 \mu\text{C}\cdot\text{m}^{-2}$) along the b axis. In addition, it also presents a giant tunability of its ferroelectric

polarization under an external magnetic fields ($\Delta\mathbf{P} = 5000 \mu\text{C}\cdot\text{m}^{-2}$). By the RXMS measurements, N. Lee *et al* [50] proposed that the Gd-Mn symmetric ES is crucial for the tunable ferroelectricity in the GdMn_2O_5 compound. Recently, a powder neutron diffraction experiment of an isotope enriched (^{160}Gd) compound of GdMn_2O_5 have evidenced the presence of a J_6 exchange interaction in GdMn_2O_5 . This additional ES mechanism through J_6 accounts for the strong polarization of GdMn_2O_5 [57].

2.5 Multiferroic Properties Affected by External Parameters

Theoretically (polar Pm space group [52]), all the compounds of the RMn_2O_5 series should exhibit multiferroic properties. As we mentioned above, the chemical pressure largely affects the multiferroic properties of RMn_2O_5 compounds. There are also some external parameters that can influence the spin structure through the interatomic distances, which can impact the multiferroicity. Here, we only select some of them, there are certainly many others.

2.5.1 Multiferroic Behavior under Magnetic Field

Since Kimura *et al.* [8] proposed that the magnetic field can switch the electric polarization in frustrated spin systems, the properties of frustrated spin multiferroics under magnetic field have been intensively studied. The control of the electric polarization by a magnetic field (and vice versa) is indeed a very important property for the applications. Generally, there are two key factors for the implementation of the magnetic field controlling the electric polarization:

- (1) the presence of commensurate d -electron spin ordering with strong magnetoelastic coupling, leading to the crystal lattice modulation, associated with the onset of spontaneous electric polarization \mathbf{P} .
- (2) the existence of $f - d$ exchange interaction, which enhances the effect of the external magnetic field \mathbf{H} to restructure d -electron state.

These key factors also suit for the RMn_2O_5 . In this family, the ferroelectric properties are controlled by the magnetic field when the magnetic field is parallel to the magnetic easy axis of R^{3+} . However, there are also some exceptions.

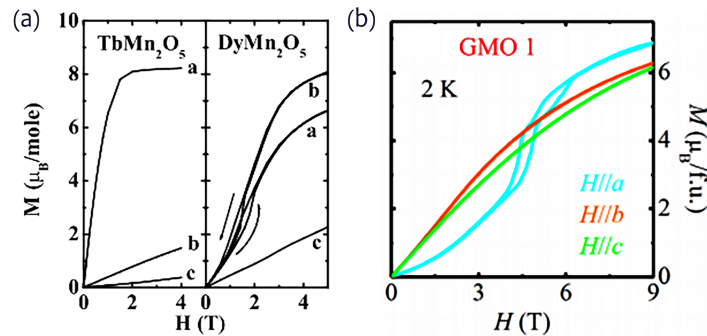


Figure 2.12 – Magnetization versus magnetic field along the three axes of (a) TbMn_2O_5 and DyMn_2O_5 at 3 K. [48]. (b) GdMn_2O_5 at 2 K. [50]

The magnetization versus magnetic field at ~ 3 K along the three principal crystallographic directions of the RMn_2O_5 compounds is shown in Figure 2.12(a) (for TbMn_2O_5 , DyMn_2O_5) and Figure 2.12(b) (for GdMn_2O_5). For TbMn_2O_5 , it clearly shows that the magnetization along the a axis is much larger than that along other axis. For DyMn_2O_5 , the magnetization along the a and b axis seems comparable, however, our recent results have shown that its magnetic easy axis is the b axis. [56]. Most interestingly, a kind of hysteresis loop appears when increasing \mathbf{H} to ~ 2 T with \mathbf{H} either parallel to the a or b axis. This suggests the presence of a \mathbf{H} induced phase transition at ~ 2 T. The magnetization versus magnetic field along the three principal crystallographic directions of GdMn_2O_5 shows that the magnetization is comparable along all the three crystallographic directions [50], which suggests that

the GdMn_2O_5 is actually magnetically isotropic, as expected for a R^{3+} ion with a zero total angular momentum (\mathbf{L}) moment. The summary of the various magnetic easy axis of the RMn_2O_5 is shown in Table 2.3.

Table 2.3 – Magnetic easy axis of the RMn_2O_5 compounds.

Magnetic easy axis	R
a	Bi [82], Tb [48]
b	Dy [56], Ho [48]
c	Sm [44], Er [61], Tm and Yb [83]
magnetically isotropic	Gd [50]

2.5.1.1 Magnetic Field \mathbf{H} Parallel to the a Axis

Electric Polarization

It is important to notice that the a axis represents the magnetic easy axis for TbMn_2O_5 and BiMn_2O_5 which will be described in details in this section. For the TbMn_2O_5 compound, at 3 K, the electric polarization starts to decrease rapidly under low magnetic field ($\mathbf{H} \sim 1$ T). Under high magnetic field ($\mathbf{H} > 2$ T), the direction of the electric polarization is completely reversed. In addition, as shown in the Figure 2.13(a), by linearly varying the magnetic field \mathbf{H} from 0 to 2 T and then from 2 T to 0, the electric polarization presents a highly reproducible flipping with the magnetic fields. Above 2 T, the \mathbf{P} changes linearly with \mathbf{H} , which indicates that the magnetoelectric effect is linear. [9]

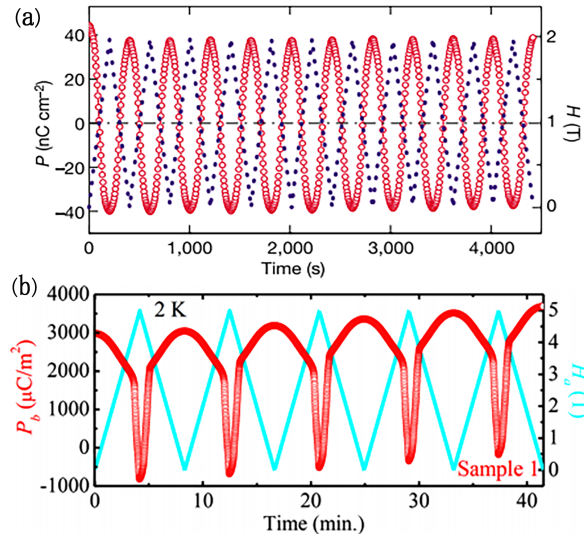


Figure 2.13 – (a) The highly reversible 180° flipping of electric polarization \mathbf{P} along the b axis in TbMn_2O_5 by applying magnetic field along the a axis at 3 K. [9] (b) repeated variation of \mathbf{P} along the b axis (red circles) in GdMn_2O_5 at 2 K by applying reversible magnetic fields along the a axis (light blue lines). [50]

Similarly to the TbMn_2O_5 compound, GdMn_2O_5 also exhibits a repeatable flipping of \mathbf{P}_b with \mathbf{H}_a linearly changing from 0 and 5 T (see Figure 2.13(b)). Compared to the flipping of \mathbf{P}_b in the TbMn_2O_5 compound, the flipping of \mathbf{P}_b in GdMn_2O_5 is not totally reproducible and \mathbf{P}_b first reverses sharply and then recovers gently.

The Mn spin-flop transition can be responsible for this electric polarization flip as proposed in BiMn_2O_5 [82]. The mechanism of Mn spin-flop is illustrated in Figure 2.14. With \mathbf{H} applied along

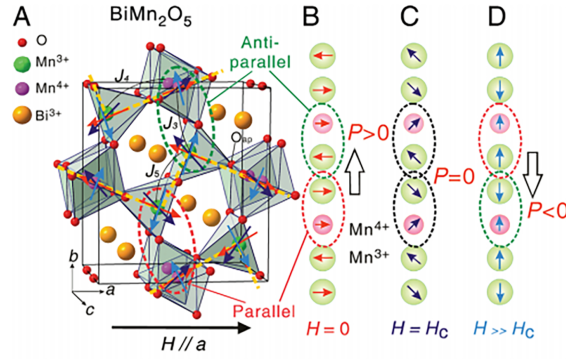


Figure 2.14 – (A) The structure and AFM zig-zag spin chains under various magnetic fields for BiMn_2O_5 . Red, dark blue, and light blue arrows represent spin directions at $\mathbf{H} = 0$, $\mathbf{H} = \mathbf{H}_C$, and $\mathbf{H} \gg \mathbf{H}_C$, respectively. (B-D) The corresponding simplified spin arrangements and the net \mathbf{P} (black open arrows) are also shown. [82]

the easy axis a , the directions of the Mn spins change continuously from the AFM situation B to the situation D. As schematically explained in Figure 2.14, this spin-flop will flip the electric polarization as well. For GdMn_2O_5 , another mechanism has been proposed. It involves the rotation by 90° of the Gd^{3+} spins, while the Mn moments remain unchanged. Thus the relative orientations of spin pairs: Gd-Mn and Mn-Mn are switched, leading to the reversal of the electric polarization [50]. As for TbMn_2O_5 , due to the existence of antiphase domain wall boundaries [84], the electric polarization flip mechanism of TbMn_2O_5 need to be further understood.

Dielectric Constant ε

Compared to the electric polarization, the dielectric constant ε under magnetic field is more intriguing for the DyMn_2O_5 . As shown in Figure 2.15, ε increases more than 100% in a broad temperature range under magnetic field $\mathbf{H} \parallel a$ (i.e. perpendicularly to the Dy easy axis b), which is called a "colossal magnetodielectric" (CMD) effect. With increasing \mathbf{H} , the broad bump at ~ 19 K becomes sharper and the magnitude of the dielectric constant ε increases rapidly (Figure 2.15(a)). This CMD effect at ~ 19 K appears to be associated with the CM-ICM transition with propagation wave vector $\mathbf{q}_{ICM1} = (\frac{1}{2} - \delta_x, 0, \frac{1}{4} + \delta_z)$. [48]

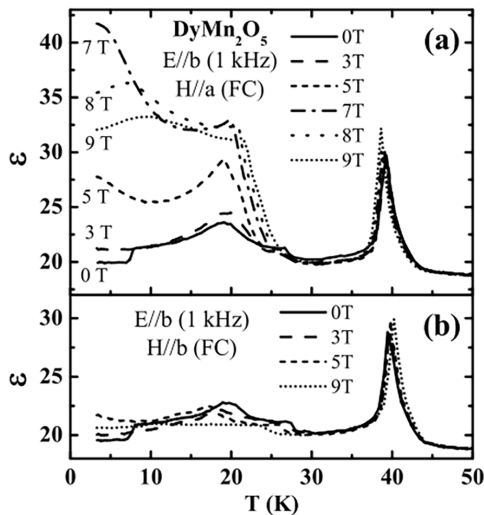


Figure 2.15 – (a) Temperature dependence of ε along the b axis in various magnetic field along the a axis. (b) ε along the b axis in \mathbf{H} applied along the b axis. [48]

2.5.1.2 Magnetic Fields \mathbf{H} Parallel to the b Axis

Importantly, the b axis is the magnetic easy axis of the compounds that will be discussed in this part namely DyMn_2O_5 and HoMn_2O_5 . For DyMn_2O_5 , if \mathbf{H} is parallel to the b axis, as illustrated in Figure 2.15(b), its effect of \mathbf{H} on the electric polarization is obvious, but not as significant as for $\mathbf{H} \parallel a$ (Figure 2.15(a)).

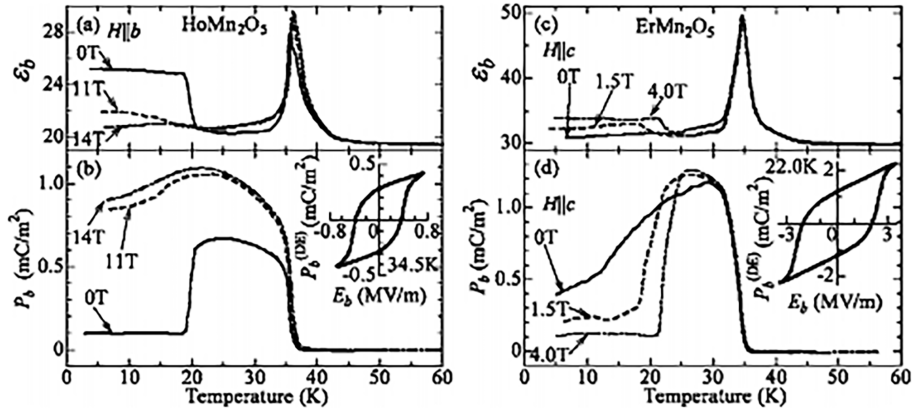


Figure 2.16 – Temperature dependence of dielectric constant ε_b and electric polarization \mathbf{P}_b parallel to the b axis under various magnetic fields in HoMn_2O_5 ((a) and (b)) and in ErMn_2O_5 ((c) and (d)). [64]

For HoMn_2O_5 , ε decreases when the magnetic field is parallel to the b axis, as shown in Figure 2.16(a). The electric polarization \mathbf{P} becomes nearly zero when the temperature is below ~ 19 K under zero magnetic field, which coincides with the steplike anomaly in the curve of ε along the b axis. This phase is smeared out and replaced by the ferroelectric phase when \mathbf{H} is above 11 T (Figure 2.16(b)). This \mathbf{H} induced phase does not extinguish when \mathbf{H} continues to increase. [64]

2.5.1.3 Magnetic Fields \mathbf{H} Parallel to the c Axis

For the case of ErMn_2O_5 , in which the c axis corresponds to the magnetic easy axis, the scenario is quite opposite, as illustrated in (Figure 2.16(c) and (d)). Under zero magnetic field, below ~ 20 K, the ferroelectric phase exists and no anomaly appears in the $\varepsilon(T)$ curve. When \mathbf{H} increases above 4 T, the electric polarization becomes nearly zero with the presence of a steplike anomaly in the $\varepsilon(T)$ curve.

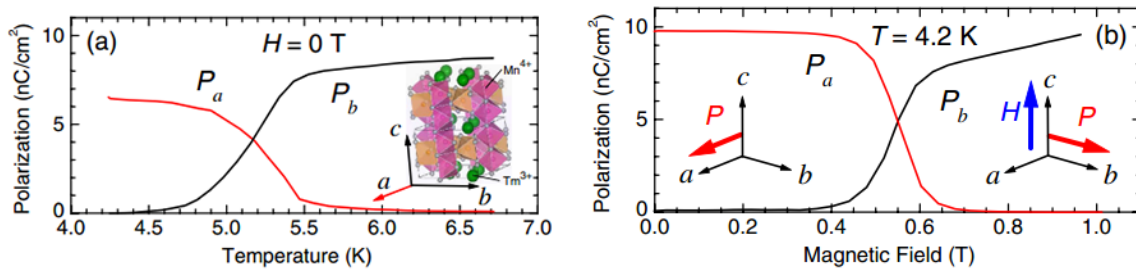


Figure 2.17 – (a) Temperature dependence of the polarization P_a and P_b of TmMn_2O_5 during heating under zero magnetic field. The inset shows the crystal structure of TmMn_2O_5 . (b) Magnetic field dependence of P_a and P_b at 4.2 K. [49]

The case of TmMn_2O_5 compound is quite different from the others even under a zero magnetic field. In the LT-ICM phase, the electric polarization \mathbf{P}_b decreases rapidly, then stabilizes at a low value. But when cooling the temperature to $T \sim 5.5$ K, \mathbf{P}_b starts to decrease again. It is associated with another electric polarization appearing along the a axis, \mathbf{P}_a . Until $T \sim 4.5$ K, \mathbf{P}_b totally smears out and \mathbf{P}_a stabilizes, as shown in Figure 2.17(a). Thus, under zero magnetic field, the electric polarization \mathbf{P}

flop (90° rotation) from the b axis to the a axis with decreasing temperature. In addition, an external magnetic field can also flop the electric polarization at low temperature (see Figure 2.17(b)). At 4.2 K, under a magnetic field of 0 to 1 T along the c axis, the direction of the electric polarization flops from the a axis to the b axis. This electric polarization flopping in the LT-ICM phase has been explained by the Dzyaloshinskii–Moriya interaction. It has also been proposed that the electric polarization is a combination of a Dzyaloshinskii–Moriya interaction mechanism and an ES mechanism. [49] This needs to be further studied.

The magnetic easy axis of YbMn_2O_5 compound is also along the c axis [83]. The situation is similar to the TmMn_2O_5 compound. For YbMn_2O_5 , the \mathbf{P}_a flops to \mathbf{P}_b with \mathbf{H} above ~ 1.5 T [67]. In addition, there is no commensurate magnetic phase in the whole temperature range in the YbMn_2O_5 compound.

2.5.2 Multiferroic Behavior under an External Pressure

Theoretically, high pressure can enhance the ferroelectricity in perovskites when the pressure increases up to a critical pressure [85, 86]. In the RMn_2O_5 compounds, the chemical pressure is an important parameter for the multiferroic properties at ambient pressure as previously mentioned. Thus the external pressure is expected to have a strong influence because it also impacts the interatomic distances. Indeed, an enhanced electric polarization has been observed under pressure in HoMn_2O_5 , TbMn_2O_5 , DyMn_2O_5 [87] and YMn_2O_5 [66].

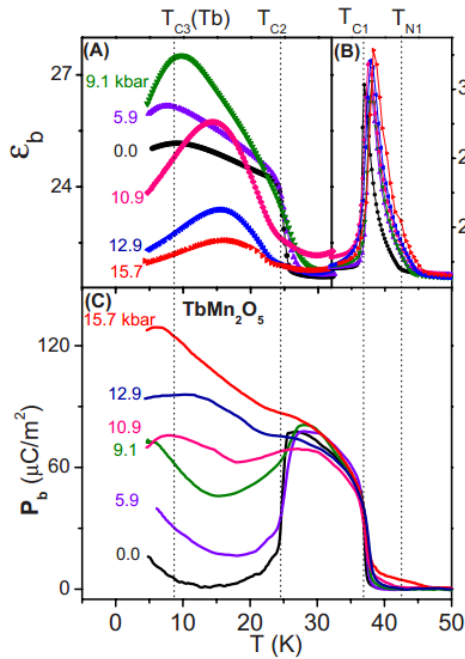


Figure 2.18 – Temperature profile of the (A) low temperature and (B) high temperature ϵ_b and (C) \mathbf{P}_b of TbMn_2O_5 under isotropic pressures (warming only). [87]

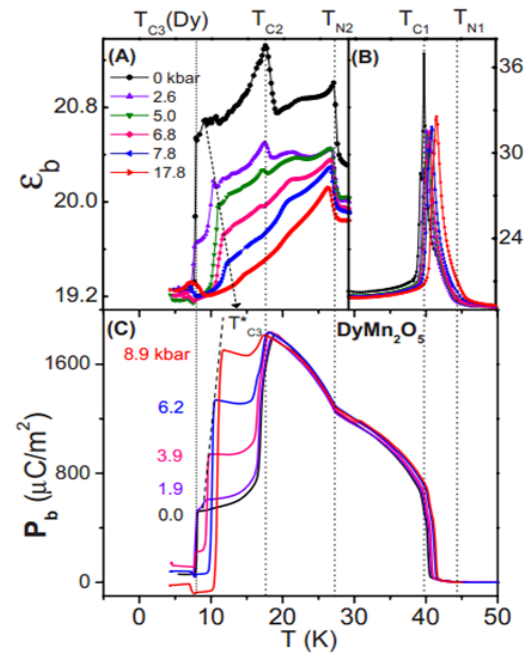


Figure 2.19 – Temperature profile of the (A) low temperature and (B) high temperature ϵ_b and (C) \mathbf{P}_b of DyMn_2O_5 under isotropic pressures (warming only). [87]

Typically, T_{C2} corresponds to the phase transition from the CM order to the LT-ICM order. Under ambient pressure, a steplike evolution appears below T_{C2} in the dielectric constant ϵ_b curve and a sudden decrease of electric polarization \mathbf{P}_b . With increasing the pressure, T_{C2} decreases, associated with a rapid decrease of the amplitude of the step. At the critical pressure p_C , the steplike anomaly fully quenches, which could indicate the absence of the transition into the LT-ICM phase, as the case of TbMn_2O_5 shown in the Figure 2.18. As for the electric polarization, it strongly increases under pressure below T_{C2} .

In the case of DyMn_2O_5 , it is much complex due to its more complicated magnetic structure and thermal evolution. At low temperature (below 10 K), the CM and ICM phase coexist [70]. The ε_b and \mathbf{P}_b of DyMn_2O_5 are illustrated in Figure 2.19. Below $T_{C3}(\text{Dy})$, the Dy^{3+} moments order involve, ε_b exhibits a sharp drop. However, for DyMn_2O_5 , the ε_b hump splits into two anomalies with increasing pressure. The step at $T_{C3}(\text{Dy})$ vanishes when the pressure is above $p_C \sim 4$ kbar. The other anomaly breaks off at T_{C3}^* (marked by an arrow and a broken line). Below $T_{C3}(\text{Dy})$, \mathbf{P}_b is null and DyMn_2O_5 is in a reentrant paraelectric (PE) phase. With increasing the pressure, between T_{C3}^* and T_{C2} , \mathbf{P}_b increases rapidly. Between $T_{C3}(\text{Dy})$ and T_{C3}^* , an intermediate phase X is observed with a very small \mathbf{P}_b at low pressure and which becomes ferromagnetic PE with increasing pressure. The corresponding pressure-temperature (p-T) phase diagram of DyMn_2O_5 is constructed from the warming data, as illustrated in Figure 2.20.

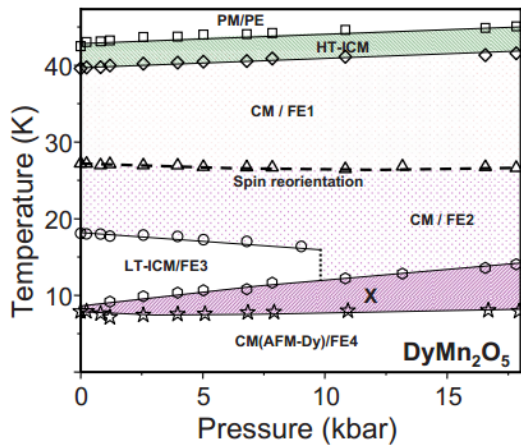


Figure 2.20 – Pressure-temperature (p-T) phase diagram for DyMn_2O_5 . The pressure separated X phase was found to be paraelectric [87]

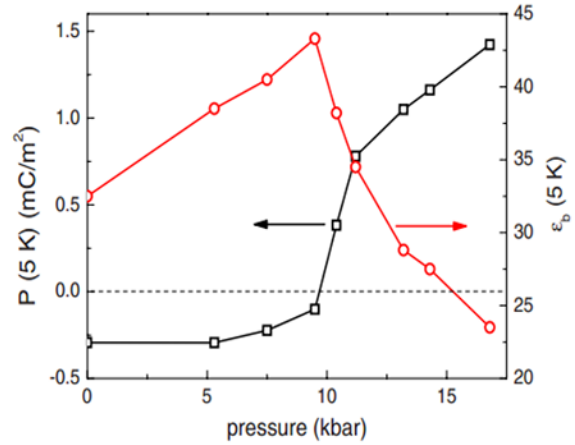


Figure 2.21 – Dielectric constant ε_b and ferroelectric polarization of YMn_2O_5 at 5 K as a function of pressure. [66]

Like the other RMn_2O_5 compounds, YMn_2O_5 experiences a CM phase transformation to LT-ICM phase at T_{C2} . Under pressure, interestingly, the electric polarization \mathbf{P}_b suddenly changes of sign at $p_C \sim 10$ kbar. It is associated with a significant lattice strain, which is interpreted as the result of the partial release of the magnetic frustration between the zigzag chains along a . Below p_C , \mathbf{P}_b increases slowly. After the sign reversal, it increases rapidly with increasing pressure, as illustrated in Figure 2.21. In addition, when the pressure increases above 14 kbar, the small peak of \mathbf{P}_b at T_{C2} extinguishes, which indicates that the ICM phase is suppressed by the pressure. [66]

In most of the RMn_2O_5 ($R = \text{Ho}, \text{Tb}, \text{Dy}$ and Y) compounds, usually the CM to LT-ICM phase transition below T_{C2} and the R^{3+} moment ordering below T_{C3} are strongly affected by the pressure. However, for GdMn_2O_5 , there is only one obvious peak of ε_b in the entire temperature range at ambient pressure, as shown in Figure 2.22(a). Most interestingly, this peak gradually splits into two peaks with increasing pressure below T_{C2} . The additional peak becomes more intense and moves to higher temperature, while the low temperature one at T_{C1} shifts to the lower temperature. The ferroelectric polarization \mathbf{P}_b at different pressures, is illustrated in Figure 2.22(b). At low pressure, \mathbf{P}_b slightly decreases with pressure. But above 10 kbar, a shoulder emerges at higher temperature and grows to about $600 \mu\text{C} \cdot \text{m}^{-2}$ at 18.2 kbar. The enhanced ferroelectricity of RMn_2O_5 ($R = \text{Ho}, \text{Tb}, \text{Dy}$ and Y) mainly in the low temperature range is accompanied by the CM to ICM phase transition [66, 87]. However, in GdMn_2O_5 , it is quite different. \mathbf{P}_b at low temperature is nearly not affected by the pressure. At low temperature T_{C1} , Gd moments actively participate in the global magnetic order, the additional ES through J_6 increases \mathbf{P}_b . But above T_{C2} , the Gd moments decouple from the Mn spins in the CM phase. With increasing the pressure, \mathbf{P}_b increases to $\sim 600 \mu\text{C} \cdot \text{m}^{-2}$, which is comparable with those of the other RMn_2O_5 compounds.

To summarize, the electric polarization is generally increased under pressure in the low temperature

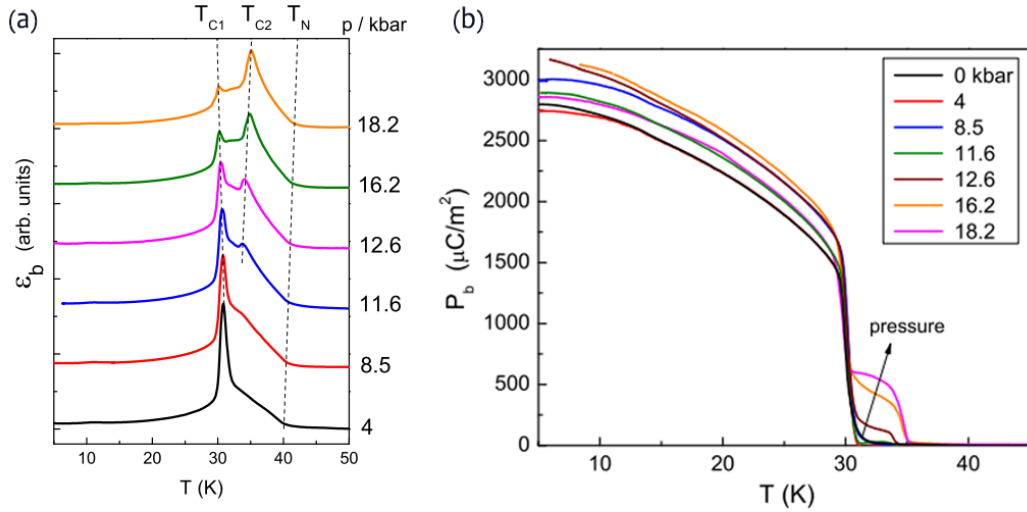


Figure 2.22 – (a) Dielectric constant ε_b , (b) ferroelectric polarization \mathbf{P}_b of GdMn_2O_5 at different pressures. [88, 89]

region of the (p, T) phase diagram, except for the case of GdMn_2O_5 . It is interesting to mention that recently in YMn_2O_5 , a new pressure induced magnetic phase has been evidenced [90] and could be at the origin of this high polarization phase.

2.6 Electromagnons in RMn_2O_5

Experimentally, Pimenov *et al* [91] first reported the observation of coupled magnetic and electric excitations in GdMnO_3 and TbMnO_3 and coined the nomenclature "electromagnons". Shortly after, the electromagnons were also observed in the RMn_2O_5 family [51]. The electromagnon is a kind of complex excitation in solids due to the strong linear coupling between the magnetic and lattice degrees of freedom. It is characterized by a magnon with electric dipole able to couple with the electromagnetic radiation. It is a mixed magnon-phonon excitation at much lower frequencies compared to optical phonons.

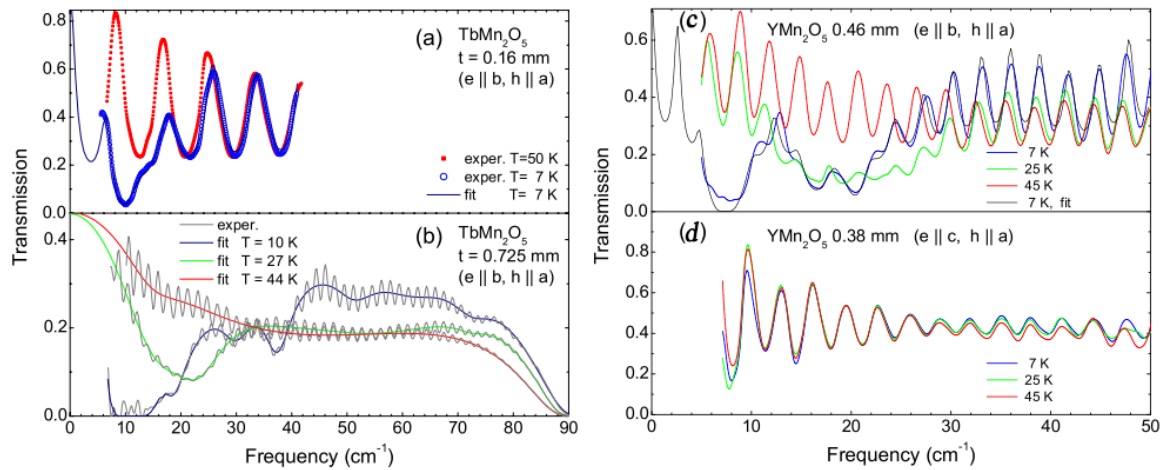


Figure 2.23 – Transmission spectra of TbMn_2O_5 : (a) thin sample, (b) thicker sample, oscillations are averaged out in model curves. \mathbf{e} and \mathbf{h} are electric and magnetic fields of light. Transmission spectra of YMn_2O_5 with $\mathbf{H} \parallel \mathbf{a}$ and (c) $\mathbf{e} \parallel \mathbf{b}$, (d) $\mathbf{e} \parallel \mathbf{c}$. [51]

The mixed magnetic-lattice excitation has been observed in GdMn_2O_5 but not present in EuMn_2O_5 [92]. In the RMn_2O_5 with a magnetic R^{3+} , the magnetic-lattice excitations can origi-

nate either from the electromagnon or from possible transitions between f -levels of R^{3+} (crystal-field excitation). It is thus always interesting to compare the excitations of compounds with magnetic R^{3+} with those without a magnetic R^{3+} such as YMn_2O_5 and EuMn_2O_5 . However, in EuMn_2O_5 , no hybrid excitation appears. It is thus interesting to consider the case of YMn_2O_5 . Interestingly, the transmission spectra of the TbMn_2O_5 and YMn_2O_5 are similar, as illustrated in Figure 2.23. The comparison of their excitation will be thus very interesting, because in YMn_2O_5 , the hybrid excitation cannot originate from the crystal - field of the $4f$ electrons.

The transmission spectra of the TbMn_2O_5 and YMn_2O_5 compounds are presented in Figure 2.23. As the lowest phonon was found at $\sim 97 \text{ cm}^{-1}$ (zero transmission in Figure 2.23(b)), all other features below this frequency should be of magnetic origin. The comparison of Figure 2.23(a) and Figure 2.23(b) shows the influence of the thickness of the sample. Compared to the paramagnetic phase, the strongest absorption for TbMn_2O_5 is observed near 10 cm^{-1} in the low temperature incommensurate (LT-ICM) phase. The transmission spectra of YMn_2O_5 compound is shown in Figure 2.23(c) and (d). In order to check if the excitations are electric or magnetic dipole active, several configurations with \mathbf{e} and \mathbf{h} along different directions are performed. As illustrated in Figure 2.23, the low energy mode in TbMn_2O_5 and YMn_2O_5 is only observed for $\mathbf{e} \parallel \mathbf{b} \parallel \mathbf{P}$ and no comparable mode is observed with $\mathbf{e} \parallel \mathbf{c}$ and $\mathbf{h} \parallel \mathbf{a}$, as well as the $\mathbf{e} \parallel \mathbf{a}$ and $\mathbf{h} \parallel \mathbf{b}$. Therefore, this excitation is electric dipole-active. As the lowest phonon is near 100 cm^{-1} , the most intense excitation appearing at $\sim 10 \text{ cm}^{-1}$ is a magnon which is electric dipole active. It is thus identified as an electromagnon.

Figure 2.24 shows the dielectric constant ε of TbMn_2O_5 from the fits of infrared spectra (lower curve) in comparison with kHz dielectric constant measurements. The comparison indicates that the steplike anomaly of ε actually originates from the electromagnon excitation. This steplike anomaly coincides with the mode observed by infrared measurements and attributed to the electromagnon. The strong low frequency electromagnon contributes to the largest part of ε in the low temperature ICM-FE phase [51].

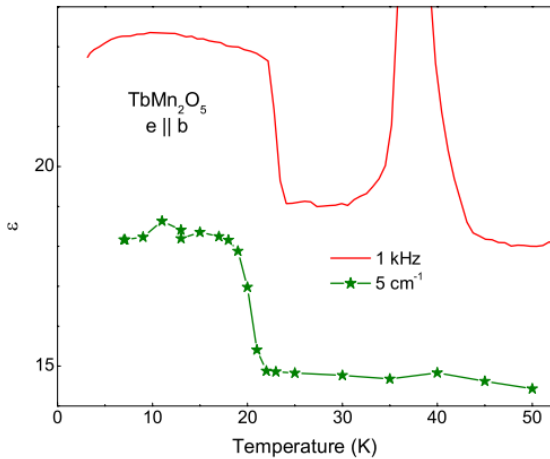


Figure 2.24 – Dielectric constant ε of TbMn_2O_5 from fits of infrared spectra (lower curve) in comparison with high frequency measurements. [51]

In the case of DM type multiferroics, the electromagnon is only electrically active with \mathbf{e} along the axis perpendicular both to the \mathbf{k} -vector of the spin structure and the polarization \mathbf{P} . However, in the RMn_2O_5 family, the electromagnon is active for $\mathbf{e} \parallel \mathbf{P}$, which is in favor for the ES mechanism. Finally, the similar behavior observed in TbMn_2O_5 and YMn_2O_5 is the indication that the Mn ions play an important role in this excitation.

2.7 The Aims of Our Work

As we mentioned above, the chemical pressure due to the radii of R^{3+} has a strong impact on the multiferroic properties of the RMn_2O_5 series. The magnetic field can manipulate the spin system to affect the multiferroic properties. And the external pressure can tune the interatomic distances, which strongly influences the magnetic exchange interaction between the Mn spins and/or the R spins.

Enormous research has been dedicated to study the influence of the magnetic field on the multiferroic properties of the RMn_2O_5 series. And the mechanism is well detailed. However, the study of the influence of the external pressure is much less documented and more intriguing. In particular the evolution of the magnetic structure under pressure is nearly unknown. It is thus essential to investigate the influence of the pressure and to compare its effect with the chemical pressure effect. It will help to understand the role of R^{3+} on the multiferroic properties of the RMn_2O_5 compounds.

This thesis will focus on the multiferroic properties of RMn_2O_5 ($\text{R} = \text{Pr}, \text{Dy}, \text{Gd}$ and Sm) under pressure. Besides the nuclear and magnetic structure under pressure, we will try to figure out the mechanism for the evolution of the ferroelectricity under pressure and we expect to shed light on the coupling between the magnetic and lattice degrees of freedom in the RMn_2O_5 compounds

Summary of this Chapter

In this chapter, we have presented the complex structure and intriguing multiferroic properties of the RMn_2O_5 family. The ferroelectric mechanism for this family proves to be different compared to the standard one proposed in Chapter 1 Section 1.5.2, as presented in Section 2.3. The multiferroic properties of the RMn_2O_5 can be largely affected by external parameters such as magnetic field and pressure, as discussed in Section 2.5. The main factors that affect the multiferroic properties of the RMn_2O_5 family are summarized in Table 2.4. Finally, we have shown the aims of this thesis in Section 2.7, which focus on the multiferroic properties under pressure.

Table 2.4 – Main factors that affect the multiferroic properties of the RMn_2O_5 family.

Factors	Direct influence/difference
chemical pressure	R^{3+} with different ionic radii and electronic configuration
magnetic field	manipulate spin system
external pressure	tune the interatomic distances

3

Experimental Techniques

Contents

3.1 X-ray Scattering	38
3.1.1 Fundamental Properties	38
3.1.2 Scattering Theory	39
3.1.3 X-ray Diffractometer	42
3.1.4 Powder X-ray Diffraction Intensity	42
3.1.4.1 General Formula of the Integrated Intensity of Powder X-ray Diffraction	46
3.1.5 Powder X-ray Diffraction Instruments	46
3.2 Neutron Scattering and Diffraction	49
3.2.1 Basic Principles	50
3.2.1.1 Neutron Scattering Length	50
3.2.1.2 Scattering Cross-Sections	51
3.2.1.3 Neutron Scattering Processes	52
3.2.2 Elastic Neutron Scattering	53
3.2.2.1 Elastic Nuclear Neutron Scattering	53
3.2.2.2 Elastic Magnetic Neutron Scattering	54
3.2.3 Intensity Corrections	55
3.2.4 Neutron Scattering Instruments	55
3.2.5 Pressure Cell	57
3.3 Powder Diffraction Refinements	58
3.3.1 Rietveld Analysis	58
3.3.2 FullProf Suite	61
3.4 Ferroelectric Properties Measurement	62
3.5 Sample Synthesis Process and Characterization	62

The majority of the experiments in Chapter 4 and Chapter 5 of this thesis use X-ray scattering diffraction and neutron scattering diffraction, very well developed and well understood techniques that are widely used within and outside of the correlated electron physics. The first part Section 3.1 will be dedicated to the X-ray scattering diffraction under pressure. The most important part of this chapter, Section 3.2, is an introduction to the important aspects of neutron scattering that are relevant for this thesis. Then, a brief introduction of the Rietveld refinement as well as the FullProf Suite we used has

been given in Section 3.3. Followed by the measurements of ferroelectric properties in Section 3.4. Finally, in Section 3.5, we present the sample synthesis process and the sample characterization part.

3.1 X-ray Scattering

We study the structure of the RMn_2O_5 compounds under pressure by X-ray diffraction. A brief introduction on X-rays and the diffraction of polycrystalline samples will be given here.

3.1.1 Fundamental Properties

X-rays were discovered by Wilhelm Conrad Röntgen in 1895. Since then they have been established as an invaluable probe of the structure of materials. X-rays are electromagnetic waves with wavelengths in the region of $\sim 1\text{\AA}$ ($\sim 10^4$ eV), which is same size as an atom. When a high voltage ($\sim\text{kV}$) is applied between two electrodes, the high speed electrons drawn out from the a Tungsten filament (cathode) are accelerated towards a water-cooled metal anode. The electrons quickly slow down with losing their kinetic energy in various way. Therefore, X-rays with different wavelengths are generated. They constitute the continuous background. A standard X-ray tube is shown in Figure 3.1(a) with a representation of its spectrum. The shortest wavelength (the maximum energy) of the generated X-rays corresponds to the energy when an electron loses all its energy in a single collision. The value of the shortest wavelength λ_S is:

$$eV \equiv h\nu_{max} \quad (3.1)$$

$$\lambda_S = \frac{c}{\nu_{max}} = \frac{hc}{eV} \quad (3.2)$$

- h : the Planck constant.
- V : the accelerating voltage between electrodes.
- ν : the velocity of the accelerated electron.
- c : the velocity of the photon.

The total X-ray intensity released is proportional to the atomic number of the metal anode target Z and the tube current i , it is:

$$I_{total} = AiZV^2 \quad (3.3)$$

- A : a constant.

In a certain time interval, it is equivalent to the area under the curve in Figure 3.1(b). Note that the kinetic energy of the electrons colliding the metal anode target is actually converted into heat and dissipates, only less than 1% is transformed into X-rays.

If the kinetic energy of the electron is sufficient to eject an inner shell electron, a K shell or L shell electron, the atom will be excited with a hole. Then this hole will be filled by an outer shell electron, the atom becomes stable again. Associated with this process, an X-ray photon is emitted with the same energy as the difference in the electron energy levels. As this energy relates to the metal anode target and the specific electron shell, the corresponding photoelectron is called characteristic X-ray. The characteristic X-rays are generated when the applied voltage exceeds the so-called excitation voltage, which corresponds to the potential required to eject an electron from the K shell. The following approximate relation is available between the applied voltage V and the excitation voltage V_K :

$$I_K = Ci(V - V_K)^{1.67} \quad (3.4)$$

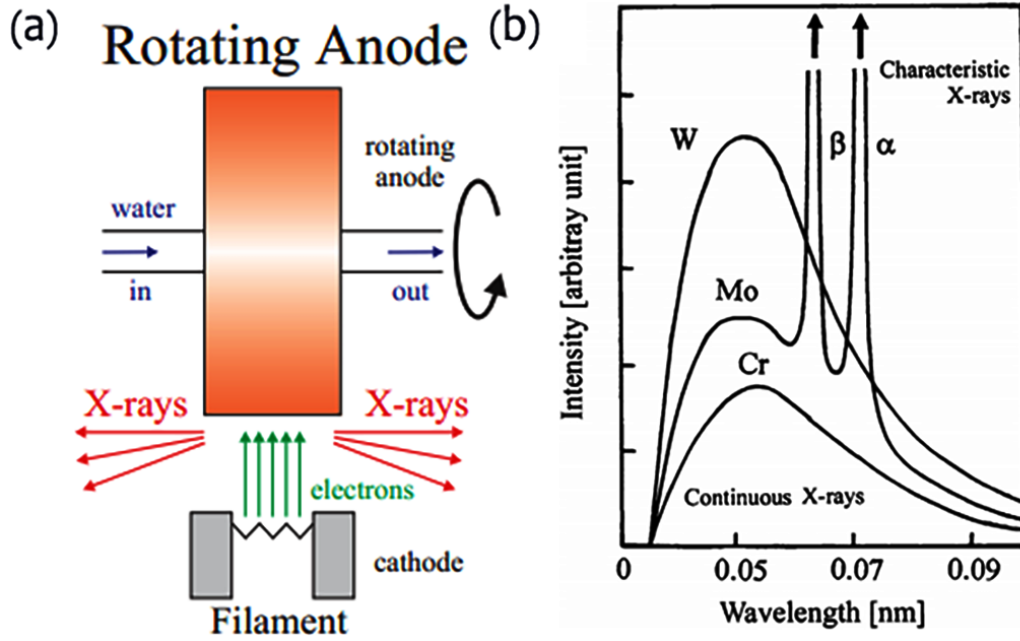


Figure 3.1 – (a) Schematic of the standard X-ray tube with power increased by rotating the anode. [93] (b) schematic representation of the X-ray spectrum. [94]

- I_K : the intensity of K_α radiation.
- C : a constant, usually the value is 4.25×10^8 .
- i : the tube current.

This process is called "photoelectric emission". The energy of the photoelectron ejected, E_{ej} , can be described:

$$E_{ej} = h\nu - E_B \quad (3.5)$$

- E_B : the binding energy for electrons of the corresponding shell, also called absorption edge of the related shell.

The line source of the X-rays can not continuously tunable, thus the optimal wavelength for the experiment cannot be chosen, or scanned. In addition, synchrotron radiation is produced in storage rings where electrons or positrons are kept circulating at constant energy. And the intensity of the X-rays generated from synchrotron sources is enormously higher than that of standard laboratory sources.

3.1.2 Scattering Theory

X-rays are scattered by charged particles in the matter and particularly by electrons. The physical phenomenon term "diffraction as a function of atomic position" is found when an X-ray beam enter into a long range periodicity atomic arrangement crystal. The intensity of diffracted X-rays relates to the atomic arrangement and the atomic species. Compared to the electrons, the nucleus of an atom is much heavier and it scatters X-rays much less. The scattering ability of an atom depends only on electrons, their number, and distribution.

The ability of a charged particle to scatter the X-rays is usually expressed in terms of the scattering length r :

$$r = \frac{e^2}{4\pi\epsilon_0 mc^2} \quad (3.6)$$

$$r_0 = \frac{e^2}{mc^2} = 2.8179 \times 10^{-5} \text{ \AA}$$

- e : the charge of the particle.
- m : the mass.
- ϵ_0 : vacuum permittivity.
- r_0 : the Thomson scattering length or classical radius of the electron.

The scattering length of the electron is known as the Thomson scattering length $r_0 = 2.82 \times 10^{-5}$ Å. From the equation above, it is clear that the scattering from electrons will be much stronger than that from the protons, since the mass of a proton is orders of magnitude larger than that of an electron. For the electrons in an atom, the distribution of the electron density $\rho(\mathbf{r})$ has to be included to consider the total scattering length of the atom, which is known as the atomic form factor:

$$f^0(\mathbf{Q}) = \int \rho(\mathbf{r}) e^{i\mathbf{Q}\cdot\mathbf{r}} d\mathbf{r} \quad (3.7)$$

- \mathbf{Q} : the scattering wave vector.
- $e^{i\mathbf{Q}\cdot\mathbf{r}}$: the scattering contribution of the volume element $d\mathbf{r}$ at position \mathbf{r} .

Further expanding from an atomic level to a crystal structure, the position of any atom in the crystal can be indicated by the combination of the lattice vectors \mathbf{R}_n and the position of the atoms within a unit cell \mathbf{r}_j . Then the scattering amplitude of the crystal can be factorize into two terms, which can be expressed:

$$F(\mathbf{Q}) = \overbrace{\sum_j f_j(\mathbf{Q}) e^{i\mathbf{Q}\cdot\mathbf{r}_j}}^{\text{Unit cell}} \overbrace{\sum_n e^{i\mathbf{Q}\cdot\mathbf{R}_n}}^{\text{Lattice}} \quad (3.8)$$

The second term is the sum over the whole lattice and it only has a meaningful value if $\mathbf{Q} \cdot \mathbf{R}_n = 2\pi \times$ integer. So the sum of the scattered waves from atoms in a unit cell, i.e. the structure factor, is:

$$F_{hkl} = \sum_1^n f_j e^{i\mathbf{Q}\cdot\mathbf{r}_j} = \sum_1^n f_j e^{2\pi i(hx+ky+lz)} \quad (3.9)$$

- \mathbf{Q} : coincides with a reciprocal lattice vector, $\mathbf{Q} = ha^* + kb^* + lc^*$.
- N : the total number of atoms involved in the unit cell.
- f_j : the atomic scattering factor of the number j atom.
- x, y, z : fractional coordinates of the j atom.

The structure factor F_{hkl} contains both the amplitude and the phase of the scattered wave obtained from the summation of all atoms in the unit cell. The intensity of the final wave scattered from all atoms in the unit cell is proportional to $|F|^2$. If the structure factor F is equal to zero, it means this reflection hkl should not appear in the diffraction pattern. Experimentally, the missing reflections of the scattering pattern can give a hint of the actual unit cell symmetry in crystals. The relationship between the Bravais lattice and the diffraction behavior is presented in Table 3.1. The structure factor F also contains information related to the symmetry of the atoms in the unit cell. For certain symmorphic symmetries, the F can be systematically nil for certain hkl reflections.

For example, the $Pbam$ space group (No. 55), which is actually $P 2_1/b 2_1/a 2/m$, the general reflection conditions are:

- a axis, 2_1 screw axis $\Rightarrow h00: h = 2n$. b glide plane $\Rightarrow 0kl: k = 2n$.
- b axis: 2_1 screw axis $\Rightarrow 0k0: k = 2n$. a glide plane $\Rightarrow h0l: h = 2n$

Table 3.1 – Relationship between Bravais lattice and reflections [94].

Crystal type	Bravais Lattice type	Reflections possible present	Reflections absent
Simple	Primitive	Any h, k, l	None
Body-centered	Body-centered	$h + k + l = \text{even}$	$h + k + l = \text{odd}$
Face-centered	Face-centered	h, k and l of same parity	h, k and l not of same parity

All information concerning space group symmetry and general conditions of reflections can be found in the international table of crystallography.

When the phase deviation of two X-ray waves is an integer multiple of the wavelength, this two waves will combine and double their amplitude. The scattered X-rays will enhance each other to produce a detectable diffraction beam. This particular condition leads to the Bragg law,

$$2d\sin\theta = n\lambda \quad (3.10)$$

- d : interplanar spacing of the crystal.
- 2θ : the diffraction angle, the angle between the diffracted X-ray beam and the transmitted beam.
- λ : the wavelength of the X-rays.
- n : the order of reflection.

The Figure 3.2 is useful to understand of Bragg law. It is required to remember these two geometric relationships [94]:

1. The angle between the incident X-ray beam and the normal to the reflection plane is equal to that between the normal and the diffracted X-ray beam. The incident X-ray beam, the plane normal, and the diffracted X-ray beam are always co-planar.
2. The angle between the diffracted X-ray beam and the transmitted one is always 2θ , and this angle is called "the diffraction angle".

presents the diffraction which occurs at several angles (both d and λ are fixed) with different path difference between two scattered X-rays, and the corresponding $n = 1, 2, 3, \dots$

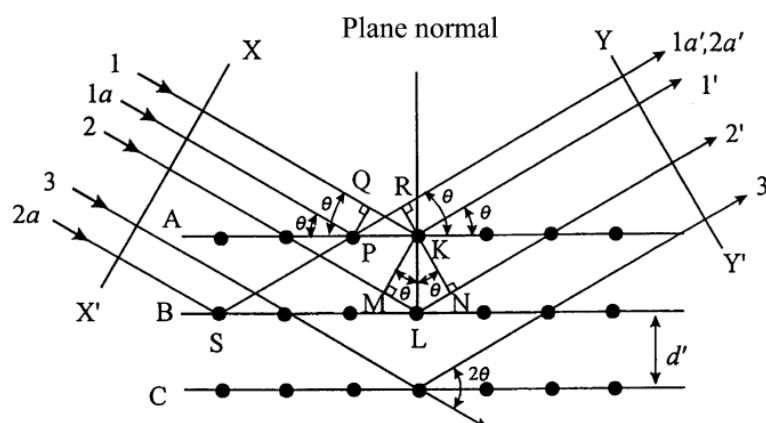


Figure 3.2 – Schematic diagram of diffraction of the X-rays by a crystal (Bragg law). [94]

3.1.3 X-ray Diffractometer

A standard diffractometer has two independent rotation axes (ω and θ). The schematic representation of the basic design of the diffractometer is illustrated in Figure 3.3. Usually the position of the X-ray source is fixed and the detector is attached on the 2θ axis. The sample is usually on the center of the diffractometer set on ω axis in a flat plate form. The line focal spot on the target of the X-ray tube is parallel to the diffractometer ω axis. During the measurements, the speed of the rotation of the 2θ axis is two times the one of the ω axis. It is also called θ - 2θ scan. In this way, the angle between the plane of the sample and the direction of the incident X-ray beam is the same as the angle between the plane of the sample and the direction of the diffracted beam, as shown in the Figure 3.3. A circle through the points F (focal spot on the target), S (the center of the diffractometer), and G (the focal point of the diffracted beam) is named as focusing circle or Rowland circle (left of the Figure 3.3, dotted line circle). This circle changes with θ . This is the θ - 2θ scan in its simplest configuration. There are some

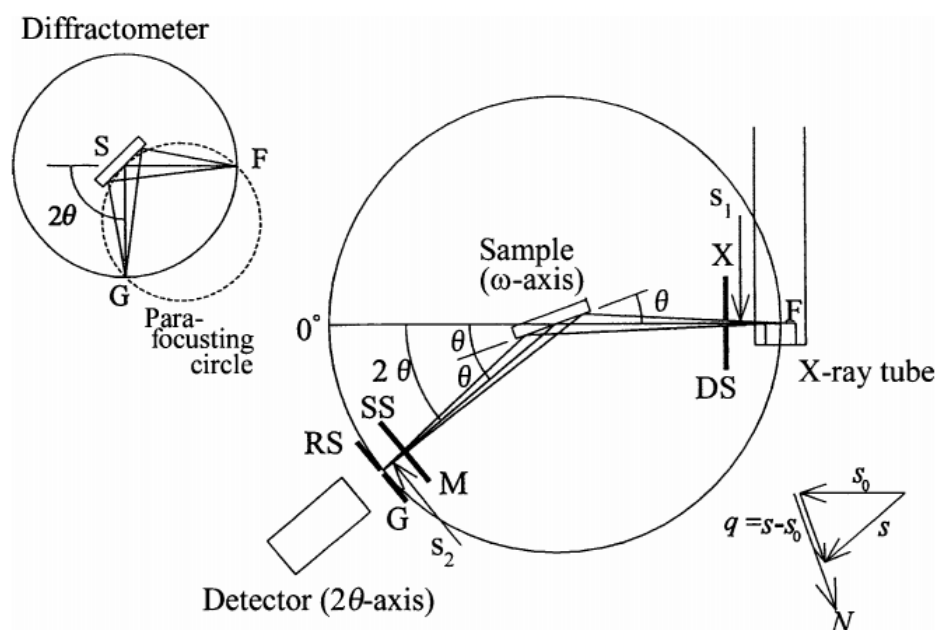


Figure 3.3 – Schematic of a standard $\theta - 2\theta$ X-ray diffractometer. [94]

slit systems, which are put into the X-ray path to minimize angular dispersion and to improve spatial resolution for the incident X-ray beam and the diffracted X-ray beam. The soller slit is used to restrict the perpendicular dispersion of both the incident and the diffracted X-ray beams. The divergent slits (DS) and the scattering slits (SS) are used to restrict the horizontal dispersion of both the incident and the diffracted X-ray beams. The receiving slit (RS) in front of the detector is set to determine the spatial resolution, as illustrated in Figure 3.3. This collimating and focusing principle is called para-focusing.

Nowadays, in research laboratory we usually use a flat 2D Mar or a multidetector to collect data with a large range of angles. See Section 3.1.5 for the set-up used in this thesis.

3.1.4 Powder X-ray Diffraction Intensity

A crystalline powder sample is treated as a large collection of small single crystals (the grains). Each grain has a crystallographic orientation different from its neighbors. If we consider the whole powder sample, the orientations of all the grains are randomly distributed. When we consider a monochromatic X-ray beam interacting with a powder sample, the Bragg law is satisfied which indicates that the plane-normal vector \mathbf{H}_{hkl} of the $(h k l)$ plane coincides with the direction of the scattering vector $(\mathbf{S} - \mathbf{S}_0)$. (\mathbf{S}_0 : the vector of incident X-ray beam; the vector \mathbf{S} of diffracted X-ray beam). These can be understood by using the Ewald sphere, as shown in Figure 3.4.

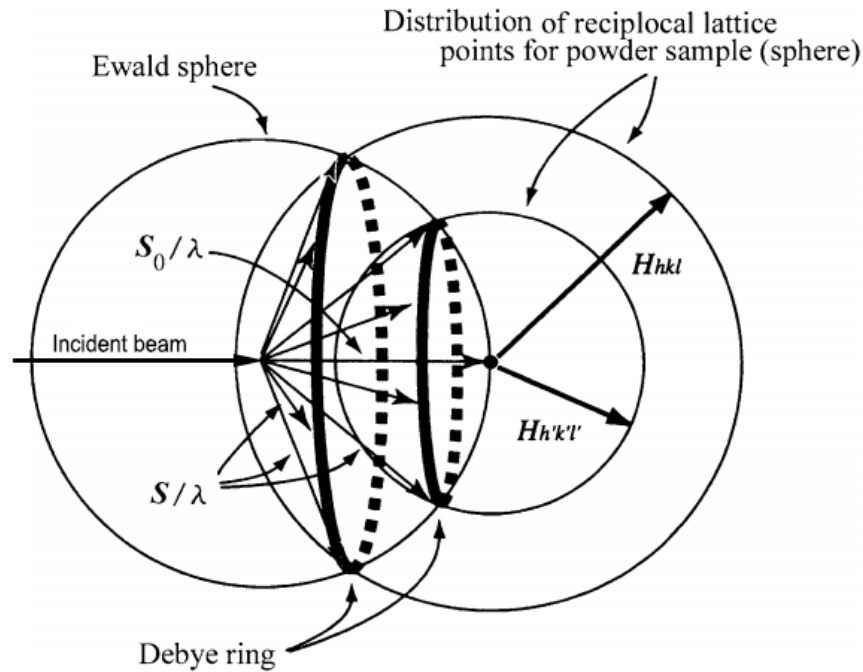


Figure 3.4 – The relationships between the reciprocal lattice (for a powder sample, they are spheres.) and the Ewald sphere (formation of a cone of diffracted X-rays) in the Debye–Scherrer method. [94]

The diffracted intensity from the $(h k l)$ plane can be obtained by integrating all directions and the cross-sectional area of the scattered intensity I of one tiny single crystal. The intensity computed in this procedure is equivalent to the total diffraction intensity uniformly distributed on the Debye ring, which forms a cone of half apex angle 2θ . The intensity measured using a diffractometer corresponds to the intensity per unit length of this Debye ring.

Compared to the intensity of incident X-rays, the intensity of diffracted X-rays is considerably weaker, in particular for the powder. In addition to the structure factor F , the scattered intensity of the X-rays of powder samples includes various components, such as, the polarization factor, the absorption factor, the multiplicity factor, the Lorentz factor and the Debye-Waller factor as detailed below.

Polarization Factor

In the X-ray interaction with the matter the polarization of the incident and the scattered beam are involved. This term is called the polarization factor P which depends on the diffracted angle. The polarization factor, P , has different form concerning different situations, three typical X-ray diffraction experiments are listed here:

- (1) Using a filter only:

$$P = \frac{1 + \cos^2(2\theta)}{2}$$

- (2) Using a crystal monochromator in the incident X-ray path:

$$P = \frac{1 + x \cos^2(2\theta)}{1 + x}$$

- (3) Using a crystal monochromator in the diffracted X-ray path:

$$P = \frac{1 + x \cos^2(2\theta)}{2}$$

- x : for both cases of (2) and (3), $x = \cos^2 2\theta_M$ for an ideally mosaic monochromator crystal or $x = \cos 2\theta_M$ for an ideally perfect monochromator crystal with $2\theta_M$ twice the Bragg angle of the monochromator crystal.

Absorption Factor

When the X-rays enter a sample, the scattering occurs in different directions besides the direction of the incident X-rays, as well as the photoelectric processes mentioned above. This corresponds to a global absorption which reduces the intensity of the incident X-rays and diffracted X-rays. So the intensity I after transmission through distance x is:

$$I = I_0 e^{-\mu x} \quad (3.11)$$

- I_0 : the intensity of the incident X-ray beam.
- the proportional factor μ : linear absorption coefficient.

The absorption process mentioned above is the reduction of the X-ray intensity after penetration of a sample. Then the measured intensity of the diffracted X-rays is:

$$\begin{aligned} dI &= \frac{I_0}{\sin \gamma} e^{-\mu x \left(\frac{1}{\sin \gamma} + \frac{1}{\sin \beta} \right)} dx \\ \Rightarrow I_D &= \frac{I_0}{\sin \theta} \int_0^t e^{-\frac{2\mu x}{\sin \theta}} dx = \frac{I_0}{2\mu} (1 - e^{-\frac{2\mu t}{\sin \theta}}) \end{aligned} \quad (3.12)$$

- μ : the linear absorption coefficient of sample materials.
- θ : the incident X-ray beam encounters the powder sample with the angle of γ , the diffracted X-rays at the angle of β from the sample surface. For an infinitely thick sample, $\gamma = \beta = \theta$.
- t : the thickness of the sample.

As the thickness of the sample can be considered as infinite, $t \rightarrow \infty$. The the absorption factor term $(1 - e^{-\frac{2\mu t}{\sin \theta}})/(2\mu)$ becomes simply $(1/2\mu)$. As the thickness of the sample can be seen as infinite, the absorption factor is considered to be constant and independent of the diffraction angle.

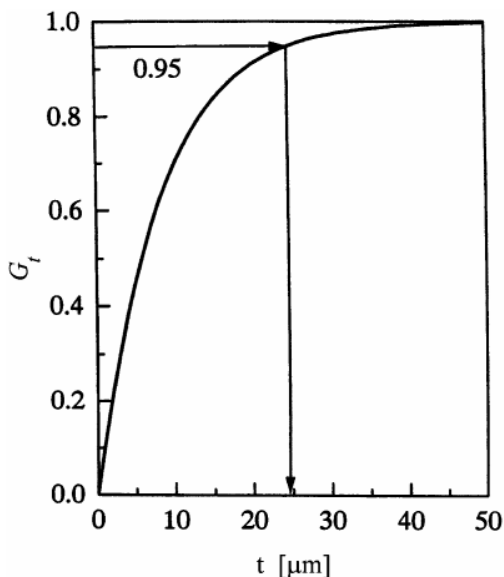


Figure 3.5 – The fraction of the diffracted intensity contributing from a surface layer of depth t to the total diffracted intensity of a sample of semi-infinite thickness. [94]

In the diffractometer, with $\gamma = \beta = \theta$ condition, the ratio of the intensity of the diffracted X-ray beam and that of the sample for the semi-infinite plate can be expressed:

$$G_t = \frac{\int_0^t \frac{I_0}{\sin\theta} e^{-\frac{2\mu x}{\sin\theta}} dx}{\int_0^\infty \frac{I_0}{\sin\theta} e^{-\frac{2\mu t}{\sin\theta}} dx} = 1 - e^{-\frac{2\mu t}{\sin\theta}} \quad (3.13)$$

$$\Rightarrow t = -\frac{\sin\theta}{2\mu} \ln(1 - G_t)$$

The value of G_t as a function of the sample thickness t is illustrated in Figure 3.5. Generally, when the value of G_t is larger than 95%, the corresponding sample thickness can be considered as infinite.

Multiplicity Factor

There are sets of equivalent lattice planes related by symmetry. Multiplicity factor indicates the number of the crystal planes with different orientation which are symmetry equivalent and have the same d spacing and structure factors. For example, the planes of a cubic crystal, (100), (010), (001), ($\bar{1}00$), (0 $\bar{1}0$), and (00 $\bar{1}$). They are called "planes of a form". For a cubic crystal, the multiplicity factor of {100} planes is 6 and 8 for {111} planes. In powder diffraction, the crystal orientations are considered as completely random. So the probability of crystal orientations satisfying the Bragg condition is actually given by the ratio of their multiplicity factors.

Lorentz Factor

During a X-ray measurement, the sample usually rotates. When the diffraction angle exactly satisfies the Bragg law, the intensity of the diffracted X-rays reaches the maximum. However, the intensity of the diffracted X-rays is detectable even when the diffraction angle slightly deviates from the Bragg law. The intensity of the diffracted X-rays as a function of 2θ is presented in Figure 3.6. The intensity of the peak can be obtained from the area under the curve of the peak. The measured intensity of the diffracted X-ray beam is the integrated values of the diffracted intensities produced from volumes with a certain size. This volumes depend on the diffraction angle. Thus for different 2θ peaks, this effect changes and should be taken into consideration. It is called the Lorentz factor. The Lorentz factor for powder samples can be expressed as:

$$\text{Lorentz factor} \equiv \frac{1}{\sin^2\theta \cos\theta} \quad (3.14)$$

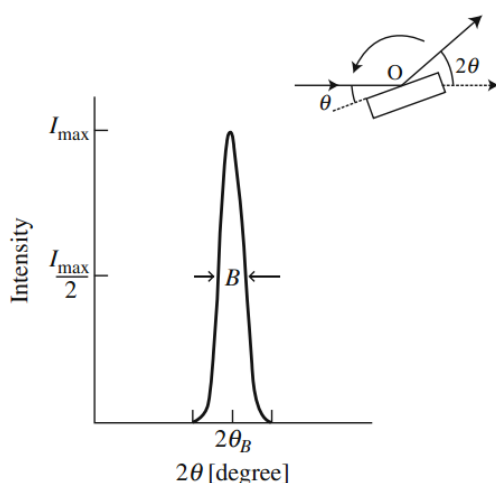


Figure 3.6 – Intensity diffracted from a crystalline sample rotated through the Bragg angle. [94]

Debye-Waller Factor

As a matter of fact, the atoms in a crystal are not fixed. They vibrate around their mean position and their vibration will be enhanced if the temperature increases. The effect of the atomic vibrations on the intensity of the diffracted X-rays is the Debye–Waller factor. This factor is expressed as e^{-M_T} and enters in the calculation of the atomic scattering factor f .

$$f = f_0 e^{-M_T} \quad (3.15)$$

$$M_T = 8\pi^2 \langle u^2 \rangle \left(\frac{\sin\theta}{\lambda} \right)^2 = B_T \left(\frac{\sin\theta}{\lambda} \right)^2 \quad (3.16)$$

- $\langle u^2 \rangle$: the mean square displacement of the atom in a direction normal to the diffraction planes.

The value of B_T is deduced from the measured intensity of diffracted X-rays.

3.1.4.1 General Formula of the Integrated Intensity of Powder X-ray Diffraction

By considering together the factors above, a general formula of the intensity of a powder X-ray diffraction can be obtained.

$$I = |F|^2 p \left(\frac{1 + \cos^2 2\theta}{2 \sin^2 \theta \cos \theta} \right) \frac{1}{2\mu} \left(1 - e^{-\frac{2\mu t}{\sin\theta}} \right) e^{-2M_T} \quad (3.17)$$

- F : the structure factor.
- p : the multiplicity factor.
- $\left(\frac{1 + \cos^2 2\theta}{2 \sin^2 \theta \cos \theta} \right)$: the Lorentz-polarization factor (LP).
- $\frac{1}{2\mu} \left(1 - e^{-\frac{2\mu t}{\sin\theta}} \right)$: the absorption factor.
- e^{-2M_T} : the Debye-Waller factor.

Note that if the thickness of the sample is considered to be infinite, then the absorption factor is independent of the diffraction angle, and can be seen as a constant $\frac{1}{2\mu}$.

3.1.5 Powder X-ray Diffraction Instruments

The instruments used in this thesis is a X-ray diffractometer with a high pressure component. Powder X-ray diffraction experiments were carried out in Laboratoire de Physique des Solides (Université Paris Sud, Orsay, France). The X-rays are emitted from a Molybdenum X-ray rotating anode and Mo- K_α emission line (0.71 Å) is selected by a low divergence optics, small size (100 μm \times 60 μm) monochromator at the focal point. The X-ray diffraction system we used is shown in Figure 3.7.

The characters of this set-up contains:

1. Beamstop with diode aligned with the incident X-ray beam.
2. The pressure cell centered on the beam using x and z scan, and the diode as detection using transmission.
3. For large angle measurement, the position is as in the Figure 3.7, the range of the cell aperture can reach $2\theta \sim 50^\circ$.
4. The 2D Mar345 detector can collect X-ray diffraction at a range of $\phi = 345$ mm, for sample-detector distance ~ 200 mm, $2\theta \sim 20^\circ$.

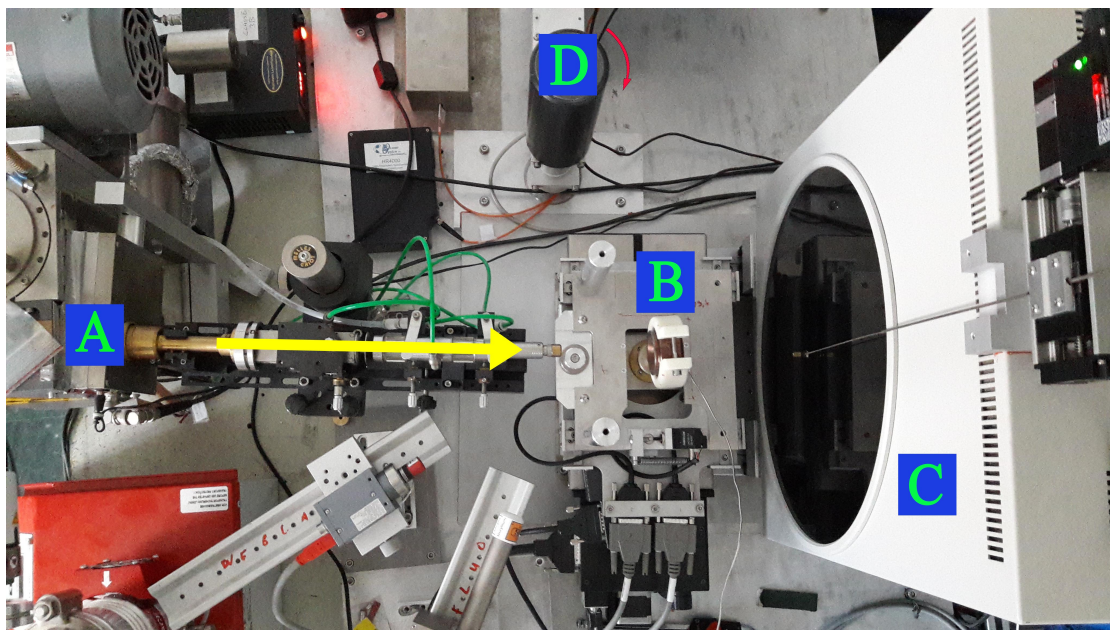


Figure 3.7 – Top view of the X-ray diffraction set-up. A: X-ray beam, B: pressure cell, C: 2D Mar345 detector, D: the motor, connected to the pressure by ruby luminescence system.

The process of preparation and loading the diamond anvil cell are as following:

1. *Indentation*: put a suitable gasket (CuBe) in the cell and close the cell, then increase the pressure (~ 80 bars) inside the cell and keep the pressure around 10 second and then release the pressure to get a good indentation at the center of the gasket.
2. *Drilling*: center the indented gasket with a drilling system, increase the voltage between the Tungsten needle and the gasket in dielectric media (petroleum) for electro-erosion to obtain the hole we need.

These two steps have presented in Figure 3.8.

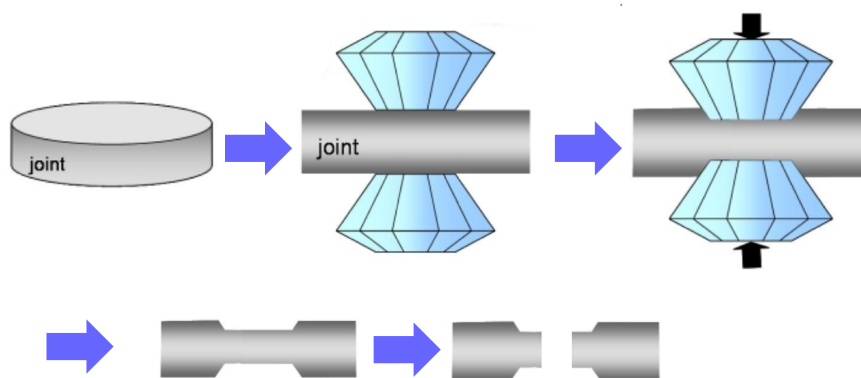


Figure 3.8 – Schematic representation of the gasket treatments.

3. *Loading*: load the powder or single crystal sample in the gasket hold, then drip a drop of transmitter media, finally put one or several medium size ruby inside the hole. Note that large size ruby can easily crack under high pressure, whereas the fluorescent intensity of small size ruby may too weak to determine the position of the peak correctly under high pressure.
4. *Checking*: to ensure that the ruby is inside the hole and have enough fluorescent intensity, it is necessary to check the fluorescent intensity of the ruby after loading the sample. If you can not see

the ruby or the fluorescent intensity of the ruby is not enough, you should reload the ruby and/or sample.

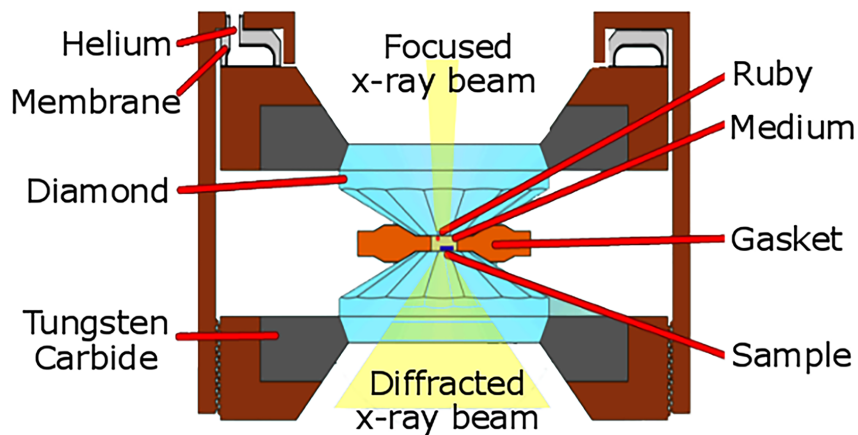


Figure 3.9 – Schematic representation of the diamond anvil cell.

Through rotating the motor (D), the pressure measurement device can measure the pressure in the diamond anvil cell via the fluorescent intensity of the ruby inside the diamond anvil cell. As shown in Figure 3.9, with increasing the amount of the helium on the membrane, forces from both sides of the diamond induce an *in situ* increase of the pressure. The maximum pressure inside the gasket depends on the inlet diameter:

$$\phi = 1\text{mm} \Rightarrow P_{max} \sim 10\text{ GPa}$$

$$\phi = 600\mu\text{m} \Rightarrow P_{max} \sim 25\text{ GPa}$$

We chose silicon oil as the transmitting liquid, as it evaporate much slowly compared to the Ethanol. For our room temperature experiment under pressure, the solidification of the silicon oil is not too problematic and we have not observed any non hydrostatic behavior. The measurement of the pressure is performed by measuring the fluorescent intensity of the ruby inside the hole.

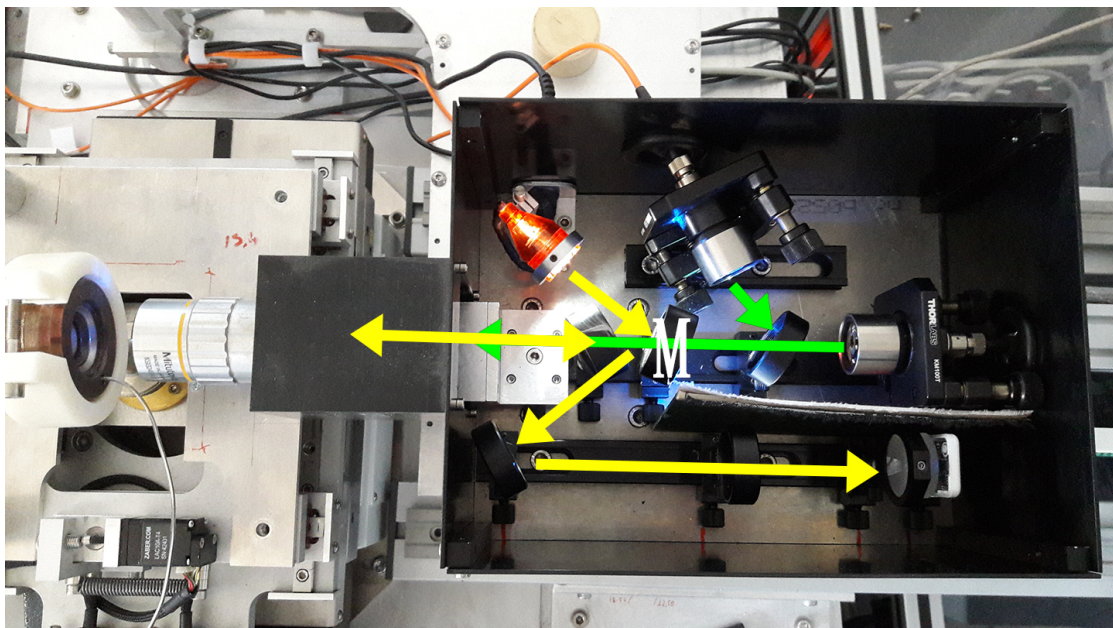


Figure 3.10 – The pressure by ruby luminescence system . *M* indicates the lens.

The pressure by ruby luminescence system is presented in Figure 3.10. When the lens *M* switches on, we can see inside of the cell (the yellow arrow path). Through the camera, we can locate the center

of the hole and/or the ruby. Then we switch off the lens M and turn on the laser (the green arrow path). By slightly adjust the position and the focus of the laser, we can target the ruby with certain fluorescent intensity. When increasing the amount of helium on the membrane, and thus the pressure inside the pressure cell and in particular on the ruby, the wavelength of the fluorescent peak of the ruby will increase. By measuring this wavelength, we can calculate the exact pressure by the following quadratic equation [95] (calculated at 300 K):

$$P(\text{GPa}) = a \left[\left(\frac{\lambda - \lambda_0}{\lambda} \right) + b \left(\frac{\lambda - \lambda_0}{\lambda} \right)^2 \right] \quad (3.18)$$

- λ_0, λ : fluorescent wave length at ambient pressure and under pressure, respectively.
- a : constant, $a = 1798 \pm 8.4$ GPa.
- b : constant, $b = 8.57 \pm 0.15$ GPa.

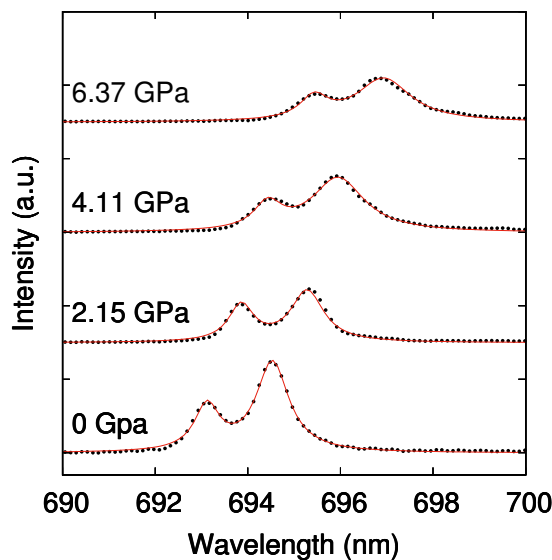


Figure 3.11 – The fluorescent curve measured under different pressure. Dots: the measured data. Lines: the fitted curve through Equation (3.18).

Usually we use the peak of the ruby with higher fluorescent intensity to calculate the pressure as the position of the peak with higher fluorescent intensity is more accurate. A example is illustrated in Figure 3.11. It is obvious that with increasing pressure, the fluorescent intensity decreases and the peaks shift to higher positions.

3.2 Neutron Scattering and Diffraction

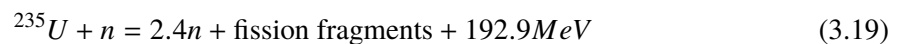
The neutron was first discovered by James Chadwick in 1932 [96] and in 1936 the first neutron diffraction experiment was done by Halban and Preiswerk [97] as well as by Mitchell and Powers [98]. Intense neutrons were produced in the first nuclear fission reactor in 1942 in the University of Chicago, USA [99]. Since then, more and more neutron facilities were built to provide neutrons for scattering measurements.

Neutron scattering is dependent on the way that a neutron interacts with matter, particularly in condensed matter. There are some basic properties of the neutron that make it a crucial tool in understanding the magnetic characteristics of matter of the atomic scale [100]:

- The wavelength of neutrons is comparable with interatomic spacing in solids and liquids, which suggests that it is well suited to detect the structural information.

- As a matter of fact, neutrons are uncharged. They do not interact with electrons or the electrical charge of nuclei, which means that they can penetrate quite far into the matter and come close to the nuclei. Thus, neutrons are scattered by nuclear forces, which is not proportional to the atomic number like the X-rays.
- The energy of neutrons has the same order of magnitude than this of many excitations in condensed matter. It makes the neutron scattering more accurate to detect the energy change of the excitations. These results can ultimately give the information of interatomic forces. This feature is usually used in the inelastic scattering measurement.
- The neutrons have a magnetic moment. In addition of the interaction with the matter via the strong nuclear force, the neutron can also interact with the magnetic moment of unpaired electrons in magnetic atoms. This interaction can give information about the arrangement of electron spins and the density distribution of unpaired electrons of matter.

Currently, there are two ways to produce the neutron beam for neutron scattering. One is to create a large amount of neutrons during a nuclear fission chain reaction. The fissile material used in the nuclear reactors can be in its elemental form (naturally occurring form or enriched isotopically in a fissionable isotope) or as a compound. A common reaction in modern research reactors can be expressed as:



- ${}^{235}\text{U}$: a fissile isotope of uranium.
- n : a neutron.

The other way to produce neutrons is through the spallation of high energy protons interacting with the nuclei of heavy elements, which involves a high energy proton entering a heavy metal target.

Neutrons from these reactions usually exhibit a wide range of energies. However, for most experiments, it requires for the neutrons to have an energy within a certain band. To fulfill this requirement, a neutron moderator is used to make all the neutrons into a certain energy range thermal neutrons or cold neutrons. For some measurements, a monochromator crystal or a chopper is used to get only one value of neutron energy. In addition, the polarization of the neutron beam can also be modified according to the experiments. Finally, a detector is used to collect the experimental information.

There are generally two diffractometers used in neutron experiments, two axis diffractometer and four-circle diffractometer. More details can be found in books about neutron scattering [99, 101].

3.2.1 Basic Principles

In order to be able to figure out the interaction between a neutron and the scattering matter, it is necessary to understand some basic principles.

3.2.1.1 Neutron Scattering Length

The wavelength of the neutron is of the order of 1 Å. The scattering of neutrons by a nucleus caused by the nuclear forces have a range of about 10^{-4} to 10^{-5} Å. When consider the nuclear scattering by a single nucleus, the incident neutron is treated as a plane wave travelling in the z -direction with the wave function:

$$\psi_i = e^{ikz} \quad (3.20)$$

- k : the neutron's wavenumber, $k = \frac{2\pi}{\lambda}$.

As the wavelength of the neutron is much larger compared to the range of nuclear forces, the scattered wave will be spherically symmetric (shown in Figure 3.12):

$$\psi_f = -b \frac{e^{ikr}}{r} \quad (3.21)$$

- r : the distance from the scattering nucleus.
- b : the scattering length.

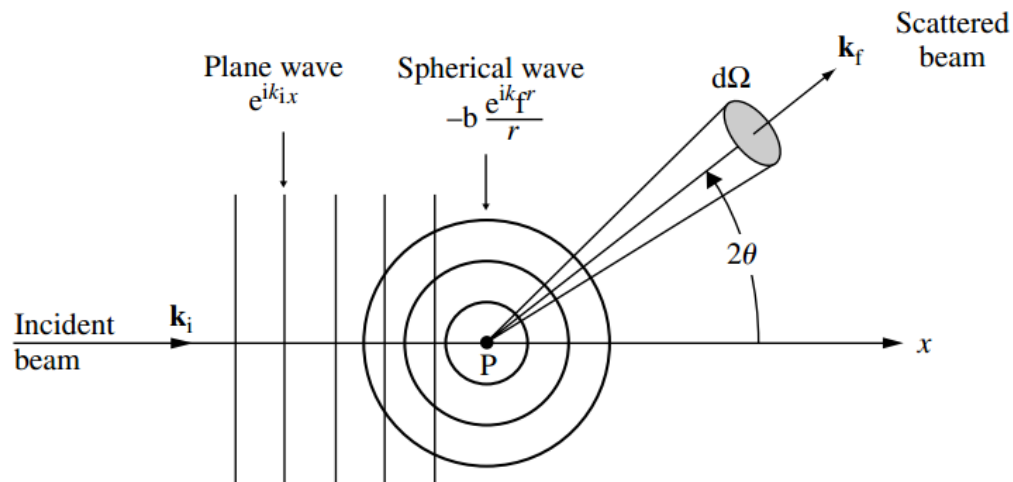


Figure 3.12 – The scattering of a plane wave of neutrons by a single scatterer. [99]

The scattering length b is a constant independent of the angles θ, ϕ . The negative sign in the equation is arbitrary, so that the majority of scattering lengths with the different elemental nuclei can have a positive value of b for a repulsive potential. Here we consider that the nucleus is fixed and the energy of the neutron is too weak to change the internal energy of the nucleus. So that the scattering is elastic with the wavenumber k keeping its value after the scattering. The scattering length can not be obtained without an appropriate theory of the nuclear forces. If the scattering length is complex and varies sharply with the energy of the neutron, this usually means that the nucleus strongly absorb the neutron. For the majority of cases, the scattering length is treated as a parameter deduced experimentally.

The scattering length is not dependent on the atomic number, for example, the scattering length of hydrogen and oxygen are very large. In addition, it is quite different for different isotopes of the same element. This behavior of the scattering length also applies for the magnetic neutron scattering, which is attributed to the interaction between the magnetic moment of the neutron and the magnetic moment distribution of an unpaired electron.

3.2.1.2 Scattering Cross-Sections

There are three important cross-sections. The first one is the total scattering cross-section, expressed as:

$$\sigma_{total} = \frac{\text{total number of neutrons scattered per second in all directions}}{\Phi} \quad (3.22)$$

- Φ : the flux of the incident neutrons

When we consider the number of neutrons incident in a certain angular, which can be characterized by the differential cross-section:

$$\frac{d\sigma}{d\Omega} = \frac{\text{total number of neutrons scattered per second into } d\Omega \text{ in the direction } \theta, \phi}{\Phi d\Omega} \quad (3.23)$$

- $d\Omega$: the solid angle in the direction.
- θ, ϕ : the spherical polar coordinates.

This cross-section is usually measured in elastic neutron scattering as the neutrons do not change of energy during the scattering process. When the scattered neutrons are detected in a certain direction with an energy between E_f and $E_f + dE_f$, we will need the last cross-section, which is called the partial differential cross-section.

$$\frac{d^2\sigma}{d\Omega dE_f} = \frac{\text{total number of neutrons scattered per second into } d\Omega \text{ in the direction } \theta, \phi \text{ with an energy between } E_f \text{ and } E_f + dE_f}{\Phi d\Omega dE_f} \quad (3.24)$$

- E_f : the final energy of the neutron after it has scattered.

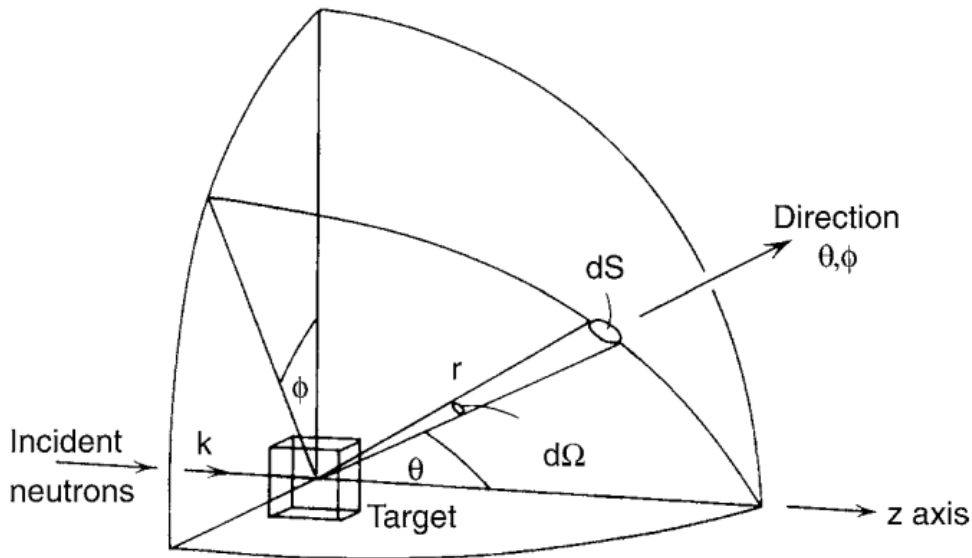


Figure 3.13 – Geometry for a scattering experiment. [100]

This cross-section is usually measured in inelastic neutron scattering, as the neutrons change the energy during the scattering process. A schematic representation of the scattering experiment is illustrated in Figure 3.13. The analysis of these cross-sections is essential in the data treatment of neutron scattering experiments.

3.2.1.3 Neutron Scattering Processes

During the neutron scattering process, the total energy and momentum of the whole scattering system must be unchanged. So the energy E and the momentum q transferred from the neutron to the scatterer can be given by:

$$E = \frac{mv^2}{2} = \frac{h^2}{2m} \cdot \frac{1}{\lambda^2} \quad (3.25)$$

$$E_{trans} = \hbar\omega = E_i - E_f \quad (3.26)$$

$$q_{trans} = q_i - q_f \Rightarrow \hbar\mathbf{Q} = \hbar(\mathbf{k}_i - \mathbf{k}_f) \quad (3.27)$$

- ω : the angular frequency.
- i and j : the initial and final state of the neutron.
- \mathbf{Q} : the scattering vector.

Neutron scattering can be classified into two types depending on whether the value of E_{trans} is zero or not.

- $E_{trans} = 0 \Rightarrow$ elastic neutron scattering.
- $E_{trans} \neq 0 \Rightarrow$ inelastic neutron scattering.

3.2.2 Elastic Neutron Scattering

For elastic neutron scattering, $|k_i| = |k_f|$, the scattering vector \mathbf{Q} is equal to the reciprocal lattice vector of the scatterer. There are four forms of contribution for the total cross-section of the elastic scattering [102], which can be expressed:

$$\sigma_{total} = \sigma_n + \sigma_m + \sigma_{nm} + \sigma_{chiral} \quad (3.28)$$

- σ_n : the contribution from a lattice of nuclei.
- σ_m : the contribution from the magnetic moment distribution in the lattice
- σ_{nm} and σ_{chiral} : the contribution from the magnetic-nuclear interference and the chiral magnetic structure. They are only relevant in polarized neutron scattering measurements.

3.2.2.1 Elastic Nuclear Neutron Scattering

The scattering length of an element is dependent on the nuclear spin and the isotope of the element, which gives rise to the coherent and incoherent scattering cross-sections. The coherent scattering can give the interference effects, which means it can give the information of the space and time correlations between different atoms. The incoherent scattering does not give interference effects. It actually arises from the deviation of the scattering lengths from their mean values for each individual atom. In Equation (3.28), the σ_n refers to the coherent neutron scattering from a nucleus. The incoherent neutron scattering produces an isotropic background, which is disturbing for experiments.

For the Bravais crystal system, the coherent nuclear elastic differential cross-section then be expressed as :

$$\left. \frac{d\sigma}{d\Omega} \right|_{\text{nuclear}} = N \frac{(2\pi)^3}{V_0} \sum_{\mathbf{H}} \delta(\mathbf{Q} - \mathbf{H}) |F_N(\mathbf{Q})|^2 \quad (3.29)$$

$$F_N(\mathbf{Q}) = \sum_j b_j e^{i\mathbf{Q} \cdot \mathbf{r}_j} e^{-W_j(\mathbf{Q})} \quad (3.30)$$

- δ : it is zero unless $\mathbf{Q} - \mathbf{H} = 0$.
- N : the number of unit cells the neutrons interact with.
- $F_N(\mathbf{Q})$: the nuclear unit cell structure factor.
- j : the j^{th} atom in the unit cell.
- r_j : the position of the atom j^{th} .
- b_j : the scattering length of the atom j^{th} .
- $e^{-W_j(\mathbf{Q})}$: the Debye-Waller factor of the atom j^{th} . It arises due to the thermal motion of the atoms.

For the measurement of the Bragg scattering of the coherent nuclear elastic, the scattering vector \mathbf{Q} is equal to a reciprocal lattice vector \mathbf{H} , i.e. $\mathbf{Q} = \mathbf{H}$.

3.2.2.2 Elastic Magnetic Neutron Scattering

The term σ_m in the Equation (3.28) corresponds to the interaction between the magnetic moment of the neutron and the magnetic moment of the unpaired electrons in the matter. The magnetic ions actually overlap on the nuclear lattice. Thus, these two cross-sections have some characters in common. The main difference comes from the fact that the magnetic moment of an electron exhibits a wide distribution of its scattering potential, while a nucleus scatters on the condition that the neutron is very close to it. Another difference is that the scattering is possible only if the moment is perpendicular to the scattering vector \mathbf{Q} . The differential cross-section for elastic magnetic scattering can be expressed as:

$$\left. \frac{d\sigma}{d\Omega} \right|_{\text{magnetic}} = N_m \frac{(2\pi)^3}{V_0} \sum_{\mathbf{H}} \delta(\mathbf{Q} - \mathbf{H}) |F_{M\perp}(\mathbf{Q})|^2 \quad (3.31)$$

$$F_{M\perp}(\mathbf{Q}) = \hat{\mathbf{Q}} \times F_M \times \hat{\mathbf{Q}} \quad (3.32)$$

- N_m : the number of magnetic ions.
- $F_M(\mathbf{Q})$: the magnetic unit cell structure factor.

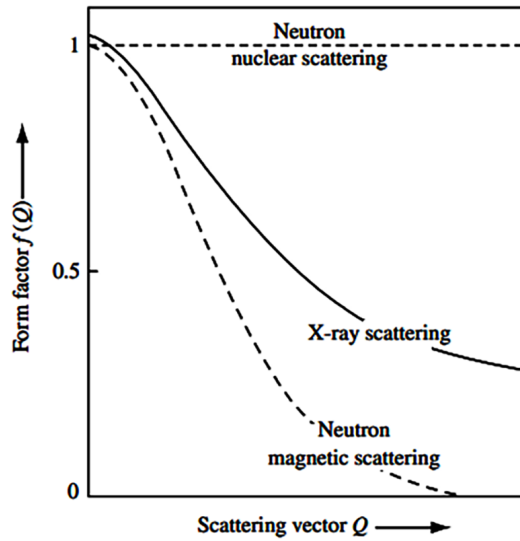


Figure 3.14 – The form factor $f(\mathbf{Q})$ for the scattering of X-rays and for the nuclear and magnetic scattering of neutrons. [99]

For the magnetic dipole, the magnetic unit cell structure factor $F_M(\mathbf{Q})$ can be expressed as:

$$F_M(\mathbf{Q}) = \gamma r_0 \sum_j f_j(\mathbf{Q}) \mu_j e^{i\mathbf{Q}\mathbf{r}_j} e^{-W(\mathbf{Q})} \quad (3.33)$$

- $f_j(\mathbf{Q})$: magnetic form factor of unpaired electrons of the atom j^{th} , which is unity for $\mathbf{Q} = 0$, as shown in Figure 3.14. It decreases quickly with increasing \mathbf{Q} , so magnetic peaks are intense only at low \mathbf{Q} . It corresponds to the Fourier transform of the unpaired electron density.
- γ : the gyromagnetic ratio, $\gamma = 1.9132$.
- r_0 : the classical radius of the electron.
- μ_j : the magnetic moment of the atom j^{th} .

3.2.3 Intensity Corrections

In addition to the Debye-Waller factor which has been already taken into consideration, several processes have to be taken into account for the scattering intensity, such as absorption, extinction and multiple diffraction [99].

Absorption

The effect of the absorption is similar to that of X-rays. The absorption effect is usually determined by fitting the data from a diffraction experiment. For most of the elements, the linear absorption coefficient is less than 1 cm^{-1} . And for most of the small crystals (less than 1 mm), the absorption effect can be generally neglected. However, some rare earth elements such as Gd, Sm and Dy, the absorption of cross-section is way too high to enable standard diffraction experiment. It is necessary to obtain suitable compounds with corresponding isotope synthesis methods.

Extinction

The extinction effect is due to the fact that the inner part of the crystal scatters less neutrons compared to the surface region, as the surface region first scattered by the primary neutron beam will reflect a little bit of incident beam. It is necessary to correct the measured cross-section from the extinction effect especially for strong reflections, which are measured with less intensity than their calculated values. Indeed, more percentage of the incident beam will be diffracted for strong intensity peaks. The extinction effect is generally treated empirically and determined by fitting the scattering data.

The extinction effect is weaker when the crystal is small. It may be ignored for small organic crystals or for large unit cells crystals. For powder samples, it can be neglected.

Multiple Diffraction

When the Bragg reflecting condition is satisfied for more than one family of reflecting planes, a multiple diffraction can be present. In that case, the diffracted beam is used as an incident beam for a second scattering. The multiple scattering is a kind of artifact which modifies the cross-section as calculated in Equation (3.31). It is important to take into account in the analysis of the diffraction pattern. The multiple diffraction effects can be minimized or even removed by rotating the crystal around the scattering vector \mathbf{Q} to avoid the secondary reflection. It is called an azimuthal scan. It is particularly true for X-ray because of the flux allowing to see this secondary diffraction process, and only for single crystal diffraction. This may be an important experimental artifact that needed to be discussed as in the article describing the polar room temperature structure of RMn_2O_5 [52]. In our powder diffraction experiments, such phenomenon can be neglected.

3.2.4 Neutron Scattering Instruments

Since there is a lot of different characteristics about different neutron beamlines, before performing the neutron scattering experiments, one should choose the neutron beamline with the correct characteristics for the experiment. The reactor source used for the experiments of this thesis is the Institute Laue-Langevin (ILL) in Grenoble. Our experiments were performed at low temperature under high pressure in beamline D1B and D20. Both are two axis diffractometer. The first axis controls the incident wavelength and the second axis controls the scattering angle by changing sample rotation (θ) and the scattering angle (2θ). The detector is a multidetector allowing to measure a large range of 2θ angles.

As shown in Figure 3.15, in D1B, seven pyrolytic graphite monochromator crystals focusing onto the sample position can provide a flux of $7.9 \times 10^6 \text{ ncm}^{-2}\text{s}^{-1}$ with wavelength $\lambda = 2.52 \text{ \AA}$ and 1280 cells covering a scattering range of 128° , which is the one we used in the experiment. The other wavelength $\lambda = 1.28 \text{ \AA}$ can be obtained by changing the monochromator to a germanium monochromator. The lowest temperature of the cryostat is 1.5 K.

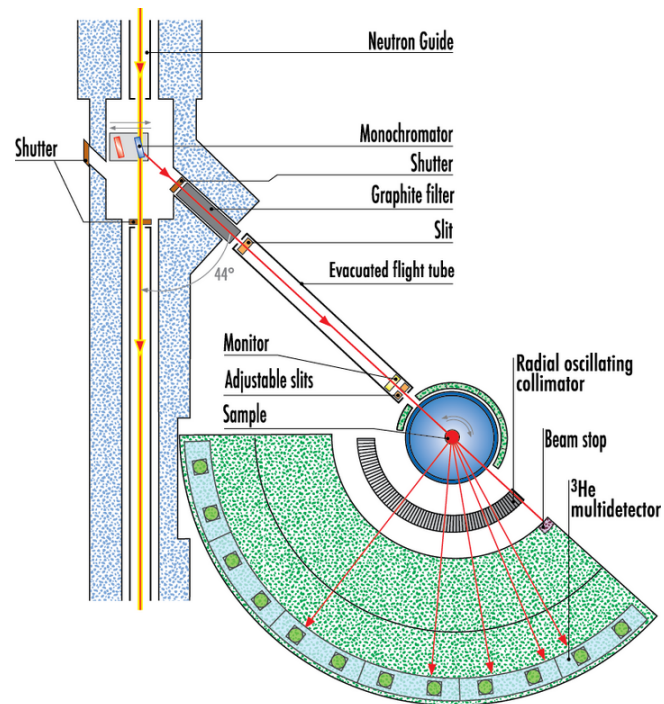


Figure 3.15 – The D1B instrument (ILL, Grenoble). From ILL [D1B website](#).

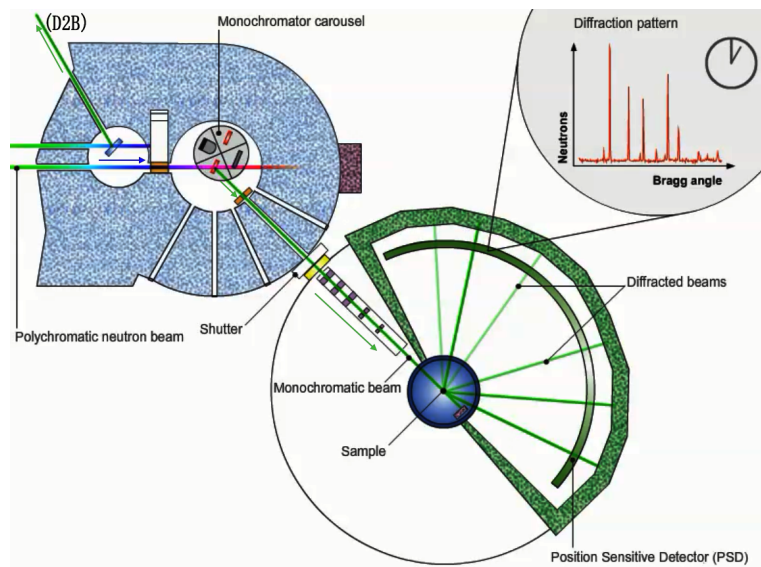


Figure 3.16 – The D20 instrument (ILL, Grenoble). From ILL [D20 website](#).

The schematic representation of the D20 instrument is presented in Figure 3.16. It is also a 2-axis diffractometer but with extremely high neutron flux. The complete diffraction pattern at 1536 positions, covering a scattering range of 153.6° . With fixed vertical focusing, a pyrolytic graphite HOPG (002) monochromator in reflection position offers a wavelength of 2.42 \AA at a take-off angle of 42° . There is a 6 cm thickness preceding pyrolytic graphite filter in the incident beam, which can suppresses the second harmonics. We can obtain other wavelengths with different take-off angle by changing the monochromator to a copper monochromator Cu (200) or a Germanium monochromator (113).

3.2.5 Pressure Cell

The pressure set-up is a Paris-Edinburgh pressure cell (shown in Figure 3.17) with a sample volume of about 50 mm^3 and a maximum pressure of $\sim 10 \text{ GPa}$. A powder sample is compressed between two opposed anvils. The pressure-transmitting medium used is methanol-ethanol. Sample confinement is achieved by using a null-scattering (TiZr) gasket with one toroidal ring, which is located into corresponding grooves machined in the anvil profile. The gasket is not a standard gasket but a thin hemispherical shell-like encapsulated gasket, which can prevent the methanol-ethanol coming into contact with the anvil surface. Application of pressure can be achieved by means of an *in situ* hydraulic ram between the two anvils. The pressure on the sample volume is estimated by the calibration of the He-gas pressure on the cell's piston. The pressure cell is inserted in a closed-circle He cryocooler.

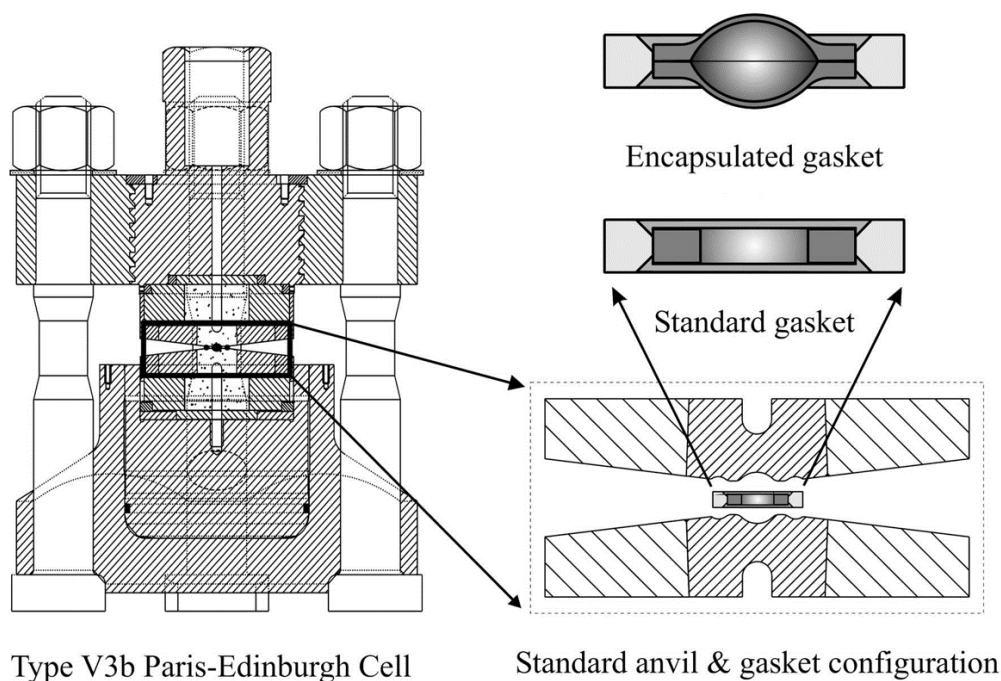


Figure 3.17 – The Paris–Edinburgh pressure cell (left), the standard anvil and gasket configuration and the standard and encapsulated gasket designs (right). [103]

Generally, we increase pressure when the mixture 4:1 methanol–ethanol transmitting medium becomes liquid. The exact temperature needed to safely change the pressure can be found through the temperature dependence of solidification pressure curve of the mixture transmitting medium [104].

In the encapsulated sample container, besides the sample powder, usually a small mount of Lead (Pb) is also introduced to measure the exact pressure of the sample. By refining the Pb diffraction peak positions, we can get its unit cell parameters. Through the equation of state (EOS) of Pb, we can calculate the exact pressure. We usually use the Rydberg-Vinet EOS [105], mostly called the "Vinet" EOS, which can be expressed as:

$$P(V) = \frac{3B_0}{X^2}(1 - X)\exp\left[\frac{3}{2}(B'_0 - 1)(1 - X)\right] \quad (3.34)$$

- X : $X = \left(\frac{V}{V_0}\right)^{\frac{1}{3}}$.
- B_0 : the bulk modulus at ambient pressure, $B_0 = -\left(\frac{\partial P}{\partial \ln V}\right)_0$.
- B'_0 : the pressure derivative at ambient pressure, $B'_0 = \left(\frac{\partial B_0}{\partial P}\right)_0$.

The final B_0 and B'_0 values to be used with the Rydberg-Vinet Equation (3.34) are summarized in Table 3.2. With these values, we can calculate the pressure through the lattice parameters of Pb.

Table 3.2 – B_0 and B'_0 values of the Rydberg-Vinet EOS equation. [106]

T(K)	B_0 (GPa)	B'_0	T(K)	B_0 (GPa)	B'_0
0	48.33	5.45	160	44.94	5.57
20	48.24	5.45	180	44.41	5.59
40	47.95	5.46	200	43.87	5.62
60	47.50	5.48	220	43.34	5.64
80	47.00	5.50	240	42.80	5.66
100	46.49	5.52	260	42.27	5.68
120	45.97	5.54	280	41.73	5.70
140	45.46	5.55	300	41.20	5.72

3.3 Powder Diffraction Refinements

In this thesis, we mainly deal with powder diffraction of X-rays and neutrons. The software we use to refine the data is FullProf Suite [107], which is mainly developed for the Rietveld analysis [108] of powder X-rays or neutron diffraction data collected at constant or variable step in scattering angle 2θ . Here, we only give a brief introduction about the Rietveld analysis and the FullProf Suite, more details can be found in Ref [109]. and the website of [FullProf Suite](#), respectively.

3.3.1 Rietveld Analysis

A lot of useful information can be deduced from powder diffraction data, as shown in Figure 3.18. However, in a polycrystalline sample it is inevitable that certain information is lost due to the random orientation of the crystallize grain. Furthermore, in practice, the loss of information can also come from the overlap of independent diffraction peaks in the powder diffractogram.

As the powder diffraction pattern is actually a smooth curve that consists of several Gaussian peaks on top of a smooth background, the method of using the total integrated intensities of the overlapping peaks in the least squares refinement of the structures leads to the loss of all the information contained in the profile of these peaks. Thus, the Rietveld powder refinement proposes to use directly the profile intensities obtained from step-scanning measurements of powder diffraction [108, 110].

The best way of extracting the maximum information from powder diffraction pattern is to employ a mathematical expression to represent the observed intensity at each step in this pattern:

$$Y_c = Y_b + \sum Y_{hkl} \quad (3.35)$$

- Y_c : the calculated powder pattern profile intensity.

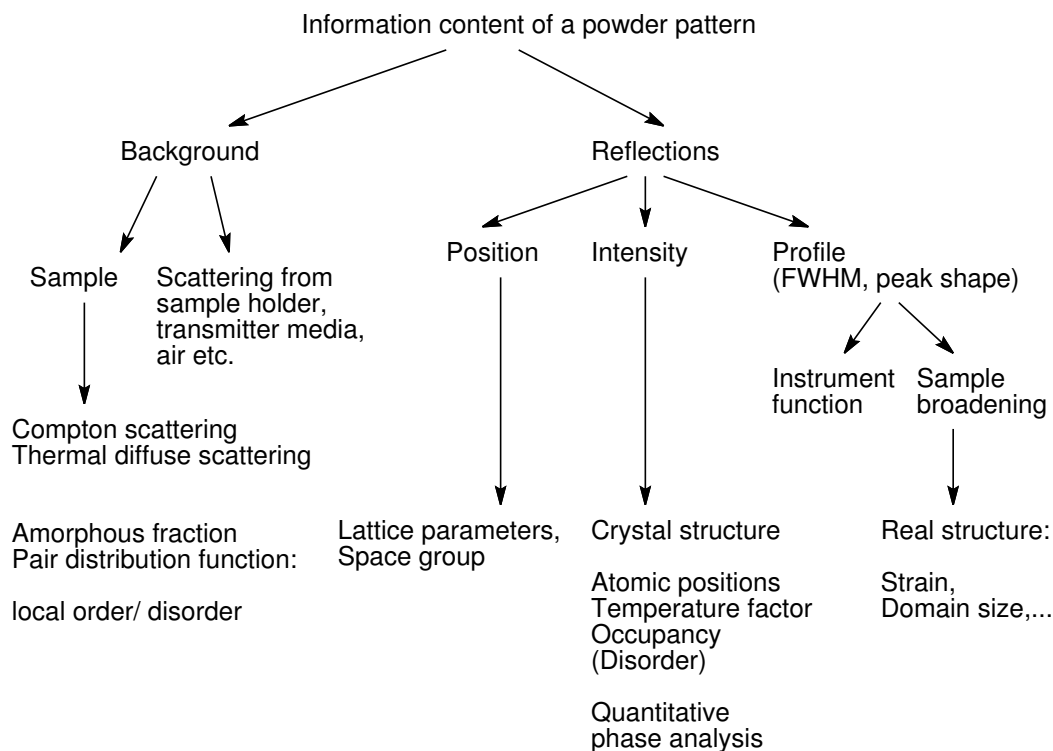


Figure 3.18 – The information deduced from the powder diffraction data.

- Y_b : the contribution from the background.
- Y_{hkl} : the contribution from each of the Bragg reflections (hkl) that are near the powder pattern step.

The adjustable parameters are refined by a least squares minimization of the weighted differences between the observed and calculated profile. The magnitudes of the peaks are modeled from crystal structure parameters (atom coordinates, *etc.*) and the shapes are a convolution of the instrumental and the microcrystalline broadening effects. The model also contains parameterized descriptions of the various systematic effects (absorption, *etc.*) that modify the profile intensity from the value of an idealized experiment. Therefore, the consequence of a Rietveld refinement consists of the crystal structure information (lattice parameters, atomic coordinates, displacement factors, and site fractions) and macroscopic sample information (crystallite size, microstrain distribution, and/or crystalline phase fractions). The peak shape used to fit the peaks in this thesis is Thompson-Cox-Hastings pseudo-Voigt convoluted with axial divergence asymmetry function [111].

Least Squares

As a powder diffraction pattern is a set of peaks, with some overlapped reflections, superimposed on a smooth and slowly varying background, a Rietveld refinement can be treated as a very complex curve fitting problem. The model function Equation (3.35) is parameterized by both the crystal structure (atomic coordinates, thermal displacements and site occupancies) and the diffraction measurement (unit cell, peak profile broadening, *etc.*) via mostly nonlinear and transcendental analytical expressions. Since the powder diffractogram is usually obtained via particle (X-ray photon or neutron) counting techniques, the intensities have a Poisson distribution of their expected value. Given sufficient counts for every powder profile step, this distribution is indistinguishable from a Gaussian fit. Consequently, when the number of observations (powder profile points in this case) exceeds the number of parameters,

a minimization by least squares can be expressed [109]:

$$M = \sum w(Y_o - Y_c)^2 \quad (3.36)$$

- w : the weight, computed from the variance σ^2 of the Y_o , $w = \frac{1}{\sigma^2}$.

It will give estimated parameters of minimum variance. The weight w is generally considered as a nonzero covariances between different Y_o across the powder pattern. The Y_c is expressed as:

$$Y_c = K |F_{hkl}|^2 H(\Delta T_{hkl}) \quad (3.37)$$

- $|F_{hkl}|^2$: the square of the module of the structure factor of the reflection. A quantity proportional to the intensity.
- K : the product of the various correction and scaling factors to the $|F_{hkl}|^2$.
- $H(\Delta T_{hkl})$: the value of the profile function for the location of the profile point relative to the reflection Bragg position.

As Equation (3.37) above is nonlinear and transcendental, the usual linear least squares analysis can not be used. The method is to obtain the approximation of the Y_c by employing a Taylor series and only retain the first term:

$$Y_c(p_i) = Y_c(a_i) + \sum_i \frac{\partial Y_c}{\partial p_i} \Delta p_i \quad (3.38)$$

The minimum is obtained from the first derivative of Equation (3.36):

$$\sum w(Y_o - Y_c) \frac{\partial Y_c}{\partial p_j} = 0 \quad (3.39)$$

$$\Rightarrow \sum w \left[\Delta Y - \sum_i \frac{\partial Y_c}{\partial p_i} \Delta p_i \right] \frac{\partial Y_c}{\partial p_j} = 0, \text{ with } \Delta Y = Y_o - Y_c(a_i) \quad (3.40)$$

$$\Rightarrow \sum w \frac{\partial Y_c}{\partial p_j} \left(\sum_i \frac{\partial Y_c}{\partial p_i} \Delta p_i \right) = \sum w \Delta Y \frac{\partial Y_c}{\partial p_j} \quad (3.41)$$

There is one for each parameter shift, Δp_i . By accumulating the terms, these equations can be given in a matrix form,

$$\mathbf{Ax} = \mathbf{v}, \text{ with} \quad (3.42)$$

$$a_{i,j} = \sum w \frac{\partial Y_c}{\partial p_i} \sum_i \frac{\partial Y_c}{\partial p_j}$$

$$x_j = \Delta p_j$$

$$v_i = \sum w(\Delta Y) \frac{\partial Y_c}{\partial p_i}$$

This matrix equation can be solved for the desired parameter shifts by :

$$\begin{aligned} \mathbf{A}^{-1} \mathbf{Ax} &= \mathbf{A}^{-1} \mathbf{v} \\ \Rightarrow \mathbf{x} &= \mathbf{A}^{-1} \mathbf{v} = \mathbf{Bv} \end{aligned} \quad (3.43)$$

The inverse matrix \mathbf{B} is normalized by the reduced χ^2 (Equation (3.47)) to give the variance-covariance matrix. The square roots of the diagonal elements of the normalized matrix are the estimated errors of the values of the shifts. These errors are based only on the statistical errors in the original powder diffraction pattern intensities and can not accommodate the possible discrepancies arising from systematic flaws in the model. Thus, the models must accurately represent a close correspondence to

the scattering process that gives rise to features in the observed pattern to avoid significant systematic errors.

The result of a Taylor series approximation is that the computed shifts, Δp_i , does not obtain a fully minimized solution to the problem accurately, but is a good approximation. Consequently, the new parameter values are needed for a subsequent refinement cycle. This process is repeated until the final parameter shifts are less than some fraction of their estimated errors as obtained from the diagonal elements of the **B** matrix.

The quality of the least squares refinement is given by some residual functions. The profile factor is:

$$R_p = \frac{\sum |Y_o - Y_c|}{\sum Y_o} \quad (3.44)$$

and the weighted profile factor, R_{wp} ,

$$R_{wp} = \sqrt{\frac{M}{\sum wY_o^2}} \quad (3.45)$$

- M : the factor minimized by the least squares.

the factor M becomes the only statistically relevant residual. The "expected R_{wp} " can be expressed as:

$$R_{wp(exp)} = \sqrt{\frac{n-p}{\sum wY_o^2}} \quad (3.46)$$

- n : total number of points in the pattern minus total number of excluded points.
- p : number of parameters.

The reduced χ^2 or "goodness of fit" is defined by the minimization function:

$$\chi^2 = \frac{M}{n-p} = \frac{R_{wp}}{R_{wp(exp)}} \quad (3.47)$$

If the weights for the observations are chosen "properly" (i.e. as reciprocal variances) then the value of reduced χ^2 will be slightly greater than unity for an optimal refinement. Miss-scaled variances will drive this value away from unity without affecting the value of R_{wp} .

3.3.2 FullProf Suite

We list some crystallographic programs, which are very often used in this thesis, marked as red rectangles in Figure 3.19.

EdPCR
FullProf
WinPLOTR
FPStudio
BasIreps



Figure 3.19 – The menu of the FullProf Suite

The *EdPCR* is a graphical editor for PCR files which are the input file for FullProf program. We can use it to create / edit the content of the PCR file, which contains all the structure profile information.

We can easily choose to refine the corresponding parameters or not. Note that the number of the variables to refine should be less than the total number of points in the pattern. The refinement is processed by the program of *FullProf*. The *WinPLOT*R is used to plot the raw or normalized data files as well as the Rietveld files. The edition of the PCR input file, plot the Rietveld plots, run the *FullProf* and the *FPStudio* ... can be directly executed through the *WinPLOT*R interface.

When dealing with magnetic samples, after the refinement, there are several FST files generated, which contain the atomic structure and magnetic moments information (if any). By using the program *FPStudio* to visualize the the FST files, it is easy to see the arrangement of magnetic spins.

If there is a magnetic phase transition, the program *BasIreps* can be useful to determine the symmetry constrains between the atoms, which can help us to reduce the number of variables. With the correct space group, k -vector and axial vector, *BasIreps* can give the results of possible irreducible representations, which can give us a hint of the right magnetic structure.

3.4 Ferroelectric Properties Measurement

The temperature dependence of dielectric ϵ and electric polarization \mathbf{P} of RMn_2O_5 compounds under pressure (up to 1.46 GPa) are also studied in this thesis. The measurements are performed along the b axis on a relatively small plate like single crystal of RMn_2O_5 , which is placed in a beryllium copper clamp cell capable of hydrostatic pressure. The Fluorinert FC 70 is used as the pressure medium and pressure is measured *in situ* by using a lead manometer in conjunction with a low-frequency (19 Hz) LR700 Inductance Bridge (Linear Research) [112]. Temperature control for both the dielectric and polarization measurements are at a rate of 1- 2 K/min. The capacitance is measured at a frequency of 1 kHz with an Andeen-Hagerling capacitance bridge (AH 2500A). The real part of the capacitance is used to calculate the dielectric constant ϵ while the imaginary (loss factor) can be helpful for the data analysis. The pyroelectric current are measured with a Keithley electrometer (K6517A) with a small poling voltage applied on cooling runs. The electric polarization can be determined by integrating the pyroelectric current over the temperature range of the measurement.

These measurement were performed by our collaborator M. J. Gooch at Texas Center of Superconductivity (University of Houston, Texas, USA) and also by C. R. Pasquier and P. Auban-Senzier in Laboratoire de Physique des Solides (Université Paris Sud, Orsay, France).

3.5 Sample Synthesis Process and Characterization

High purity polycrystalline samples of RMn_2O_5 (R=Pr, Nd, Sm, Gd, Tb and Dy) were synthesized from a precursor-based flux, following a method described in Ref. [113], by our collaborators M. Greenblatt and M. Whitaker (The State University of New Jersey, USA). As an example, the synthesis process of PrMn_2O_5 powder sample has been shown in Figure 3.20.

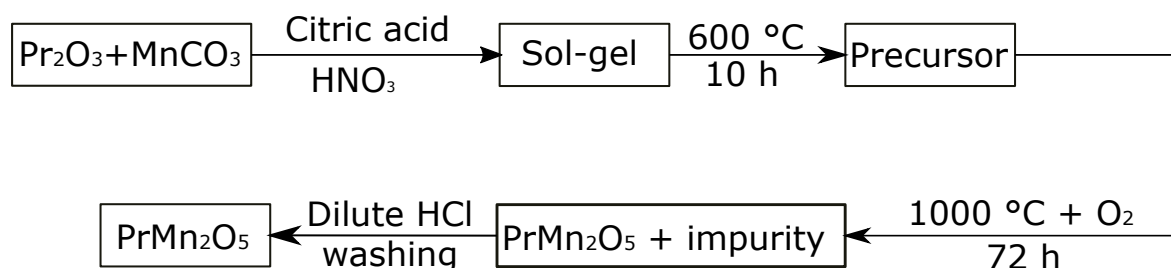


Figure 3.20 – The synthesis process of PrMn_2O_5 powder sample.

Synchrotron radiation diffraction experiments have been performed for this sample on the CRISTAL beamline at the Soleil synchrotron light source (Saint-Aubin, France), with a two-circle diffractometer with 21 analyzer crystals at 4 K ambient pressure. The refinement diffractogram of PrMn_2O_5 at 4 K ambient pressure is illustrated in Figure 3.21, which has shown a good fit for the X-ray diffraction data.

In addition, the previous ambient pressure neutron diffraction measurements have been performed [44, 54, 56, 57, 59, 60], which can ensure the purity of the samples.

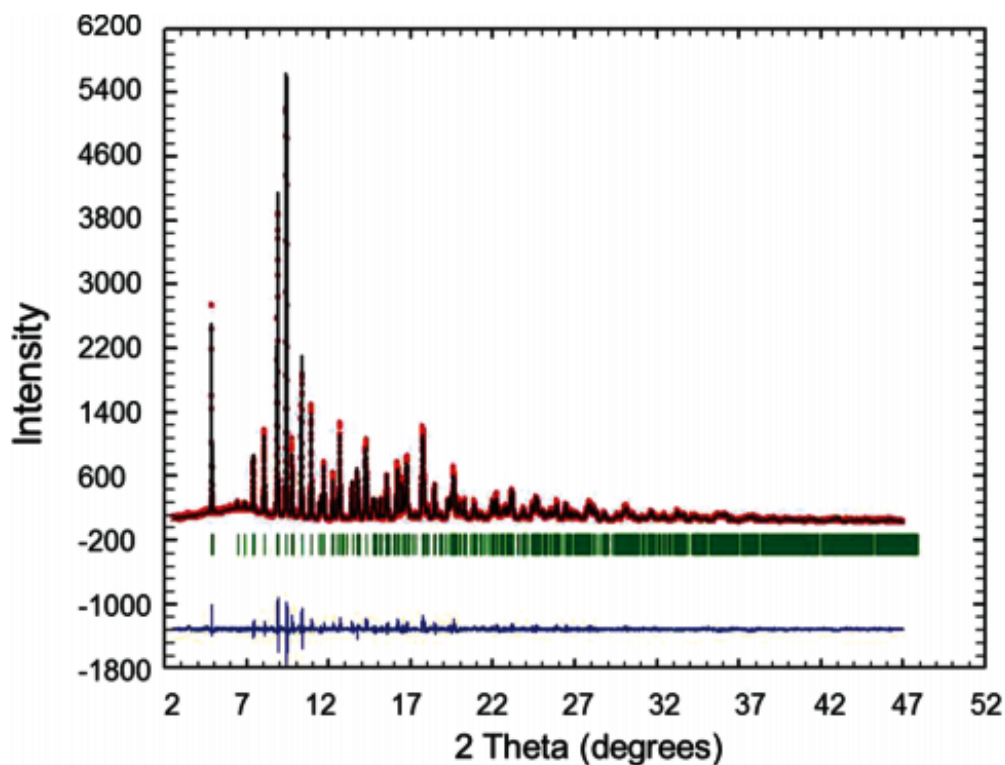


Figure 3.21 – Rietveld refinement (experimental data: black open circles, calculated profile: red continuous line, allowed Bragg reflections: blue ticks). The difference between the experimental and calculated profiles is displayed at the bottom of the graph of the crystal structure of PrMn_2O_5 at 4 K [59].

Summary of this Chapter

The main part of this chapter is about the theory of X-ray and neutron diffraction. A brief description of the X-ray instrument Section 3.1.5 and neutron instruments Section 3.2.4 are listed. Then, the Rietveld refinement and the FullProf Suite we use to refine the powder diffraction data are shown in Section 3.3. Finally, we also discussed the set-up for measuring the dielectric ϵ and electric polarization \mathbf{P} in Section 3.4.

4

Pressure-dependent x-ray diffraction of multiferroic RMn_2O_5

Contents

4.1 Basics of Density Functional Theory (DFT)	65
4.2 Experimental Details	66
4.3 Ab Initio Calculations	69
4.4 Results	69
4.5 Analysis and Discussion	75

In this Chapter, we systematically studied the structural properties of the RMn_2O_5 ($\text{R} = \text{Pr}, \text{Nd}, \text{Sm}, \text{Gd}, \text{Tb}$ and Dy) compounds under pressure by powder X-ray diffraction as well as numerical calculations. We firstly introduce the basics of density functional theory (DFT) in Section 4.1, followed by the experimental measurement and refinement strategies in Section 4.2. A brief description of our DFT calculation setting is presented in Section 4.3. Then the section on the results (Section 4.4) is about the X-ray diffractograms at different pressure and the corresponding refined lattice parameters. Finally, in Section 4.5, the atomic displacements of R^{3+} , Mn^{3+} , Mn^{4+} under different pressure are extracted. In addition, with the help of DFT calculations, we were able to estimate the pressure evolution of the exchange interactions J_i to study the origin of the pressure-induced modification of the multiferroic properties in this series of compounds.

4.1 Basics of Density Functional Theory (DFT)

In principle, the quantum mechanical wavefunction contains all the information about a given system. Unfortunately, it is impossible to solve the Schrödinger equation for a many-body system without any approximations. The many-body electronic wavefunction is a functional of $3N$ variables (the coordinates (x, y, z) of all N atoms in the system). The density functional theory (DFT) considers the electron density is only a functional of only three variables (x, y, z) rather than the many-body wavefunction. An early density functional theory was proposed by Thomas [114] and Fermi [115], which suggested that the kinetic energy was a functional of the electron density, but in common with the Hartree and Hartree-Fock methods, only introduced electron-electron interactions via a mean field potential. However, in this way, it ignored the exchange and correlation interactions. A subsequent theory proposed by Dirac [116], which added an expression for the exchange energy within the terms of the electron density. However, the Thomas–Fermi–Dirac theory turned to be inaccurate for most

applications. The representation of the kinetic energy is the main source of the error due to the complete neglect of the electron correlation, followed by the errors in the exchange energy.

The Hohenburg-Kohn theorems proposed that the density of any system determines all ground state properties of the system. The Hohenberg-Kohn theorems can be applied to any system consisting of electrons, which are moving under the influence of an external potential. They have been used in practice to investigate the structural, magnetic and electronic properties of molecules, materials and defects.

The Hohenburg-Kohn theorems are based on the following remarkable theorems:

- *Theorem I:* The external potential and hence the total energy are a unique functional of the electron density only. Thus the Hamiltonian \mathcal{H} , and hence all ground state properties of the system, are determined solely by the electron density.
- *Theorem II:* The input density that minimizes the total energy is the true ground state density.

These two theorems prove the existence of a universal functional. However, there is no indication of any information about the functional, or how to actually calculate the ground state density. In order to do so, approximation methods (Kohn-Sham formulation) for treating an inhomogeneous system of interacting electrons are developed [117]. It maps fully the N interacting electrons system onto a auxiliary system of N non-interacting electrons, coupled by moving within an effective Kohn-Sham potential. The single particle Kohn-Sham orbitals are constrained to yield the same ground state density as that of the fully interacting electrons system, thus the Hohenberg-Kohn theorems are still valid.

Therefore, the Kohn-Sham formulation succeeds in transforming the N -body problem into N single-body problems, each coupled via the Kohn-Sham effective potential. More details can be found in Ref. [118–120]

Consequently, the terms contributing to the total energy of the system in terms of all functionals of the electron density are:

- Ion-electron potential energy.
- Ion-ion potential energy.
- Electron-electron energy.
- Kinetic energy.
- Exchange-correlation energy.

4.2 Experimental Details

Powder X-ray diffraction experiments under pressure were carried out in Laboratoire de Physique des Solides (Université Paris Sud, Orsay, France). The measurements were performed at room temperature from ambient pressure to ~ 9 GPa.

The X-ray diffraction data were collected by exposing the sample to a 2D Mar 345 device for 20 min for low pressure and 30 min for high pressure ones. High pressure needed to be counted more because of the shrink of the gasket hole diminishing the flux on the sample. During the measurement, the pressure cell oscillates between -10 and 10° to average the possible preferred orientation (texture in the powder). In this thesis, the Dioptas software [121] has been used to treat the exposed X-ray diffraction images.

A standard CeO_2 (space group: $Fm\bar{3}m$, $a = 5.412 \text{ \AA}$) sample has been measured to find the experimental setup parameters: center of the image (direct beam), angles between image and incident beam, distance between sample and detector. The raw MAR image of CeO_2 and the starting values of the calibration are shown in Figure 4.1. The distance parameter is the real distance between the MAR and the pressure. The center of the image should be the center of beam-stop. The Bragg

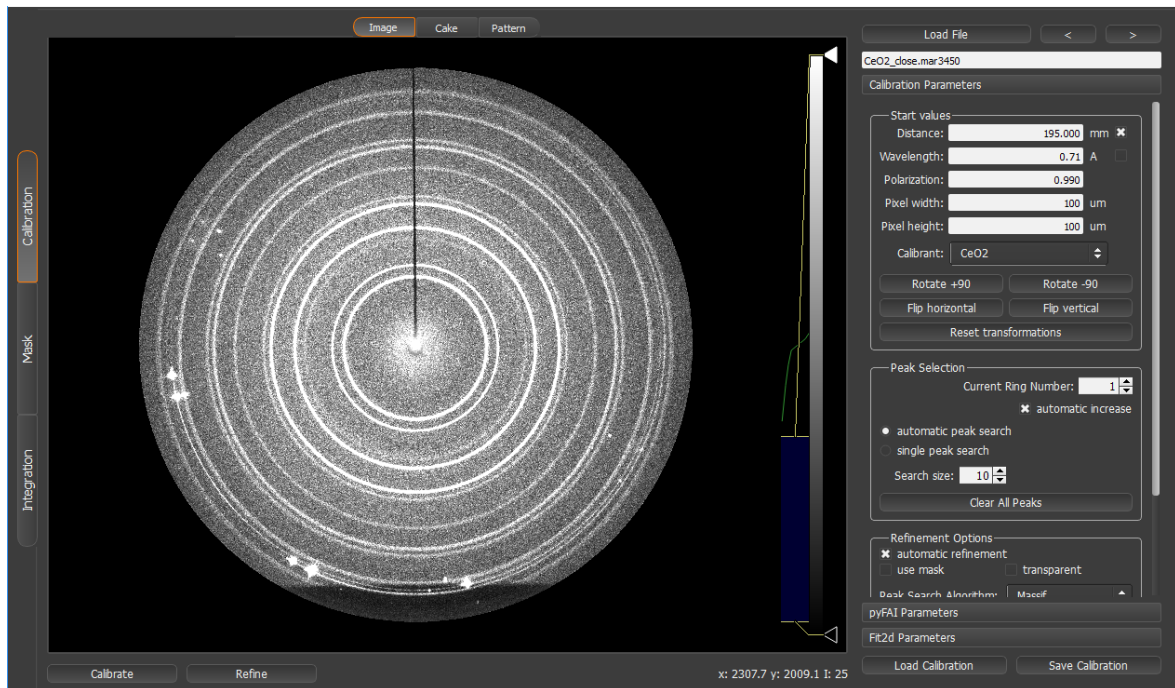


Figure 4.1 – The raw MAR image of CeO₂ and the starting values of the calibration from Dioplas

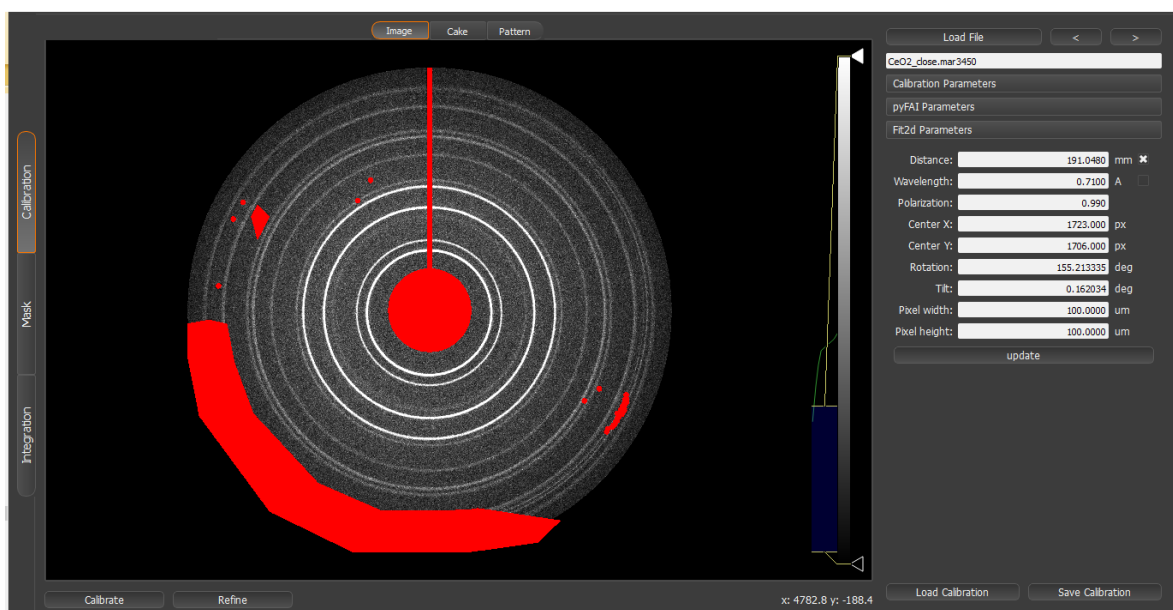


Figure 4.2 – The MAR image of CeO₂ with masks and the refined values of the calibration from Dioplas

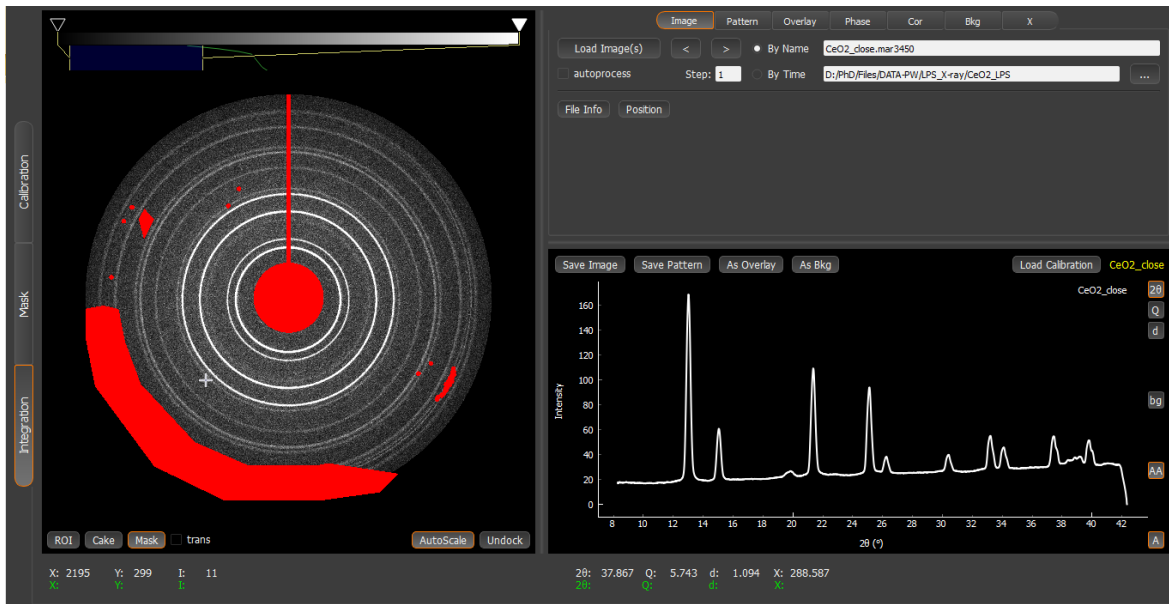


Figure 4.3 – The MAR image of CeO_2 with masks and the integrated data from the Dioptas. The masks can exclude the obvious diffraction peaks from the diamond and some of the preferred orientations diffraction dots.

reflection dots on the big rings of the image belong to the diamond of the pressure cell. The refined calibration parameters are presented in Figure 4.2 with necessary masks on the image. With these refined parameters, the integration of the data can be obtained, as shown in Figure 4.3

The X-ray diffraction pattern of CuBe gasket alone (without any sample) is illustrated in Figure 4.4(a). The regions of the gasket peaks are $19.2^\circ \sim 20.5^\circ$ and $22.1^\circ \sim 23.6^\circ$. As shown in Figure 4.4(b), the diffraction of the gasket can influence the refinement of the standard CeO_2 . The effect is more obvious with increasing the pressure because of the shrinking of the hole, increasing the incident flux on the gasket and decreasing the flux on the sample.

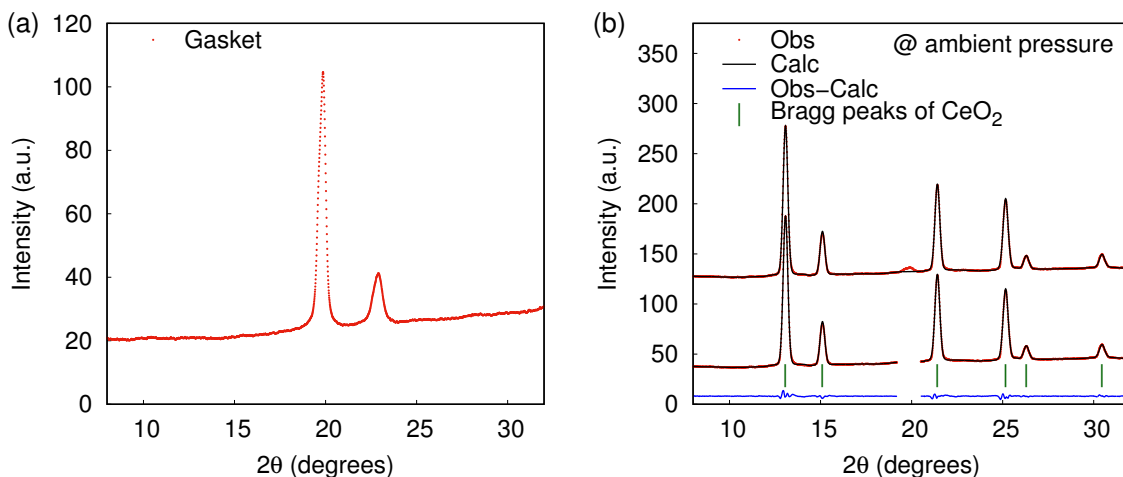


Figure 4.4 – (a) The X-ray diffraction of CuBe gasket. (b) The refined X-ray diffraction of standard CeO_2 with and without the peaks of the gasket.

The X-ray diffraction patterns were analyzed by the Rietveld method [108], using the FullProf software [107]. The regions belonging to the peaks of the gasket are excluded in the refinements. The initial information of the atomic position comes from Ref. [44, 56, 57, 122]. At ambient pressure, in the final run, the following parameters are refined: zero-point, scale factor, the lattice parameters, the atomic positions of R^{3+} , Mn^{3+} , Mn^{4+} and the oxygens (if possible). With increasing pressure, the

positions of the oxygens were fixed to the values at ambient pressure and the other parameters were refined.

4.3 Ab Initio Calculations

In order to further analyze our experimental data, we have performed a geometry optimization of the structure using DFT calculations for two compounds of the series $R = \text{Dy}$ and Gd . The DFT calculations were performed by M.-B. Lepetit, E. Rebolini from CNRS, Institut Laue Langevin and A. Vaunat from Laboratoire de Physique des Solides, Université Paris-Sud/Université Paris-Saclay.

The calculations were done using the density functional formalism with the CRYSTAL code [123]. The functional used is the PBE functional optimized for solids [124]. The rare-earth atoms have been treated using a relativistic core effective potential from the Stuttgart-Köln group [125, 126] and the associated basis set [127] of valence 3- ζ quality, adapted for solid state calculations. The manganese and oxygen atoms were treated using the Peintinger *et al.* all electrons basis set of 3- ζ quality [128]. We performed a full geometry optimization calculations within the Pm space group, in a $2a \times b \times c$ unit cell, and the AFM ordering for the manganese spins. The optimization was done in the CM phase ($\mathbf{q}_{\text{CM3}} = (\frac{1}{2}, 0, 0)$), which corresponds to the ground state even under pressure. A detailed description of these calculations is beyond the scope of this thesis.

4.4 Results

We systematically studied the various structures of RMn_2O_5 ($R = \text{Pr, Nd, Sm, Gd, Tb}$ and Dy) as a function of pressure. The diffraction patterns of RMn_2O_5 compounds are shown in Figure 4.5 and Figure 4.6. The influence of the diffraction of the gasket is obvious for RMn_2O_5 ($R = \text{Nd, Sm, Gd}$ and Dy) but not so obvious for RMn_2O_5 ($R = \text{Pr}$ and Tb).

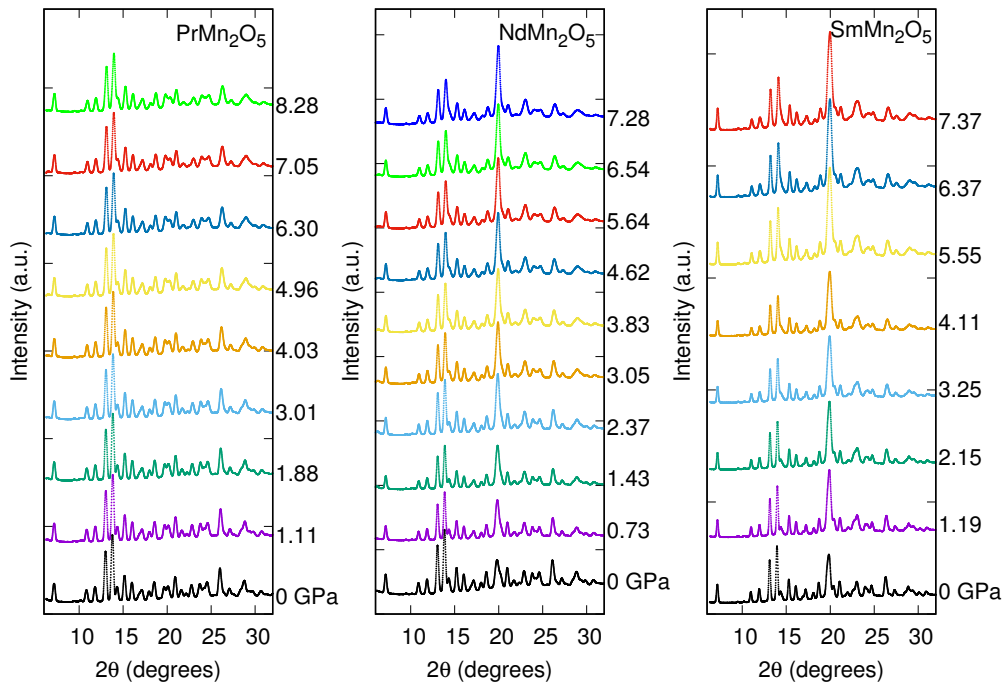


Figure 4.5 – The X-ray diffraction patterns of RMn_2O_5 ($R = \text{Pr, Nd}$ and Sm) under different pressures.

As can be seen in Figure 4.5 and Figure 4.6, the quality of the X-ray patterns is good. However, it is important to recall that these patterns obtained under pressure have not the optimum accuracy due to a low signal over noise ratio, the presence of contamination peaks from the diamond and the gasket and due to the small opening of the pressure cell. For the refinements, the initial values of the atomic

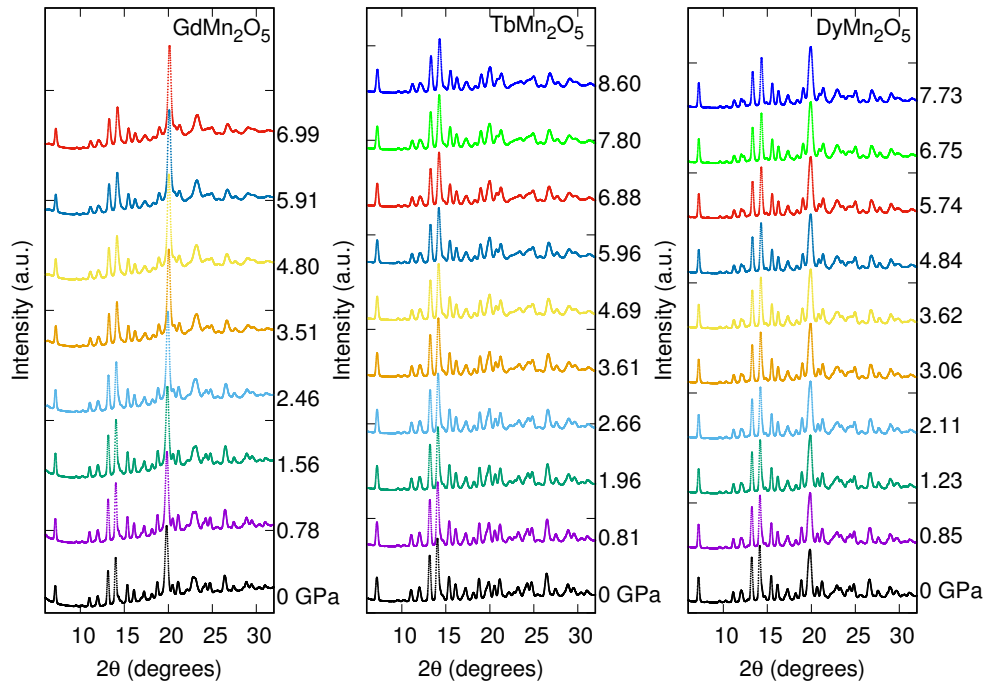


Figure 4.6 – The X-ray diffraction patterns of RMn_2O_5 ($R = \text{Gd}, \text{Tb}$ and Dy) under different pressures.

positions come from Ref [122], Ref [53] and Ref [56]. The instrumental parameters (U, V, W) come from the refinement of the standard CeO_2 . For the refinement, the R^{3+} , Mn^{4+} , Mn^{3+} atomic positions as well as the lattice parameters were refined for all the measured pressures. At ambient pressure, the atomic positions of the oxygens were also refined. The refined lattice parameters at ambient pressure are presented in Table 4.1. The corresponding atomic positions of all the structure refined are shown in Table 4.2. With increasing the pressure, we fixed the atomic positions of the oxygens to the ambient pressure ones and only refined the atomic positions of R^{3+} , Mn^{4+} and Mn^{3+} .

Table 4.1 – Lattice parameters of RMn_2O_5 ($R = \text{Pr}, \text{Nd}, \text{Sm}, \text{Gd}, \text{Tb}$ and Dy) at ambient pressure, room temperature in the $Pbam$ space group.

R	Pr	Nd	Sm	Gd	Tb	Dy
a (Å)	7.5666(3)	7.5248(5)	7.4392(2)	7.3778(2)	7.3540(5)	7.3006(1)
b (Å)	8.6544(9)	8.6248(5)	8.5843(6)	8.5579(2)	8.5451(3)	8.5103(8)
c (Å)	5.7154(3)	5.7081(4)	5.6948(7)	5.6948(4)	5.6927(4)	5.6742(6)

We were easily able to find the unit cell parameters up to highest pressure for all compounds. The refinements at high pressure were of high quality for the compounds with $R = \text{Gd}, \text{Pr}$ and Sm . As an example, the refinement for GdMn_2O_5 at 6.99 GPa is shown in Figure 4.8(a) with a very good agreement between the data (red points) and the calculated intensity (black line). However, in the case of the compounds with $R = \text{Dy}, \text{Tb}$ and Nd , the refinements at high pressure were difficult. A comparison between the PrMn_2O_5 and TbMn_2O_5 has been shown in Figure 4.7. With increasing the pressure, the peaks slightly shifted to higher angle. Above 4 GPa, for TbMn_2O_5 , the strong peak overlap at high angle and due to the fact that the oxygens were not refined which lead to that the high pressure diffractograms were not reliably fitted for compounds with $R = \text{Nd}, \text{Dy}$ and Tb . We have thus limited our analysis to the pressures below 4 GPa for which the refinements were of good quality as evidenced in Figure 4.8(b) (the refinement of TbMn_2O_5 at 3.61 GPa). The refined atomic positions of the RMn_2O_5 at the highest pressure are presented in Table 4.3.

Table 4.2 – Refined structural parameters of RMn_2O_5 ($\text{R} = \text{Pr, Nd, Sm, Gd, Tb}$ and Dy) at ambient pressure, room temperature in the $Pbam$ space group.

Atom		Pr	Nd	Sm	Gd	Tb	Dy
R	x	0.1457(5)	0.1422(9)	0.1412(1)	0.1391(6)	0.1404(4)	0.1387(4)
	y	0.1735(2)	0.1745(3)	0.1748(3)	0.1717(5)	0.1719(9)	0.1716(9)
Mn1	z	0.2544(5)	0.2570(9)	0.2556(6)	0.2419(0)	0.2502(4)	0.2548(0)
Mn2	x	0.4113(5)	0.4165(5)	0.4131(8)	0.4039(4)	0.4101(9)	0.4119(0)
	y	0.3531(2)	0.3661(5)	0.3542(6)	0.3535(7)	0.3536(3)	0.3500(0)
O1	z	0.2690(5)	0.2349(7)	0.2527(1)	0.2697(2)	0.2598(4)	0.2741(0)
O2	x	0.1656(5)	0.1571(6)	0.1760(5)	0.1526(1)	0.1693(1)	0.1647(1)
	y	0.4454(4)	0.4469(4)	0.4694(6)	0.4486(1)	0.4431(6)	0.4452(2)
O3	x	0.1337(3)	0.1524(6)	0.1429(7)	0.1454(2)	0.1429(3)	0.1537(5)
	y	0.4377(0)	0.4374(4)	0.4339(5)	0.4356(1)	0.4322(5)	0.4354(3)
O4	x	0.4046(3)	0.4009(3)	0.4016(3)	0.3994(8)	0.3988(1)	0.3951(0)
	y	0.2028(7)	0.2067(3)	0.2054(6)	0.2076(9)	0.2017(8)	0.2082(0)
	z	0.2550(7)	0.2515(6)	0.2522(0)	0.2450(1)	0.2473(5)	0.2414(4)
χ^2		0.071	0.107	0.029	0.039	0.067	0.055
R_p (%)		4.47	8.21	7.03	6.76	5.47	6.87
R_{wp} (%)		4.84	8.79	6.46	5.60	5.42	7.21

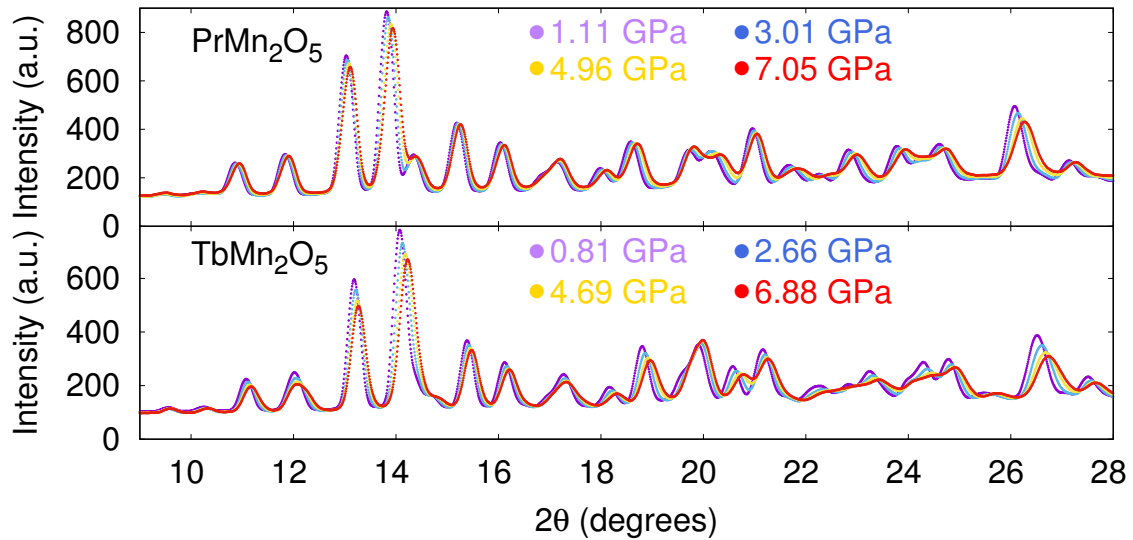


Figure 4.7 – The X-ray diffraction patterns of PrMn_2O_5 and TbMn_2O_5 at some selected pressure.

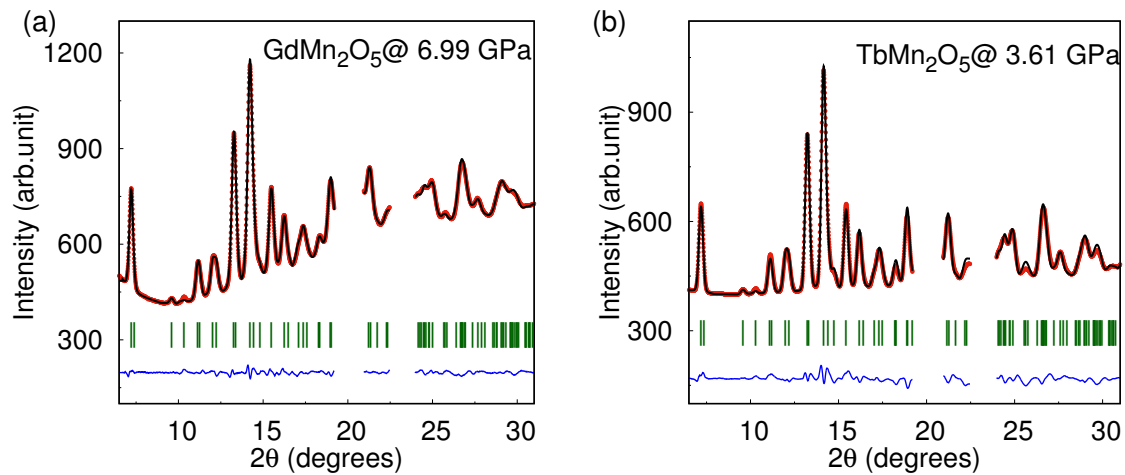


Figure 4.8 – The refinements of (a) GdMn_2O_5 at 6.99 GPa and of (b) TbMn_2O_5 at 3.61 GPa. The experimental data are in red, the calculated profile in black, and their difference in blue. The green ticks refer to the nuclear reflections. The peaks of the gasket have been excluded.

Table 4.3 – Refined structural parameters of RMn_2O_5 ($R = \text{Pr, Nd, Sm, Gd, Tb}$ and Dy) at the highest pressure, room temperature. The position of the oxygens are fixed to the ones of the ambient pressure.

Atom		Pr	Nd	Sm	Gd	Tb	Dy
		8.28 GPa	3.05 GPa	6.37 GPa	6.99 GPa	3.61 GPa	3.57 GPa
R	x	0.1484(4)	0.1433(1)	0.1411(5)	0.1433(9)	0.1428(3)	0.1417(0)
	y	0.1755(9)	0.1769(1)	0.1750(9)	0.1739(0)	0.1747(9)	0.1712(3)
Mn1	z	0.2508(4)	0.2637(8)	0.2496(2)	0.2461(3)	0.2449(9)	0.2453(2)
Mn2	x	0.4117(3)	0.4268(6)	0.4137(2)	0.4171(6)	0.4116(5)	0.4154(2)
	y	0.3531(2)	0.3661(1)	0.3566(0)	0.3519(0)	0.3584(3)	0.3537(5)
O1	z	0.2690	0.2349	0.2527	0.2697	0.2598	0.2741
O2	x	0.1656	0.1571	0.1760	0.1526	0.1693	0.1647
	y	0.4454	0.4469	0.4694	0.4486	0.4431	0.4452
O3	x	0.1337	0.1524	0.1429	0.1454	0.1429	0.1537
	y	0.4377	0.4374	0.4339	0.4356	0.4322	0.4354
O4	x	0.4046	0.4009	0.4016	0.3994	0.3988	0.3951
	y	0.2028	0.2067	0.2054	0.2076	0.2017	0.2082
	z	0.2550	0.2515	0.2522	0.2450	0.2473	0.2414
χ^2		0.438	0.265	0.023	0.034	0.229	0.109
R_p (%)		13.0	11.3	4.58	4.19	10.0	12.5
R_{wp} (%)		14.1	13.5	5.11	4.40	10.5	11.8

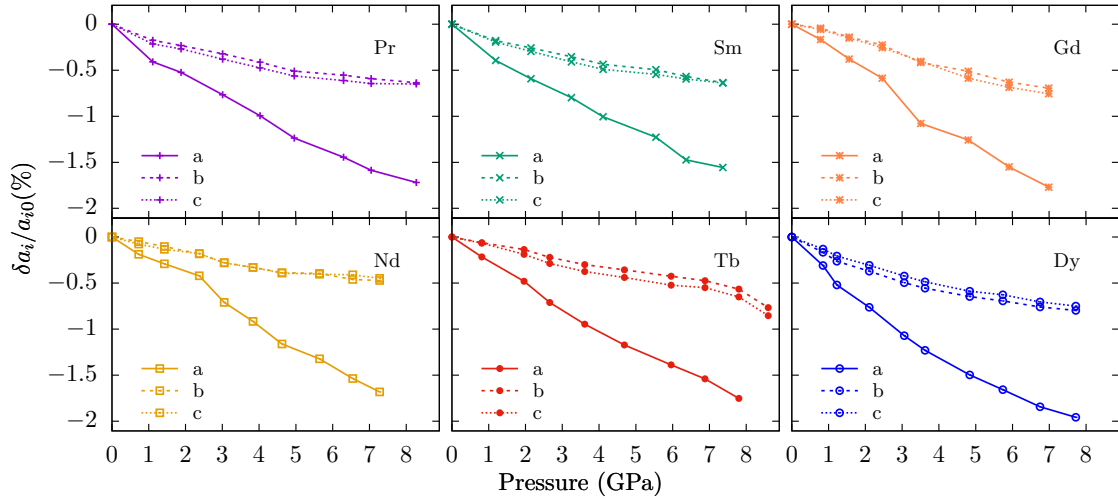


Figure 4.9 – Measured unit cell parameters ($(a_i - a_{i0})/a_{i0}$) of RMn_2O_5 with respect to their ambient pressure values. The error bars are of the size of the symbols. a_{i0} : unit cell parameters at ambient pressure. Note that for the sake of clarity in all the figures of the paper, the data related to a given R^{3+} compound are always represented with the same color.

The relative pressure evolution of the unit cell parameters with respect to their ambient pressure values is shown in Figure 4.9 for the various members of the RMn_2O_5 series measured. The computed values for the Dy and Gd compounds are displayed in Figure 4.10. The computed and experimental results agree very well for the Gd and the Dy at small pressure. The difference is a little larger for the Dy at high pressures. In both experimental and theoretical curves we can observe a strong anisotropy between the curve related to the lattice parameter a and the ones of b and c . The compressibility along the a direction at 9 GPa is twice the one along the b and c directions indicating that the structure is softer along the a direction. Such a behavior is observed for all the compounds measured as well as for the Y, Bi, and Ho compounds [129, 130]. It is interesting to notice that the a direction is the apical direction of the Mn^{3+}O_5 pyramids. The apical distortion of the pyramidal environment of the $\text{Mn}^{3+} 3d$ electrons could be electronically favorable. It is important to compare the lattice compressibility to the effect of temperature on the lattice presented in Ref. [59]. It is obvious that the effect of the external pressure on the structural properties is much stronger than the effect of temperature. This could explain the strong modifications of the multiferroic properties under pressure observed in PrMn_2O_5 [131].

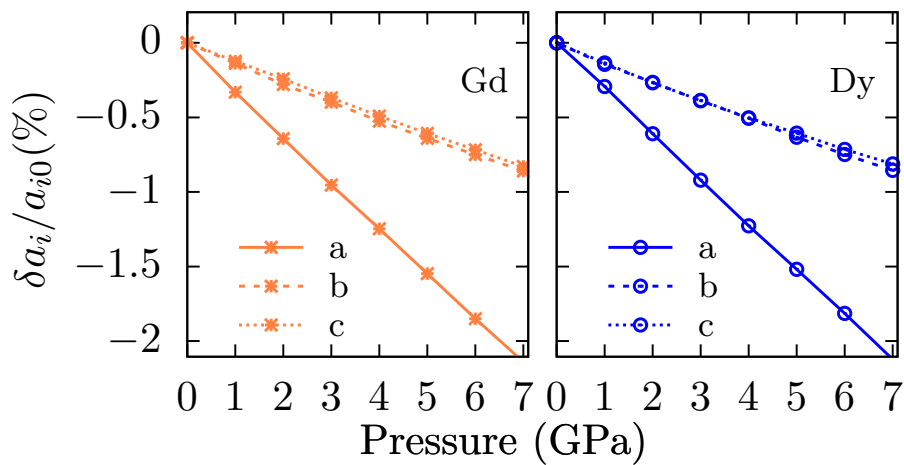


Figure 4.10 – Unit cell parameters ($(a_i - a_{i0})/a_{i0}$) of GdMn_2O_5 and DyMn_2O_5 with respect to their ambient pressure values calculated by DFT. a_{i0} : unit cell parameters at ambient pressure.

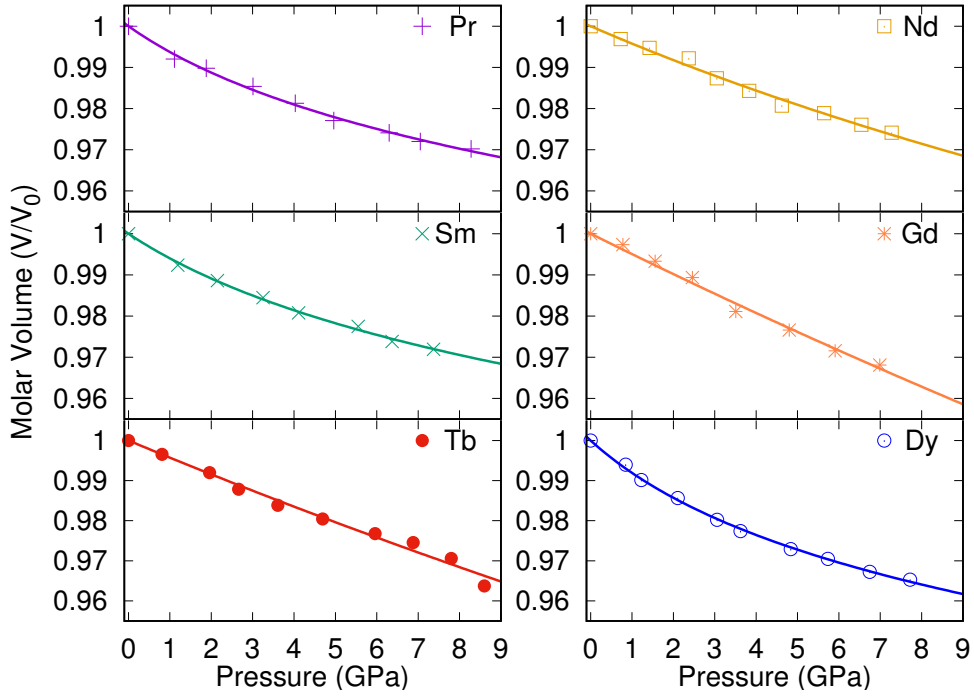


Figure 4.11 – Relative pressure dependence of the molar volume V/V_0 of the RMn₂O₅ with respect to their ambient pressure values. The solid lines show the fits using the EoS of Ref [132] with the Equation (4.1).

The relative evolution of the molecular volume as a function of the pressure is presented in Figure 4.11 for the various compounds. It has been fitted by the equation of state (EoS), shown in Equation (4.1) [132]. The fitted curves of RMn₂O₅ (R = Pr, Sm and Dy) present a similar behavior. As long as the pressure is high enough, all the members will present the similar curve. But the fit is nearly linear for RMn₂O₅ (R = Nd, Gd and Tb), which means that the pressure for RMn₂O₅ (R = Nd, Gd and Tb) is not high enough. The fitted parameters V^* , P^* , B_0 and B'_0 for the various members are listed in Table 4.4.

Table 4.4 – The Pressure – volume data fitted of RMn₂O₅ compounds.

R	V_0 (cm ³)	V^* (cm ³)	P^* (GPa)	B_0 (GPa)	B'_0
Pr	901.253	841.612	9.860	148.998	29.222
Nd	891.629	750.974	36.315	230.209	11.678
Sm	875.729	815.798	10.685	156.141	28.224
Gd	865.704	429.171	100.747	199.797	2.966
Tb	861.401	529.156	89.686	232.527	4.185
Dy	850.993	790.291	8.026	112.524	27.038

$$V - V^* = (V_0 - V^*) \frac{P^*}{P + P^*}, \quad \text{with}$$

$$B_0 = P^* \frac{V_0}{V_0 - V^*}$$

$$B'_0 = \frac{V_0 + V^*}{V_0 - V^*}$$
(4.1)

- V_0 : the volume at $P = 0$. It is temperature dependent.
- V^* : the hard-core volume independent of P and T .
- P^* : the characteristic pressure.
- B_0 : the zero-pressure bulk modulus.
- B'_0 : the pressure derivative of bulk modulus.

For the various compounds, the B_0 and the B'_0 are comparable to the HoMn_2O_5 ($B_0 = 138$ GPa, $B'_0 = 4$), BiMn_2O_5 ($B_0 = 173$ GPa, $B'_0 = 4$) [130], and YMn_2O_5 ($B_0 = 192$ GPa, $B'_0 = 3$) [129] compounds whose values have been published before our work..

4.5 Analysis and Discussion

From our refinements, we extracted the pressure evolution of the atomic positions of the R^{3+} , Mn^{3+} and Mn^{4+} heavy ions. Using the software Amplitudes of the Bilbao server [133, 134], we compared these atomic positions for a given pressure with their initial pressure (~ 1 GPa) value. We were only interested in the absolute value of the distance difference between the lowest pressure position of an atom and its position at a given pressure. Indeed, we have not performed a detailed mode analysis due to the lack of accuracy using this powder diffraction X-ray experiment. The atomic displacements $|u|$ obtained are represented in Figure 4.12 for the various compounds studied. For all the members excepted GdMn_2O_5 , the atomic displacements as a function of pressure are weak and nearly monotonous. In the case of GdMn_2O_5 , for which our refinements were of high quality and thus highly reliable, the atomic positions of Gd^{3+} and Mn^{3+} present a step-like anomaly between 3 and 4 GPa. It is worth noting that the pressure evolution of the unit cell parameter a also presents an anomaly between 3 and 4 GPa which induces a slight anomaly between 3 and 4 GPa in the V/V_0 curve as well. Interestingly, preliminary Raman measurements at 300 K have also evidenced a splitting of the mode at 230 cm^{-1} around 4 GPa.

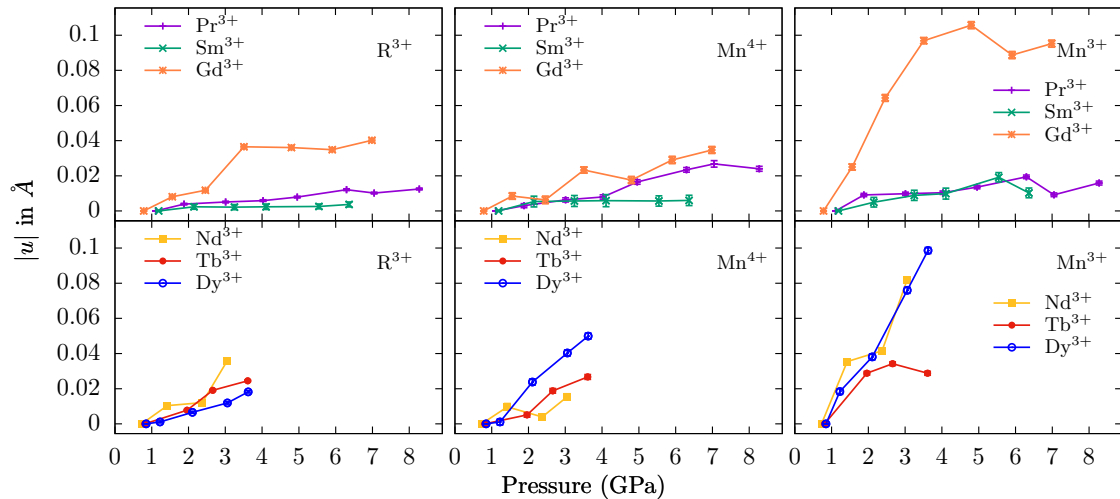


Figure 4.12 – Measured ionic displacements $|u|$ of the RMn_2O_5 ($\text{R} = \text{Pr}, \text{Sm}, \text{Gd}, \text{Nd}, \text{Tb}, \text{Dy}$) with respect to their initial pressure values, of R^{3+} (left), of Mn^{4+} (middle) and of Mn^{3+} (right). The error bars are within the width of the points.

Figure 4.10 presents the relative pressure evolution of the unit cell parameters deduced from our DFT calculations. We can observe for both compounds an excellent agreement between the pressure evolution of the unit cell parameters (see Figure 4.10). The unit cell parameters evolve similarly as a function of pressure and the strong anisotropy between a and the b, c axis observed experimentally is also clear from the DFT calculation. Furthermore, the numerical values of the compressibility ($\delta a_i/a_{i0}$)

are identical to the experimental ones. With increasing the pressure, even the position information of the Mn ions becomes unreliable. Thus in the Figure 4.13, we only present the calculated relative displacements (with respect to the initial pressure value) for the Gd^{3+} and Dy^{3+} . One sees immediately that they are close to the measured ones. However, in the case of GdMn_2O_5 , the calculated Gd^{3+} displacements do not present any anomaly between 3 and 4 GPa. One can thus relate the effect observed experimentally to a possible structure transition.

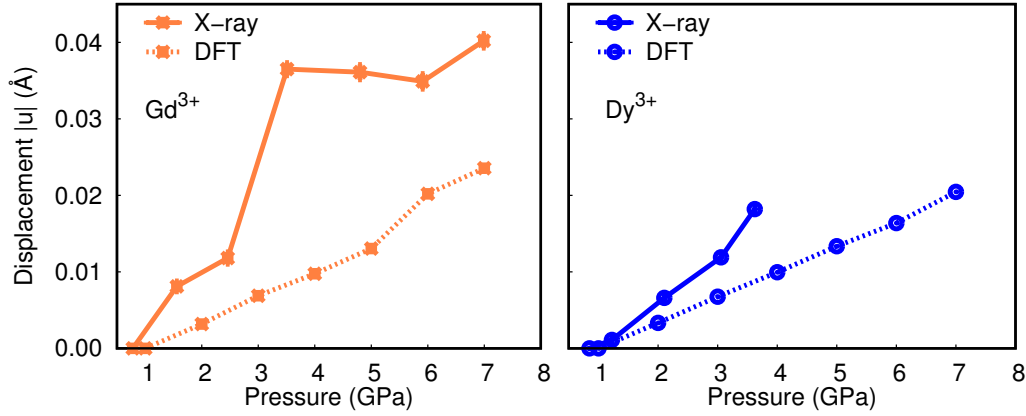


Figure 4.13 – Comparison of pressure evolution of the ionic displacements $|u|$ of Gd^{3+} and Dy^{3+} by X-ray experiments and DFT calculations, with respect to their initial pressure values.

The pressure evolution of the optimized structures calculated from DFT is in good agreement with the evolution of the experimental structures deduced from our X-ray measurements concerning the unit cell parameters as well as the atomic positions of the heavy atoms. The only reliable information for the positions of the light oxygen atoms comes from the DFT calculations. From this information as well as the position of the Mn ions, it is possible to infer information on the pressure evolution of the exchange interactions in the system. This information is essential to understand the multiferroic properties under pressure.

The analysis of the superexchange paths for the Mn^{4+} - Mn^{4+} magnetic interactions along the c direction yield similar results for J_1 and J_2 [54]. These two paths account for the following components to the J values:

$$\begin{aligned} J &= -4 \frac{\langle d_{xz}^A | \hat{h} | p_y^a \rangle^2 \langle p_y^a | \hat{h} | d_{yz}^B \rangle^2}{U(U + \delta_{pd})^2} - 4 \frac{\langle d_{yz}^A | \hat{h} | p_y^b \rangle^2 \langle p_y^b | \hat{h} | d_{xz}^B \rangle^2}{U(U + \delta_{pd})^2} \\ &= -4 \frac{t_{xzA,pya}^2 t_{yzB,pya}^2}{U(U + \delta_{pd})^2} - 4 \frac{t_{yzA,pyb}^2 t_{xzB,pyb}^2}{U(U + \delta_{pd})^2} \end{aligned}$$

- A, B : the two Mn sites while a and b for the two bridging O atoms.
- U : the on-site repulsion on the Mn t_{2g} orbitals.
- δ_{pd} : the orbital energy difference between the Mn t_{2g} and O $2p_y$ orbitals.

As can be seen from [54], the p to d hopping integrals only depend (exponentially) on the Mn-O distances and not on any angle. The Mn-O distances vary in a quasi-linear way as a function of pressure. It let us expect an associated quasi-linear increase in amplitude of the two J values by a few percent. As far as J_2 is concerned, this increase should not qualitatively modify the ferromagnetic ordering of the Mn^{4+} ions on each side of the Mn^{3+} ones. However the J_1 magnetic exchange is in competition with the Mn^{4+} - R^{3+} magnetic exchanges, that can be expected to be small. An increase of J_1 with respect to the interactions between the Mn^{4+} and the rare-earth ions could modify the propagation vector of the magnetic structure along the c axis. Indeed, an increase of J_1 favors an AFM ordering between neighboring Mn^{4+} ions and thus a $\frac{1}{2}$ component along the c axis. This could leads to the PCM

phase which has recently been discovered under pressure in the R=Y, Tb, Pr and Dy compounds [90, 131, 135].

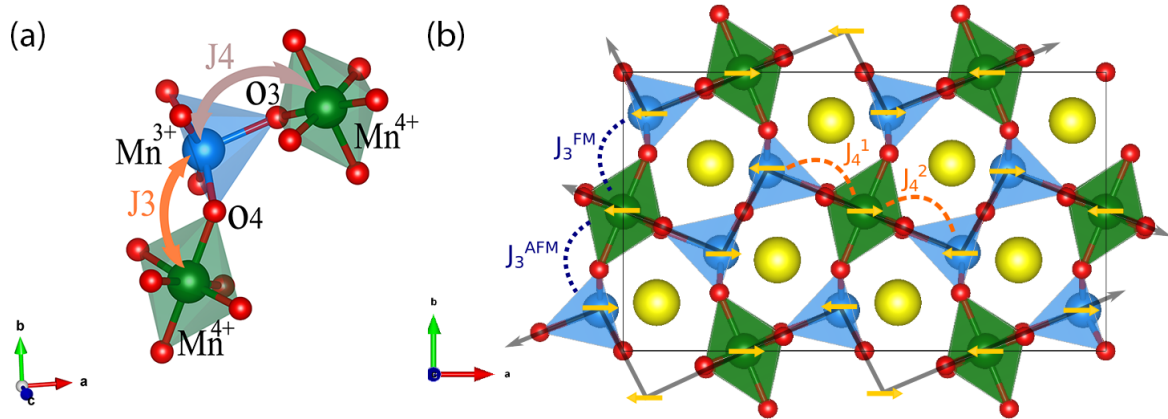


Figure 4.14 – (a) A magnified representation of Mn⁴⁺O₆ octahedra and Mn³⁺O₅ pyramid involved in the super-exchange J_3 and J_4 . (b) Structure of RMn₂O₅ in the (a, b) plane in Pm space group within CM magnetic phase ($q = (\frac{1}{2}, 0, 0)$). Inequivalent super-exchange interactions J_3 and J_4 are indicated.

As for the super-exchange J_3 and J_4 , a scheme of the Mn⁴⁺O₆ octahedra and Mn³⁺O₅ pyramid related to the super-exchange J_3 and J_4 is illustrated in Figure 4.14(a). It is the release of the frustration over J_3 (that couples the AFM chains running along the a axis) that is responsible for the polarization inset [57, 58]. There are two different exchange interactions J_3 , as shown in Figure 4.14(b), one involved in a FM ordered pair of Mn spins and one in an AFM ordered pair. The two different J_3 couplings are non symmetry equivalent in the Pm space group. Let us recall that the effective exchange integrals are the sum of the direct exchange (J_d , FM), the through space or direct superexchange (J_{sd} , AFM) and the through-bridge superexchange ($J_{3, sb}$) mediated by the ligands (AFM). Unless symmetry forbidden, the latter term is usually the dominant one. Its structural dependence is exponentially decreasing as a function of the Mn⁴⁺–O4 and Mn³⁺–O4 distances and varies as a function of $\cos^2 \alpha$ where α is the Mn⁴⁺–O4–Mn³⁺ angle [54]. Figure 4.15 displays the variation of the two Mn–O distances (a) and the cosine (b) as a function of applied pressure, for the two J_3 interactions (involved in a FM or AFM ordering of the spins). As expected [57], one sees immediately the Mn⁴⁺–O4 distance contraction, and the Mn⁴⁺–O4–Mn³⁺ angle increment, between atoms involved in the AFM ordering compared to the ones involved in the FM one. These structural differences are releasing the J_3 frustration and are responsible for the inset of the polarization. Surprisingly the Mn³⁺–O4 are affected neither by the spin arrangement, nor by the nature of the rare-earth (all four curves are on top of each other). The quasi-linear variations of both the distances and angle cosine as a function the applied pressure clearly indicates an overall increase of the J_3 values of a few percent. However, as no significant evolution of the difference between the two J_3 can be witnessed from these data, one can safely infer that the amplitude of the polarization should not be affected by the pressure within the dominant CM phase ($q = (\frac{1}{2}, 0, 0)$), which has been evidenced by the high pressure measurements of DyMn₂O₅ (below ~ 10 K, the amplitude of the electric polarization nearly unchanged under pressure [87] with only CM phase [135]). As for the super-exchange interactions J_3 , it is much more complex. Both J_3 (FM) and J_3 (AFM) should take into consideration. The pressure-induced enhancement of the polarization in certain temperature range is more likely related to the appearance of the pressure-induced commensurate magnetic (PCM) phase, as proposed in Ref. [90].

The J_4 interactions are a bit more complicated. First, there are two inequivalent J_4 interaction in the Pm space group related to two Mn⁴⁺–O3–Mn³⁺ angles (α_1 and α_2), as shown in Figure 4.14(b). In addition, there are two superexchange paths that add up, the first one scales as $\sin^2 \alpha$ and the second one as $\cos^2 \alpha$. The factors in front of the sine and cosine terms depend on the exact values of the ligand field splitting between the d_{xz} and d_{z^2} orbitals of the pyramids (z being the local apical axis). It is thus quite difficult to estimate the effect of the Mn–O–Mn angle variation. We will here only consider the angle contribution of J_4 to evolve under pressure as $\sin \alpha$. Nevertheless, J_4 still scales as a

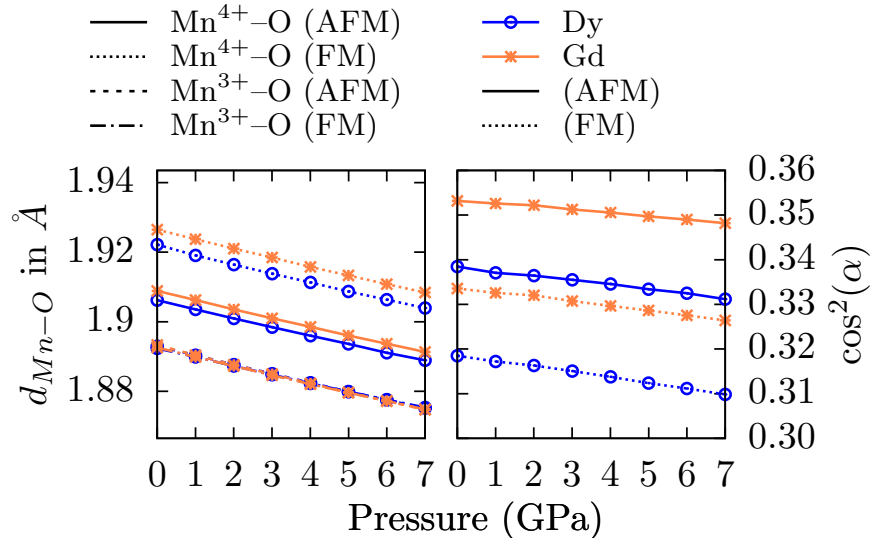


Figure 4.15 – Variation of the structural parameters involved in the J_3 amplitudes as a function of the applied pressure. The circles are for the DyMn_2O_5 compound and the crosses for the GdMn_2O_5 one. left) $\text{Mn}^{4+}\text{-O4}$ and $\text{Mn}^{3+}\text{-O4}$ distances (Å), right) $\cos^2 \alpha$, α being the $\text{Mn}^{4+}\text{-O4-Mn}^{3+}$ angle. (AFM) refers to the geometrical parameters between the atoms involved in AFM ordered $\text{Mn}^{4+}\text{-Mn}^{3+}$ ions, while (FM) refers to the parameters between the FM ordered ones.

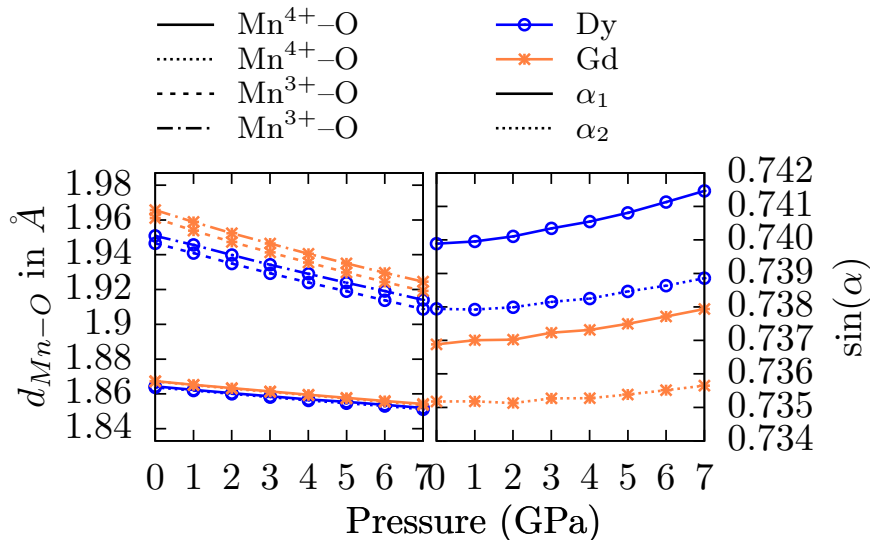


Figure 4.16 – Variation of the structural parameters involved in the J_4 amplitudes as a function of the applied pressure. The circles are for the DyMn_2O_5 compound and the crosses for the GdMn_2O_5 one. left) $\text{Mn}^{4+}\text{-O3}$ and $\text{Mn}^{3+}\text{-O3}$ distances (Å), right) $\sin \alpha$, α_1 and α_2 being the two inequivalent $\text{Mn}^{4+}\text{-O3-Mn}^{3+}$ angles.

decreasing exponential with the Mn-O distances. These parameters are displayed in Figure 4.16 as a function of the pressure. Unlike the equatorial bond of the Mn^{3+}O_5 pyramid involved in J_3 , the apical bond involved in the J_4 interaction strongly varies with the pressure. Indeed, there is about 0.04 Å of difference between its value at ambient pressure and at 7 GPa. On the contrary the $\text{Mn}^{4+}-\text{O}_3-\text{Mn}^{3+}$ angles display little distortion under pressure, despite the fact that they are along the most contracted direction (a axis). One can thus expect a relative increase of J_4 compared to the J_3 parameters when the pressure is applied, and thus an increase of the 1D character of the magnetic interactions.

It is important to notice that the increase of J_4 induces a stronger exchange coupling between the Mn^{4+} and Mn^{3+} ions. It can be the origin of the transition observed in PrMn_2O_5 under pressure [131]. This transition stabilizes a multiferroic state with a PCM phase above 2 GPa while at low pressure the state is non ferroelectric and with a decoupling between the magnetic orders of the two Mn sublattices. Finally, we still do not understand clearly the difference between Gd and Dy observed experimentally. The analysis of this part is under progress.

Summary of this Chapter

In this Chapter, we have shown that our refinements present a good agreement with the DFT calculations. We have shown that the effect of an external pressure up to 9 GPa on the structural properties is more obvious than the thermal contraction from 300 K to 10 K. The evolution of the unit cell parameters under pressure is strongly anisotropic with a softer direction along the a direction. It is the direction of the dominant magnetic interactions, resulting in a magnetic structure that can be described by weakly coupled AFM chains running along the a axis. The refinement of our X-ray diffractograms gave indications on the positions of the heavy ions (R^{3+} , Mn^{3+} and Mn^{4+}). We have thus detected a possible structural transition at 3 GPa in GdMn_2O_5 . Thanks to the DFT calculation, we are able to obtain the positions of the oxygen atoms. Through the atomic information of O and Mn ions, we are able to extract information concerning the evolution of the super-exchange interactions J_1 and J_4 as a function of pressure and thus to explain the strong modification of multiferroic properties observed under pressure in this series of compounds. Through the DFT calculations, we are able to obtain the missing information from our experimental investigation namely the positions of the oxygen atoms as a function of the pressure. From the O and Mn positions, we can extract information concerning the evolution of the exchange interactions J_i as a function of pressure. From this analysis we were able to conclude that within the dominant CM ($q = (\frac{1}{2}, 0, 0)$) phase, the polarization should be only weakly affected by the applied pressure. The 1D AFM character of the magnetic structure should be reinforced. As for the PCM phase, under pressure, the increase of super-exchange interactions J_1 , J_2 and J_4 can be expected. The super-exchange interactions J_3 is much more complex. Further investigations of the pressure evolution of the structure at low temperature is in progress. The study of the structural properties on single crystals would also be very interesting to detect weaker effects such as those related to the symmetry breaking from the $Pbam$ space group to the Pm one [52].

5

Powder Neutron Diffraction of RMn_2O_5 under Pressure

Contents

5.1	Introduction	82
5.2	Information Concerning the Magnetic Structures Determined in This Chapter:	83
5.3	Study of PrMn_2O_5 under Pressure	85
5.3.1	Introduction: Magnetic Structure at Ambient Pressure	85
5.3.2	Dielectric Properties under Pressure	86
5.3.3	Powder Neutron Diffraction (PND) Experiment under Pressure	86
5.3.4	Analysis of the PND under Pressure	87
5.3.5	Discussion	90
5.4	Study of DyMn_2O_5 under Pressure	92
5.4.1	Introduction: Magnetic Structure at Ambient Pressure	92
5.4.2	PND Experiment under Pressure	93
5.4.3	Analysis of the PND under Pressure	93
5.4.4	Discussion	97
5.5	Study of GdMn_2O_5 under Pressure	99
5.5.1	Introduction	99
5.5.2	PND Experiment under Pressure	100
5.5.3	Analysis of the PND under Pressure	100
5.5.4	Discussion	104
5.6	Study of SmMn_2O_5 under Pressure	105
5.6.1	Introduction: Magnetic Structure at Ambient Pressure	105
5.6.2	PND Experiment under Pressure	105
5.6.3	Analysis of the PND under Pressure	105
5.6.4	Discussion	109

This chapter presents powder neutron diffraction experiments of RMn_2O_5 ($\text{R} = \text{Pr}, \text{Dy}, \text{Gd}$ and Sm) under pressure. Although all these compounds show the similar PCM phase under high pressure, each one has its specific behavior. The properties of PrMn_2O_5 under pressure are given in Section 5.3. The collinear Mn spins with nearly nil spins of Pr^{3+} associated with hints of ferroelectricity makes it exceptional. In the Section 5.4, together with the properties of DyMn_2O_5 , we propose one realistic

model to explain the pressure dependence of the \mathbf{k}_z component of the propagation wave vector of the magnetic phase. The case of GdMn_2O_5 is similar to the one of DyMn_2O_5 , but with even a stronger $3d - 4f$ coupling, presented in Section 5.5. The study of the SmMn_2O_5 having spins along the c axis is presented in Section 5.6.

5.1 Introduction

As already mentioned in Section 2.5.2, the external pressure may have a similar effect as the chemical pressure, known to greatly influence the multiferroic properties of RMn_2O_5 .

For the case of YMn_2O_5 , at ambient pressure, \mathbf{P} strongly depends on the temperature. Below ~ 20 K, \mathbf{P} changes from $100 \text{ nC}\cdot\text{cm}^{-2}$ in the CM phase to $-20 \text{ nC}\cdot\text{cm}^{-2}$ in the LT-ICM phase. Under an external pressure of $\sim 1.7 \text{ GPa}$ (17 kbar) at low temperature, \mathbf{P} increases to reach $150 \text{ nC}\cdot\text{cm}^{-2}$, as shown in Figure 5.1(a). [66].

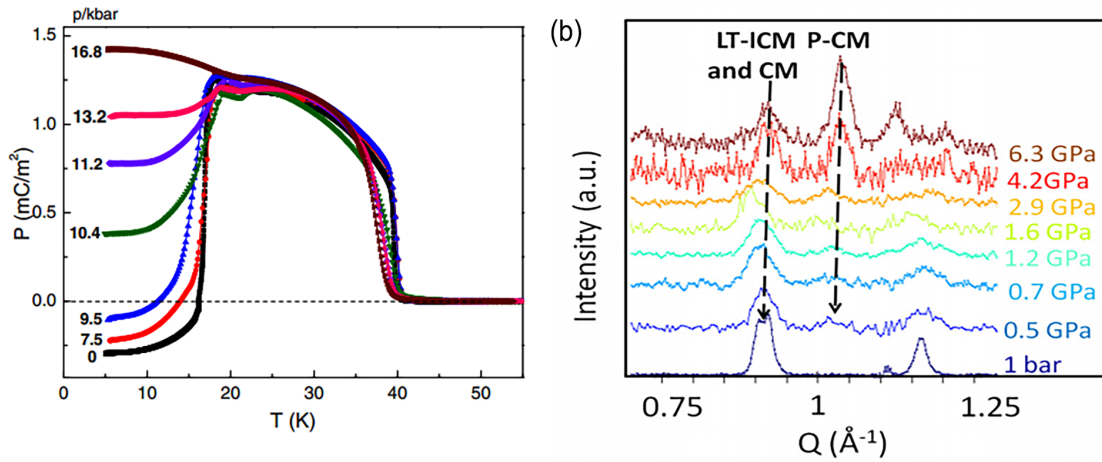


Figure 5.1 – Pressure evolution of (a) temperature dependence of the ferroelectric polarization [66] and (b) the magnetic patterns at 1.5 K subtracted from the 40 K diffraction pattern of YMn_2O_5 [90].

A recent powder neutron diffraction experiment has attributed the enhancement of the electric polarization in YMn_2O_5 [129] to a new pressure induced magnetic phase [90]. The phase transitions of YMn_2O_5 at ambient pressure presented in Figure 2.11, show that below $T_C \sim 38$ K, a CM order appears with $\mathbf{q}_1 = (\frac{1}{2}, 0, \frac{1}{4})$. By further cooling below ~ 20 K, a LT-ICM phase with propagation wave vector $\mathbf{q}_2 = (0.48, 0, 0.29)$ [90] coexists with the CM phase. A pressure commensurate magnetic phase (PCM), associated with the propagation wave vector $\mathbf{q}_{\text{PCM}} = (\frac{1}{2}, 0, \frac{1}{2})$, emerges under pressure. It becomes more intense at the expense of the ambient pressure magnetic phases, as illustrated in Figure 5.1(b).

By applying the Equation (2.1), the net electric polarization of YMn_2O_5 can be expressed as:

$$\mathbf{P} = 4C\alpha\mathbf{S}_3 \cdot \mathbf{S}_4 \quad (5.1)$$

- C : the magnetoelastic coupling constant.
- \mathbf{S}_3 and \mathbf{S}_4 : the magnetic moments of Mn^{3+} and Mn^{4+} , respectively.
- α : constant coefficient, $\alpha \approx -0.2, 0.9, 0.7$ for CM, LT-ICM and PCM phase, respectively.

The phase diagram is very complicated. As shown in Figure 5.1(b), although the PCM phase becomes gradually dominant with increasing pressure, the CM and LT-ICM phases still coexist in a large proportion with the PCM phase up to 6.3 GPa, which makes it hard to determine the exact magnetic structure of the PCM phase.

Furthermore, preliminary measurements on TbMn_2O_5 also indicate the appearance of the PCM phase under pressure, as illustrated in Figure 5.2.

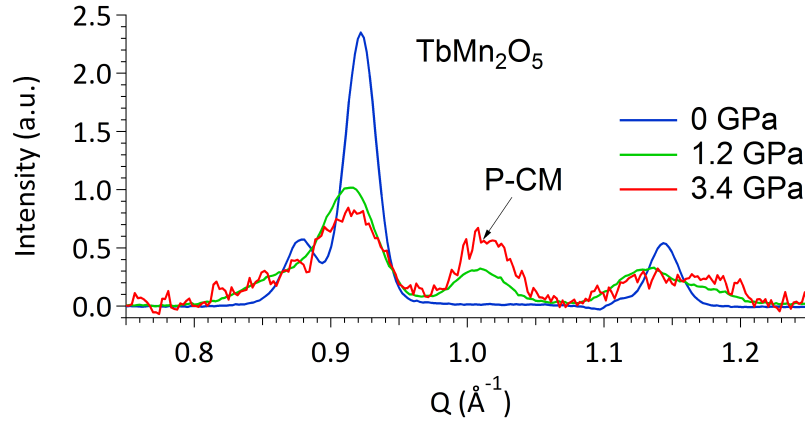


Figure 5.2 – Magnetic patterns of TbMn_2O_5 at 1.5 K. The magnetic peak $\sim 1 \text{ \AA}^{-1}$ indicates the onset of the pressure-induced commensurate (PCM) phase. [90]

5.2 Information Concerning the Magnetic Structures Determined in This Chapter:

It is important to mention that in the following, we will describe several magnetic structures that we have obtained from various refinements using Fullprof Suite [107]. Through the *BasIreps*, we can obtain some indications about the possible constrains for the refined moments coming from symmetry analysis. For the RMn_2O_5 , the real space group is Pm [52], which slightly differs from the average structure with the $Pbam$ space group. With the propagation wave vector $(\frac{1}{2}, 0, \frac{1}{2})$, we ran the *BasIreps* in Pm space group (actually input space group is $P11m$). Here we only show some selected results of Pr^{3+} from the example of PrMn_2O_5 . In Figure 5.4, we show the two irreducible representations. The direction of the Pr^{3+} moments is either along c or in the (a, b) plane. And the corresponding Real(0)-Imaginary(1) indicator for the Fourier coefficients C_i of the basic functions are shown in Figure 5.4.

Notice that the *BasIreps* notation for these irreducible representations is Γ_1 and Γ_2 . From Bilbao server [136] and general group theory, we can obtain the same two irreducible representations with $\mathbf{q}_{\text{PCM}} = (\frac{1}{2}, 0, \frac{1}{2})$ in Pm space group. They have been labeled as D_1 and D_2 ¹.

- D_1 (Γ_1 for *BasIreps* analysis): the magnetic moments of R^{3+} are compelled to be along the c axis, while the magnetic moments of Mn^{3+} are in the (a, b) plane. No constraints on Mn^{4+} moments' orientations.
- D_2 (Γ_2 for *BasIreps* analysis): the magnetic moments of R^{3+} are compelled in the (a, b) plane, while the magnetic moments of Mn^{3+} should be along the c axis. No constraints on Mn^{4+} moments' orientations.

Through the symmetry analysis of *BasIreps*, with the basic functions, we can obtain the PCM magnetic structure by refining coefficients (C_i) of the linear combinations of the basis functions. However, as for our case, usually the amplitude of the moments is nearly known but their direction have to be determined. It is not convenient to perform the refinement by the basic functions of the

¹The transformation to the standard setting is:

$$\begin{pmatrix} 0 & 1 & 0 \\ 0 & 0 & 1 \\ 1 & 0 & 0 \end{pmatrix} \begin{pmatrix} c \\ a \\ b \end{pmatrix} = \begin{pmatrix} a \\ b \\ c \end{pmatrix}$$

The propagation vector $\mathbf{q}_{\text{PCM}} = (\frac{1}{2}, 0, \frac{1}{2})$ in the standard setting transforms to $(0, \frac{1}{2}, \frac{1}{2})$, which refers to the D point of the Brillouin zone. Note that the setting chosen for the structure of the RMn_2O_5 compounds is not the standard one.

```

=> Atomic components of the BASIS FUNCTIONS using PROJECTION OPERATORS:
      Calculation for SITE number: 1
      (Only non-null functions are written)

*****
=> Basis functions of Representation IRrep( 1) of dimension 1 contained 1 times in GAMMA
*****

      SYMM x,y,z
      Atoms: Pr_1
BsU( 1, 1: 1):Re ( 0 0 1)

----- The Fourier coefficients are LINEAR COMBINATIONS of Basis Functions: coefficients u,v,w,p,q ....(may be complex!)
      The general expressions of the Fourier coefficients Sk(j) of the atoms non-related
      by lattice translations are the following:

      SYMM x,y,z                               Atom: Pr_1      0.1500 0.1000 0.0000
      Sk(1): (0,0,u)

*****
=> Basis functions of Representation IRrep( 2) of dimension 1 contained 2 times in GAMMA
*****

      SYMM x,y,z
      Atoms: Pr_1
BsU( 1, 1: 1):Re ( 1 0 0)
BsU( 2, 1: 1):Re ( 0 1 0)

----- The Fourier coefficients are LINEAR COMBINATIONS of Basis Functions: coefficients u,v,w,p,q ....(may be complex!)
      The general expressions of the Fourier coefficients Sk(j) of the atoms non-related
      by lattice translations are the following:

      SYMM x,y,z                               Atom: Pr_1      0.1500 0.1000 0.0000
      Sk(1): (u,v,0)

```

Figure 5.3 – Selected information of Pr^{3+} from the output BSR file of *BasIreps*.

```

=> Basis functions of Representation IRrep( 1) of dimension 1 contained 1 times in GAMMA
      Representation number : 1 for Site: 1
      Number of basis functions: 1

----- Block-of-lines for PCR start just below this line
P -1 <--Space group symbol for hkl generation
? Nsym Cen Laue Ireps N_Bas
  1 1 1 -1 1
? Real(0)-Imaginary(1) indicator for Ci
  0
SYMM x,y,z
BASR 0 0 1
BASI 0 0 0
----- End-of-block of lines for PCR

=> Basis functions of Representation IRrep( 2) of dimension 1 contained 2 times in GAMMA
      Representation number : 2 for Site: 1
      Number of basis functions: 2

----- Block-of-lines for PCR start just below this line
P -1 <--Space group symbol for hkl generation
? Nsym Cen Laue Ireps N_Bas
  1 1 1 -1 2
? Real(0)-Imaginary(1) indicator for Ci
  0 0
SYMM x,y,z
BASR 1 0 0 0 1 0
BASI 0 0 0 0 0 0
----- End-of-block of lines for PCR

```

Figure 5.4 – Selected basic function information of Pr^{3+} from the output FP file *BasIreps*.

irreducible representations. Thus most of the refinements have been performed using the spherical mode for the moments. Using these modes, the relevant parameters for the magnetic moments are the amplitude M , azimuthal angle ϕ and the polar angle θ . This mode is helpful to determine the direction of the moments.

However, for both D_1 and D_2 , the spins of Mn^{3+} and R^{3+} are perpendicular to each other, and one of them is along the c axis. Such spin arrangements are difficult to justify from a physical point of view for some RMn_2O_5 compounds, considering that:

- (1) : for some RMn_2O_5 compounds with high spin R^{3+} , the dominant R^{3+} - Mn^{3+} ($3d$ - $4f$) exchange interaction is J_6 , and the corresponding energy term is minimized by collinear configurations between the spins of R^{3+} and Mn^{3+} .
- (2) : for most RMn_2O_5 compounds, the magnetic easy axis of the R^{3+} ion (see Section 2.5.1) lies in the (a, b) plane.
- (3) : for most RMn_2O_5 compounds, the spins of Mn ions also lie in or close to the (a, b) plane, no matter R is magnetic or not.

Thus, we considered a third model with a further symmetry lowering to the lowest symmetry $P1$, which corresponds to the disappearance of the mirror m . This consideration unlocks the constraint on the spins of R^{3+} and Mn^{3+} to be perpendicular, and makes it possible to refine the spins of R^{3+} and Mn^{3+} in the (a, b) plane. In this model the spins of Mn^{4+} are also in the (a, b) plane as in the ambient pressure ICM or CM phases. This model is called "*planar*" in the following.

The symmetry analysis presented in the different subsections of this chapter are general symmetry considerations using standard notations of group theory.

5.3 Study of PrMn_2O_5 under Pressure

The PrMn_2O_5 compound is very special in the RMn_2O_5 family. It is non-ferroelectric and has no ICM phase in the whole temperature range at ambient pressure. In addition, there are two CM magnetic phases evolved two subsystem of Mn^{3+} and Mn^{4+} spins. It is thus important to study this compound under pressure as one can expect to mimic the effect of chemical pressure and induced ferroelectricity.

5.3.1 Introduction: Magnetic Structure at Ambient Pressure

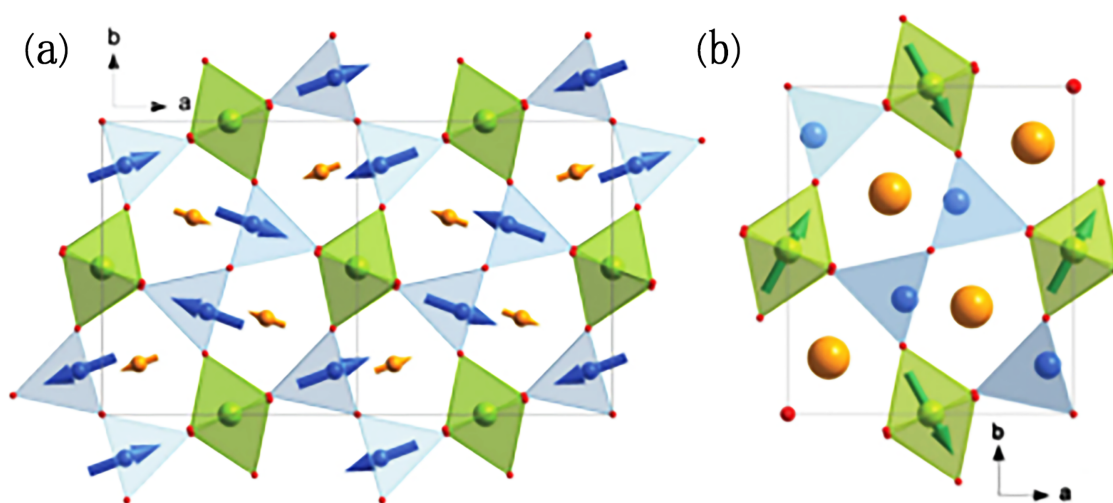


Figure 5.5 – The magnetic ordering in the (a, b) plane of PrMn_2O_5 : (a) the CM1 phase at 20 K; (b) the CM2 phase at 1.5 K. [59]

On cooling, a CM1 phase appears below $T_1 \sim 25$ K, the corresponding magnetic structure is shown in Figure 5.5(a). The propagation wave vector is $\mathbf{q}_{\text{CM3}} = (\frac{1}{2}, 0, 0)$. The magnetic moment of Mn^{4+} of the CM3 phase is zero [59], which indicates the total decoupling between the Mn^{3+} and Mn^{4+} spins. This total decoupling between the two Mn ions is also observed in EuMn_2O_5 [80]. In addition, a small ordered magnetic moment is needed on the Pr^{3+} ions to improve the refinement. The moment of Pr^{3+} lies in the (a, b) plane. A CM2 phase appears when the temperature decreases below $T_2 \sim 18$ K. It is associated to the Mn^{4+} ordering with $\mathbf{q}_{\text{CM2}} = (0, 0, \frac{1}{2})$. The magnetic structure of the CM2 phase is presented in Figure 5.5(b). At low temperature, both phases coexist. Note that the direction of the magnetic moment of Pr^{3+} has a small component along the c axis at low temperature.

5.3.2 Dielectric Properties under Pressure

The dielectric constant ϵ_b measured under various pressures from 0 to 1.46 GPa as a function of temperature on a small single crystal, as shown in Figure 5.6(a). The thermal variation of $\epsilon_b(T)$ at ambient pressure is similar to the one published in Ref. [51, 59]. Besides the peak at ~ 18 K, there is another broad peak at ~ 10 K. These two peaks in the $\epsilon_b(T)$ curve recall the one observed in TbMn_2O_5 and attributed to the ferroelectric transition and the electromagnons, respectively [51]. These effects can be the indication of a ferroelectric-like behavior in PrMn_2O_5 , associated with an electric polarization too small to be detected. With increasing pressure, these two peaks merge into a broad one located at 15 K. The amplitude of this peak first increases to reach a maximum at 0.5 GPa. Continuing to increase the pressure, the amplitude of ϵ_b decreases. This phenomenon is much more obvious in the corresponding pressure evolution of the temperature dependence of the dielectric loss, illustrated in Figure 5.6(b). It is interpreted as a hint for pressure induced multiferroicity. Electric polarization \mathbf{P} measurements under pressure have been attempted. However, no obvious signal has been detected even at the highest pressures (1.46 GPa) [131].

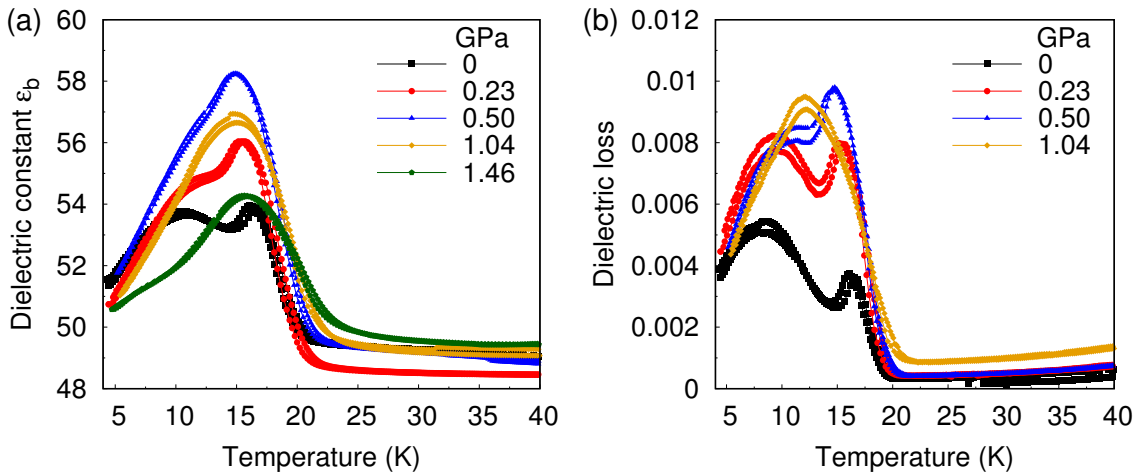


Figure 5.6 – (a) Dielectric constant ϵ_b measurement and (b) dielectric loss measurement of PrMn_2O_5 single crystal as a function of temperature under various pressures (warming and cooling)

5.3.3 Powder Neutron Diffraction (PND) Experiment under Pressure

The PND has been performed on the D1B diffractometer (CRG, CNRS ILL-Grenoble, France) with the wavelength of 2.52 Å. The measurements have been carried out by heating up from 6 to 70 K at 3, 5, 7 and 8 GPa. The refinements of the nuclear and magnetic structures have been performed using the FULLPROF program [107].

All the nuclear structures were refined above the Néel temperature ~ 60 K. The ambient pressure diffractogram was refined by applying the model of Ref. [59].

5.3.4 Analysis of the PND under Pressure

Already at 3 GPa, just below T_1 , ~ 25 K, the PND pattern shows obvious new magnetic reflections (shown in Figure 5.7(a) indicated by solid circles) besides the reflections observed at ambient pressure ($\mathbf{q}_{CM3} = (\frac{1}{2}, 0, 0)$). These additional reflections are well indexed by the propagation wave vector $\mathbf{q}_{PCM} = (\frac{1}{2}, 0, \frac{1}{2})$, which is similar to the one observed under pressure in YMn₂O₅ [90]. By further cooling down below T_2 , no other additional reflections appear, which suggests that the lower CM2 phase smears out within the 0 to 3 GPa pressure range.

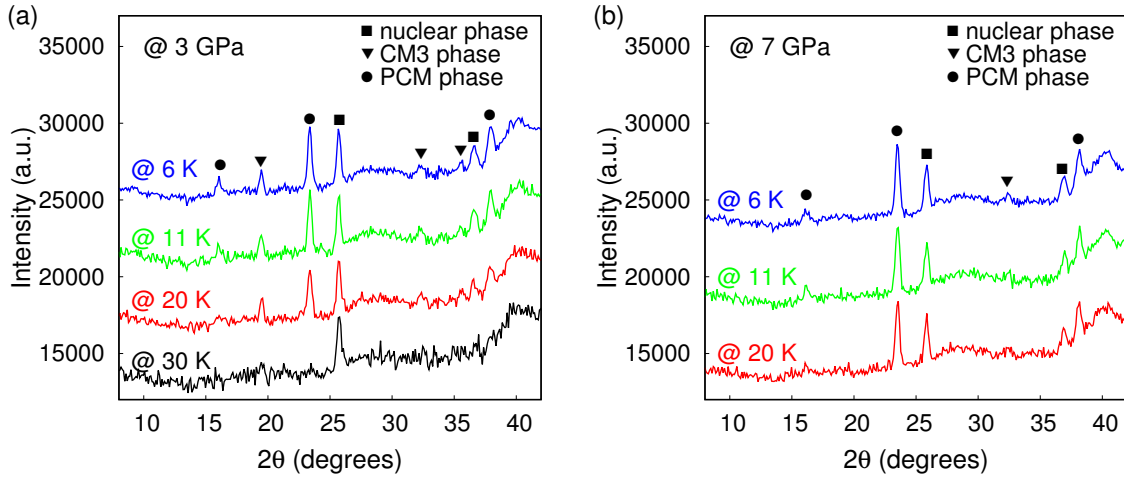


Figure 5.7 – PND diffractograms of PrMn₂O₅ (a) under 3 GPa, at 6 K, 11 K, 20 K and 30 K (b) under 7 GPa at 6 K, 11 K and 20 K.

As illustrated in Figure 5.8, at 5 GPa, the intensity of the $\mathbf{q}_{PCM} = (\frac{1}{2}, 0, \frac{1}{2})$ reflections increases at the expense of the intensity of the $\mathbf{q}_{CM3} = (\frac{1}{2}, 0, 0)$ reflections. The critical temperature of the PCM phase is $T_{PCM} = 30.5$ K. At 7 GPa, the PCM phase appears at $T_{PCM} = 37.5$ K and the CM1 phase has nearly disappeared from the diffractogram (shown in Figure 5.7(b) indicated by solid upside-down triangle). Finally, at the highest pressure, 8 GPa, the PCM phase exists alone without the persistence of another magnetic phase below $T_{PCM} = 43$ K.

As shown in Figure 5.8, at the lowest temperature, 6 K, the intensity of the reflections of the PCM phase increases rapidly with increasing the pressure. The corresponding pressure dependence of the ratio between the intensities of the PCM reflections over the CM3 ones is illustrated in Figure 5.9. It clearly exhibits a competition between both magnetic orders in the 0-8 GPa pressure range. At 8 GPa, the CM3 phase totally smears out, which makes it more convenient and reliable to refine the magnetic structure of the PCM phase.

The pressure-temperature phase diagram of PrMn₂O₅ is shown in Figure 5.10 constructed from the neutron diffraction under pressure. The pressure evolution of T_{CM2} is not accurate. The black dot line, separating the ambient pressure ground state to the PCM phase, is arbitrarily drawn just above 2 GPa. In this phase diagram, although we have no information about this, we assumed that $T_2(p)$ does not change. Finally, concerning the high pressure phase, although there is no solid evidence of the presence of the ferroelectricity, we indicate that the phase can be ferroelectric (marked as FE?), more details, see in Section 5.3.5.

The diffractogram of this new PCM phase has been analyzed at the lowest temperature and the highest pressure (6 K, 8 GPa) at which the PCM phase is totally developed and all the other magnetic phases have vanished. The magnetic structure of the PCM phase has been determined by Rietveld refinement [108], using symmetry considerations derived from representation analysis.

The real space group of RMn₂O₅ is Pm [52], the magnetic space group leaving the magnetic structure invariant is a subgroup of Pm : Pm or Pm' . But the magnetic space group commuting with the Hamiltonian of the system can only be Pm' , because the Pr³⁺ ions are located on the m plane, and their spin-orbit operator does not commute with the m operation.

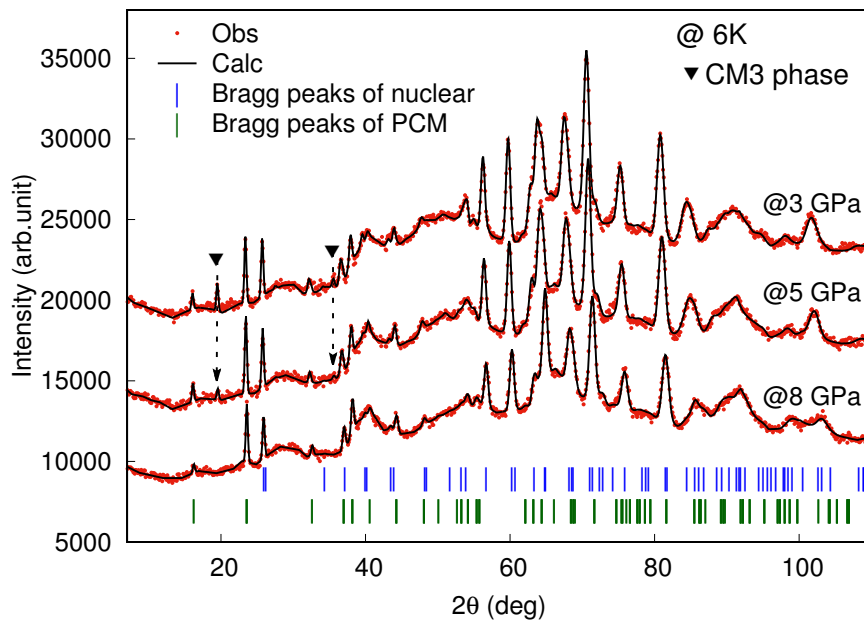


Figure 5.8 – Rietveld refinements of the neutron diffraction data of PrMn_2O_5 at the lowest temperature, 6 K, and under 3 GPa, 5 GPa and 8 GPa.

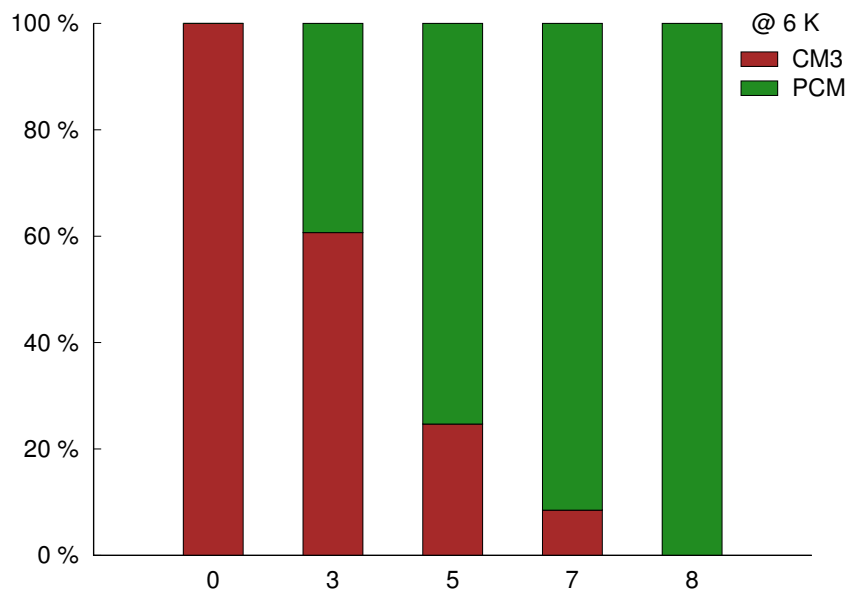


Figure 5.9 – Evolution as a function of pressure of the ratio between the ambient pressure CM3 and the pressure induced PCM phases in PrMn_2O_5 at 6 K.

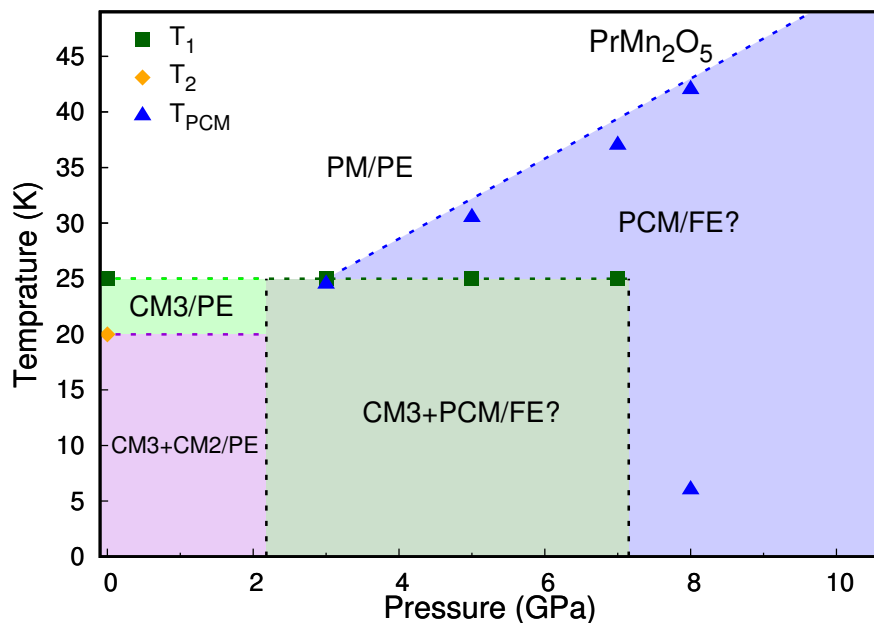


Figure 5.10 – Pressure-temperature phase diagram of PrMn_2O_5 . The lines are a guide to the eye.

As we have mentioned in Section 2.2.2, the Pr^{3+} ion is a non-Kramers ion. In a spin-orbit plus crystal field atomic model, the ground-state of the Pr^{3+} ion is in a non-degenerate one-dimensional co-representation of its spin-electronic structure. As a result, its magnetic moment is nil within this atomic scale picture. Thus non-zero Pr magnetic moments can only be attributed to the hybridization of the Pr 4*f* orbitals with the neighboring atoms. Therefore, the Pr^{3+} contribution was ignored in our initial model. We enforced pairing arising from the weakly broken symmetries of the *Pbam* space group to reduce the number of degrees of freedom ((*x*, *y*, *z*) with (*-x*, *-y*, *z*) and (*-x* + 1/2, *y* + 1/2, *-z*) with (*x* + 1/2, *-y* + 1/2, *-z*)). In addition, the identical ions were considered to have the same amplitude value of the magnetic moments.

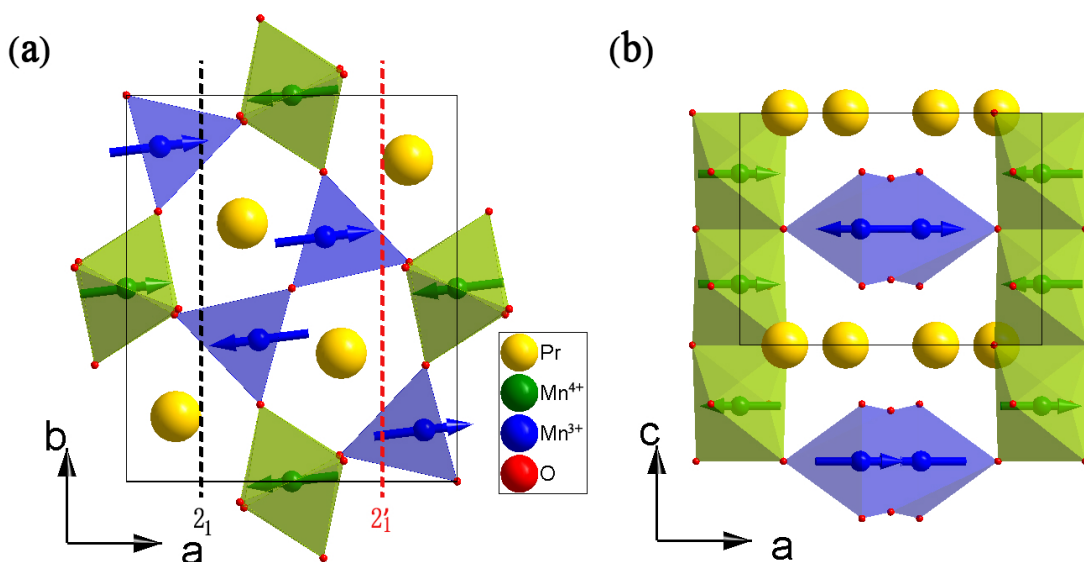


Figure 5.11 – Magnetic structure of PrMn_2O_5 at 6 K and 8 GPa (a) in the (*a*, *b*) plane with the 2_1 (*b*) and a $2'_1$ (*b'*) screw axis (glide plane) between Mn^{3+} and Mn^{4+} , and (b) in the (*a*, *c*) plane.

The amplitude and the orientation of the moments of Mn^{3+} , Mn^{4+} and Pr^{3+} have been refined. The refinement with the configuration of the D_2 representation turned out to be much better than

with the D_1 representation. The best refinement is obtained when all spins lie nearly along the a axis. Furthermore, the refined amplitude of Pr^{3+} moments is zero, which means that the D_2 model is equivalent to *plana* model. The magnetic structure is characterized by a FM arrangement along the c axis for the Mn^{4+} spins in the same unit cell, and an AFM arrangement between neighboring unit cells (see Figure 5.11). For Mn^{3+} , there is an AFM pairing concerning the spins at (x, y, z) and $(-x, -y, z)$ and a FM arrangement concerning the spins at $(-x + 1/2, y + 1/2, -z)$ and $(x + 1/2, -y + 1/2, -z)$. Note that the refinement is not improved when one introduces a partial order of the Pr^{3+} .

Table 5.1 – Refined results for the magnetic structure parameters of PrMn_2O_5 at 6 K and 8 GPa in the magnetic space group $Pmc'2'_1$ with $\chi^2 = 2.09$, $R_p = 33.5\%$, $R_{wp} = 20.3\%$, $R_{exp} = 14.1\%$, $R_{Bragg} = 9.1\%$ and $R_{mag} = 21.7\%$

Atom	x	y	z	$M(\mu_B)$	$\Phi(^{\circ})$	$\theta(^{\circ})$
Pr^{3+}	0.15	0.17	0	0	–	90
Mn^{3+}	0.39	0.36	0.5	2.8(2)	5.0(1)	90
Mn^{4+}	0	0.5	0.26(2)	2.6(4)	5.0(5)	90

The magnetic ordering at 8 GPa and 6 K is illustrated in Figure 5.11 and the accurate values of moments are given in Table 5.1. The moments of the Mn^{3+} and Mn^{4+} have a very similar amplitude and they are quasi-aligned along the a axis. If we consider that all the spins are strictly along the a axis, we have additional quasi-symmetries. Indeed, the Mn^{3+} and Mn^{4+} pairs are related either by a 2_1 (b) or a $2'_1$ (b') screw axis (glide plane), as shown in Figure 5.11(a). Thus, the symmetry operations leaving this magnetic structure invariant are the generators issued from the $Pbam$ crystallographic group $\{E, m, 2'_1, b', t'_a, t'_c\}$. These generators can be expressed as (BNS and OG setting):

$$\begin{aligned}
 &x, y, z, +1 \\
 &x, y, -z, +1 \\
 &-x + \frac{1}{2}, y + \frac{1}{2}, z, -1 \\
 &-x + 1, y + 1/2, z, -1
 \end{aligned}$$

This corresponds to the $Pmc'2'_1$ (No. 26.69) magnetic space group according to the Bilbao Crystallographic server [137, 138].

5.3.5 Discussion

The influence of the pressure on the magnetic structure of PrMn_2O_5 is very similar to the one previously observed in YMn_2O_5 [90] with the appearance of a new PCM phase with $\mathbf{q}_{\text{PCM}} = (\frac{1}{2}, 0, \frac{1}{2})$. The magnetic propagation wave vector associated with can be a universal feature of the RMn_2O_5 compounds under pressure. However, this new PCM phase is much better stabilized and intense in PrMn_2O_5 than in YMn_2O_5 . Firstly, at 3 GPa, the $(\frac{1}{2}, 0, \frac{1}{2})$ magnetic reflections exhibit an intensity which is the largest of the diffractogram. Secondly, the intensity of the CM3 phase decreases rapidly with increasing pressure and has completely extinguished at 8 GPa, while the CM phase still exists with a proportion of $\sim 70\%$ in YMn_2O_5 at this pressure [90]. Finally, the increase of T_{PCM} with pressure in the PrMn_2O_5 compound is the fingerprint of the exceptional stability of this PCM phase at high pressure. Therefore, PrMn_2O_5 is the outstanding model in understanding the high pressure magnetic structure.

It is important and essential to figure out the origin of the stabilization of the PCM phase under pressure. Let us first pay attention to the propagation wave vector and in particular its c^* component. As mentioned in Section 2.2.1, the order along the c axis is related to the interaction between Mn^{4+} , either through the Mn^{3+} (J_1) or through the R^{3+} layer (J_2), the ordering related to J_2 is always FM. For

non-magnetic R³⁺ such as La³⁺ [78] and Bi³⁺ [81], the only contribution to J_1 is the superexchange Mn⁴⁺ - O - Mn⁴⁺, which is AFM. The same scenario can be expected for non-Kramers R³⁺ ion, such as Pr³⁺, because the R³⁺ magnetic moment is considered to be close to nil at the atomic scale at least. So the term $J\mathbf{S}_{\text{Pr}} \cdot \mathbf{S}_{\text{Mn}}$ is small whatever the magnitude of J since $\mathbf{S}_{\text{Pr}} \ll 1$. At ambient pressure two quasi-degenerate ground states are stabilized: one concerns the Mn³⁺ ions (with a weak participation of the Pr³⁺ ions) and the other concerns the Mn⁴⁺ ions [59]. The two Mn subsystems are orthogonal to each other, thus there is no coupling between them. The unusual presence of two Mn subsystems in PrMn₂O₅ is certainly related to a weak J_4 interaction. J_4 is strongly affected by the Mn³⁺ - O3 - Mn⁴⁺ angle [54]. But, as shown in Figure 5.12 for neutron diffraction, and Figure 4.9 for X-ray diffraction of the Pr compound and as observed in Y, Bi, and Ho [129, 130], the a lattice parameter strongly decreases with increasing pressure. This lead to a increase in absolute value (as shown in Section 4.5). As a result, the coupling between the Mn⁴⁺ and Mn³⁺ subsystems increases and the energy of the PCM state decreases below the energy of the two ambient pressure lowest energy states.

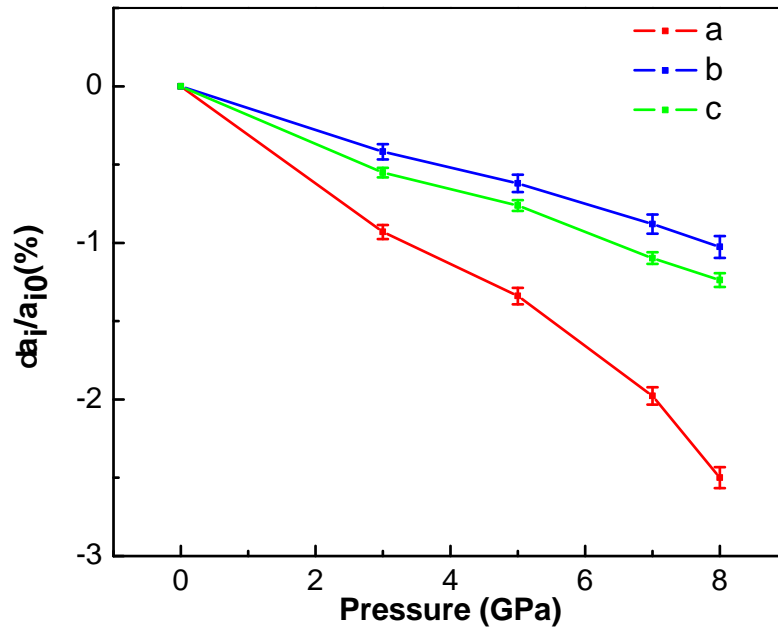


Figure 5.12 – Relative pressure dependence of the unit cell parameters $((a_i - a_{i0})/a_{i0})$ of PrMn₂O₅ with respect to their ambient pressure values at 6 K. a_{i0} is a unit cell parameter under ambient pressure at 6 K. Lattice parameters from the refinement of the PND data.

In the light of our recent result validating the exchange striction mechanism for the RMn₂O₅ series [44], the quasi-collinear spin alignment in the PCM phase of PrMn₂O₅ can explain the important modification observed on the dielectric properties. Indeed, in the exchange-striction model, the magnitude of the electric polarization is proportional to the scalar product of the spins related to J_3 . This explains why the total disconnection of the Mn³⁺ and Mn⁴⁺ arrangement of PrMn₂O₅ at low pressure leads to the absence of ferroelectricity. On the other hand, this mechanism also suggests that the collinear PCM phase including all the Mn moments of PrMn₂O₅ at 8 GPa should present an electric polarization as all spins are collinear and $J_{\text{Mn}^{3+}-\text{Mn}^{4+}} \neq 0$. Dielectric constant and electric polarization measurements are very difficult in the range of pressure we have investigated (2 GPa ~ 10 GPa) It is important to notice that the calculation of the electric polarization in the PCM phase is also very difficult requiring an accurate crystallographic structure refined in a non-centrosymmetric space group. Such an accuracy is not reachable using the powder neutron diffraction data we had and would require further measurements on single crystal under pressure.

The most remarkable feature of PrMn₂O₅ under pressure is that the Mn spins become collinear, which is expected to induce ferroelectricity according to the exchange striction model. This presages a

pressure induced multiferroic transition in the non-ferroelectric PrMn_2O_5 and paves the way to the conception of new multiferroic materials with tunable properties.

5.4 Study of DyMn_2O_5 under Pressure

DyMn_2O_5 has been recognized as "a golden touchstone" [139] in the RMn_2O_5 series due to its complex and intriguing ferroelectric properties. In addition, at ambient pressure, the magnetic structures of Mn^{3+} and Mn^{4+} appear to have a spiral ICM arrangement at 15 K. Furthermore, an additional exchange interaction J_6 has been proposed in this compound. The pressure dependence of the multiferroic properties in this compound is thus of great interest.

5.4.1 Introduction: Magnetic Structure at Ambient Pressure

Recently, our PND work on an isotope enriched powder of DyMn_2O_5 [56] has shown that above ~ 8 K, a HT-ICM phase stabilizes with the propagation wave vector $\mathbf{q}_{\text{ICM1}} = (\frac{1}{2}-\sigma_x, 0, \frac{1}{4}-\sigma_z)$ ($\delta_x \sim 0.01$, $\delta_z \sim 0.004$). As shown in Figure 5.13(a), all the Mn ions of the refined structure appear to have a spiral arrangement in the (a, b) plane, which is different from the previous report [70, 140]. Below ~ 8 K, a LT-CM with $\mathbf{q}_{\text{CM3}} = (\frac{1}{2}, 0, 0)$ coexists with the HT-ICM phase. The structures illustrated in Figure 5.13(b) are similar to the ones proposed by Blake *et al* [58]. With decreasing the temperature, the LT-CM phase gradually becomes dominant.

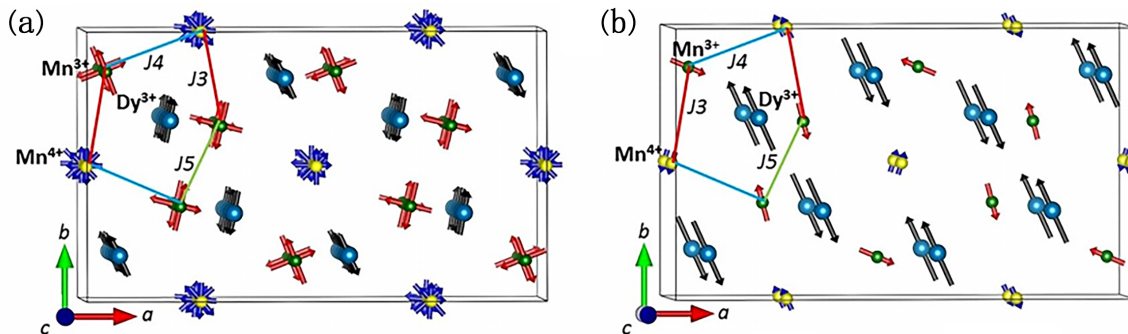


Figure 5.13 – Magnetic structure of (a) the HT phase at 15 K with the spiral arrangement of Mn ions; (b) the LT phase at 2 K. Magnetic interactions J_3 , J_4 and J_5 are also shown [56].

Generally, there are five super-exchange interactions among the RMn_2O_5 compounds, J_i ($i = 1, 2, 3, 4, 5$). However, for R^{3+} with a high magnetic moment, as for Dy^{3+} , it is essential to introduce another super-exchange interaction, J_6 . J_6 corresponds to the Heisenberg R-Mn ($3d-4f$) coupling, shown in Figure 5.14.

In the HT-ICM phase, the Mn^{3+} spins have a spiral arrangement with a rotation of 90° . The magnetic easy axis of Dy^{3+} is along the b axis and the amplitude of the spins of Dy^{3+} are modulated with an $\uparrow\downarrow\downarrow$ arrangement, which can minimize the Heisenberg energy through ES mechanism. For the spin of Mn^{3+} nearly along the a axis, the J_6 exchange term in the Hamiltonian is nil, because the spins of Dy^{3+} and Mn^{3+} are perpendicular. In the HT-ICM phase, it is the $J_1 - J_2$ exchange couplings which are dominant, and favor the spiral arrangement. Therefore, the HT-ICM phase exists when the term with J_6 is small. However, with decreasing the temperature, the amplitude of the spins of Dy^{3+} increases. The competition between the $J_1 - J_2$ and J_6 terms in the Hamiltonian becomes in favor of the J_6 exchange energy. Finally, in the LT-CM phase, the spiral arrangement of the Mn ions is destabilized towards a quasi-collinear spin structure where the spins of all Dy^{3+} , all Mn^{4+} and half of the Mn^{3+} align anti-parallel along the b axis. This spin arrangement satisfies the Dy anisotropy and the R-Mn exchange term J_6 over the $J_1 - J_2$ ones.

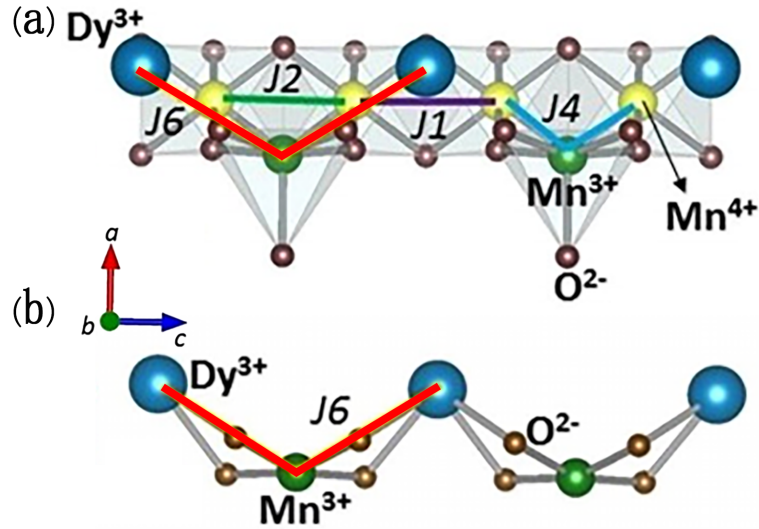


Figure 5.14 – (a) The dominant Mn-Mn exchange interactions in the (a, c) plane. It also shows Mn³⁺-Dy³⁺ interaction J_6 along c . (b) Detailed paths of interaction for J_6 [56].

5.4.2 PND Experiment under Pressure

In collaboration with M. Greenblatt (The State University of New Jersey, USA), we were able to use the isotope-enriched ¹⁶³Dy sample of DyMn₂O₅ to avoid the strong neutron absorption. The powder neutron diffraction (PND) experiments were performed on the high flux diffractometer D20 of the Institute Laue Langevin (ILL, Grenoble, France) with the wavelength of 2.42 Å. Measurements were carried out by heating up from 6 to 70 K at 2.4 and 6.6 GPa for several temperatures. Rietveld refinements [108] of the nuclear and magnetic structures were performed by using the FullProf Suite [107].

All the nuclear structures were refined above Néel temperature ~ 60 K. Under pressure, the PCM phase was indexed with the new propagation wave vector $\mathbf{q}_{\text{PCM}} = (\frac{1}{2}, 0, \frac{1}{2})$, identical to the one of PrMn₂O₅.

5.4.3 Analysis of the PND under Pressure

At 2.4 GPa, we have not evidenced any pressure induced magnetic phase in all the temperature range. The neutron diffractograms are similar to those at ambient pressure (shown in Figure 5.15). Thus we used the model at ambient pressure as the initial model to refine the magnetic structure. At 14 K, the diffractogram was well fitted by the HT-ICM model with only refining the amplitude of the spins of Dy and Mn. Below 8 K, the LT-CM phase appears. Due to the coexistence of these two phases at 6 K yielding overlapping reflections, and due to the weak number of Bragg peaks for each phase, the refinement was difficult. However, we checked that the ambient pressure LT-CM model fits quite well the diffractogram at 2.4 GPa if we reduce the amplitude of the moment of Dy³⁺ and Mn³⁺ and increase a little bit the amplitude of the moment of Mn⁴⁺. The ratio between the HT-ICM phase and the LT-CM phase at this pressure was found to be 85% : 15%.

At 6.6 GPa, the HT-ICM has totally disappeared and a PCM phase emerges in all the temperature range below ~ 40 K with a propagation wave vector $\mathbf{q}_{\text{PCM}} = (\frac{1}{2}, 0, \frac{1}{2})$. This PCM phase has the same propagation vector than the one of the YMn₂O₅ [90], PrMn₂O₅ [131] and TbMn₂O₅ [135]. The neutron diffractograms at several temperatures are presented in Figure 5.16 between 15° and 40°. Although the PCM phase is still present at the lowest temperature (6 K), the dominant magnetic phase at this temperature is the LT-CM phase. With increasing the temperature, the PCM phase grows. Above ~ 10 K, the LT-CM phase fully vanishes and the PCM phase becomes the unique magnetic phase. The PCM phase found in DyMn₂O₅ is probably responsible for the enhanced ferroelectricity above ~ 10 K in the electric polarization measurement under pressure [87], thus we indicate that the PCM phase is

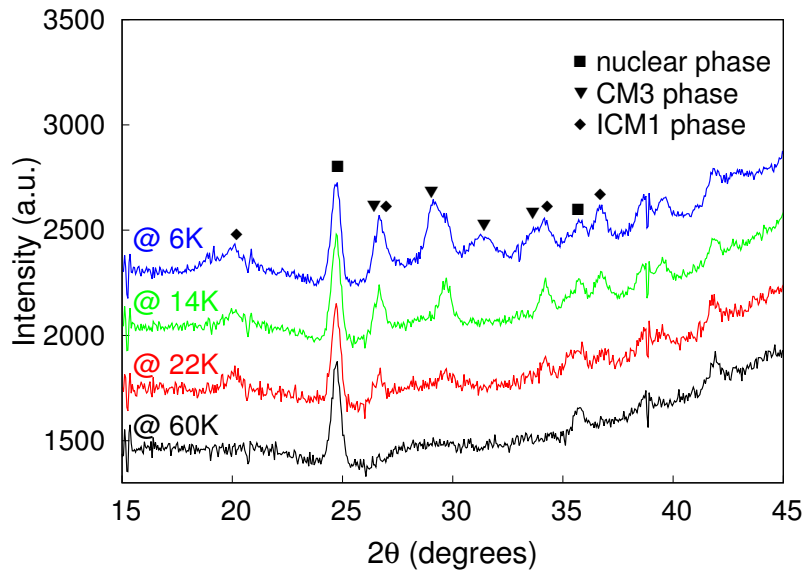


Figure 5.15 – PND curves under 2.4 GPa, at 6 K, 14 K, 22 K and 60 K. Reflections of nuclear phase, CM phase and ICM phase are indicated respectively.

ferroelectric (FE). The corresponding phase diagram is presented in Figure 5.17.

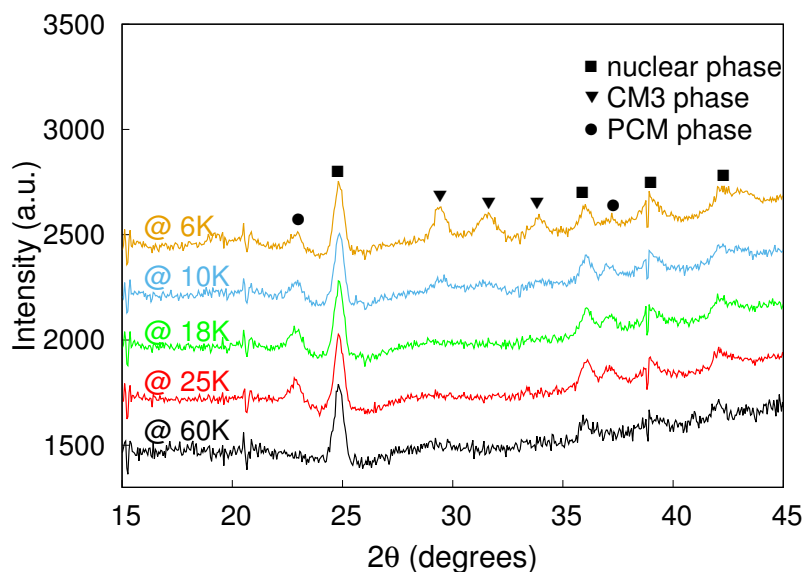


Figure 5.16 – PND curves under the highest pressure, 6.6 GPa, at 6 K, 10 K, 18 K, 25 K and 60 K. Reflections of nuclear phase, CM phase and PCM phase are indicated respectively.

We refined the magnetic structure of the PCM phase at 18 K and 6.6 GPa at which it is a single magnetic phase. We have used the 3 models described previously (D_1 , D_2 and *planar*). For each model, the amplitude of the Dy and the Mn spins have been refined. The direction of the moments in the (a , b) plane has been chosen similar to the HT-ICM phase for the *planar* model, but we suppressed the spiral and chose the orientation of the Mn^{4+} to be -45° and -4° (as in the case of YMn_2O_5 [75] and TbMn_2O_5 [135] at ambient pressure). The D_1 , D_2 and *planar* models fit the data with equivalent qualities, suggesting that the refinement is not strongly sensitive to the moment orientations. The refined parameters and reliability factors for the different models are listed in Table 5.2. The refinement of the PND at 18 K and 6.6 GPa and the corresponding magnetic structure are shown in Figure 5.18 for different models.

Among these models, the *planar* model yields to more plausible orientations for the Dy moment

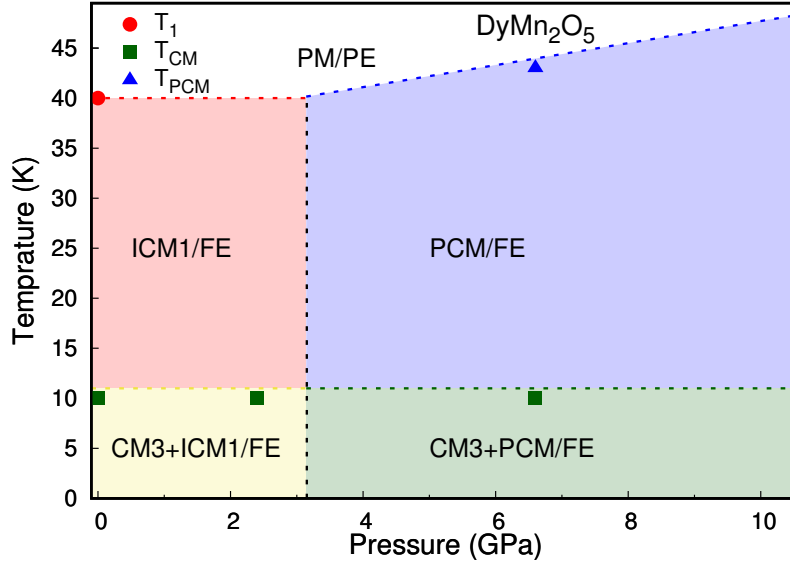


Figure 5.17 – Pressure-temperature phase diagram of DyMn₂O₅. The lines are a guide to the eye.

Table 5.2 – Refined parameters of the PCM phase of DyMn₂O₅ at 18 K, 6.6 GPa with different models. Magnetic moments of Dy³⁺ and Mn ions are in μ_B and the agreement factors are in %.

Model	$M(\text{Dy}^{3+})$	$M(\text{Mn}^{3+})$	$M(\text{Mn}^{4+})$	χ^2	R_p	R_{wp}	R_{exp}	R_{Bragg}	R_{mag}
D_1	1.9(3)	0.7(1)	0.9(4)	4.72	40.5	25.3	11.7	8.1	31.2
D_2	0.7(5)	2.3(4)	1.2(5)	4.74	40.5	25.4	11.7	7.9	40.7
<i>planar</i>	0.4(3)	2.2(7)	1.8(5)	4.73	40.5	25.4	11.7	8.0	36.8

Table 5.3 – Refined results for the magnetic structure parameters of DyMn₂O₅ at 18 K, 6.6 GPa with the *planar* model in $P1$ space group. ϕ and θ refer to the polar angle and the azimuthal angle, respectively.

Atom	x	y	z	$M(\mu_B)$	$\phi(^{\circ})$	$\theta(^{\circ})$
Dy ³⁺	0.1409	0.1708(2)	0	0.4(3)	114.9(7)	90
	0.3590	0.6708(2)	0	0.4(3)	79.1(6)	90
	0.6409	0.3291(8)	0	0.4(3)	259.1(6)	90
	0.8590	0.8291(8)	0	0.4(3)	114.9(7)	90
Mn ³⁺	0.4001	0.3491(7)	0.5	2.2(7)	-193.6(0)	90
	0.5998	0.6508(3)	0.5	2.2(7)	-13.6(0)	90
	0.0998	0.8491(7)	0.5	2.2(7)	-158.7(7)	90
	0.9001	0.1508(3)	0.5	2.2(7)	-158.7(7)	90
Mn ⁴⁺	0	0.5	0.2403	1.8(5)	-45.4(2)	90
	0	0.5	0.7596	1.8(5)	-45.4(2)	90
	0	0.5	0.2403	1.8(5)	-3.8(0)	90
	0	0.5	0.7596	1.8(5)	-3.8(0)	90

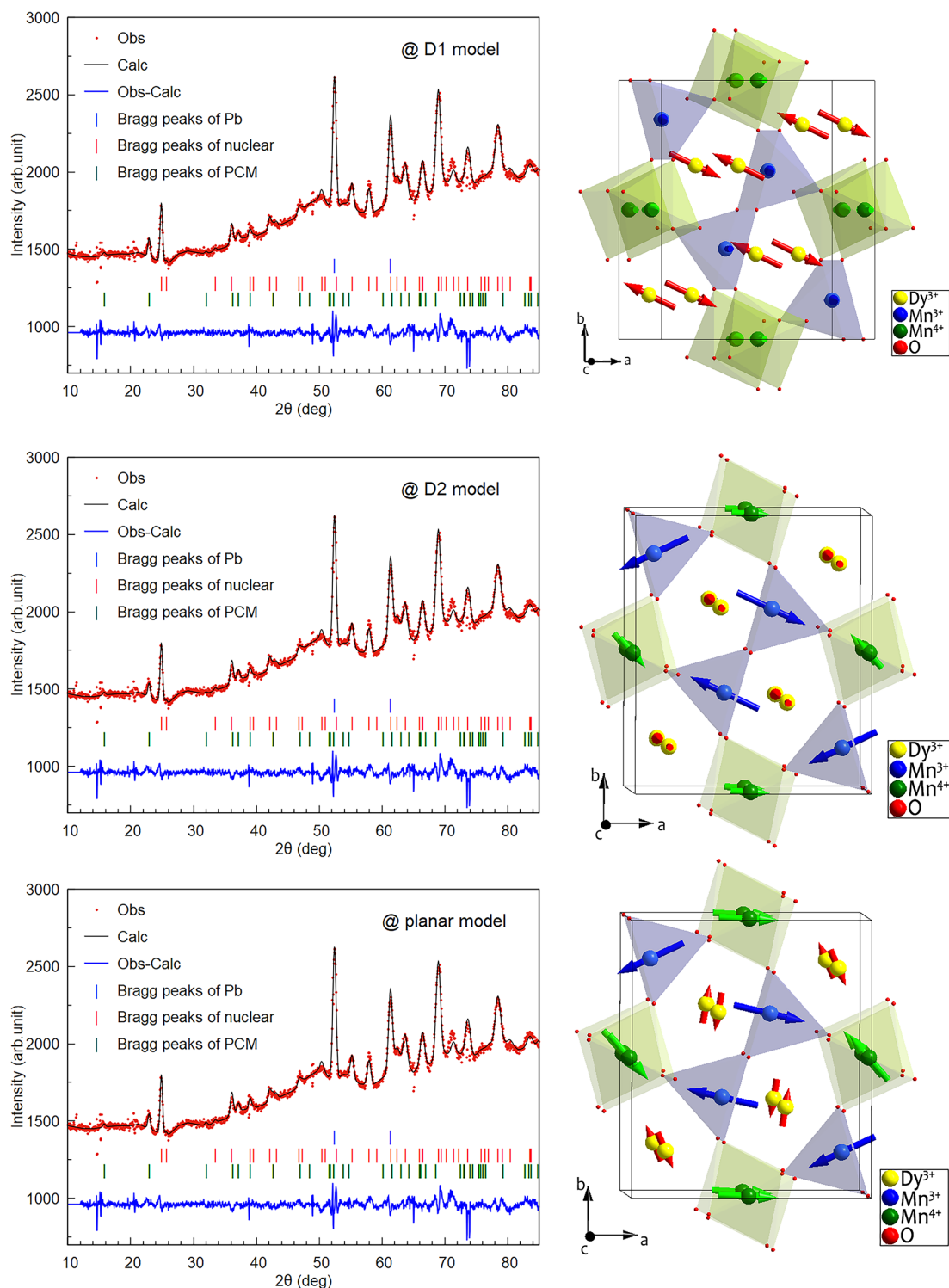


Figure 5.18 – Magnetic structure of DyMn_2O_5 at 18 K, 6.6 GPa with the D_1 , D_2 and *planar* models. For the sake of clarity, the amplitude of the moments of Mn^{3+} and Mn^{4+} in D_1 model have multiplied by a factor 2, the amplitude of the moments of Dy^{3+} in D_2 model have multiplied by a factor 2 and the amplitude of the moments of Dy^{3+} in *planar* model have multiplied by a factor 3.

(close to its magnetic easy axis, b) than the D_1 and D_2 models (along the a and c axis, respectively). However, as there is not enough independent PCM peaks to determine accurately the structure, the exact orientation of the moments (especially for the *planar* model) in the (a, b) plane is not easy to optimize which leads to a bad value of R_{mag} compared to the one of the D_1 model. However, as previously indicated, this model leads to more physical results concerning the direction of the R^{3+} , Mn^{3+} and Mn^{4+} magnetic moments. The result of the refinement for the planar model is given in the Table 5.3 and the corresponding PCM structure is illustrated in Figure 5.18. For the Mn moments, it exhibits the same AFM zig-zag chains close to the a axis as in TbMn₂O₅ at ambient pressure [135]. In addition, the amplitude of the moments present the right relation of magnitude at this intermediate temperature ($\mathbf{M}(Mn^{3+}) > \mathbf{M}(Mn^{4+}) > \mathbf{M}(Dy^{3+})$).

5.4.4 Discussion

Under pressure, a pressure induced PCM phase with propagation vector $\mathbf{q}_{PCM} = (\frac{1}{2}, 0, \frac{1}{2})$ has been now observed in the RMn₂O₅ (R = Y [90], Pr [131], Tb and Dy [135]) in spite of their different propagation vectors at ambient pressure. Thus, this periodicity is most likely attributed to a high pressure ground state which is common to the RMn₂O₅ compounds. Considering the *planar* structure, the PCM phase must correspond to a lowering of symmetry. Although this symmetry lowering is undetectable in our experiment, it could play a role to relieve the frustration of the R-Mn exchange. At the highest pressure (6.6 GPa), the moments of Dy³⁺ are nearly along the magnetic easy axis, b , to minimize the anisotropy of Dy³⁺. A similar situation is observed in TbMn₂O₅, but with a noticeable reorientation of the Tb³⁺ moments under pressure [135].

To explain the origin of the PCM phase in the RMn₂O₅ family, we have proposed a simple scenario based on Heisenberg exchange couplings between the spins of the Mn ions, J_i ($i = 1, 2, 3, 4, 5$), as well as the J_6 interaction introduced above. The Ising-like anisotropy of the R^{3+} ions is also taken into consideration. It is accounted for a single ion anisotropy term $-D\sigma^2$, where σ is the rare earth ordered moment and D is a positive constant. At the mean field level, σ should depend on the (local) molecular field \mathbf{H}_R created on the R site by the $3d-4f$ J_6 interaction coupling. It is expected to be strongly temperature dependent, as it is usually the case for rare earth ions.

We further assume that J_4 and J_5 are the strongest couplings, which is the usual assumption in this series. It leads to the AFM arrangement of the zig-zag chains $Mn^{4+} - Mn^{3+} - Mn^{3+} - Mn^{4+}$ along the a axis and undoubtedly gives the propagation wave vector $\mathbf{k}_x = \frac{1}{2}$. Note that this is consistent with the fact that this component of the propagation vector persists throughout the (T, p) phase diagram. To simplify the magnetic structures discussed, we systematically represent chains of Mn^{4+} , Mn^{3+} and R^{3+} spins running along the c axis, as represented in Figure 5.19. Although we simplify this mapping of the real structures to 1 dimensional chains, it allows us to focus on the stacking arrangement along the c axis, (and thus on \mathbf{k}_z), which is the main issue in these compounds. In this simplified model, we intend to merge J_4 and J_5 into an effective $Mn^{4+} - Mn^{3+}$ interaction and call it exchange interaction J , as shown in Figure 5.19. S is the modulus of the Mn moment, assumed here to be the same for Mn^{3+} and Mn^{4+} ions. We also assume that the super-exchange J_6 term concerns the R - Mn^{3+} interaction only [135]. A positive sign is taken for AF interactions.

For the PCM phase, $\mathbf{k}_z = \frac{1}{2}$, as shown in Figure 5.19 (a), the calculated energy and the (local) molecular field \mathbf{H}_R are:

$$\begin{aligned} E &= (-4J_1 - 4J_2 - 8J)S^2 - 4D\sigma^2 \\ \mathbf{H}_R &= 0 \end{aligned} \quad (5.2)$$

for the CM phase of DyMn₂O₅ at ambient pressure, $\mathbf{k}_z = 0$, as shown in Figure 5.19 (b), the calculated energy is:

$$\begin{aligned} E &= (4J_1 - 4J_2 - 8J)S^2 - 8J_6S\sigma - 4D\sigma^2 \\ \mathbf{H}_R &= -2J_6 \end{aligned} \quad (5.3)$$

Note that for the sake of simplicity, the J_i parameters here are taken always positive, a term $+J_iS^2$ is thus not energetically favorable.

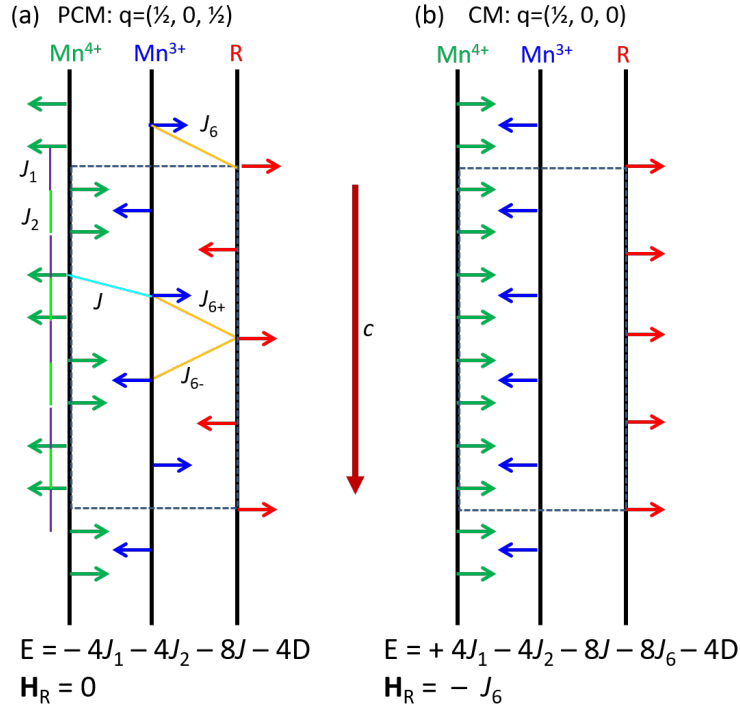


Figure 5.19 – Schematic 1D chains representing the energy gains for different propagation components \mathbf{k}_z along the c axis. (a) $\mathbf{k}_z = \frac{1}{2}$ (as for the PCM phase). (b) $\mathbf{k}_z = 0$ (as for the CM phase of DyMn_2O_5 at ambient pressure).

Importantly, it is found that the contributions related to J_2 and J are identical for the two different structures. A careful inspection of the different sketches shows that the magnetic ground state is clearly the result of a dominant J . The arrangement of two neighboring Mn^{4+} across an Mn^{3+} layer is always (nearly) FM, giving systematically a $-4J_2$ contribution. Two neighboring Mn^{4+} across an R^{3+} layer (J_1) is either AFM for the PCM phase (it gives a $-4J_1$ contribution), or FM for the CM phase (it gives a $4J_1$ energy gain). Concerning the J_6 term, it is clear that the energy gain cancels each other when $\mathbf{k}_z = \frac{1}{2}$ and sums to $-8J_6$ for $\mathbf{k}_z = 0$.

Therefore, we propose that the stability of the various phases (with various \mathbf{k}_z) observed in the RMn_2O_5 family is attributed to the delicate compromises involving J_1 , J_6 and the Ising anisotropy of the rare earth D . This competition determines the stacking along the c axis, which is the value of the propagation vector \mathbf{k}_z . As shown in Figure 5.19, both $\mathbf{k}_z = \frac{1}{2}$ and $\mathbf{k}_z = 0$ orders have a gain in energy with the term related to the R^{3+} anisotropy, $4D\sigma^2$. It has to be compared with the case of $\mathbf{k}_z = \frac{1}{4}$ ($-2D\sigma^2$) in TbMn_2O_5 at ambient pressure [135]. However, in the case of the CM phase ($\mathbf{k}_z = 0$), it is favored by a strong J_6 due to the large R^{3+} moment. On the contrary, the PCM phase ($\mathbf{k}_z = \frac{1}{2}$) is favored by a strong J_1 . Thus, we conclude that the pressure enhances the J_1 term over the J_6 one and leads to the $\mathbf{k}_z = \frac{1}{2}$ propagation wave vector if the R^{3+} moment is small enough. At ambient pressure or low pressure, the value of the R^{3+} moment is large (especially at low temperature), as for Dy^{3+} and the J_6 term dominates compared to the J_1 one. The system thus switches to the $\mathbf{k}_z = 0$ stacking.

It is important to recall here our results obtained by X-ray diffraction at 300 K under pressure in Chapter 4. We have evidenced that for Dy and Gd (but it is probably general), J_1 increases as a function of pressure (see Section 4.5).

In the PCM phase, the R^{3+} moment is sandwiched between two AFM pairs of Mn^{3+} or Mn^{4+} spins and the J_6 interaction is always frustrated. We could expect a symmetry lowering associated with a small shift of the R^{3+} ions to release this frustration by spin lattice coupling. In this scenario, the degenerated J_6 interaction will be replaced by J_{6+} and J_{6-} interactions with slightly different values.

In conclusion, at ambient and low pressure, the strong anisotropy of the Dy^{3+} spin and the Dy-Mn J_6 exchange interaction results in a $\mathbf{k}_z = 0$ stacking. The stabilization of the PCM phase can be

explained by the reinforcement under pressure of the Mn-Mn interaction J_1 with respect to the other Mn-Mn interactions.

5.5 Study of GdMn_2O_5 under Pressure

5.5.1 Introduction

At ambient pressure, GdMn_2O_5 presents a high electrical polarization ($\mathbf{P} = 3600 \mu\text{C}\cdot\text{m}^{-2}$) and a giant tunability of the electrical polarization ($\Delta\mathbf{P} = 5000 \mu\text{C}\cdot\text{m}^{-2}$) under an external magnetic field. In addition, through resonant X-ray magnetic scattering (RXMS) measurements, the magnetic structure has been estimated. From this study, a new Gd-Mn symmetric ES mechanism has been proposed to explain the giant tunable ferroelectricity [50].

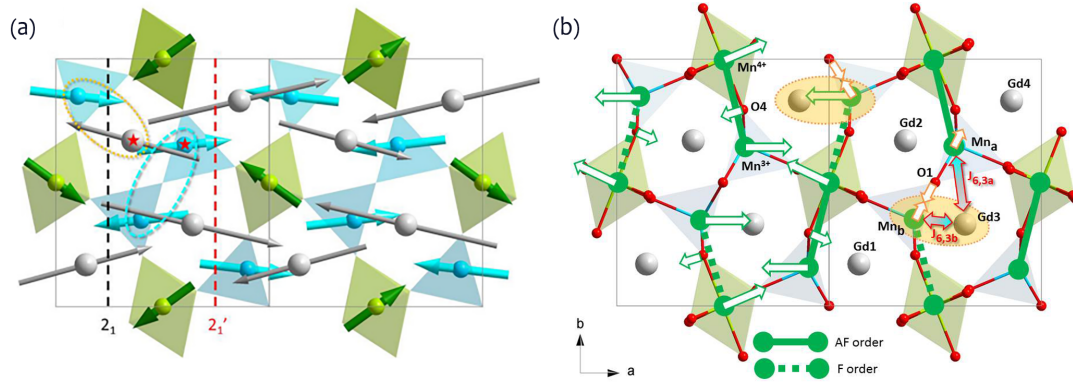


Figure 5.20 – (a) Magnetic structure of GdMn_2O_5 at 1.5 K. The blue (orange) ellipses show the $\text{Mn}^{3+} / \text{Mn}^{3+}$ ($\text{Gd}^{3+} / \text{Mn}^{3+}$) AFM pairs. Stars identify the $\text{Gd}^{3+} / \text{Mn}^{3+}$ pair proposed by Lee *et al.* in their model for a Gd - Mn ES mechanism[50]. (b) Atomic displacements associated with the release of the magnetic frustration at the origin of the two ES mechanisms, leading to the polarization. [57]

As the neutron absorption cross section of Gadolinium is too high (49700 barns [141]) to obtain a sufficient signal, no neutron experiment was performed on GdMn_2O_5 until recently. In collaboration with M. Greenblatt (The State University of New Jersey, USA), we were able to synthesize an isotope (^{160}Gd) enriched powder of GdMn_2O_5 to perform the PND experiment [57]. Below ~ 40 K, we observed a ICM phase with a propagation wave vector $\mathbf{q}_{\text{ICM8}} = (\frac{1}{2}-\sigma_x, 0, \frac{1}{5}-\sigma_z)$ ($\sigma_x \sim 0.01, \sigma_z \sim 0.02$). Below ~ 32 K, several new strong magnetic Bragg reflections replace those of the ICM phase with a propagation wave vector $\mathbf{q}_{\text{CM3}} = (\frac{1}{2}, 0, 0)$. Note that below ~ 12 K, two additional reflections appear, which correspond to an anomaly in the temperature dependence of the electric polarization [50, 142]. It is confirmed that the magnetic space group of the CM phase is P_63cm2_1 (in the standard setting) as proposed after the RXMS study. The corresponding magnetic structure is shown in Figure 5.20(a). Within each pair, the Gd^{3+} spins are related by a 2_1 or a $2'_1$ screw axis.

As previously explained, the magnetic frustration between AFM zig-zag chains directly related to the J_3 interaction is the source of the ES mechanism. In the non-centrosymmetric space group Pm , the various J_3 terms in the Hamiltonian no more cancel. To release the magnetic frustration, the J_3 exchange terms between Mn ions AFM ordered can increase and the J_3 exchange terms between Mn ions FM ordered can decrease, thanks to atomic displacements (see the green arrows in the Figure 5.20(b)). Following the analysis of Ref. [57], the atomic shifts lead to a global relative displacement of the Mn^{3+} along $-b$ and of the oxygen along the $+b$ direction. Thus an electric polarization appears via the ES mechanism. In the case of Gd, another ES mechanism occurs due to the J_6 interaction.

The strongest J_6 interaction is the one bridging the oxygens closest to the Gd. At low temperature, the closest oxygen, O1, mediates the interaction between two Mn^{3+} and two Gd^{3+} . This results in a strong magnetic frustration. Gold ellipses contain the $\text{Gd}^{3+} - \text{Mn}^{3+}$ coupled by J_6 through O1. To release the frustration, the bond O1 - Mn_a^{3+} must shorten while the bond O1 - Mn_b^{3+} must stretch. In the

right half part of the Figure 5.20(b), gold arrows indicate these displacements. These displacements contribute to an additional electric polarization along the b axis, which leads to the high electrical polarization in GdMn_2O_5 . [57]

Under pressure, unlike the other RMn_2O_5 ($R = \text{Y}, \text{Ho}, \text{Tb}$ and Dy) compounds [66, 87], the electric polarization at low temperature does not change significantly. However, as shown in Section 2.5.2 Figure 2.22, the peak of the dielectric constant ϵ_b gradually splits into two peaks with increasing pressure and a pressure-enhanced electric polarization appears at high temperature, between ~ 31 K and ~ 35 K. [88]

5.5.2 PND Experiment under Pressure

In this experiment, we used an isotope-enriched ^{160}Gd sample of GdMn_2O_5 synthesized by M. Greenblatt (The State University of New Jersey, USA). The PND experiment was performed on the high flux diffractometer D20 of the Institute Laue Langevin (ILL, Grenoble, France) with the wavelength of 2.42 Å. Measurements were carried out by heating up from 6 to 70 K at 2.4, 3.6, 5 and 8.4 GPa. Rietveld refinements [108] of the nuclear and magnetic structures were performed by using the FullProf Suite [107]. All the nuclear structures were refined above the Néel temperature ~ 60 K.

5.5.3 Analysis of the PND under Pressure

a) CM phase under pressure

The CM phase persists in the entire pressure range at low temperature (7 K), as shown in Figure 5.21(a). The reflections of the CM phase are very intense and the intensity of the magnetic peaks only slightly decrease with increasing pressure (they remain comparable to the intensity of the nuclear structure). We used the model of the CM phase at ambient pressure ($P_a b 2_1 a$ space group) as the initial model to refine the magnetic structure of the CM phase under pressure. The refinement has been performed at the lowest temperature (7 K), at which the phase is the more prominent. We have adjusted the amplitude and the direction of the moments from the initial model. Figure 5.22 shows the result of the refinement and the magnetic structure at 8 GPa and 7 K. The pressure evolution of the amplitude of the Mn and Gd moments at 7 K is given in Figure 5.21(b). We can see that at low temperature the moments of all the ions are not so much affected by the pressure.

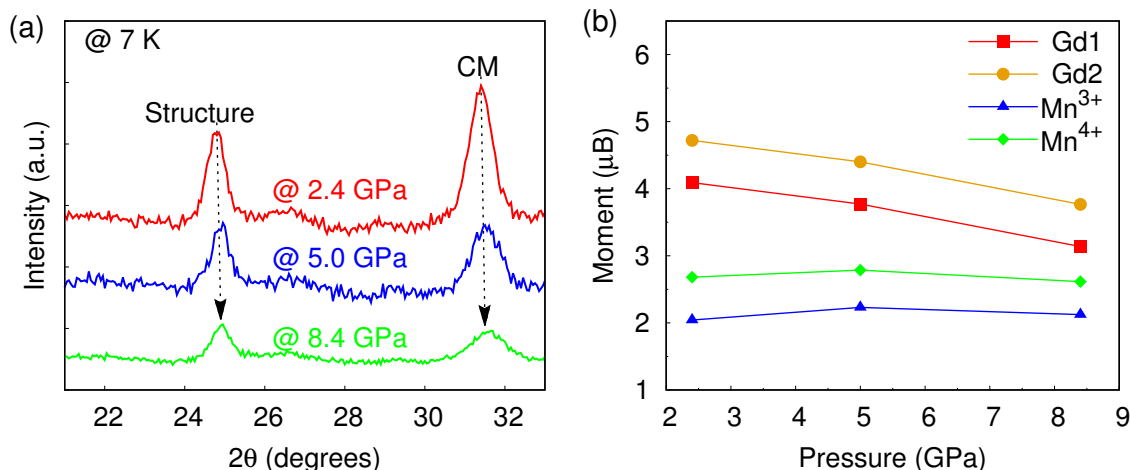


Figure 5.21 – Pressure evolutions of the CM phase at 7 K (a) the PND curves at 2.4, 5.0 and 8.4 GPa and (b) the corresponding amplitude of the moments of Gd and Mn.

It is also interesting to study the thermal evolution of the CM phase at low pressure (2.4 GPa), illustrated in Figure 5.23. We observe that the intensity of the magnetic peaks of the CM phase decreases rapidly as a function of temperature (Figure 5.23(a)). At 32 K, the CM phase has nearly disappeared. It is quite different to the thermal evolution at ambient pressure. Indeed, with increasing

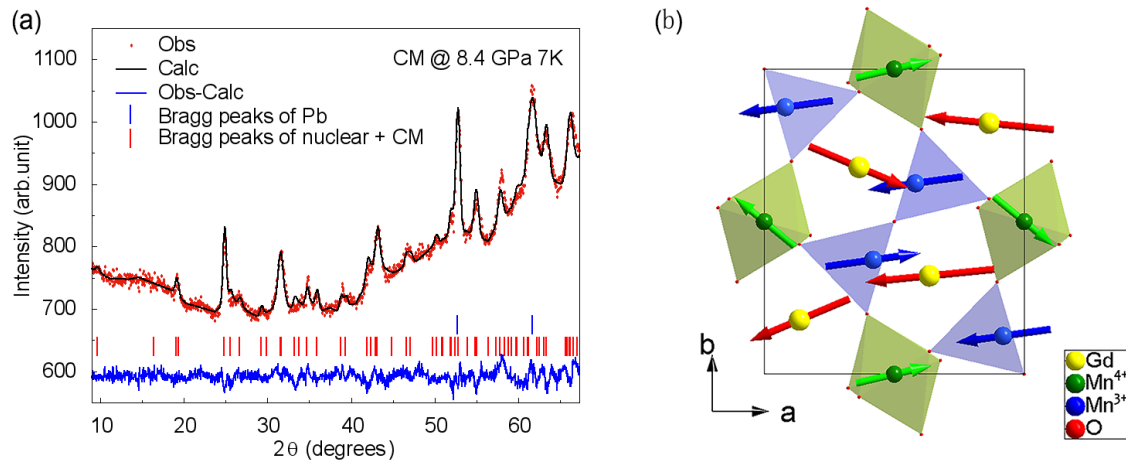


Figure 5.22 – (a) PND curves and (b) the magnetic structure in the (a, b) plane of the CM phase of GdMn_2O_5 at 8.4 GPa, 7 K.

temperature, even at 2.4 GPa, the magnetic moments of the Gd^{3+} and the Mn ions rapidly drop (Figure 5.23(b)) whereas those of the Mn ions at ambient pressure decrease more slowly up to 32 K [57]. This indicates that the magnetic moments are more sensitive to the temperature under pressure.

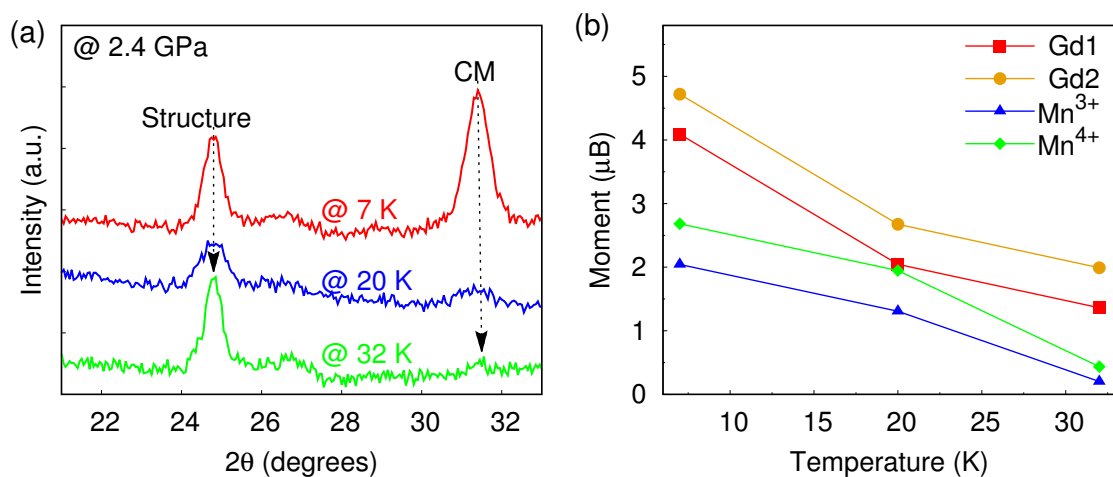


Figure 5.23 – Temperature evolutions of CM phase at 2.4 GPa (a) at 7, 20 and 32 K and (b) the corresponding amplitude of moments of Gd and Mn ions.

b) PCM phase under pressure

Below 5 GPa, we have not evidenced any pressure induced magnetic phase in the entire temperature range. At 8.4 GPa and above 32 K, two peaks of weak intensity of the PCM phase appear accompanied by a total disappearance of the CM phase. This new phase exists with the propagation wave vector $\mathbf{q}_{\text{PCM}} = (\frac{1}{2}, 0, \frac{1}{2})$, which is identical to the one of the other RMn_2O_5 ($R = \text{Y, Tb, Pr}$ and Dy) compounds [90, 131, 135].

As mentioned in Section 5.2, the propagation wave vector $(\frac{1}{2}, 0, \frac{1}{2})$ corresponds to the D point of the Brillouin zone in the standard setting and there are three possible irreducible representations: D_1 , D_2 , and *planar*. The fitting of PND with these three models are illustrated in Figure 5.24. The D_1 model did not fit the data correctly, especially for the first reflection of the PCM phase. The D_2 and *planar* models turned out to fit the data in an equivalent way. In the refinements, we used the ambient pressure CM phase as a starting point but released the $2'_1$ restriction. For the D_2 model, the

directions of the Mn^{3+} and Mn^{4+} moments were fixed to the one at ambient pressure and only the three amplitudes of the moments were refined. For the *planar* model, we refined the direction of the Gd^{3+} moments and the amplitudes of the Gd and Mn moments. Table 5.4 lists the moment values obtained for both models at 32 K.

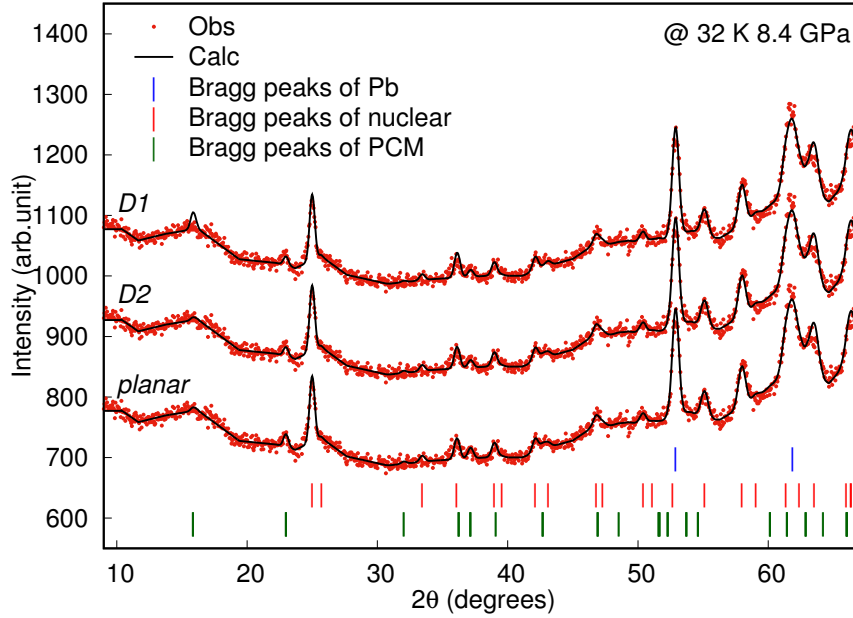


Figure 5.24 – PND curves under the highest pressure, 8.4 GPa, at 32 K for the D_1 , D_2 and *planar* models

Table 5.4 – Refined parameters of the PCM phase of the GdMn_2O_5 at 8.4 GPa and 32 K with the D_2 and *planar* models. Magnetic moments of Gd^{3+} and Mn ions are in μ_B and the agreement factors are in %

Model	$M(\text{Gd}^{3+})$	$M(\text{Mn}^{3+})$	$M(\text{Mn}^{4+})$	χ^2	R_p	R_{wp}	R_{exp}	R_{Bragg}	R_{mag}
D_2	0.1(9)	1.8(6)	1.2(3)	1.85	43.2	27.4	20.1	3.8	28.6
<i>planar</i>	0.2(1)	1.9(2)	1.3(9)	1.85	43.2	27.4	20.2	4.0	27.4

As the Gd^{3+} has no magnetic easy axis (anisotropy) [50] and the moment is quite similar for both models, it is hard to choose between these models. However, as the Gd^{3+} is isotropic, it should be sensitive to the molecular field of the Mn ions. Under this condition, we chose the *planar* model as the most probable. As there is not enough independent PCM peaks, the structure refined is not fully accurate. Compared to the CM phase, the moments of the Gd ions decrease to be nearly nil ($0.2 \mu_B$), whereas the amplitude of the moments of Mn ions only slightly decrease. The refined parameters are listed in Table 5.5. The PCM structure is illustrated in Figure 5.25.

The pressure-temperature phase diagram of GdMn_2O_5 is shown in Figure 5.26 constructed from the neutron diffractograms under pressure. The boundary between ICM and PCM is indicated arbitrary. As proposed in Ref. [88], between 30 and 35 K, a new FE phase appears for pressures above ~ 1.5 GPa, corresponding to the PCM phase. However, we are unable to observe the PCM phase below 5 GPa, this can be attributed to the low resolution of the PND measurements. Although the PCM phase could exist at a larger temperature range with increasing the pressure at the expense of CM phase, the CM is always the absolute dominant phase at low temperature up to 8.4 GPa in our study.

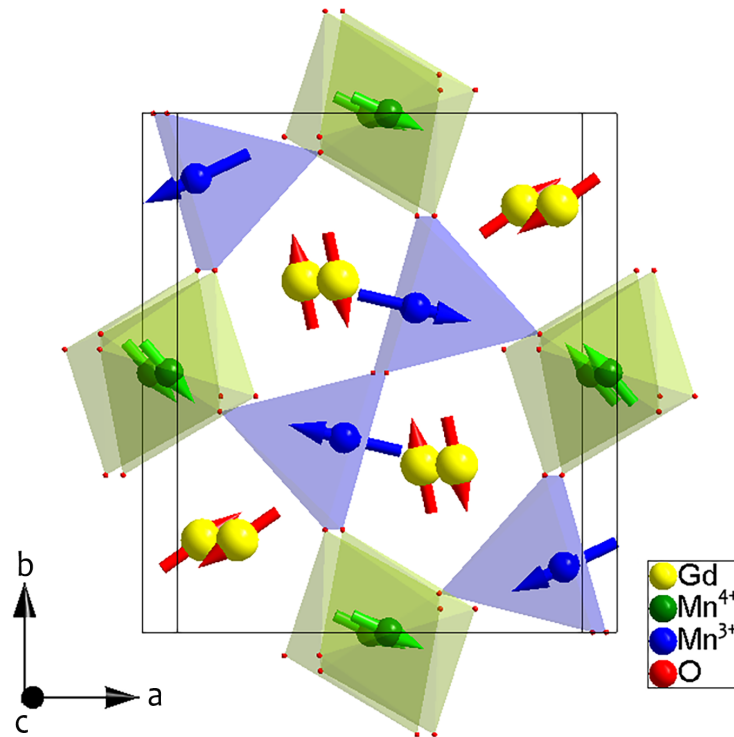


Figure 5.25 – Magnetic structure of the PCM phase of GdMn_2O_5 at 32 K, 8.4 GPa. The amplitude of the moments of Gd^{3+} are multiplied by a factor 8 for the sake of clarity.

Table 5.5 – Refined results for the magnetic structure parameters of GdMn_2O_5 at 32 K, 8.4 GPa with the *planar* model in $P1$ space group with $\chi^2 = 1.85$, $R_p = 43.2\%$, $R_{wp} = 27.7\%$, $R_{exp} = 20.1\%$, $R_{Bragg} = 4.0\%$ and $R_{mag} = 27.4\%$. ϕ and θ refer to the polar angle and the azimuthal angle, respectively.

Atom	x	y	z	$M(\mu_B)$	$\phi(^{\circ})$	$\theta(^{\circ})$
Gd^{3+}	0.1354	0.1776	0	0.2(1)	-327.6(2)	90
	0.3645	0.6776	0	0.2(1)	105.2(2)	90
	0.6354	0.3223	0	0.2(1)	105.2(2)	90
	0.8645	0.8223	0	0.2(1)	-327.6(2)	90
Mn^{3+}	0.4187	0.3746	0.5	1.9(2)	-193.6(0)	90
	0.5812	0.6253	0.5	1.9(2)	-13.6(0)	90
	0.1812	0.8746	0.5	1.9(2)	-158.7(7)	90
	0.9187	0.1253	0.5	1.9(2)	-158.7(7)	90
Mn^{4+}	0	0.5	0.2479	1.3(9)	-45.2(7)	90
	0	0.5	0.7520	1.3(9)	-45.2(7)	90
	0	0.5	0.2479	1.3(9)	-21.0(7)	90
	0	0.5	0.7520	1.3(9)	-21.0(7)	90

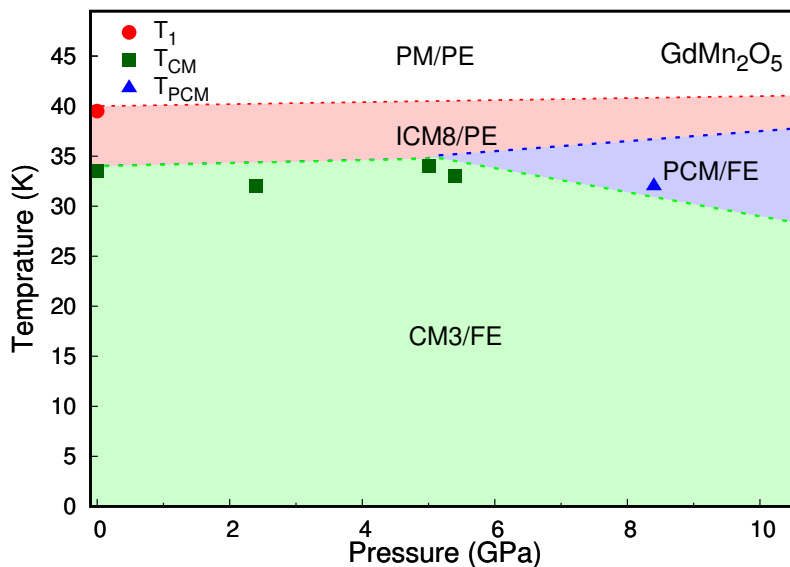


Figure 5.26 – Pressure-temperature phase diagram of GdMn_2O_5 . The lines are a guide to the eye.

5.5.4 Discussion

Under high pressure, a pressure induced PCM phase with propagation vector $\mathbf{q}_{\text{PCM}} = (\frac{1}{2}, 0, \frac{1}{2})$ is observed in the GdMn_2O_5 . It is similar to the one of the other RMn_2O_5 ($R = \text{Y}$ [90], Pr [131], Tb and Dy [135]) compounds in spite of their different propagation vectors at ambient pressure. The magnetic ordering at $(\frac{1}{2}, 0, \frac{1}{2})$ observed at high pressure is thus a universal character of the RMn_2O_5 compounds. With increasing pressure, the intensity of the PCM phase grows at the expense of the high temperature ICM phase and quickly replaces it totally. This behavior is identical to the case of TbMn_2O_5 and DyMn_2O_5 [135].

However in the case of DyMn_2O_5 , the PCM phase totally replaces the LT-ICM magnetic ground state which is not the case for GdMn_2O_5 (the PCM phase totally replaces the HT-ICM phase). The CM magnetic ground state is of the highest polarization due to the additional J_6 ES mechanism. As it is barely modified under pressure, the electric polarization under pressure at low temperature should not be modified as well. It is indeed what is discovered experimentally [88]. In addition, the electric polarization at high temperature (above 30 K) is strongly enhanced with increasing pressure [88] (see Figure 2.22(b)), which can be attributed to the PCM phase discovered at high temperature under pressure.

As proposed in Section 5.4.4, the competition of the CM and the PCM phases can be seen as the competition of J_1 ($\mathbf{k}_z = \frac{1}{2}$) and J_6 ($\mathbf{k}_z = 0$). The R^{3+} ordering of GdMn_2O_5 is similar to the one of DyMn_2O_5 , and even stronger, as the CM phase is really the dominant phase. Indeed it exists alone below 30 K at ambient pressure and is barely affected by pressure. In the Hamiltonian, the term related to the J_6 interaction is strong at ambient pressure due to the large amplitude of the Gd moments. At high temperature and high pressure the J_6 term strikingly weakens and the J_1 term can be dominant and leads to the PCM phase.

In conclusion, at ambient and low pressure, the strong Gd-Mn J_6 exchange interaction results in a $\mathbf{k}_z = 0$ stacking. Even under pressure, it is still dominant at low temperature. The PCM phase only exists at high temperature and high pressure. It is related to an increase of the electric polarization under pressure [88].

5.6 Study of SmMn_2O_5 under Pressure

5.6.1 Introduction: Magnetic Structure at Ambient Pressure

Similarly to the Gadolinium, the neutron absorption cross section of the Samarium is very high (5922 barns [141]). A RXMS experiment previously performed has determined that the main magnetic phase observed in a large temperature range is a CM phase with the propagation wave vector $\mathbf{q}_{\text{CM3}} = (\frac{1}{2}, 0, 0)$ [79], as for DyMn_2O_5 and GdMn_2O_5 . The proposed magnetic structure of the CM phase was a structure where the moments of Sm^{3+} , Mn^{3+} and Mn^{4+} have a dominant c axis component [79].

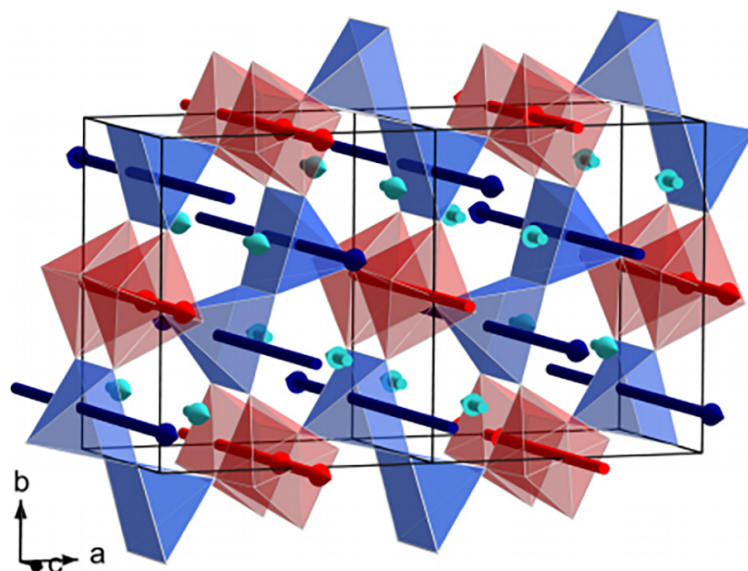


Figure 5.27 – Perspective view of the magnetic structure of SmMn_2O_5 at 6 K. The blue Mn^{3+} pyramids and the red Mn^{4+} octahedra are represented. [44]

Thanks to the collaboration with M. Greenblatt (The State University of New Jersey, USA), we were able to obtain an isotope enriched (^{154}Sm) SmMn_2O_5 sample to perform a PND experiment. [44]. Below ~ 34 K, a HT-ICM phase appears with the propagation wave vector $\mathbf{q}_{\text{ICM5}} = (\frac{1}{2}, 0, \frac{1}{2}-\sigma_z)$ ($\sigma_z \sim 0.173$). Below ~ 26 K, a CM phase replaces the HT-ICM phase, with $\mathbf{q}_{\text{CM3}} = (\frac{1}{2}, 0, 0)$. At low temperature, below ~ 6 K, a LT-ICM coexists with the CM phase, the propagation wave vector being $\mathbf{q}_{\text{ICM6}} = (\frac{1}{2}, 0, \frac{1}{2}-\sigma'_z)$ ($\sigma'_z \sim 0.165$). The structure of the main CM phase is illustrated in Figure 5.27. All the moments are strictly along the c axis and the magnetic space group is P_{2am} [44]. The structure is similar to the one proposed by Ishii *et al* [79], except that the direction of one pair of the Sm^{3+} is reversed.

5.6.2 PND Experiment under Pressure

The PND has been performed on the D1B diffractometer (CRG, CNRS ILL-Grenoble, France) with the wavelength of 2.52 \AA on the same isotope enriched powder sample used for ambient pressure measurement. Measurements have been carried out by heating up from 6 to 70 K at 1.9, 5.5, 7.7 and 10.3 GPa. Refinements of the nuclear and magnetic structures have been performed using the FULLPROF program [107]. All the nuclear structures were refined above the Néel temperature ~ 60 K.

5.6.3 Analysis of the PND under Pressure

a) CM phase under pressure

The CM phase exists in the entire pressure range studied, below a temperature $T_2(p)$ which decreases under pressure ($T_2(0) \sim 32\text{K}$ and $T_2(10 \text{ GPa}) \sim 25 \text{ K}$). At low pressure, the neutron diffractograms are

similar to those at ambient pressure. So we have used the same model as the ambient pressure one to refine the CM phase under pressure. As shown in Figure 5.28 at 15K and 1.9 GPa, the only phase present in the diffractogram is the CM phase. We thus refined the CM phase by adjusting slightly the amplitude and the direction of the moments of the initial model. Table 5.6 gives the result of the refinement. We were then able to obtain the amplitude of the moments from our refinement. With increasing the pressure, at 15 K, the intensity of the CM phase weakens coincide with the appearance of the PCM phase. The corresponding phase ratio of the CM and PCM phase also given in Figure 5.28). Above 5.5 GPa, the phase ration between these two magnetic phase at 15 K nearly become balanced, which is around 50 %. This indicates that with increasing the pressure, there is no significant change for the CM phase.

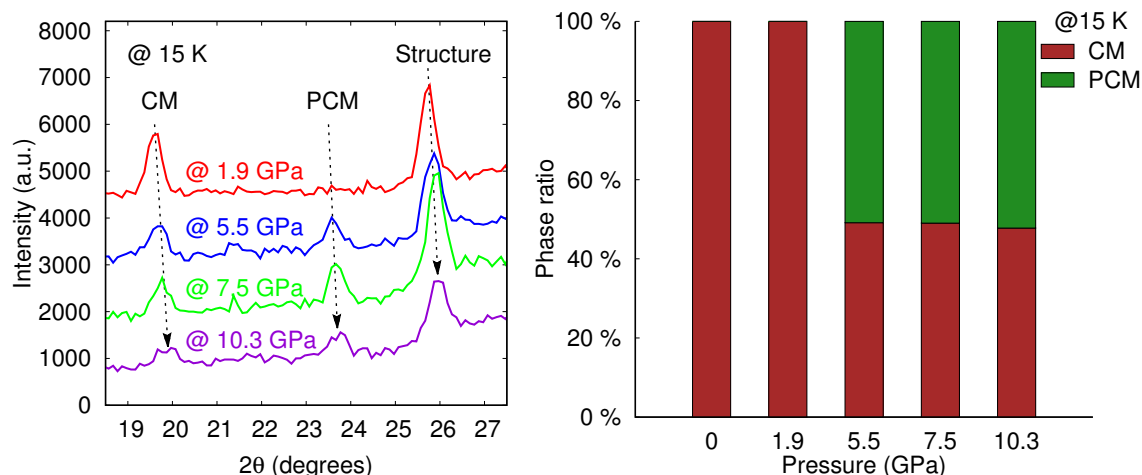


Figure 5.28 – Diffractograms and phase ratio of the pressure evolutions of the CM and PCM phases at 15 K.

Table 5.6 – Magnetic structure parameters of the CM phase of SmMn_2O_5 at 1.9 GPa, 15 K in the $P_{2_1}m$ space group with $\chi^2 = 30.7$, $R_p = 30.2\%$, $R_{wp} = 18.7\%$, $R_{exp} = 3.4\%$, $R_{Bragg} = 2.9\%$ and $R_{mag} = 21.5\%$. All the moments are along the c direction.

Atom	x	y	z	$M(\mu_B)$
Mn^{3+}	0.409(8)	0.352(5)	0.5	2.6(6)
Mn^{4+}	0	0.5	0.260(9)	1.5(7)
Sm^{3+}	0.142(2)	0.173(1)	0	0.5(2)

b) PCM phase under pressure

Under high pressure, the intensity of the PCM phase increases at the expense of the CM phase with increasing the temperature. Above 32 K, at the highest pressure, 10.3 GPa, the CM phase totally disappears and the PCM phase becomes the unique magnetic phase. The PCM phase exists alone with the propagation wave vector $\mathbf{q}_{\text{PCM}} = (\frac{1}{2}, 0, \frac{1}{2})$, which is the same for the other RMn_2O_5 ($R = \text{Y, Tb, Pr, Dy}$ and Gd) compounds [90, 131, 135]. We followed the same symmetry analysis as for the other systems (see Section 5.4.3).

At 15 K, phase ratio between the CM and PCM phases changes weakly (around 50%) with increasing the pressure, as shown in Figure 5.28, which means that no significant evolution for the CM phase under pressure. This indicates that the anisotropy of the Sm^{3+} is kept under pressure, the moments of Sm^{3+} are along the magnetic easy axis, c , which minimizes the anisotropy energy of Sm^{3+} .

Thus we chose the $D2$ model with the magnetic moments of Mn^{3+} compelled in the (a, b) plane, while the magnetic moments of Sm^{3+} are along the c axis. We also ascribed the Mn^{4+} to align in the (a, b) plane. The Mn^{3+} and Mn^{4+} are in the (a, b) plane, which also minimizes the anisotropy of Mn spins. With these restrictions, we refined the neutron diffractogram, presented in Figure 5.29.

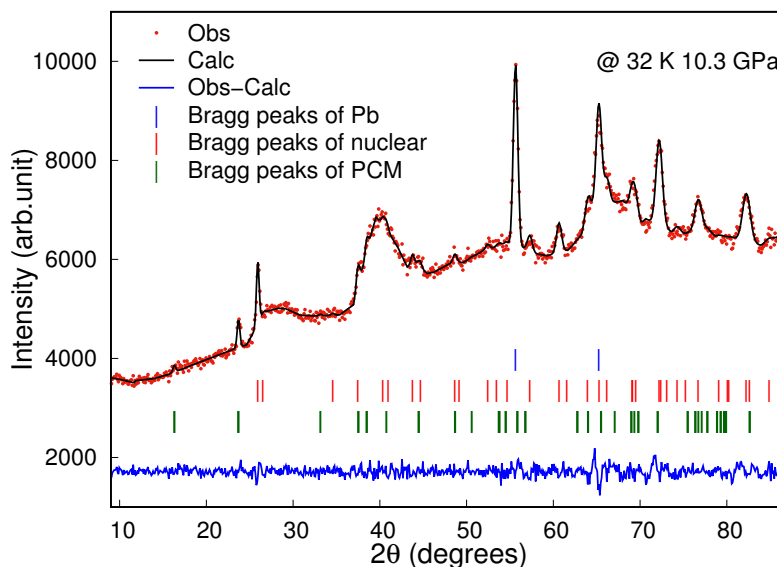


Figure 5.29 – PND curves of SmMn_2O_5 at 10.3 GPa and 32 K. No CM phase is present.

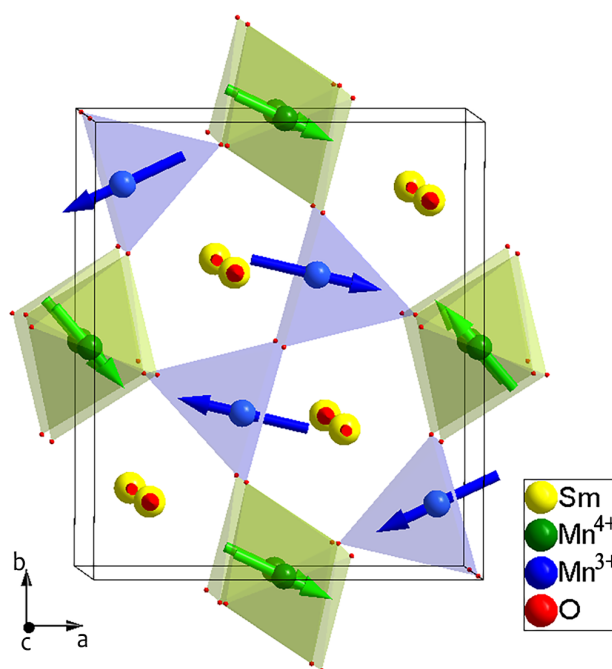


Figure 5.30 – Magnetic structure of SmMn_2O_5 at 32 K, 10.3 GPa. The moments of Sm^{3+} are along the c axis. The amplitude of the moments of Sm^{3+} are multiplied by a factor 2 for the sake of clarity

The corresponding magnetic structure of the PCM phase is shown in Figure 5.30. The Sm^{3+} spins are along the c axis, their amplitude is small as at ambient pressure. It is interesting to note that the good agreement of this model with the PND data indicates that the anisotropy of the Sm^{3+} spins is not modified under pressure and remains along the c axis. The refined moments are given in Table 5.7.

The pressure-temperature phase diagram of SmMn_2O_5 is shown in Figure 5.31. Under pressure, the PCM phase replaces the HT-ICM phase to become the unique magnetic phase at high temperature. With

Table 5.7 – Refinement results for the PCM phase of SmMn_2O_5 at 32 K, 10.3 GPa in $P1$ space group with $\chi^2 = 52.9$, $R_p = 47.6\%$, $R_{wp} = 25.6\%$, $R_{exp} = 3.5\%$, $R_{Bragg} = 2.5\%$ and $R_{mag} = 34.1\%$. ϕ and θ refer to the polar angle and the azimuthal angle, respectively.

Atom	x	y	z	$M(\mu_B)$	ϕ ($^\circ$)	θ ($^\circ$)
Sm^{3+}	0.1419	0.1709	0	0.7(6)	–	0
	0.3580	0.6709	0	0.7(6)	–	0
	0.6419	0.3290	0	0.7(6)	–	0
	0.8580	0.8290	0	0.7(6)	–	0
Mn^{3+}	0.4045	0.3488	0.5	2.5(5)	-193.9(0)	90
	0.5954	0.6511	0.5	2.5(5)	-13.9(1)	90
	0.0954	0.8488	0.5	2.5(5)	-158.7(7)	90
	0.9045	0.1511	0.5	2.5(5)	-158.7(7)	90
Mn^{4+}	0	0.5	0.2490	2.0(0)	-45.6(9)	90
	0	0.5	0.7509	2.0(0)	-45.6(8)	90
	0	0.5	0.2490	2.0(0)	-21.0(6)	90
	0	0.5	0.7509	2.0(0)	-21.0(7)	90

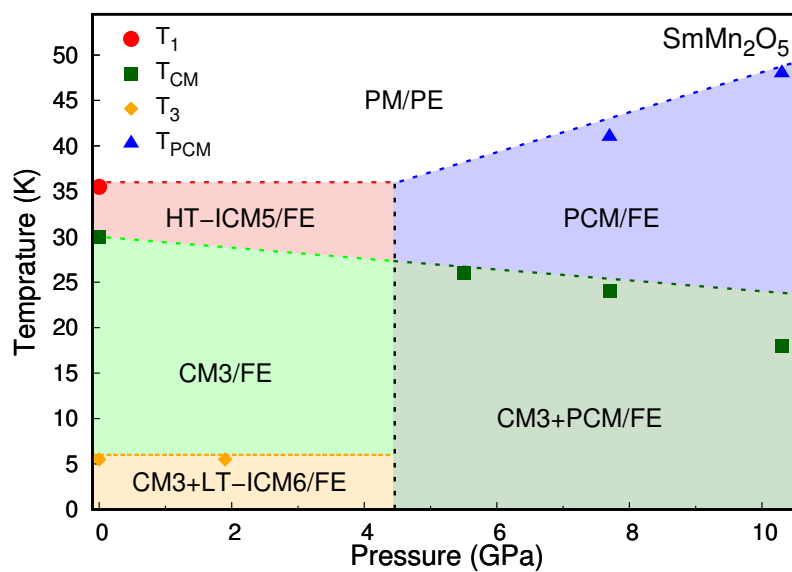


Figure 5.31 – Pressure-temperature phase diagram of SmMn_2O_5 . The lines are a guide to the eye.

increasing pressure, the critical temperature of the CM phase decreases and the critical temperature of the PCM phase increases. At 10.3 GPa, T_{PCM} reaches 48 K. In addition, the PCM phase becomes stronger at the expense of the CM phase. However, at low temperature even at high pressure, the CM phase still exists and coexists with the PCM phase. Finally, at higher pressure, the LT-ICM phase totally vanishes.

5.6.4 Discussion

Under high pressure, the pressure induced magnetic phase has also been observed in the SmMn_2O_5 . This PCM phase has the same propagation vector $\mathbf{q}_{\text{PCM}} = (\frac{1}{2}, 0, \frac{1}{2})$ as the one of the other RMn_2O_5 ($R = \text{Y}$ [90], Pr [131], Tb , Dy [135], and Gd). This definitively indicates that the propagation wave vector of this phase is a universal character of this series of compounds. With increasing pressure, both the HT-ICM and the LT-ICM phases disappear and the PCM phase takes place. In addition, the critical temperature of the PCM phase increases linearly at high pressure, which is probably a common feature to this family too.

With increasing pressure, the intensity of the PCM phase grows at the expense of the high temperature ICM phase and quickly replaces it totally, similarly to the case of TbMn_2O_5 and DyMn_2O_5 [135]. At high temperature, with increasing the pressure, the PCM phase replaces the HT-ICM phase and becomes the unique magnetic phase. Although the robust CM phase is dominant in the intermediate temperature range at low pressure, the PCM phase coexist with the CM phase at high pressure.

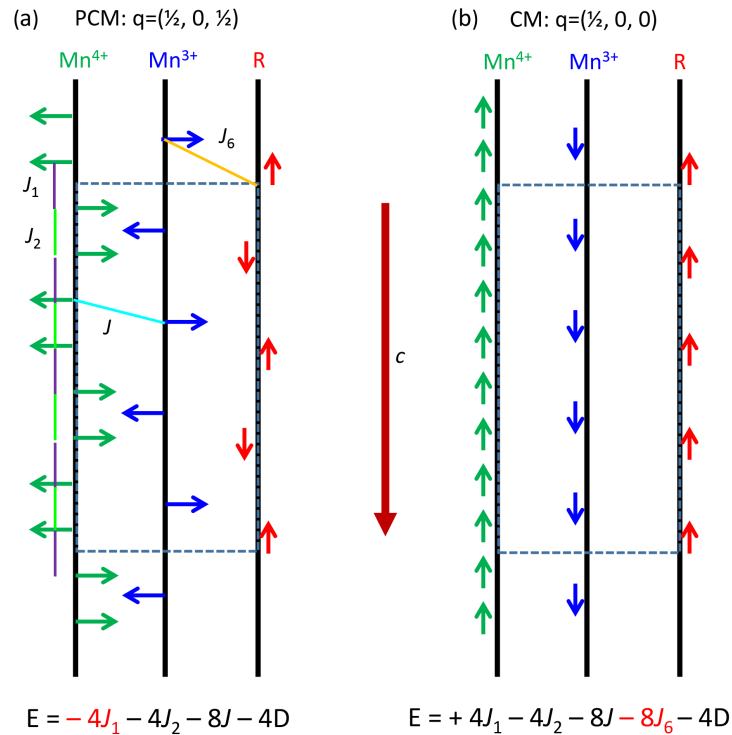


Figure 5.32 – Schematic 1D chains representing the energy gains for different propagation components \mathbf{k}_z along the c axis. (a) $\mathbf{k}_z = \frac{1}{2}$ (as for the PCM phase). (b) $\mathbf{k}_z = 0$ (as for the CM phase of SmMn_2O_5 at ambient pressure with all the spins along c axis.).

At ambient pressure, the CM phase is dominant with both Sm and Mn ions along the c axis. However the natural easy axis for Mn moment in both pyramidal and octahedra environment is in the (a, b) plane as observed in all other members of the series. Despite this specialty, the stabilization of the PCM phase has shown the same origin as we proposed in Section 5.4.4. A simplified structure with 1D chains of Mn^{4+} , Mn^{3+} and Sm^{3+} along c are presented in Figure 5.32. Through these 1D chains, we can obtain the calculated energy and the (local) molecular field \mathbf{H}_R , which are the same as those of

the DyMn_2O_5 . For the PCM phase, $\mathbf{k}_z = \frac{1}{2}$, as shown in Figure 5.32 (a), the J_6 terms do not cancel each other as for DyMn_2O_5 . But the J_6 terms in the Hamiltonian are always nul due to the fact that the spins involved are perpendicular. Thus the calculated energy and the (local) molecular field \mathbf{H}_R are:

$$\begin{aligned} E &= (-4J_1 - 4J_2 - 8J)S^2 - 4D\sigma^2 \\ \mathbf{H}_R &= 0 \end{aligned} \quad (5.4)$$

for the CM phase of SmMn_2O_5 at ambient pressure, $\mathbf{k}_z = 0$, as shown in Figure 5.32 (b), the calculated energy is:

$$\begin{aligned} E &= (4J_1 - 4J_2 - 8J)S^2 - 8J_6S\sigma - 4D\sigma^2 \\ \mathbf{H}_R &= -2J_6 \end{aligned} \quad (5.5)$$

At ambient pressure, the dominant CM phase with all the spins along the c axis leads to a strong J_6 term. Under pressure, the J_6 term is balanced with the local Mn anisotropy term and the two orders coexist at low temperature, one with all moments along c (CM phase) and one with the moments of the Mn ions in the (a, b) plane and the moments of Sm^{3+} along the c (PCM phase). Above 32 K at high pressure, the J_1 term is maximized.

In conclusion, at ambient and low pressure, the strong Sm-Mn J_6 exchange term favors a $\mathbf{k}_z = 0$ stacking. It is robust at low temperature under high pressure. The anisotropy of Sm^{3+} is along the c axis, even at high pressure. The PCM phase favored by a strong J_1 term is stabilized in all temperature range under high pressure, and becomes a unique magnetic phase at high temperature (Above 32 K).

Summary of this Chapter

In this chapter we have presented our work about the multiferroic properties of RMn_2O_5 (R = Pr, Dy, Gd and Sm) under pressure. We have previously seen that the pressure greatly influences the multiferroic properties of the RMn_2O_5 compounds. Our work has shown that under pressure, a pressure induced commensurate magnetic phase (PCM) appears with the same propagation wave vector $\mathbf{q}_{\text{PCM}} = (\frac{1}{2}, 0, \frac{1}{2})$ for all the RMn_2O_5 (R = Pr, Dy, Gd and Sm) studied. The magnetic structure of the PCM phase of RMn_2O_5 (R = Pr, Dy, Gd and Sm) is presented in Figure 5.33.

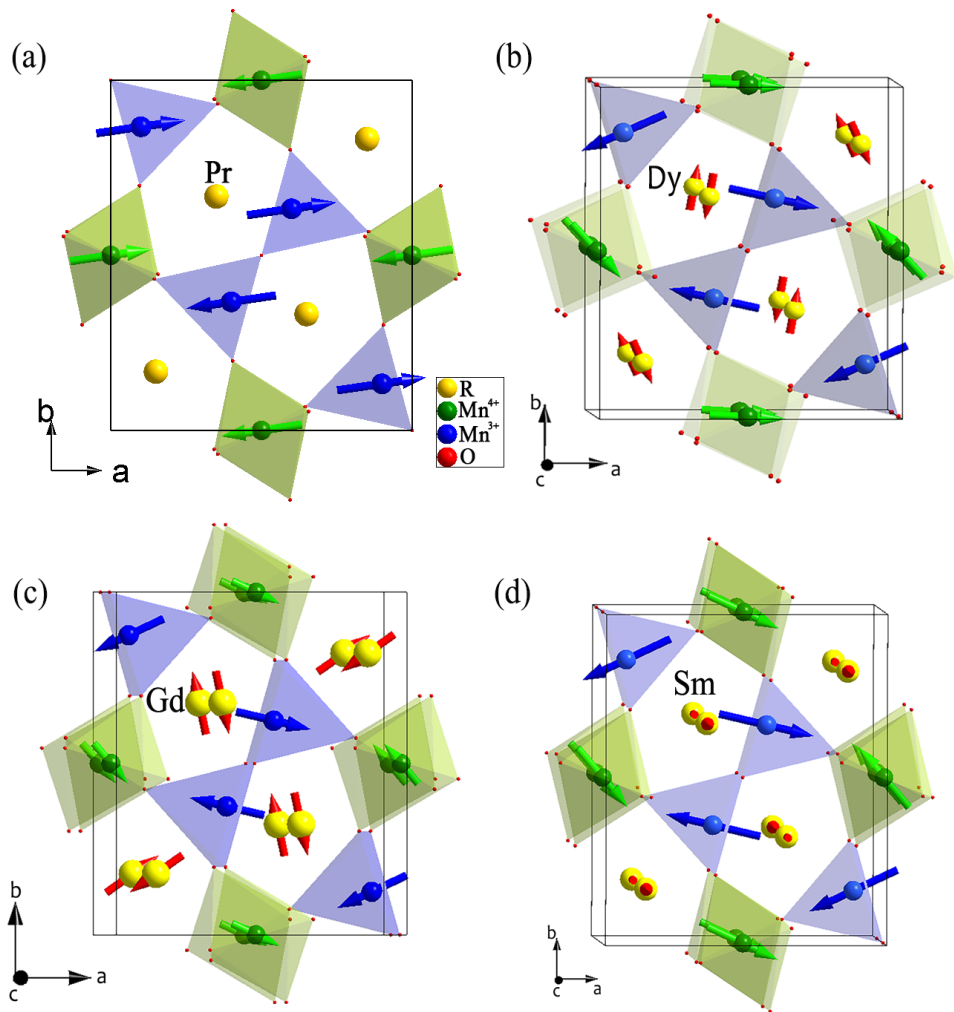


Figure 5.33 – Magnetic structure of the PCM phase of (a) PrMn_2O_5 at 8 GPa, 6K. (b) DyMn_2O_5 at 6.6 GPa, 18 K. The amplitude of the moments of Dy^{3+} have multiplied by a factor 3. (c) GdMn_2O_5 at 8.4 GPa, 32 K. The amplitude of the moments of Gd^{3+} have multiplied by a factor 8. (d) SmMn_2O_5 at 10.3 GPa, 32 K. The moments of Sm^{3+} are along the c axis. The amplitude of the moments of Sm^{3+} have multiplied by a factor 2.

6

Conclusion and Perspectives

The aim of this thesis was to study the multiferroic properties of the RMn_2O_5 family under pressure and to try to understand the different behaviors related to the pressure induced commensurate magnetic (PCM) phase observed under pressure.

6.1 Conclusion

The PCM phase of the RMn_2O_5 ($R = \text{Pr, Gd, Sm}$ and Dy) compounds studied in this thesis always presents the same commensurate propagation wave vector $\mathbf{q}_{\text{PCM}} = (\frac{1}{2}, 0, \frac{1}{2})$, as for the previous measurements of YMn_2O_5 and TbMn_2O_5 .

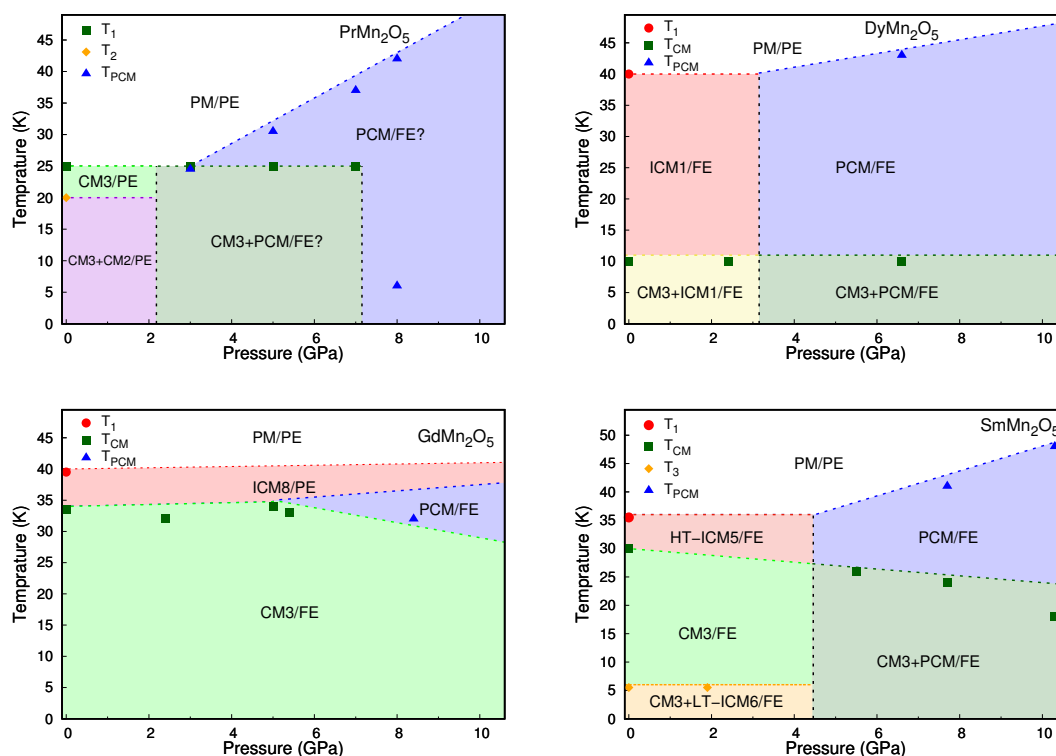


Figure 6.1 – Pressure-temperature phase diagrams of RMn_2O_5 ($R = \text{Pr, Gd, Sm}$ and Dy).

For the RMn_2O_5 ($R = \text{Dy, Gd}$ and Sm) studied, this PCM phase replaces the ICM phase under

pressure. With increasing the pressure, the PCM phase grows at the expense of the CM phase and the critical temperature of this PCM phase becomes higher. However, for the ground state at low temperature, the CM phase is always dominant even at high pressure. The PCM phase can only exist as a unique phase at high temperature. The corresponding phase diagrams are illustrated in Figure 6.1.

At ambient pressure, the CM phase, associated with $\mathbf{k}_z = 0$, is observed for RMn_2O_5 with a high R^{3+} spin such as $\text{R}=\text{Dy}$, Gd and Sm . It is dominant at low temperature up to a certain pressure. As for the PCM phase ($\mathbf{k}_z = \frac{1}{2}$), it is favored by a strong J_1 term in the Hamiltonian. An external pressure is expected to enhance the J_1 interaction term. To investigate this issue we have performed at room temperature, powder X-ray experiments of the RMn_2O_5 ($\text{R} = \text{Pr}$, Nd , Sm , Gd , Tb and Dy) compounds under pressure. The results of the refinement have been compared with our DFT calculations. We have found a very good agreement. Thanks to these calculations, we have been able to obtain the positions of the oxygen atoms difficult to extract from the X-ray measurement. Through the atomic positions of O and Mn ions, we have extracted the information concerning the evolution of the exchange interactions J_1 and J_4 as a function of pressure. The J_1 has been enhanced under pressure, which further confirms the mechanism presented above. An overall increase of the J_3 values of a few percent with no significant evolution of the difference between the two J_3 interactions, which infer that the amplitude of the polarization should not be affected by the pressure within the dominant CM phase ($q = (\frac{1}{2}, 0, 0)$). Thus the pressure-induced enhancement of the polarization of RMn_2O_5 compounds can only be attributed to the PCM phase. In addition, the $J_6\mathbf{S}(\text{R}^{3+}) \cdot \mathbf{S}(\text{Mn}^{3+})$ term in the Hamiltonian can be very small above a certain temperature due to the decrease of the amplitude of the ordered moments of the R^{3+} , even for R^{3+} with a high R^{3+} spin. Indeed, the Table 6.1 shows the values of the R^{3+} moments extracted from our magnetic refinements at high pressure and intermediate temperature. As shown in the table, the moments are smaller than $1 \mu\text{B}$.

Table 6.1 – Moments of R^{3+} at the highest pressure, $\sim 8 \pm 2$ GPa, at different temperature

R	Pr	Dy	Gd	Sm
moment (μ_B)	0 (@ 6 K)	0.6 (@ 18 K)	0.2 (@ 32 K)	0.5 (@ 32 K)

The competition between the J_1 and J_6 terms in the Hamiltonian can be expressed in Figure 6.2. This figure shows the (p,T) regions of the phase diagram for which the term J_i in the Hamiltonian (named \mathcal{H}_i) is dominant. The low temperature high pressure phase could be CM or PCM phase, depending on the R^{3+} .

We were able to refine the magnetic structure of the PCM phase in the compounds $\text{R} = \text{Dy}$, Gd , Sm and Pr . For DyMn_2O_5 and GdMn_2O_5 , the *planar* model fits the PCM phase well and is more physically acceptable than the other ones (anisotropy of R^{3+} and Mn ions respected). For SmMn_2O_5 , as the anisotropy of Sm^{3+} is along the c axis, the D_2 model obtained from our refinement satisfies the anisotropy of all the spins.

Furthermore, the case of PrMn_2O_5 is special as it presents two CM phases at ambient pressure and the system is non-ferroelectric. These two CM phases with either the moment of Mn^{3+} or the moment of Mn^{4+} which is nil, are orthogonal to each other. Note also that the J_6 term on the Hamiltonian is negligible because the spin of Pr^{3+} is nearly nil. For PrMn_2O_5 , the D_2 and *planar* models are identical because the spins on Pr^{3+} is zero. Finally, the collinearity of the Mn spins under high pressure might turn the PrMn_2O_5 to ferroelectric.

We can further compare the external pressure effect to the chemical pressure effect. As shown in Figure 6.3, the values of the lattice a and b of GdMn_2O_5 at ambient pressure are similar to the ones of SmMn_2O_5 at ~ 3 GPa and the values of the lattice a and b of TbMn_2O_5 at ambient pressure are similar to the ones of SmMn_2O_5 at ~ 5 GPa. The values of the lattice parameter c at ambient pressure are similar for all the three compounds. The contraction of the lattice parameter c is much less compared to the other two lattice parameters, which is only $\sim 0.03 \text{ \AA}$ up to the highest pressure (~ 8 GPa). With the pressure - temperature diagrams of the SmMn_2O_5 , GdMn_2O_5 and TbMn_2O_5 [135], we can see that

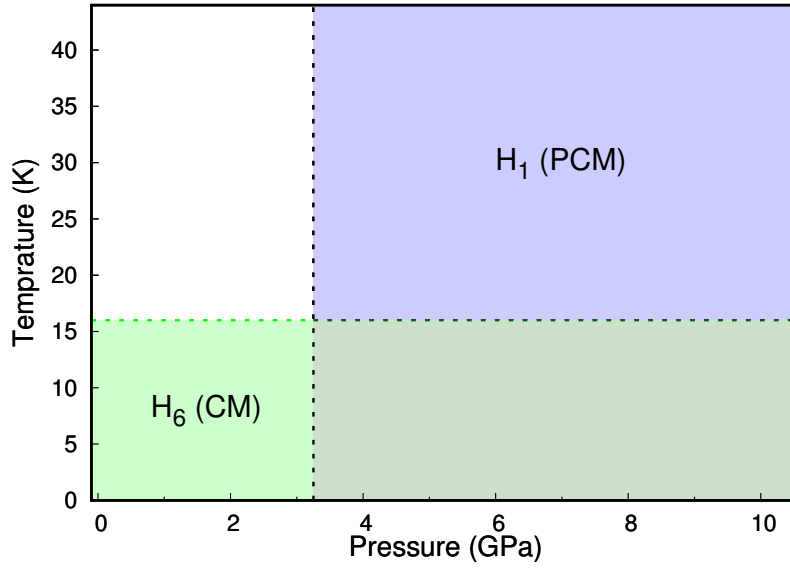


Figure 6.2 – Temperature - pressure phase diagram concerning the Hamiltonian $\mathcal{H}_i = \sum_{j,k} J_i \mathbf{S}_j \cdot \mathbf{S}_k$ ($i = 1$ and 6), \mathbf{S}_j and \mathbf{S}_k refer to the corresponding spin of Mn^{3+} and Mn^{4+} for J_1 or Mn^{3+} and R^{3+} for J_6 .

the magnetic phases of the SmMn_2O_5 at 3 GPa and 5 GPa have no relation with the ones of GdMn_2O_5 and TbMn_2O_5 . From the magnetic properties point of view, we can conclude that the effect of the external pressure and the effect of the chemical pressure are quite different. Our results show that the impact of the external pressure is very similar for all the members of the series. The phase diagram at high pressure is simple and involves the PCM which is probably the unique magnetic phase at very high pressure as for the PrMn_2O_5 case. Concerning the chemical pressure effect, it is more complex due to the fact that in addition to the contraction of the unit cell parameters, the chemical effect induces also a modification of the number of $4f$ electrons. The number of the $4f$ electrons is of tremendous importance on the magnetic properties firstly because it gives the amplitude of the magnetic moment and secondly due to the possible Kramers effect.

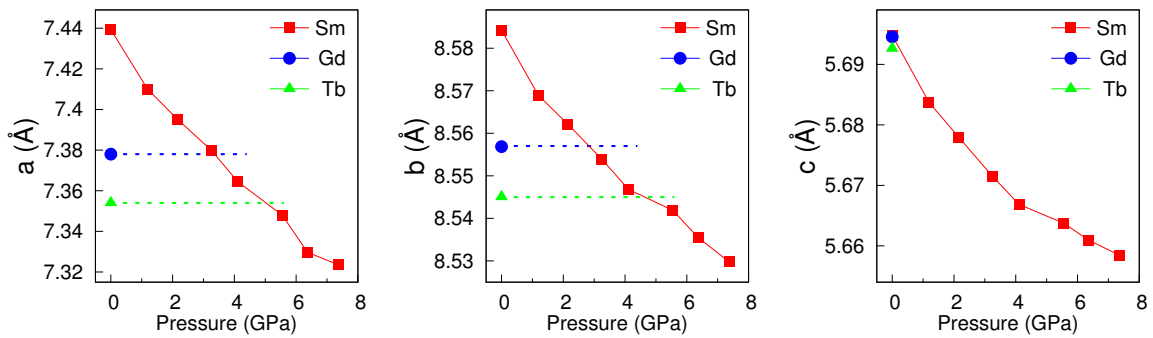


Figure 6.3 – Lattice parameters a , b , c of SmMn_2O_5 at different pressures with ambient lattice parameters of GdMn_2O_5 and TbMn_2O_5

6.2 Perspectives

This thesis work has answered a number of questions. There are, however, still some obscure points. In particular with regards to the fine determination of the PCM structure and the exact role of the exchange interactions J_i ($i = 1, 2, 3, 4, 5, 6$) to stabilize the various magnetic phases.

The PCM phase appears at high pressure and only becomes the unique magnetic phase at high

temperature for the RMn_2O_5 with high R^{3+} spins, $\text{R} = \text{Dy}, \text{Gd}$ and Sm . However, for the ambient pressure non-ferroelectric PrMn_2O_5 , the PCM phase appears at low pressure and becomes the unique phase in the whole temperature at high pressure. It would be thus interesting to study the weak ferroelectric compounds, such as NdMn_2O_5 . The origin of PCM phase in these compounds is a necessary complement for our study in this thesis.

As the PCM phase is stabilized at high pressure, it is necessary to continue to perform single crystal X-ray diffraction at low temperature and high pressure to extract information on the low temperature evolution of the J_i interactions as well as to study the evolution of the symmetry breaking associated with the $Pbam$ to Pm symmetry.

It would be very important to try to calculate the J_i exchange interactions, which can surely help us to understand the influence of the pressure and the origin of the different propagation wave vectors of the entire phase diagram. This approach could also be complemented by a single crystal inelastic neutron scattering study under pressure. Compared to simulations of the scattered intensities, this experiment can help to extract the values of the various exchange interactions in the system. In addition, it is interesting and crucial to study the spin dynamics such as the electromagnon under pressure. These could give even more convincing analysis for the multiferroic properties of the PCM phase.

List of Figures

1	Number of publications per year on multiferroics from year 1995 to 2017. Data from the web of science (key word:multiferroic OR magnetoelectric)	xix
1.1	The electric field \mathbf{E} , magnetic field \mathbf{H} , and stress control of the electric polarization \mathbf{P} , magnetization \mathbf{M} , and strain σ , respectively. In a ferroic material, \mathbf{P} , \mathbf{M} , or ε are spontaneously formed to produce ferromagnetism, ferroelectricity, or ferroelasticity, respectively [11].	2
1.2	Four primary forms of ferroic order under the parity operations of space and time [15].	2
1.3	Sketches of ferroelectricity and ferromagnetism as well as the mutual control between them in magnetoelectric coupling [16].	3
1.4	Types of multiferroicity [18].	5
1.5	(a) Shift of transition metal ion towards one of the oxygens, and (b) schematic energy levels with empty d levels (solid arrows) and with partially filled d levels (dashed arrow) [12].	6
1.6	A calculation of the charge density in multiferroic BiFeO_3 . The gold blobs are the Bi^{3+} ions' (black) lone-pair electrons; their alignment results in a ferroelectric polarization (\mathbf{P}) [27].	7
1.7	Illustration of how charge ordering can lead to ferroelectricity (the inversion centers are marked by \otimes) [28].	7
1.8	(a) Site-centered charge ordering in half-doped manganites like $\text{Pr}_{1/2}\text{Ca}_{1/2}\text{MnO}_3$, (b) bond-centred ordering, and (c) combined ordering, giving ferroelectricity [29].	8
1.9	The geometric mechanism responsible for the ferroelectricity in the YMnO_3 at low temperature [22].	8
1.10	Schematic illustrations of types of spiral magnetic structure that may give rise to multiferroicity [28].	10
1.11	Spin order for a one-dimensional spin chain with competing exchange interactions (a) sinusoidal. (b) spiral ground state [33].	11
1.12	(a) Effects of the antisymmetric Dzyaloshinskii–Moriya interaction. (b) antiferromagnets LaCu_2O_4 layers system. (c) cycloidal magnetic structure of RMnO_3 system [26].	12
1.13	Chain of Ising spins $\sigma_n = \pm 1$ with up–up–down–down ($\uparrow\uparrow\downarrow\downarrow$) ground state [26].	13
1.14	(a) One-dimensional chain with alternating charges. (b) one-dimensional chain with alternating spins and up–up–down–down ($\uparrow\uparrow\downarrow\downarrow$) spins. (c) exchange striction (ES) mechanism (magnetostriction), which shortens the ferromagnetic bonds, thus generates a ferroelectric polarization along the chain.	13
1.15	The (a, c) plane structure (in the $Pbnm$ notation) and magnetic (E-type antiferromagnetic) structure of orthorhombic RMnO_3 . The spins are denoted by arrows. The particular zigzag spin chains are highlighted by shaded areas. α^P and α^{aP} denote the Mn – O – Mn bond angles between the parallel and antiparallel spin pairs, respectively, noting that they are different due to the ES mechanism. [43]	14
1.16	A metal ion in an anion cage can break the inversion symmetry (left), in case of a metal-ligand hybridization because it gives rise to spin-dependent dipoles for the three different bonds allowing a net electric polarization (right). [46].	14

2.1	Projections of the crystal structure of RMn_2O_5 along (a) c and (b) b axis. The different J_i exchange interactions are indicated.	20
2.2	The CM structures of TbMn_2O_5 (27 K), HoMn_2O_5 (26 K) and DyMn_2O_5 (2 K) in the (a, b) plane. The unit cells are doubled along the a axis. [58]	20
2.3	The rare earth elements with weights and electrons distribution. From Wikipedia.	21
2.4	Dependence of the lattice parameters of the RMn_2O_5 compounds at room temperature and ambient pressure as a function of the ionic radii of R^{3+} . [13]	21
2.5	(a) Dependence of the electric polarization of the RMn_2O_5 compounds at ambient pressure as a function of the ionic radii of R^{3+} . Data from Ref. [48, 50, 60–68]. (b) Relation between the T_C of RMn_2O_5 and the ionic radii of R^{3+} . Data from Ref. [42, 50, 60, 62–66, 69, 70].	21
2.6	Magnetic and electric phase diagram of the RMn_2O_5 compounds. Here, PM, ICM, CM, PE, and FE are abbreviated forms used to denote paramagnetic, incommensurate magnetic, commensurate magnetic, paraelectric, and ferroelectric states, respectively.	22
2.7	Dielectric constant ε along b open circles, left scale and specific heat C_p/T closed circles, right scale of (a) TbMn_2O_5 and (b) DyMn_2O_5 [14]	23
2.8	Temperature dependence of the electric polarization for RMn_2O_5 ($\text{R} = \text{Y, Sm, Eu, Gd, Tb, Dy, Ho, Er, Tm, Yb}$ and Lu) by heating. [74]	23
2.9	(a) A schematic representation of the magnetic structure of the ICM phase of YMn_2O_5 . Magnetic exchange pathways are also indicated. (b) Symbols: electrical polarization of YMn_2O_5 , as calculated from Equation (2.1). Solid line: experimental values of the electrical polarization, extracted from [76]. [75]	24
2.10	Projection in the (a, b) plane of the magnetic moments along c represented by + and – symbols. The gray lines represent the AFM chains coupled through the J_3 exchange interactions (represented as red and blue ellipses: red for FM order; blue for AFM order).	25
2.11	The phase transitions of the RMn_2O_5 compounds and the corresponding magnetic propagation wave vectors presented on the right side. R means the low temperature R^{3+} ordering, which is stabilized at the same propagation wave vector as the Mn ordering. The values of δ_x (δ_z) range between 0.012 ~ 0.028 (-0.013 ~ 0.027). [42, 44, 56–60, 65, 67, 77–81]	26
2.12	Magnetization versus magnetic field along the three axes of (a) TbMn_2O_5 and DyMn_2O_5 at 3 K. [48]. (b) GdMn_2O_5 at 2 K. [50]	27
2.13	(a) The highly reversible 180° flipping of electric polarization \mathbf{P} along the b axis in TbMn_2O_5 by applying magnetic field along the a axis at 3 K. [9] (b) repeated variation of \mathbf{P} along the b axis (red circles) in GdMn_2O_5 at 2 K by applying reversible magnetic fields along the a axis (light blue lines). [50]	28
2.14	(A) The structure and AFM zig-zag spin chains under various magnetic fields for BiMn_2O_5 . Red, dark blue, and light blue arrows represent spin directions at $\mathbf{H} = 0$, $\mathbf{H} = \mathbf{H}_C$, and $\mathbf{H} \gg \mathbf{H}_C$, respectively. (B-D) The corresponding simplified spin arrangements and the net \mathbf{P} (black open arrows) are also shown. [82]	29
2.15	(a) Temperature dependence of ε along the b axis in various magnetic field along the a axis. (b) ε along the b axis in \mathbf{H} applied along the b axis. [48]	29
2.16	Temperature dependence of dielectric constant ε_b and electric polarization \mathbf{P}_b parallel to the b axis under various magnetic fields in HoMn_2O_5 ((a) and (b)) and in ErMn_2O_5 ((c) and (d)). [64]	30
2.17	(a) Temperature dependence of the polarization \mathbf{P}_a and \mathbf{P}_b of TmMn_2O_5 during heating under zero magnetic field. The inset shows the crystal structure of TmMn_2O_5 . (b) Magnetic field dependence of \mathbf{P}_a and \mathbf{P}_b at 4.2 K. [49]	30
2.18	Temperature profile of the (A) low temperature and (B) high temperature ε_b and (C) \mathbf{P}_b of TbMn_2O_5 under isotropic pressures (warming only). [87]	31
2.19	Temperature profile of the (A) low temperature and (B) high temperature ε_b and (C) \mathbf{P}_b of DyMn_2O_5 under isotropic pressures (warming only). [87]	31

2.20	Pressure-temperature (p-T) phase diagram for DyMn_2O_5 . The pressure separated X phase was found to be paraelectric [87]	32
2.21	Dielectric constant ε_b and ferroelectric polarization of YMn_2O_5 at 5 K as a function of pressure. [66]	32
2.22	(a) Dielectric constant ε_b (b) ferroelectric polarization \mathbf{P}_b of GdMn_2O_5 at different pressures. [88, 89]	33
2.23	Transmission spectra of TbMn_2O_5 : (a) thin sample, (b) thicker sample, oscillations are averaged out in model curves. \mathbf{e} and \mathbf{h} are electric and magnetic fields of light. Transmission spectra of YMn_2O_5 with $\mathbf{H} \parallel \mathbf{a}$ and (c) $\mathbf{e} \parallel \mathbf{b}$, (d) $\mathbf{e} \parallel \mathbf{c}$. [51]	33
2.24	Dielectric constant ε of TbMn_2O_5 from fits of infrared spectra (lower curve) in comparison with high frequency measurements. [51]	34
3.1	(a) Schematic of the standard X-ray tube with power increased by rotating the anode. [93] (b) schematic representation of the X-ray spectrum. [94]	39
3.2	Schematic diagram of diffraction of the X-rays by a crystal (Bragg law). [94]	41
3.3	Schematic of a standard $\theta - 2\theta$ X-ray diffractometer. [94]	42
3.4	The relationships between the reciprocal lattice (for a powder sample, they are spheres.) and the Ewald sphere (formation of a cone of diffracted X-rays) in the Debye–Scherrer method. [94]	43
3.5	The fraction of the diffracted intensity contributing from a surface layer of depth t to the total diffracted intensity of a sample of semi-infinite thickness. [94]	44
3.6	Intensity diffracted from a crystalline sample rotated through the Bragg angle. [94]	45
3.7	Top view of the X-ray diffraction set-up. A: X-ray beam, B: pressure cell, C: 2D Mar345 detector, D: the motor, connected to the pressure by ruby luminescence system.	47
3.8	Schematic representation of the gasket treatments.	47
3.9	Schematic representation of the diamond anvil cell.	48
3.10	The pressure by ruby luminescence system . M indicates the lens.	48
3.11	The fluorescent curve measured under different pressure. Dots: the measured data. Lines: the fitted curve through Equation (3.18).	49
3.12	The scattering of a plane wave of neutrons by a single scatterer. [99]	51
3.13	Geometry for a scattering experiment. [100]	52
3.14	The form factor $f(\mathbf{Q})$ for the scattering of X-rays and for the nuclear and magnetic scattering of neutrons. [99]	54
3.15	The D1B instrument (ILL, Grenoble). From ILL D1B website.	56
3.16	The D20 instrument (ILL, Grenoble). From ILL D20 website.	56
3.17	The Paris–Edinburgh pressure cell (left), the standard anvil and gasket configuration and the standard and encapsulated gasket designs (right). [103]	57
3.18	The information deduced from the powder diffraction data.	59
3.19	The menu of the FullProf Suite	61
3.20	The synthesis process of PrMn_2O_5 powder sample.	62
3.21	Rietveld refinement (experimental data: black open circles, calculated profile: red continuous line, allowed Bragg reflections: blue ticks). The difference between the experimental and calculated profiles is displayed at the bottom of the graph of the crystal structure of PrMn_2O_5 at 4 K [59].	63
4.1	The raw MAR image of CeO_2 and the starting values of the calibration from Dioplas	67
4.2	The MAR image of CeO_2 with masks and the refined values of the calibration from Dioplas	67
4.3	The MAR image of CeO_2 with masks and the integrated data from the Dioplas. The masks can exclude the obvious diffraction peaks from the diamond and some of the preferred orientations diffraction dots.	68
4.4	(a) The X-ray diffraction of CuBe gasket. (b) The refined X-ray diffraction of standard CeO_2 with and without the peaks of the gasket.	68

4.5	The X-ray diffraction patterns of RMn_2O_5 ($\text{R} = \text{Pr}, \text{Nd}$ and Sm) under different pressures.	69
4.6	The X-ray diffraction patterns of RMn_2O_5 ($\text{R} = \text{Gd}, \text{Tb}$ and Dy) under different pressures.	70
4.7	The X-ray diffraction patterns of PrMn_2O_5 and TbMn_2O_5 at some selected pressure. .	71
4.8	The refinements of (a) GdMn_2O_5 at 6.99 GPa and of (b) TbMn_2O_5 at 3.61 GPa. The experimental data are in red, the calculated profile in black, and their difference in blue. The green ticks refer to the nuclear reflections. The peaks of the gasket have been excluded.	72
4.9	Measured unit cell parameters $((a_i - a_{i0})/a_{i0})$ of RMn_2O_5 with respect to their ambient pressure values. The error bars are of the size of the symbols. a_{i0} : unit cell parameters at ambient pressure. Note that for the sake of clarity in all the figures of the paper, the data related to a given R^{3+} compound are always represented with the same color. . .	73
4.10	Unit cell parameters $((a_i - a_{i0})/a_{i0})$ of GdMn_2O_5 and DyMn_2O_5 with respect to their ambient pressure values calculated by DFT. a_{i0} : unit cell parameters at ambient pressure.	73
4.11	Relative pressure dependence of the molar volume V/V_0 of the RMn_2O_5 with respect to their ambient pressure values. The solid lines show the fits using the EoS of Ref [132] with the Equation (4.1).	74
4.12	Measured ionic displacements $ u $ of the RMn_2O_5 ($\text{R} = \text{Pr}, \text{Sm}, \text{Gd}, \text{Nd}, \text{Tb}, \text{Dy}$) with respect to their initial pressure values, of R^{3+} (left), of Mn^{4+} (middle) and of Mn^{3+} (right). The error bars are within the width of the points.	75
4.13	Comparison of pressure evolution of the ionic displacements $ u $ of Gd^{3+} and Dy^{3+} by X-ray experiments and DFT calculations, with respect to their initial pressure values.	76
4.14	(a) A magnified representation of Mn^{4+}O_6 octahedra and Mn^{3+}O_5 pyramid involved in the super-exchange J_3 and J_4 . (b) Structure of RMn_2O_5 in the (a, b) plane in Pm space group within CM magnetic phase ($q = (\frac{1}{2}, 0, 0)$). Inequivalent super-exchange interactions J_3 and J_4 are indicated.	77
4.15	Variation of the structural parameters involved in the J_3 amplitudes as a function of the applied pressure. The circles are for the DyMn_2O_5 compound and the crosses for the GdMn_2O_5 one. left) $\text{Mn}^{4+}\text{-O4}$ and $\text{Mn}^{3+}\text{-O4}$ distances (\AA), right) $\cos^2 \alpha$, α being the $\text{Mn}^{4+}\text{-O4-Mn}^{3+}$ angle. (AFM) refers to the geometrical parameters between the atoms involved in AFM ordered $\text{Mn}^{4+}\text{-Mn}^{3+}$ ions, while (FM) refers to the parameters between the FM ordered ones.	78
4.16	Variation of the structural parameters involved in the J_4 amplitudes as a function of the applied pressure. The circles are for the DyMn_2O_5 compound and the crosses for the GdMn_2O_5 one. left) $\text{Mn}^{4+}\text{-O3}$ and $\text{Mn}^{3+}\text{-O3}$ distances (\AA), right) $\sin \alpha$, α_1 and α_2 being the two inequivalent $\text{Mn}^{4+}\text{-O3-Mn}^{3+}$ angles.	78
5.1	Pressure evolution of (a) temperature dependence of the ferroelectric polarization [66] and (b) the magnetic patterns at 1.5 K subtracted from the 40 K diffraction pattern of YMn_2O_5 [90].	82
5.2	Magnetic patterns of TbMn_2O_5 at 1.5 K. The magnetic peak $\sim 1 \text{\AA}^{-1}$ indicates the onset of the pressure-induced commensurate (PCM) phase. [90]	83
5.3	Selected information of Pr^{3+} from the output BSR file of <i>BasIreps</i>	84
5.4	Selected basic function information of Pr^{3+} from the output FP file <i>BasIreps</i>	84
5.5	The magnetic ordering in the (a, b) plane of PrMn_2O_5 : (a) the CM1 phase at 20 K; (b) the CM2 phase at 1.5 K. [59]	85
5.6	(a) Dielectric constant ϵ_b measurement and (b) dielectric loss measurement of PrMn_2O_5 single crystal as a function of temperature under various pressures (warming and cooling)	86
5.7	PND diffractograms of PrMn_2O_5 (a) under 3 GPa, at 6 K, 11 K, 20 K and 30 K (b) under 7 GPa at 6 K, 11 K and 20 K.	87
5.8	Rietveld refinements of the neutron diffraction data of PrMn_2O_5 at the lowest temperature, 6 K, and under 3 GPa, 5 GPa and 8 GPa.	88
5.9	Evolution as a function of pressure of the ratio between the ambient pressure CM3 and the pressure induced PCM phases in PrMn_2O_5 at 6 K.	88

5.10	Pressure-temperature phase diagram of PrMn_2O_5 . The lines are a guide to the eye.	89
5.11	Magnetic structure of PrMn_2O_5 at 6 K and 8 GPa (a) in the (a, b) plane with the 2_1 (b) and a $2'_1$ (b') screw axis (glide plane) between Mn^{3+} and Mn^{4+} , and (b) in the (a, c) plane.	89
5.12	Relative pressure dependence of the unit cell parameters $((a_i - a_{i0})/a_{i0})$ of PrMn_2O_5 with respect to their ambient pressure values at 6 K. a_{i0} is a unit cell parameter under ambient pressure at 6 K. Lattice parameters from the refinement of the PND data.	91
5.13	Magnetic structure of (a) the HT phase at 15 K with the spiral arrangement of Mn ions; (b) the LT phase at 2 K. Magnetic interactions J_3, J_4 and J_5 are also shown [56].	92
5.14	(a) The dominant Mn-Mn exchange interactions in the (a, c) plane. It also shows Mn^{3+} - Dy^{3+} interaction J_6 along c . (b) Detailed paths of interaction for J_6 [56].	93
5.15	PND curves under 2.4 GPa, at 6 K, 14 K, 22 K and 60 K. Reflections of nuclear phase, CM phase and ICM phase are indicated respectively.	94
5.16	PND curves under the highest pressure, 6.6 GPa, at 6 K, 10 K, 18 K, 25 K and 60 K. Reflections of nuclear phase, CM phase and PCM phase are indicated respectively.	94
5.17	Pressure-temperature phase diagram of DyMn_2O_5 . The lines are a guide to the eye.	95
5.18	Magnetic structure of DyMn_2O_5 at 18 K, 6.6 GPa with the D_1, D_2 and <i>planar</i> models. For the sake of clarity, the amplitude of the moments of Mn^{3+} and Mn^{4+} in D_1 model have multiplied by a factor 2, the amplitude of the moments of Dy^{3+} in D_2 model have multiplied by a factor 2 and the amplitude of the moments of Dy^{3+} in <i>planar</i> model have multiplied by a factor 3.	96
5.19	Schematic 1D chains representing the energy gains for different propagation components \mathbf{k}_z along the c axis. (a) $\mathbf{k}_z = \frac{1}{2}$ (as for the PCM phase). (b) $\mathbf{k}_z = 0$ (as for the CM phase of DyMn_2O_5 at ambient pressure).	98
5.20	(a) Magnetic structure of GdMn_2O_5 at 1.5 K. The blue (orange) ellipses show the $\text{Mn}^{3+} / \text{Mn}^{3+}$ ($\text{Gd}^{3+} / \text{Mn}^{3+}$) AFM pairs. Stars identify the $\text{Gd}^{3+} / \text{Mn}^{3+}$ pair proposed by Lee <i>et al.</i> in their model for a Gd - Mn ES mechanism[50]. (b) Atomic displacements associated with the release of the magnetic frustration at the origin of the two ES mechanisms, leading to the polarization. [57]	99
5.21	Pressure evolutions of the CM phase at 7 K (a) the PND curves at 2.4, 5.0 and 8.4 GPa and (b) the corresponding amplitude of the moments of Gd and Mn.	100
5.22	(a) PND curves and (b) the magnetic structure in the (a, b) plane of the CM phase of GdMn_2O_5 at 8.4 GPa, 7 K.	101
5.23	Temperature evolutions of CM phase at 2.4 GPa (a) at 7, 20 and 32 K and (b) the corresponding amplitude of moments of Gd and Mn ions.	101
5.24	PND curves under the highest pressure, 8.4 GPa, at 32 K for the D_1, D_2 and <i>planar</i> models	102
5.25	Magnetic structure of the PCM phase of GdMn_2O_5 at 32 K, 8.4 GPa. The amplitude of the moments of Gd^{3+} are multiplied by a factor 8 for the sake of clarity.	103
5.26	Pressure-temperature phase diagram of GdMn_2O_5 . The lines are a guide to the eye.	104
5.27	Perspective view of the magnetic structure of SmMn_2O_5 at 6 K. The blue Mn^{3+} pyramids and the red Mn^{4+} octahedra are represented. [44]	105
5.28	Diffraction patterns and phase ratio of the pressure evolutions of the CM and PCM phases at 15 K.	106
5.29	PND curves of SmMn_2O_5 at 10.3 GPa and 32 K. No CM phase is present.	107
5.30	Magnetic structure of SmMn_2O_5 at 32 K, 10.3 GPa. The moments of Sm^{3+} are along the c axis. The amplitude of the moments of Sm^{3+} are multiplied by a factor 2 for the sake of clarity	107
5.31	Pressure-temperature phase diagram of SmMn_2O_5 . The lines are a guide to the eye.	108
5.32	Schematic 1D chains representing the energy gains for different propagation components \mathbf{k}_z along the c axis. (a) $\mathbf{k}_z = \frac{1}{2}$ (as for the PCM phase). (b) $\mathbf{k}_z = 0$ (as for the CM phase of SmMn_2O_5 at ambient pressure with all the spins along c axis.).	109

5.33	Magnetic structure of the PCM phase of (a) PrMn_2O_5 at 8 GPa, 6K. (b) DyMn_2O_5 at 6.6 GPa, 18 K. The amplitude of the moments of Dy^{3+} have multiplied by a factor 3. (c) GdMn_2O_5 at 8.4 GPa, 32 K. The amplitude of the moments of Gd^{3+} have multiplied by a factor 8. (d) SmMn_2O_5 at 10.3 GPa, 32 K. The moments of Sm^{3+} are along the c axis. The amplitude of the moments of Sm^{3+} have multiplied by a factor 2.	111
6.1	Pressure-temperature phase diagrams of RMn_2O_5 ($R = \text{Pr, Gd, Sm and Dy}$).	113
6.2	Temperature - pressure phase diagram concerning the Hamiltonian $\mathcal{H}_i = \sum_{j,k} J_i \mathbf{S}_j \cdot \mathbf{S}_k$ ($i = 1$ and 6), \mathbf{S}_j and \mathbf{S}_k refer to the corresponding spin of Mn^{3+} and Mn^{4+} for J_1 or Mn^{3+} and R^{3+} for J_6	115
6.3	Lattice parameters a, b, c of SmMn_2O_5 at different pressures with ambient lattice parameters of GdMn_2O_5 and TbMn_2O_5	115

List of Tables

1.1	Classification of multiferroics due to different microscopic mechanism of ferroelectricity [19].	15
2.1	Atomic positions of DyMn ₂ O ₅ at 298 K in the <i>Pbam</i> space group. The lattice parameters are $a = 7.2940 \text{ \AA}$, $b = 8.5510 \text{ \AA}$, $c = 5.6875 \text{ \AA}$. [53]	18
2.2	Atomic positions of DyMn ₂ O ₅ at 300 K in the <i>Pm</i> space group. The lattice parameters are $a = 7.2931 \text{ \AA}$, $b = 8.5025 \text{ \AA}$, $c = 5.6743 \text{ \AA}$. $\gamma = 90^\circ$. [52]	19
2.3	Magnetic easy axis of the RMn ₂ O ₅ compounds.	28
2.4	Main factors that affect the multiferroic properties of the RMn ₂ O ₅ family.	35
3.1	Relationship between Bravais lattice and reflections [94].	41
3.2	B_0 and B'_0 values of the Rydberg-Vinet EOS equation. [106]	58
4.1	Lattice parameters of RMn ₂ O ₅ (R = Pr, Nd, Sm, Gd, Tb and Dy) at ambient pressure, room temperature in the <i>Pbam</i> space group.	70
4.2	Refined structural parameters of RMn ₂ O ₅ (R = R = Pr, Nd, Sm, Gd, Tb and Dy) at ambient pressure, room temperature in the <i>Pbam</i> space group.	71
4.3	Refined structural parameters of RMn ₂ O ₅ (R = R = Pr, Nd, Sm, Gd, Tb and Dy) at the highest pressure, room temperature. The position of the oxygens are fixed to the ones of the ambient pressure.	72
4.4	The Pressure – volume data fitted of RMn ₂ O ₅ compounds.	74
5.1	Refined results for the magnetic structure parameters of PrMn ₂ O ₅ at 6 K and 8 GPa in the magnetic space group $Pmc'2'_1$ with $\chi^2 = 2.09$, $R_p = 33.5\%$, $R_{wp} = 20.3\%$, $R_{exp} = 14.1\%$, $R_{Bragg} = 9.1\%$ and $R_{mag} = 21.7\%$	90
5.2	Refined parameters of the PCM phase of DyMn ₂ O ₅ at 18 K, 6.6 GPa with different models. Magnetic moments of Dy ³⁺ and Mn ions are in μ_B and the agreement factors are in %	95
5.3	Refined results for the magnetic structure parameters of DyMn ₂ O ₅ at 18 K, 6.6 GPa with the <i>planar</i> model in <i>P1</i> space group. ϕ and θ refer to the polar angle and the azimuthal angle, respectively.	95
5.4	Refined parameters of the PCM phase of the GdMn ₂ O ₅ at 8.4 GPa and 32 K with the <i>D</i> ₂ and <i>planar</i> models. Magnetic moments of Gd ³⁺ and Mn ions are in μ_B and the agreement factors are in %	102
5.5	Refined results for the magnetic structure parameters of GdMn ₂ O ₅ at 32 K, 8.4 GPa with the <i>planar</i> model in <i>P1</i> space group with $\chi^2 = 1.85$, $R_p = 43.2\%$, $R_{wp} = 27.7\%$, $R_{exp} = 20.1\%$, $R_{Bragg} = 4.0\%$ and $R_{mag} = 27.4 \%$. ϕ and θ refer to the polar angle and the azimuthal angle, respectively.	103
5.6	Magnetic structure parameters of the CM phase of SmMn ₂ O ₅ at 1.9 GPa, 15 K in the <i>P</i> _{2am} space group with $\chi^2 = 30.7$, $R_p = 30.2\%$, $R_{wp} = 18.7\%$, $R_{exp} = 3.4\%$, $R_{Bragg} = 2.9\%$ and $R_{mag} = 21.5\%$. All the moments are along the <i>c</i> direction.	106
5.7	Refinement results for the PCM phase of SmMn ₂ O ₅ at 32 K, 10.3 GPa in <i>P1</i> space group with $\chi^2 = 52.9$, $R_p = 47.6\%$, $R_{wp} = 25.6\%$, $R_{exp} = 3.5\%$, $R_{Bragg} = 2.5\%$ and $R_{mag} = 34.1\%$. ϕ and θ refer to the polar angle and the azimuthal angle, respectively.	108

6.1	Moments of R^{3+} at the highest pressure, $\sim 8 \pm 2$ GPa, at different temperature	114
-----	---	-----

Bibliography

- [1] P. Curie. “Sur la symétrie dans les phénomènes physiques, symétrie d’un champ électrique et d’un champ magnétique.” In: *J. Phys. Theor. Appl.* 3.1 (1894), pp. 393–415 (cit. on p. [xix](#)).
- [2] L. D. Landau and E. M. Lifshitz. *Electrodynamics of Continuous Media*. Oxford: Pergamon Press, 1960, p. 119. DOI: [10.1119/1.1937882](#) (cit. on p. [xix](#)).
- [3] I. Dzyaloshinskii. “On the magneto-electrical effect in antiferromagnets.” In: *Sov. Phys. JETP-USSR* 10.3 (1960), pp. 628–629 (cit. on p. [xix](#)).
- [4] D. N. Astrov. “Discovery of the electrically induced magnetoelectric effect.” In: *Theor. Phys.(USSR.)* 38 (1960), pp. 984–990 (cit. on p. [xix](#)).
- [5] H. Schmid. “Multi-ferroic magnetoelectrics.” In: *Ferroelectrics* 162.1 (1994), pp. 317–338. DOI: [10.1080/00150199408245120](#) (cit. on pp. [xix](#), [1](#)).
- [6] N. A. Hill. “Why Are There so Few Magnetic Ferroelectrics?” In: *J. Phys. Chem. B* 104.29 (2000), pp. 6694–6709. DOI: [10.1021/jp000114x](#) (cit. on pp. [xix](#), [6](#)).
- [7] J. Wang, J. B. Neaton, H. Zheng, et al. “Epitaxial BiFeO₃ Multiferroic Thin Film Heterostructures.” In: *Science (80-.)*. 299.5613 (2003), pp. 1719–1722. DOI: [10.1126/science.1080615](#) (cit. on p. [xix](#)).
- [8] T. Kimura, T. Goto, H. Shintani, et al. “Magnetic control of ferroelectric polarization.” In: *Nature* 426.6962 (2003), pp. 55–58. DOI: [10.1038/nature02018](#) (cit. on pp. [xix](#), [5](#), [9](#), [27](#)).
- [9] N. Hur, S. Park, P. A. Sharma, et al. “Electric polarization reversal and memory in a multiferroic material induced by magnetic field.” In: *Nature* 429.6990 (2004), pp. 392–395. DOI: [10.1038/nature02572](#) (cit. on pp. [xix](#), [5](#), [9](#), [18](#), [28](#)).
- [10] M. Fiebig. “Revival of the magnetoelectric effect.” In: *J. Phys. D: Appl. Phys.* 38.8 (2005), R123–R152. DOI: [10.1088/0022-3727/38/8/R01](#) (cit. on pp. [xix](#), [3](#), [4](#)).
- [11] N. A. Spaldin. “MATERIALS SCIENCE: The Renaissance of Magnetoelectric Multiferroics.” In: *Science (80-.)*. 309.5733 (2005), pp. 391–392. DOI: [10.1126/science.1113357](#) (cit. on pp. [xix](#), [2](#)).
- [12] D. I. Khomskii. “Multiferroics: Different ways to combine magnetism and ferroelectricity.” In: *J. Magn. Magn. Mater.* 306.1 (2006), pp. 1–8. DOI: [10.1016/j.jmmm.2006.01.238](#) (cit. on pp. [xix](#), [6](#)).
- [13] I. Kagomiya, K. Kohn, and T. Uchiyama. “Structure and Ferroelectricity of RMn₂O₅.” In: *Ferroelectrics* 280.1 (2002), p. 131. DOI: [10.1080/00150190214799](#) (cit. on pp. [xix](#), [21](#)).
- [14] C. R. dela Cruz, F. Yen, B. Lorenz, et al. “Structural anomalies at the magnetic and ferroelectric transitions in RMn₂O₅ (R=Tb, Dy, Ho).” In: *Phys. Rev. B* 73.10 (2006), p. 100406. DOI: [10.1103/PhysRevB.73.100406](#) (cit. on pp. [xx](#), [22](#), [23](#)).
- [15] B. B. Van Aken, J. P. Rivera, H. Schmid, et al. “Observation of ferrotoroidic domains.” In: *Nature* 449.7163 (2007), pp. 702–705. DOI: [10.1038/nature06139](#) (cit. on pp. [1](#), [2](#)).
- [16] Y. Tokura. “Multiferroics—toward strong coupling between magnetization and polarization in a solid.” In: *J. Magn. Magn. Mater.* 310.2 (2007), pp. 1145–1150. DOI: [10.1016/j.jmmm.2006.11.198](#) (cit. on p. [3](#)).

- [17] C. W. Nan, M. I. Bichurin, S. Dong, et al. “Multiferroic magnetoelectric composites: Historical perspective, status, and future directions.” In: *J. Appl. Phys.* 103.3 (2008), p. 31101. doi: [10.1063/1.2836410](https://doi.org/10.1063/1.2836410) (cit. on p. 3).
- [18] M. Fiebig. “The evolution of multiferroics.” In: *Nat. Rev. Mater.* 1 (2016), p. 16046. doi: [10.1038/natrevmats.2016.46](https://doi.org/10.1038/natrevmats.2016.46) (cit. on p. 5).
- [19] D. Khomskii. “Trend: Classifying multiferroics: Mechanisms and effects.” In: *Physics (College Park, Md)*. 2 (2009), p. 20 (cit. on pp. 5, 15).
- [20] T. Zhao, A. Scholl, F. Zavaliche, et al. “Electrical control of antiferromagnetic domains in multiferroic BiFeO₃ films at room temperature.” In: *Nat. Mater.* 5.10 (2006), pp. 823–829. doi: [10.1038/nmat1731](https://doi.org/10.1038/nmat1731) (cit. on p. 5).
- [21] Z. Huang, Y. Cao, Y. Sun, et al. “Coupling between the ferroelectric and antiferromagnetic orders in YMnO₃.” In: *Phys. Rev. B* 56.5 (1997), pp. 2623–2626. doi: [10.1103/PhysRevB.56.2623](https://doi.org/10.1103/PhysRevB.56.2623) (cit. on p. 5).
- [22] B. B. Van Aken, T. T. Palstra, A. Filippetti, et al. “The origin of ferroelectricity in magnetoelectric YMnO₃.” In: *Nat. Mater.* 3.3 (2004), pp. 164–170. doi: [10.1038/nmat1080](https://doi.org/10.1038/nmat1080) (cit. on pp. 5, 8).
- [23] J. B. Goodenough and J. M. Longo. “Landolt-Brönstein, Numerical Data and Functional Relationships in Science and Technology, New Series.” In: *Springer, Berlin* III.4 (1970), p. 126 (cit. on p. 5).
- [24] T. Mitsui. “Landolt-Brönstein, Numerical Data and Functional Relationships in Science and Technology, New Series.” In: *Springer, Berlin* 16(1) (1981) (cit. on p. 5).
- [25] R. E. Cohen. “Origin of ferroelectricity in perovskite oxides.” In: *Nature* 358.6382 (1992), pp. 136–138. doi: [10.1038/358136a0](https://doi.org/10.1038/358136a0) (cit. on p. 6).
- [26] S. W. Cheong and M. Mostovoy. “Multiferroics: a magnetic twist for ferroelectricity.” In: *Nat. Mater.* 6.1 (2007), pp. 13–20. doi: [10.1038/nmat1804](https://doi.org/10.1038/nmat1804) (cit. on pp. 7, 8, 12, 13).
- [27] N. A. Spaldin, S. W. Cheong, and R. Ramesh. “Multiferroics: past, present, and future.” In: *Phys. Today* 63.10 (2010), pp. 38–43. doi: [10.1063/1.3502547](https://doi.org/10.1063/1.3502547) (cit. on p. 7).
- [28] J. L. Wang. “Multiferroic Materials: Properties, Techniques, and Applications.” In: *CRC Press*. Elsevier, 2016, pp. 155–191. doi: [10.1016/B978-0-12-385142-0.00004-0](https://doi.org/10.1016/B978-0-12-385142-0.00004-0) (cit. on pp. 7, 10).
- [29] D. V. Efremov, J. van den Brink, and D. I. Khomskii. “Bond- versus site-centred ordering and possible ferroelectricity in manganites.” In: *Nat. Mater.* 3.12 (2004), pp. 853–856. doi: [10.1038/nmat1236](https://doi.org/10.1038/nmat1236) (cit. on p. 8).
- [30] P. Monceau, F. Y. Nad, and S. Brazovskii. “Ferroelectric Mott-Hubbard Phase of Organic (TMTTF)₂X Conductors.” In: *Phys. Rev. Lett.* 86.18 (2001), pp. 4080–4083. doi: [10.1103/PhysRevLett.86.4080](https://doi.org/10.1103/PhysRevLett.86.4080) (cit. on p. 8).
- [31] A. P. Pyatakov and A. K. Zvezdin. “Magnetoelectric and multiferroic media.” In: *Physics-Uspokhi* 55.6 (2012), p. 557. doi: [10.3367/UFNe.0182.201206b.0593](https://doi.org/10.3367/UFNe.0182.201206b.0593) (cit. on p. 9).
- [32] M. Mostovoy. “Ferroelectricity in Spiral Magnets.” In: *Phys. Rev. Lett.* 96.6 (2006), p. 067601. doi: [10.1103/PhysRevLett.96.067601](https://doi.org/10.1103/PhysRevLett.96.067601) (cit. on p. 9).
- [33] K. F. Wang, J. M. Liu, and Z. F. Ren. “Multiferroicity: the coupling between magnetic and polarization orders.” In: *Adv. Phys.* 58.4 (2009), pp. 321–448. doi: [10.1080/00018730902920554](https://doi.org/10.1080/00018730902920554) (cit. on pp. 10, 11).
- [34] I. Dzyaloshinskii. “Theory of helical structures in antiferromagnets I: Nonmetals.” In: *Sov. Phys. JETP* 19 (1964), pp. 960–971 (cit. on p. 11).
- [35] T. Moriya. “Anisotropic superexchange interaction and weak ferromagnetism.” In: *Phys. Rev.* 120 (1960), pp. 91–98. doi: [10.1103/PhysRev.120.91](https://doi.org/10.1103/PhysRev.120.91) (cit. on p. 11).

- [36] I. A. Sergienko, C. Şen, and E. Dagotto. “Ferroelectricity in the magnetic E-phase of orthorhombic perovskites.” In: *Phys. Rev. Lett.* 97.22 (2006), pp. 3–6. doi: [10.1103/PhysRevLett.97.227204](https://doi.org/10.1103/PhysRevLett.97.227204) (cit. on pp. 11, 13).
- [37] H. Katsura, N. Nagaosa, and A. V. Balatsky. “Spin current and magnetoelectric effect in noncollinear magnets.” In: *Phys. Rev. Lett.* 95.5 (2005), pp. 1–4. doi: [10.1103/PhysRevLett.95.057205](https://doi.org/10.1103/PhysRevLett.95.057205) (cit. on p. 11).
- [38] M. E. Fisher and W. Selke. “Infinitely Many Commensurate Phases in a Simple Ising Model.” In: *Phys. Rev. Lett.* 44.23 (1980), pp. 1502–1505. doi: [10.1103/PhysRevLett.44.1502](https://doi.org/10.1103/PhysRevLett.44.1502) (cit. on p. 12).
- [39] Y. J. Choi, H. T. Yi, S. Lee, et al. “Ferroelectricity in an ising chain magnet.” In: *Phys. Rev. Lett.* 100.4 (2008). doi: [10.1103/PhysRevLett.100.047601](https://doi.org/10.1103/PhysRevLett.100.047601) (cit. on p. 12).
- [40] A. Muñoz, M. T. Casáis, J. A. Alonso, et al. “Complex magnetism and magnetic structures of the metastable HoMnO₃ perovskite.” In: *Inorg. Chem.* 40.5 (2001), pp. 1020–1028. doi: [10.1021/ic0011009](https://doi.org/10.1021/ic0011009) (cit. on pp. 12, 13).
- [41] G. Giovannetti, A. Stroppa, S. Picozzi, et al. “Dielectric properties and magnetostriction of the collinear multiferroic spinel CdV₂O₄.” In: *Phys. Rev. B* 83.6 (2011), p. 060402. doi: [10.1103/PhysRevB.83.060402](https://doi.org/10.1103/PhysRevB.83.060402) (cit. on p. 12).
- [42] L. C. Chapon, G. R. Blake, M. J. Gutmann, et al. “Structural anomalies and multiferroic behavior in magnetically frustrated TbMn₂O₅.” In: *Phys. Rev. Lett.* 93.17 (2004), pp. 10–13. doi: [10.1103/PhysRevLett.93.177402](https://doi.org/10.1103/PhysRevLett.93.177402) (cit. on pp. 12, 21, 24, 26).
- [43] S. Picozzi, K. Yamauchi, B. Sanyal, et al. “Dual nature of improper ferroelectricity in a magnetoelectric multiferroic.” In: *Phys. Rev. Lett.* 99.22 (2007), pp. 1–4. doi: [10.1103/PhysRevLett.99.227201](https://doi.org/10.1103/PhysRevLett.99.227201) (cit. on p. 14).
- [44] G. Yahia, F. Damay, S. Chattopadhyay, et al. “Recognition of exchange striction as the origin of magnetoelectric coupling in multiferroics.” In: *Phys. Rev. B* 95.18 (2017), p. 184112. doi: [10.1103/PhysRevB.95.184112](https://doi.org/10.1103/PhysRevB.95.184112) (cit. on pp. 14, 25, 26, 28, 63, 68, 91, 105).
- [45] T. Arima. “Ferroelectricity induced by proper-screw type magnetic order.” In: *J. Phys. Soc. Japan* 76.7 (2007), pp. 1–4. doi: [10.1143/JPSJ.76.073702](https://doi.org/10.1143/JPSJ.76.073702) (cit. on p. 14).
- [46] S. Dong, J. M. Liu, S. W. Cheong, et al. “Multiferroic materials and magnetoelectric physics: Symmetry, entanglement, excitation, and topology.” In: *Adv. Phys.* 64.5-6 (2015), pp. 519–626. doi: [10.1080/00018732.2015.1114338](https://doi.org/10.1080/00018732.2015.1114338) (cit. on p. 14).
- [47] W. Prellier, M. P. Singh, and P. Murugavel. “The single-phase multiferroic oxides: from bulk to thin film.” In: *J. Phys. Condens. Matter* 17.30 (2005), R803. doi: [10.1088/0953-8984/17/30/R01](https://doi.org/10.1088/0953-8984/17/30/R01) (cit. on p. 18).
- [48] N. Hur, S. Park, P. A. Sharma, et al. “Colossal Magnetodielectric Effects in DyMn₂O₅.” In: *Phys. Rev. Lett.* 93.10 (2004), p. 107207. doi: [10.1103/PhysRevLett.93.107207](https://doi.org/10.1103/PhysRevLett.93.107207) (cit. on pp. 18, 21, 27–29).
- [49] M. Fukunaga, Y. Sakamoto, H. Kimura, et al. “Magnetic-field-induced polarization flop in multiferroic TmMn₂O₅.” In: *Phys. Rev. Lett.* 103.7 (2009), pp. 2–5. doi: [10.1103/PhysRevLett.103.077204](https://doi.org/10.1103/PhysRevLett.103.077204) (cit. on pp. 18, 24, 30, 31).
- [50] N. Lee, C. Vecchini, Y. J. Choi, et al. “Giant tunability of ferroelectric polarization in GdMn₂O₅.” In: *Phys. Rev. Lett.* 110.13 (2013), pp. 2–5. doi: [10.1103/PhysRevLett.110.137203](https://doi.org/10.1103/PhysRevLett.110.137203) (cit. on pp. 18, 21, 27–29, 99, 102).
- [51] A. B. Sushkov, R. V. Aguilar, S. Park, et al. “Electromagnons in multiferroic YMn₂O₅ and TbMn₂O₅.” In: *Phys. Rev. Lett.* 98.2 (2007), p. 27202. doi: [10.1103/PhysRevLett.98.027202](https://doi.org/10.1103/PhysRevLett.98.027202) (cit. on pp. 18, 33, 34, 86).

- [52] V. Balédent, S. Chattopadhyay, P. Fertey, et al. “Evidence for Room Temperature Electric Polarization in RMn_2O_5 Multiferroics.” In: *Phys. Rev. Lett.* 114.11 (2015), p. 117601. doi: [10.1103/PhysRevLett.114.117601](https://doi.org/10.1103/PhysRevLett.114.117601) (cit. on pp. 18, 19, 25, 27, 55, 79, 83, 87).
- [53] C. Wilkinson, F. Sinclair, P. Gardner, et al. “The antiferromagnetic structure of DyMn_2O_5 at 4.2 K.” In: *J. Phys. C Solid State Phys.* 14.11 (1981), p. 1671. doi: [10.1088/0022-3719/14/11/027](https://doi.org/10.1088/0022-3719/14/11/027) (cit. on pp. 18, 70).
- [54] S. Petit, V. Balédent, C. Doubrovsky, et al. “Investigation of the electromagnon excitations in the multiferroic TbMn_2O_5 .” In: *Phys. Rev. B* 87.14 (2013), p. 140301. doi: [10.1103/PhysRevB.87.140301](https://doi.org/10.1103/PhysRevB.87.140301) (cit. on pp. 20, 63, 76, 77, 91).
- [55] P. G. Radaelli and L. C. Chapon. “A neutron diffraction study of RMn_2O_5 multiferroics.” In: *J. Phys. Condens. Matter* 20.43 (2008), p. 434213. doi: [10.1088/0953-8984/20/43/434213](https://doi.org/10.1088/0953-8984/20/43/434213) (cit. on pp. 20–22).
- [56] S. Chattopadhyay, S. Petit, E. Ressouche, et al. “3d-4f coupling and multiferroicity in frustrated Cairo Pentagonal oxide DyMn_2O_5 .” In: *Sci. Rep.* 7.1 (2017), p. 14506. doi: [10.1038/s41598-017-15150-w](https://doi.org/10.1038/s41598-017-15150-w) (cit. on pp. 20, 26–28, 63, 68, 70, 92, 93).
- [57] G. Yahia, F. Damay, S. Chattopadhyay, et al. “Experimental evidence for the microscopic mechanism of the unusual spin-induced electric polarization in GdMn_2O_5 .” In: *Phys. Rev. B* 97.8 (2018), p. 085128. doi: [10.1103/PhysRevB.97.085128](https://doi.org/10.1103/PhysRevB.97.085128) (cit. on pp. 20, 26, 27, 63, 68, 77, 99–101).
- [58] G. R. Blake, L. C. Chapon, P. G. Radaelli, et al. “Spin structure and magnetic frustration in multiferroic RMn_2O_5 .” In: *Phys. Rev. B* 71.21 (2005), p. 214402. doi: [10.1103/PhysRevB.71.214402](https://doi.org/10.1103/PhysRevB.71.214402) (cit. on pp. 20, 22, 26, 77, 92).
- [59] C. Doubrovsky, G. André, A. Gukasov, et al. “Magnetic phase transitions in PrMn_2O_5 : Importance of ion-size threshold size effects in RMn_2O_5 compounds (R=rare earth).” In: *Phys. Rev. B* 86.17 (2012), p. 174417. doi: [10.1103/PhysRevB.86.174417](https://doi.org/10.1103/PhysRevB.86.174417) (cit. on pp. 21, 26, 63, 73, 85, 86, 91).
- [60] S. Chattopadhyay, V. Balédent, F. Damay, et al. “Evidence of multiferroicity in NdMn_2O_5 .” In: *Phys. Rev. B* 93.10 (2016), p. 104406. doi: [10.1103/PhysRevB.93.104406](https://doi.org/10.1103/PhysRevB.93.104406) (cit. on pp. 21, 24, 26, 63).
- [61] Y. Koyata and K. Kohn. “Low-temperature phase transition in ErMn_2O_5 .” In: *Ferroelectrics* 204.1 (1997), pp. 115–124. doi: [10.1080/00150199708222193](https://doi.org/10.1080/00150199708222193) (cit. on pp. 21, 28).
- [62] I. Kagomiya and K. Kohn. “Ferroelectric transitions of LuMn_2O_5 .” In: *Ferroelectrics* 219.1 (1998), pp. 169–176. doi: [10.1080/00150199808213513](https://doi.org/10.1080/00150199808213513) (cit. on p. 21).
- [63] T. Fujita and K. Kohn. “Ferroelectricity of SmMn_2O_5 .” In: *Ferroelectrics* 219.1 (1998), pp. 155–160. doi: [10.1080/00150199808213511](https://doi.org/10.1080/00150199808213511) (cit. on p. 21).
- [64] D. Higashiyama, S. Miyasaka, and Y. Tokura. “Magnetic-field-induced polarization and depolarization in HoMn_2O_5 and ErMn_2O_5 .” In: *Phys. Rev. B* 72.6 (2005), p. 064421. doi: [10.1103/PhysRevB.72.064421](https://doi.org/10.1103/PhysRevB.72.064421) (cit. on pp. 21, 30).
- [65] S. Kobayashi, H. Kimura, Y. Noda, et al. “Neutron Diffraction Study of Magnetic Ordering Associated with Ferroelectricity in TmMn_2O_5 .” In: *J. Phys. Soc. Japan* 74.1 (2005), pp. 468–472. doi: [10.1143/JPSJ.74.468](https://doi.org/10.1143/JPSJ.74.468) (cit. on pp. 21, 26).
- [66] R. P. Chaudhury, C. R. dela Cruz, B. Lorenz, et al. “Pressure-induced polarization reversal in multiferroic YMn_2O_5 .” In: *Phys. Rev. B* 77.22 (2008), p. 220104. doi: [10.1103/PhysRevB.77.220104](https://doi.org/10.1103/PhysRevB.77.220104) (cit. on pp. 21, 31, 32, 82, 100).
- [67] M. Fukunaga, Y. Sakamoto, H. Kimura, et al. “Magnetic phase transitions and magnetic-field-induced polarization flops in multiferroic YbMn_2O_5 .” In: *J. Phys. Soc. Japan* 80.1 (2011), pp. 1–5. doi: [10.1143/JPSJ.80.014705](https://doi.org/10.1143/JPSJ.80.014705) (cit. on pp. 21, 24, 26, 31).

- [68] Z. Y. Zhao, M. F. Liu, X Li, et al. “Experimental observation of ferrielectricity in multiferroic DyMn_2O_5 .” In: *Sci. Rep.* 4.1 (2015), p. 3984. doi: [10.1038/srep03984](https://doi.org/10.1038/srep03984) (cit. on pp. 21, 26).
- [69] T. Doi and K. Kohn. “Magnetoelectric effect and simultaneous electric and magnetic transition in EuMn_2O_5 .” In: *Phase Transitions* 38.4 (1992), pp. 273–284. doi: [10.1080/01411599208213207](https://doi.org/10.1080/01411599208213207) (cit. on p. 21).
- [70] W. Ratcliff, V. Kiryukhin, M. Kenzelmann, et al. “Magnetic phase diagram of the colossal magnetoelectric DyMn_2O_5 .” In: *Phys. Rev. B* 72.6 (2005), p. 60407. doi: [10.1103/PhysRevB.72.060407](https://doi.org/10.1103/PhysRevB.72.060407) (cit. on pp. 21, 23, 26, 32, 92).
- [71] P. P. Gardner, C. Wilkinson, J. B. Forsyth, et al. “The magnetic structures of the rare-earth manganates ErMn_2O_5 and TbMn_2O_5 .” In: *J. Phys. C Solid State Phys.* 21.33 (1988), pp. 5653–5661. doi: [10.1088/0022-3719/21/33/009](https://doi.org/10.1088/0022-3719/21/33/009) (cit. on pp. 22, 26).
- [72] E. Golovenchits and V. Sanina. “Magnetic and magnetoelectric dynamics in RMn_2O_5 (R = Gd and Eu).” In: *J. Phys. Condens. Matter* 16.24 (2004), pp. 4325–4334. doi: [10.1088/0953-8984/16/24/014](https://doi.org/10.1088/0953-8984/16/24/014) (cit. on p. 22).
- [73] Y. Noda, H. Kimura, M. Fukunaga, et al. “Magnetic and ferroelectric properties of multiferroic RMn_2O_5 .” In: *J. Phys. Condens. Matter* 20.43 (2008), p. 434206. doi: [10.1088/0953-8984/20/43/434206](https://doi.org/10.1088/0953-8984/20/43/434206) (cit. on p. 22).
- [74] M. Fukunaga and Y. Noda. “Classification and interpretation of the polarization of multiferroic RMn_2O_5 .” In: *J. Phys. Soc. Japan* 79.5 (2010), pp. 1–5. doi: [10.1143/JPSJ.79.054705](https://doi.org/10.1143/JPSJ.79.054705) (cit. on p. 23).
- [75] L. C. Chapon, P. G. Radaelli, G. R. Blake, et al. “Ferroelectricity induced by acentric spin-density waves in YMn_2O_5 .” In: *Phys. Rev. Lett.* 96.9 (2006), pp. 1–4. doi: [10.1103/PhysRevLett.96.097601](https://doi.org/10.1103/PhysRevLett.96.097601) (cit. on pp. 24, 26, 94).
- [76] I. Kagomiya, S. Matsumoto, K. Kohn, et al. “Lattice distortion at ferroelectric transition of YMn_2O_5 .” In: *Ferroelectrics* 286.January 2014 (2003), pp. 167–174. doi: [10.1080/00150190390206347](https://doi.org/10.1080/00150190390206347) (cit. on pp. 24, 25).
- [77] J. H. Kim, M. A. Van Der Vegte, A. Scaramucci, et al. “Magnetic excitations in the low-temperature ferroelectric phase of multiferroic YMn_2O_5 using inelastic neutron scattering.” In: *Phys. Rev. Lett.* 107.9 (2011), pp. 1–4. doi: [10.1103/PhysRevLett.107.097401](https://doi.org/10.1103/PhysRevLett.107.097401) (cit. on p. 26).
- [78] A. Muñoz, J. A. Alonso, M. T. Casais, et al. “A Study of the Magnetic Structure of LaMn_2O_5 from Neutron Powder Diffraction Data.” In: *Eur. J. Inorg. Chem.* 2005.4 (2005), pp. 685–691. doi: [10.1002/ejic.200400548](https://doi.org/10.1002/ejic.200400548) (cit. on pp. 26, 91).
- [79] Y. Ishii, S. Horio, M. Mitarashi, et al. “Observation of magnetic order in multiferroic SmMn_2O_5 studied by resonant x-ray magnetic scattering.” In: *Phys. Rev. B* 93.6 (2016), p. 64415. doi: [10.1103/PhysRevB.93.064415](https://doi.org/10.1103/PhysRevB.93.064415) (cit. on pp. 26, 105).
- [80] V. Polyakov, V. Plakhty, M. Bonnet, et al. “Coupled magnetic and structural transitions in EuMn_2O_5 as studied by neutron diffraction and three-dimensional polarization analysis.” In: *Phys. B Condens. Matter* 297.1-4 (2001), pp. 208–212. doi: [10.1016/S0921-4526\(00\)00851-6](https://doi.org/10.1016/S0921-4526(00)00851-6) (cit. on pp. 26, 86).
- [81] A. Muñoz, J. A. Alonso, M. Casais, et al. “Magnetic structure and properties of BiMn_2O_5 .” In: *Phys. Rev. B* 65.14 (2002), p. 144423. doi: [10.1103/PhysRevB.65.144423](https://doi.org/10.1103/PhysRevB.65.144423) (cit. on pp. 26, 91).
- [82] J. W. Kim, S. Y. Haam, Y. S. Oh, et al. “Observation of a multiferroic critical end point.” In: *Proc. Natl. Acad. Sci.* 106.37 (2009), pp. 15573–15576. doi: [10.1073/pnas.0907589106](https://doi.org/10.1073/pnas.0907589106) (cit. on pp. 28, 29).
- [83] Y. Koyata, H. Nakamura, N. Iwata, et al. “Electric and Magnetic Low-Temperature Phase Transitions of YbMn_2O_5 .” In: *J. Phys. Soc. Japan* 65.5 (1996), pp. 1383–1386. doi: [10.1143/JPSJ.65.1383](https://doi.org/10.1143/JPSJ.65.1383) (cit. on pp. 28, 31).

- [84] J. Koo, C. Song, S. Ji, et al. “Non-resonant and resonant X-ray scattering studies on multiferroic TbMn_2O_5 .” In: *Phys. Rev. Lett.* 99.19 (2007), pp. 1–4. doi: [10.1103/PhysRevLett.99.197601](https://doi.org/10.1103/PhysRevLett.99.197601) (cit. on p. 29).
- [85] I. A. Kornev, L. Bellaiche, P. Bouvier, et al. “Ferroelectricity of perovskites under pressure.” In: *Phys. Rev. Lett.* 95.19 (2005), pp. 4–7. doi: [10.1103/PhysRevLett.95.196804](https://doi.org/10.1103/PhysRevLett.95.196804) (cit. on p. 31).
- [86] E. Bousquet and P. Ghosez. “First-principles study of barium titanate under hydrostatic pressure.” In: *Phys. Rev. B* 74.18 (2006), p. 180101. doi: [10.1103/PhysRevB.74.180101](https://doi.org/10.1103/PhysRevB.74.180101) (cit. on p. 31).
- [87] C. R. dela Cruz, B. Lorenz, Y. Y. Sun, et al. “Pressure-induced enhancement of ferroelectricity in multiferroic RMn_2O_5 (R=Tb, Dy, Ho).” In: *Phys. Rev. B* 76.17 (2007), p. 174106. doi: [10.1103/PhysRevB.76.174106](https://doi.org/10.1103/PhysRevB.76.174106) (cit. on pp. 31, 32, 77, 93, 100).
- [88] N. Poudel, M. Gooch, B. Lorenz, et al. “Pressure-induced decoupling of rare-earth moments and Mn spins in multiferroic GdMn_2O_5 .” In: *Phys. Rev. B* 92.14 (2015), p. 144430. doi: [10.1103/PhysRevB.92.144430](https://doi.org/10.1103/PhysRevB.92.144430) (cit. on pp. 33, 100, 102, 104).
- [89] N. Poudel, M. Gooch, B. Lorenz, et al. “Pressure Effect on Ferroelectric Properties of GdMn_2O_5 and TmMn_2O_5 .” In: *IEEE Trans. Magn.* 52.7 (2016), pp. 1–4. doi: [10.1109/TMAG.2016.2528169](https://doi.org/10.1109/TMAG.2016.2528169) (cit. on p. 33).
- [90] M. Deutsch, T. C. Hansen, M. T. Fernandez-Diaz, et al. “Pressure-induced commensurate phase with potential giant polarization in YMn_2O_5 .” In: *Phys. Rev. B* 92.6 (2015), p. 060410. doi: [10.1103/PhysRevB.92.060410](https://doi.org/10.1103/PhysRevB.92.060410) (cit. on pp. 33, 77, 82, 83, 87, 90, 93, 97, 101, 104, 106, 109).
- [91] A. Pimenov, A. A. Mukhin, V. Y. Ivanov, et al. “Possible evidence for electromagnons in multiferroic manganites.” In: *Nat. Phys.* 2.2 (2006), pp. 97–100. doi: [10.1038/nphys212](https://doi.org/10.1038/nphys212) (cit. on p. 33).
- [92] E. I. Golovenchits and V. A. Sanina. “Magnetic and Magneto-Lattice Dynamics in GdMn_2O_5 .” In: *J. Exp. Theor. Phys. Lett.* 78.2 (2003), pp. 88–91. doi: [10.1134/1.1615536](https://doi.org/10.1134/1.1615536) (cit. on p. 33).
- [93] J. Als-Nielsen and D. McMorrow. *Elements of Modern X-ray Physics*. Hoboken, NJ, USA: John Wiley & Sons, Inc., 2011. doi: [10.1002/9781119998365](https://doi.org/10.1002/9781119998365) (cit. on p. 39).
- [94] Y. Waseda, E. Matsubara, and K. Shinoda. *X-Ray Diffraction Crystallography: Introduction, Examples and Solved Problems*. Berlin, Heidelberg: Springer Berlin Heidelberg, 2011, p. 322. doi: [10.1007/978-3-642-16635-8](https://doi.org/10.1007/978-3-642-16635-8) (cit. on pp. 39, 41–45).
- [95] A. D. Chijioke, W. J. Nellis, A. Soldatov, et al. “The ruby pressure standard to 150 GPa.” In: *J. Appl. Phys.* 98.11 (2005), pp. 1–9. doi: [10.1063/1.2135877](https://doi.org/10.1063/1.2135877) (cit. on p. 49).
- [96] J. Chadwick. “The existence of a neutron.” In: *Proc. R. Soc. London. Ser. A* 136.830 (1932), pp. 692–708 (cit. on p. 49).
- [97] H. V. Halban and P. Preiswerk. “Preuve expérimentale de la diffraction des neutrons.” In: *C.R. Acad. Sci. Paris* 203 (1936), pp. 73–75 (cit. on p. 49).
- [98] D. P. Mitchell and P. N. Powers. “Bragg Reflection of Neutrons.” In: *Phys. Rev.* 50.1 (1936), pp. 486–487 (cit. on p. 49).
- [99] B. T. M. Willis and C. J. Carlile. *Experimental Neutron Scattering*. 2013, p. 344 (cit. on pp. 49–51, 54, 55).
- [100] G. L. Squires. *Introduction to the Theory of Thermal Neutron Scattering*. 3rd. Cambridge: Cambridge University Press, 2012. doi: [10.1017/CB09781139107808](https://doi.org/10.1017/CB09781139107808) (cit. on pp. 49, 52).
- [101] T. Chatterji. *Neutron Scattering from Magnetic Materials*. Elsevier Science, 2005 (cit. on p. 50).
- [102] B. Roessli and P. Böni. *Scattering: Scattering and inverse scattering in pure and applied science. Chap. Polarised Neutron Scattering*. Academic Press, 2002, pp. 1242–1263 (cit. on p. 53).

- [103] W. G. Marshall and D. J. Francis. “Attainment of near-hydrostatic compression conditions using the Paris-Edinburgh cell.” In: *J. Appl. Crystallogr.* 35.1 (2002), pp. 122–125. doi: [10.1107/S0021889801018350](https://doi.org/10.1107/S0021889801018350) (cit. on p. 57).
- [104] S. Klotz, L. Paumier, G. Le March, et al. “The effect of temperature on the hydrostatic limit of 4:1 methanol-ethanol under pressure.” In: *High Press. Res.* 29.4 (2009), pp. 649–652. doi: [10.1080/08957950903418194](https://doi.org/10.1080/08957950903418194) (cit. on p. 57).
- [105] P. Vinet, J. R. Smith, J. Ferrante, et al. “Temperature effects on the universal equation of state of solids.” In: *Phys. Rev. B* 35.4 (1987), pp. 1945–1953. doi: [10.1103/PhysRevB.35.1945](https://doi.org/10.1103/PhysRevB.35.1945) (cit. on p. 57).
- [106] T. Strässle, S. Klotz, K. Kunc, et al. “Equation of state of lead from high-pressure neutron diffraction up to 8.9 GPa and its implication for the NaCl pressure scale.” In: *Phys. Rev. B - Condens. Matter Mater. Phys.* 90.1 (2014), pp. 1–8. doi: [10.1103/PhysRevB.90.014101](https://doi.org/10.1103/PhysRevB.90.014101) (cit. on p. 58).
- [107] J. Rodríguez-Carvajal. “Recent advances in magnetic structure determination by neutron powder diffraction.” In: *Phys. B Condens. Matter* 192.1-2 (1993), pp. 55–69. doi: [10.1016/0921-4526\(93\)90108-I](https://doi.org/10.1016/0921-4526(93)90108-I) (cit. on pp. 58, 68, 83, 86, 93, 100, 105).
- [108] H. M. Rietveld. “A profile refinement method for nuclear and magnetic structures.” In: *J. Appl. Crystallogr.* 2.2 (1969), pp. 65–71. doi: [10.1107/S0021889869006558](https://doi.org/10.1107/S0021889869006558) (cit. on pp. 58, 68, 87, 93, 100).
- [109] R. E. Dinnebier and S. J. L. Billinge. *Powder Diffraction: Theory and Practice*. 2008, p. 2. doi: [10.1039/9781847558237](https://doi.org/10.1039/9781847558237) (cit. on pp. 58, 60).
- [110] H. M. Rietveld. “Line profiles of neutron powder-diffraction peaks for structure refinement.” In: *Acta Crystallogr.* 22.1 (1967), pp. 151–152. doi: [10.1107/S0365110X67000234](https://doi.org/10.1107/S0365110X67000234) (cit. on p. 58).
- [111] L. W. Finger, D. E. Cox, and A. P. Jephcoat. “Correction for powder diffraction peak asymmetry due to axial divergence.” In: *J. Appl. Crystallogr.* 27.pt 6 (1994), pp. 892–900. doi: [10.1107/S0021889894004218](https://doi.org/10.1107/S0021889894004218) (cit. on p. 59).
- [112] A. Eichler and J. Wittig. “Pressure dependence of the superconducting transition temperature of lead.” In: *Z. Angew. Phys.* 25.5 (1968), pp. 319–327 (cit. on p. 62).
- [113] G. Popov, M. Greenblatta, and W. H. McCarroll. “Synthesis of LnMn_2O_5 (Ln = Nd, Pr) crystals using fused salt electrolysis.” In: *Mater. Res. Bull.* 35.10 (2000), pp. 1661–1667. doi: [10.1016/S0025-5408\(00\)00372-X](https://doi.org/10.1016/S0025-5408(00)00372-X) (cit. on p. 62).
- [114] L. H. Thomas. “The calculation of atomic fields.” In: *Math. Proc. Cambridge Philos. Soc.* 23.5 (1927), pp. 542–548. doi: [10.1017/S0305004100011683](https://doi.org/10.1017/S0305004100011683) (cit. on p. 65).
- [115] E. Fermi. “Eine statistische Methode zur Bestimmung einiger Eigenschaften des Atoms und ihre Anwendung auf die Theorie des periodischen Systems der Elemente.” In: *Zeitschrift für Phys.* 48.1-2 (1928), pp. 73–79. doi: [10.1007/BF01351576](https://doi.org/10.1007/BF01351576) (cit. on p. 65).
- [116] P. A. M. Dirac. “Note on Exchange Phenomena in the Thomas Atom.” In: *Math. Proc. Cambridge Philos. Soc.* 26.3 (1930), pp. 376–385. doi: [10.1017/S0305004100016108](https://doi.org/10.1017/S0305004100016108) (cit. on p. 65).
- [117] W. Kohn and L. J. Sham. “Self-consistent equations including exchange and correlation effects.” In: *Phys. Rev.* 140.4A (1965). doi: [10.1103/PhysRev.140.A1133](https://doi.org/10.1103/PhysRev.140.A1133) (cit. on p. 66).
- [118] R. O. Jones and O. Gunnarsson. “The density functional formalism, its applications and prospects.” In: *Rev. Mod. Phys.* 61.3 (1989), pp. 689–746. doi: [10.1103/RevModPhys.61.689](https://doi.org/10.1103/RevModPhys.61.689) (cit. on p. 66).
- [119] W. Kohn. “Nobel Lecture: Electronic structure of matter—wave functions and density functionals.” In: *Rev. Mod. Phys.* 71.5 (1999), pp. 1253–1266. doi: [10.1103/RevModPhys.71.1253](https://doi.org/10.1103/RevModPhys.71.1253) (cit. on p. 66).

- [120] W. Koch and M. C. Holthausen. *A Chemist's Guide to Density Functional Theory*. Vol. 3. Weinheim, FRG: Wiley Online Library, 2001, p. 294. DOI: [10.1002/3527600043](https://doi.org/10.1002/3527600043) (cit. on p. 66).
- [121] C. Prescher and V. B. Prakapenka. "DIOPTAS: A program for reduction of two-dimensional X-ray diffraction data and data exploration." In: *High Press. Res.* 35.3 (2015), pp. 223–230. DOI: [10.1080/08957959.2015.1059835](https://doi.org/10.1080/08957959.2015.1059835) (cit. on p. 66).
- [122] J. A. Alonso, M. T. Casais, M. J. Martínez-Lope, et al. "A structural study from neutron diffraction data and magnetic properties of RMn_2O_5 (R = La, rare earth)." In: *J. Phys. Condens. Matter* 9.40 (1997), pp. 8515–8526. DOI: [10.1088/0953-8984/9/40/017](https://doi.org/10.1088/0953-8984/9/40/017) (cit. on pp. 68, 70).
- [123] R. Dovesi, R. Orlando, A. Erba, et al. "CRYSTAL14: A program for the ab initio investigation of crystalline solids." In: *Int. J. Quantum Chem.* 114.19 (2014), pp. 1287–1317. DOI: [10.1002/qua.24658](https://doi.org/10.1002/qua.24658) (cit. on p. 69).
- [124] J. P. Perdew, A. Ruzsinszky, G. I. Csonka, et al. "Restoring the Density-Gradient Expansion for Exchange in Solids and Surfaces." In: *Phys. Rev. Lett.* 100.13 (2008), p. 136406. DOI: [10.1103/PhysRevLett.100.136406](https://doi.org/10.1103/PhysRevLett.100.136406) (cit. on p. 69).
- [125] M. Dolg, H. Stoll, and H. Preuss. "Energy-adjusted *ab initio* pseudopotentials for the rare earth elements." In: *J. Chem. Phys.* 90.3 (1989), pp. 1730–1734. DOI: [10.1063/1.456066](https://doi.org/10.1063/1.456066) (cit. on p. 69).
- [126] M. Dolg, H. Stoll, and H. Preuss. "A combination of quasirelativistic pseudopotential and ligand field calculations for lanthanoid compounds." In: *Theor. Chim. Acta* 85.6 (1993), pp. 441–450. DOI: [10.1007/BF01112983](https://doi.org/10.1007/BF01112983) (cit. on p. 69).
- [127] J. Yang and M. Dolg. "Valence basis sets for lanthanide 4f-in-core pseudopotentials adapted for crystal orbital ab initio calculations." In: *Theor. Chem. Acc.* 113.4 (2005), pp. 212–224. DOI: [10.1007/s00214-005-0629-0](https://doi.org/10.1007/s00214-005-0629-0) (cit. on p. 69).
- [128] M. F. Peintinger, D. V. Oliveira, and T. Bredow. "Consistent Gaussian basis sets of triple-zeta valence with polarization quality for solid-state calculations." In: *J. Comput. Chem.* 34.6 (2013), pp. 451–459. DOI: [10.1002/jcc.23153](https://doi.org/10.1002/jcc.23153) (cit. on p. 69).
- [129] D. P. Kozlenko, N. T. Dang, S. E. Kichanov, et al. "Competing magnetic and structural states in multiferroic YMn_2O_5 at high pressure." In: *Phys. Rev. B* 92.13 (2015), p. 134409. DOI: [10.1103/PhysRevB.92.134409](https://doi.org/10.1103/PhysRevB.92.134409) (cit. on pp. 73, 75, 82, 91).
- [130] A. Grzechnik, M. Tolkiehn, W. Morgenroth, et al. "High-pressure behaviours of HoMn_2O_5 and BiMn_2O_5 ." In: *J. Phys. Condens. Matter* 22.27 (2010), p. 275401. DOI: [10.1088/0953-8984/22/27/275401](https://doi.org/10.1088/0953-8984/22/27/275401) (cit. on pp. 73, 75, 91).
- [131] W. Peng, V. Balédent, S. Chattopadhyay, et al. "Toward pressure-induced multiferroicity in PrMn_2O_5 ." In: *Phys. Rev. B* 96.5 (2017), p. 054418. DOI: [10.1103/PhysRevB.96.054418](https://doi.org/10.1103/PhysRevB.96.054418) (cit. on pp. 73, 77, 79, 86, 93, 97, 101, 104, 106, 109).
- [132] J. Rault. "A universal modified van der Waals equation of state. Part I: Polymer and mineral glass formers." In: *Eur. Phys. J. E* 37.11 (2014), pp. 1–20. DOI: [10.1140/epje/i2014-14113-3](https://doi.org/10.1140/epje/i2014-14113-3) (cit. on p. 74).
- [133] D. Orobengoa, C. Capillas, M. I. Aroyo, et al. "AMPLIMODES : symmetry-mode analysis on the Bilbao Crystallographic Server." In: *J. Appl. Crystallogr.* 42.5 (2009), pp. 820–833. DOI: [10.1107/S0021889809028064](https://doi.org/10.1107/S0021889809028064) (cit. on p. 75).
- [134] J. M. Perez-Mato, D. Orobengoa, and M. I. Aroyo. "Mode crystallography of distorted structures." In: *Acta Crystallogr. Sect. A Found. Crystallogr.* 66.5 (2010), pp. 558–590. DOI: [10.1107/S0108767310016247](https://doi.org/10.1107/S0108767310016247) (cit. on p. 75).

- [135] M. Deutsch, W. Peng, P. Foury-Leykian, et al. “Pressure-induced commensurate order in TbMn_2O_5 and DyMn_2O_5 : Influence of rare-earth anisotropy and $3d-4f$ exchange.” In: *Phys. Rev. B* 98.2 (2018), p. 024408. DOI: [10.1103/PhysRevB.98.024408](https://doi.org/10.1103/PhysRevB.98.024408) (cit. on pp. 77, 93, 94, 97, 98, 101, 104, 106, 109, 114).
- [136] L. Elcoro, B. Bradlyn, Z. Wang, et al. “Double crystallographic groups and their representations on the Bilbao Crystallographic Server.” In: *J. Appl. Crystallogr.* 50.5 (2017), pp. 1457–1477. DOI: [10.1107/S1600576717011712](https://doi.org/10.1107/S1600576717011712) (cit. on p. 83).
- [137] M. I. Aroyo, J. M. Perez-Mato, D. Orobengoa, et al. “Crystallography online: Bilbao crystallographic server.” In: *Bulg. Chem. Commun.* 43.2 (2011), pp. 183–197. DOI: [10.1107/S205327331303091X](https://doi.org/10.1107/S205327331303091X) (cit. on p. 90).
- [138] S. V. Gallego, E. S. Tasci, G. De La Flor, et al. “Magnetic symmetry in the Bilbao Crystallographic Server: A computer program to provide systematic absences of magnetic neutron diffraction.” In: *J. Appl. Crystallogr.* 45.6 (2012), pp. 1236–1247. DOI: [10.1107/S0021889812042185](https://doi.org/10.1107/S0021889812042185) (cit. on p. 90).
- [139] J. M. Liu and S. Dong. “Ferrielectricity in DyMn_2O_5 : A golden touchstone for multiferroicity of RMn_2O_5 family.” In: *J. Adv. Dielectr.* 05.02 (2015), p. 1530003. DOI: [10.1142/S2010135X15300030](https://doi.org/10.1142/S2010135X15300030) (cit. on p. 92).
- [140] G. E. Johnstone, R. A. Ewings, R. D. Johnson, et al. “Magnetic structure of DyMn_2O_5 determined by resonant x-ray scattering.” In: *Phys. Rev. B* 85.22 (2012), p. 224403. DOI: [10.1103/PhysRevB.85.224403](https://doi.org/10.1103/PhysRevB.85.224403) (cit. on p. 92).
- [141] V. F. Sears. “Neutron scattering lengths and cross section.” In: *Neutron News* 3.3 (1992), pp. 26–37. DOI: [10.1080/10448639208218770](https://doi.org/10.1080/10448639208218770) (cit. on pp. 99, 105).
- [142] C. L. Lu, J. Fan, H. M. Liu, et al. “An investigation on magnetism, spin-phonon coupling, and ferroelectricity in multiferroic GdMn_2O_5 .” In: *Appl. Phys. A Mater. Sci. Process.* 96.4 (2009), pp. 991–996. DOI: [10.1007/s00339-009-5133-2](https://doi.org/10.1007/s00339-009-5133-2) (cit. on p. 99).

Titre : Influence de la pression sur la multiferroïcité de RMn_2O_5

Mots clés : multiferroïque, pression, RMn_2O_5 , électrique-magnéto couplage

Résumé : La série de RMn_2O_5 multiferroïques a été largement étudiée en raison de son fort couplage magnéto-électrique. L'origine de la ferroélectricité a été clarifiée en tant que mécanisme de striction d'échange. Comme les variations des distances interatomiques modifiées par la pression externe peuvent grandement affecter les propriétés multiferroïques, il est essentiel de comprendre l'origine microscopique de cet effet.

Nous avons déterminé la structure magnétique de la phase magnétique commensurable induite par la pression (PCM) et dessiné le diagramme de phase $p - T$. Sur la base d'un équilibre énergétique subtil entre l'interaction d'échange J_1 , l'interaction d'échange R-Mn J_6 et l'anisotropie de la terre rare, nous avons proposé un mécanisme de stabilisation des différentes phases magnétiques en fonction de la pression pour les différents composés avec R=Dy, Gd et Sm. L'augmentation de J_1 sous pression à température ambiante obtenue grâce à l'étude par diffraction X confirme ce mécanisme. Une explication supplémentaire a été proposée pour le cas particulier de PrMn_2O_5 . Ces résultats ouvrent certainement la voie à une compréhension complète de l'origine de l'influence de la pression dans la famille RMn_2O_5 .

Title: Influence of the pressure on the multiferroicity of RMn_2O_5

Keywords: multiferroic, pressure, RMn_2O_5 , magneto-electric coupling

Abstract: The series of multiferroic RMn_2O_5 has been extensively studied due to its strong magneto-electric coupling. The ferroelectricity origin has been clarified as the exchange striction mechanism. As the variations of the interatomic distances modified by the external pressure can greatly affect the multiferroic properties, it is essential to understand the microscopic origin of this effect.

In this thesis, we have systematically studied the multiferroic properties of the RMn_2O_5 compounds by using powder X-rays diffraction and powder neutron diffraction (PND) under pressure. We have determined the magnetic structure of the pressure induced commensurate magnetic (PCM) phase and drawn the $p - T$ phase diagram. Based on a subtle energy balance among the exchange interaction J_1 , the R-Mn exchange interaction J_6 and the anisotropy of the rare earth, we have proposed a mechanism for stabilizing the different magnetic phases as a function of the pressure for the different compounds with R = Dy, Gd and Sm. The enhanced J_1 under pressure at room temperature from the X-ray diffraction study further confirms this mechanism. An additional explanation has been proposed for the special case of the PrMn_2O_5 . These results certainly pave the way to fully understand the origin of the pressure influence in the RMn_2O_5 family.



